# Optimizing accuracy of determinations of $CO_2$ storage capacity and permanence, and designing more efficient storage operations: An example from the Rock Springs Uplift, Wyoming

Final Report to U.S. Department of Energy

Reporting Period Start Date: October 2012
Reporting Period End Date: September 2015

Principal Author: J. Fred McLaughlin - Principal Investigator

Contributing Authors
Ramsey Bentley
Shanna Dahl
Allory Deiss
Andrew Duguid
Yuri Ganshin
Zunsheng Jiao
Scott Quillinan

*Date Report was issued: December 2015*

DOE Award Number: DE-FE0009202

Carbon Management Institute
University of Wyoming
1020 E. Lewis Street, Energy Innovation Center
Dept. 4902, 1000 E. University Ave.
Laramie, WY 82071-2000


University of Wyoming Carbon Management Institute
School of Energy Resources
U.S. Department of Energy Final Report

DOE Award Number: DE-FE0009202

# Optimizing accuracy of determinations of $CO_2$ storage capacity and permanence, and designing more efficient storage operations: An example from the Rock Springs Uplift, Wyoming

Carbon Management Institute
University of Wyoming
1020 E. Lewis Street, Energy Innovation Center
Dept. 4902, 1000 E. University Ave.
Laramie, WY 82071-2000

# DISCLAIMER*

# ABSTRACT

At a potential injection site on the Rock Springs Uplift in southwest Wyoming, an investigation of confining layers was undertaken to develop and test methodology, identify key data requirements, assess previous injection scenarios relative to detailed confining layer properties, and integrate all findings in order to reduce the uncertainty of $CO_2$ storage permanence. The assurance of safe and permanent storage of $CO_2$ at a storage site involves a detailed evaluation of the confining layers. Four suites of field data were recognized as crucial for determining storage permanence relative to the confining layers; seismic, core and petrophysical data from a wellbore, formation fluid samples, and in-situ formation tests. Core and petrophysical data were used to create a vertical heterogenic property model that defined porosity, permeability, displacement pressure, geomechanical strengths, and diagenetic history.

These analyses identified four primary confining layers and multiple redundant confining layers. In-situ formation tests were used to evaluate fracture gradients, regional stress fields, baseline microseismic data, step-rate injection tests, and formation perforation responses. Seismic attributes, correlated with the vertical heterogenic property models, were calculated and used to create a 3-D volume model over the entire site. The seismic data provided the vehicle to transform the vertical heterogenic property model into a horizontal heterogenic property model, which allowed for the evaluation of confining layers across the entire study site without risking additional wellbore perforations. Lastly, formation fluids were collected and analyzed for geochemical and isotopic compositions from stacked reservoir systems. These data further tested primary confining layers, by evaluating the evidence of mixing between target reservoirs (mixing would imply an existing breach of primary confining layers).

All data were propagated into a dynamic, heterogenic geologic property model used to test various injection scenarios. These tests showed that the study site could retain 25MT of injected $CO_2$ over an injection lifespan of 50 years. Major findings indicate that active reservoir pressure management through reservoir fluid production (minimum of three production wells) greatly reduces the risk of breaching a confining layer. To address brine production, a well completion and engineering study was incorporated to reduce the risks of scaling and erosion during injection and production. These scenarios suggest that the dolostone within the Mississippian Madison Limestone is the site's best injection/production target by two orders of magnitude, and that commercial well equipment would meet all performance requirements. This confirms that there are multiple confining layers in southwest Wyoming that are capable of retaining commercial volumes of CO2, making Wyoming's Paleozoic reservoirs ideal storage targets for low-risk injection and long-term storage.

This study also indicates that column height retention calculations are reduced in a $CO_2$-brine system relative to a hydrocarbon-brine system, which is an observation that affects all potential CCS sites. Likewise, this study identified the impacts that downhole testing imparts on reservoir fluids, and the likelihood of introducing uncertainty in baseline site assumptions and later modeling.

# TABLE OF CONTENTS

# EXECUTIVE SUMMARY

## Introduction

The goal of this project was to improve estimates of $CO_2$ storage reservoir storage capacity, evaluate the long-term integrity and performance of confining layers, and manage injection pressures and brine production to optimize $CO_2$ storage efficiency for the Rock Springs Uplift (RSU), Wyoming - Wyoming's highest-priority $CO_2$ storage site containing the most promising storage reservoirs. Ensuring the permanence of long-term storage is a major challenge for all potential carbon capture and storage (CCS) projects. This study builds on previous work such as the reservoir characterization of a potential CCS site on the Rock Springs Uplift (RSU) in southwest Wyoming (DE-FE0002142) through a complete investigation of potential confining layers relative to long-term $CO_2$ injection and storage. Previous studies of the RSU study site identified two Paleozoic reservoirs as having the potential to store commercial volumes of $CO_2$ over a probable lifespan of a power plant (approximately 50 years) (DE-FE0002142). This study concluded that the best reservoir interval, dolostones in the upper Madison Limestone, could effectively receive 1MT of injected $CO_2$ per year without compromising the storage volume. However, these simulations did not account for the physical properties of associated confining layers (also deemed seals and/or sealing formations).

This project was implemented to meet the following three objectives to validate storage permanence at one of the most promising CCS sites in the Rocky Mountains;

1. Reduce uncertainty in estimates of $CO_2$ storage capacity relative to confining layers
2. Evaluate and ensure the permanence of $CO_2$ storage at the RSU
3. Improve the efficiency of storage operations on the RSU

The Carbon Management Institute (CMI) collected subsurface data from a stratigraphic test well and a 3-D seismic survey. We recognize four critical data components for determining $CO_2$ storage permanence; seismic data, core and petrophysical data from a wellbore, formation fluid data, and in-situ formation tests. Core and petrophysical data were used to create a vertical heterogenic property model that defined porosity, permeability, displacement pressure, geomechanical strengths, diagenetic history, and to identify four primary confining layers and multiple redundant confining layers. In-situ formation tests were used to evaluate fracture gradients, regional stress fields, baseline microseismic data, step-rate injection tests, and formation perforation responses. Seismic attributes, correlated with the vertical heterogenic property models, were calculated and used to create a 3-D volume model over the entire site. The seismic data provided the vehicle to transform the vertical heterogenic property model into a horizontal heterogenic property model, which allowed for the evaluation of confining layers across the entire study site without risking additional wellbore perforations. Lastly, formation fluids were collected and analyzed for geochemical and isotopic compositions from stacked reservoir systems. These data further tested primary confining layers, by evaluating the evidence of mixing between target reservoirs (mixing would imply an existing breach of primary confining layers).

Petrographic and mechanical analysis determined that there were four primary confining layers that could competently retain injected $CO_2$ associated within the targeted reservoirs, and at least three redundant (secondary) confining layers. The confining layers were analyzed by facies to determine lithologic controls; unaltered micritic limestones were identified as having the greatest sealing capacities with displacement pressures that were >3,630 psi; all seals were shown to be more mechanically competent than targeted seals indicating reservoirs would fail before sealing lithologies. Several confining layers were also identified as having increased sealing capacities due to diagenetic alteration, supporting the need for site-specific evaluations at potential CCS sites. Seismic attribute data showed the relative homogeneity of one of the thickest confining layers across the study site. In addition, the seismic analysis was able to characterize two seal bypass systems, greatly reducing the risk of unidentified breaching systems. Geochemical brine analysis showed no evidence of mixing between different reservoir fluids, helping to validate the assumption of existing effective confining layers. This helped to define new methodologies for the evaluation of seals within stacked reservoir systems. However, brine analysis did identify the effects of in-situ well testing; oxidation of a second set of samples resulted in differing conclusions in well scaling and geochemical models and specify the importance of determining realistic baseline conditions.

New numerical simulation models were developed and populated with the confining layer data obtained from the field data. Multiple injection scenarios were run to determine the likelihood of seal failure and to assess long-term storage. The refined models suggested that the ideal low-risk, high probability injection scenario was to implement 0.5Mt of injection per year into the best reservoir zone over a 50-year project interval. The low-risk injection scenario storage estimate was developed to account for new $CO_2$ column height estimates of approximately 450 feet. This refinement helped to reduce the uncertainty in storage estimates to a great degree (Objective 1). Analysis of confining layer data relative to numerical injection scenarios identified major risks, such as diffusion and fault systems, which were crucial to validating storage permanence (Objective 2). Dynamic fluid injection models also identified the period of highest risk relative to confinement as the injection period, though the risk of seal failure is greatly reduced if an active reservoir pressure management plan is implemented.

Coupled injection/production well scenarios were designed to address reservoir pressure management, which helped to improve the efficiency of storage operations on the RSU (Objective 3). These scenarios suggest that a minimum of three production wells will be necessary to maintain low-risk pressures for a total of 1MT/year of $CO_2$ injection within the Madison and Weber reservoirs, which provides a highly conservative, low uncertainty estimate based on a presumed injection volume of 0.5MT/year. These models also showed that the Madison reservoir was more than two orders of magnitude more efficient for injection/production schemes, helping CMI to further constrain the site's ideal confining zones.

**Major conclusions relative to the validation of confining layers at the RSU $CO_2$ storage site**

*Geochemical, mineralogical, and isotopic laboratory test results*- The objectives of the laboratory tests were to geologically evaluate and characterize potential sealing lithologies in the study area. Shear strength test were performed on potential sealing lithologies and associated reservoirs. The compressive strength of all targeted seals were greater than the best injection

interval in the Madison dolostone, suggesting initial mechanical pressure failure would be limited to the reservoir. Capillary pressure entry tests were analyzed from core plugs and cuttings from potential sealing lithologies, and compared to reservoir data. Nine lithologies/formations had measured entry pressures that would competently retain the predicted $CO_2$ volumes. The primary seal, the upper Madison Limestone, had the highest measured entry pressures (>1250 psi). These data prove the study site has competent primary seals, and multiple redundant seals. Porosity and permeability of the targeted sealing lithologies is within an expected range for seals, further supporting the displacement pressure data. The upper limestone facies of the Madison Limestone has the lowest overall porosity and permeability, which is ideal for the primary seal.

Numerous analyses were performed to determine the geologic and geochemical characteristics of the sites best seals. The sealing capabilities of the upper limestone facies of the Madison formation were largely related to its deposition. It is primarily a tightly-cemented, micritic limestone with little evidence of diagenetic alteration. Similar micritic carbonates are found to be sealing lithologies in the Amsden and basal unit of the Weber formations. The siltstones of the Chugwater Group are matrix dominated, with abundant carbonate and evaporate cements. The Amsden Formation is composed of multiple, stacked marine facies, some of which have a relatively high amount of diagenetic alteration.

*Fluid characterization*- Fluid characterization is a vital component of reservoir characterization projects. Geochemical and isotopic results of reservoir fluids and dissolved gases from the Mississippian Madison Limestone and Pennsylvanian Weber Sandstone were used to evaluate brine evolution, calculate thermodynamic equilibrium, estimate geochemical reactions with respect to $CO_2$ injection, evaluate geochemical reactions in case of seal failure, and to investigate stacked reservoir confinement.

The brines are Na-Cl type with total dissolved solid concentrations in excess of 85,000 mg/L. Conservative analytes indicate that the evolution of the brines in both formations have been heavily influenced by evaporite dissolution, increasing the molar ratio of Br-Na-Cl. Dolomitization at depth in each reservoir results in magnesium depletion. Comparative analysis suggests that dissolution of evaporite and other minerals has had a large influence on the evolution of the formation fluids. This has resulted in increased TDS post-burial, resulting in some of the most saline formation fluids collected in Wyoming.

*Porosity heterogeneity from well logs*- Continuous spectral analysis of wireline logs from the RSU #1 well were used to quantitatively describe the porosity heterogeneity in the borehole section at an intermediate scale of several feet to tens of feet. We found that spectrograms generate useful information from well-log responses that can be utilized for identification of intervals with variable reservoir/sealing capacity within a formation. The amplitude and distribution of spectral peaks appear to correspond with the relative importance of confining layers.

*Projecting reservoir seal properties throughout the study area*- In this study we used seismic horizons within the Jim Bridger 3-D survey that correspond to the target formation tops based on the RSU #1 VSP and log data. Joint analysis of well logs, VSP, and surface seismic identified five seismic horizons corresponding to the Chugwater, Dinwoody, Weber, Amsden, and Madison formations. The above-mentioned five horizons were tracked automatically within the

5 x 5 x 3-mile seismic amplitude volume at every grid sample, and the auto-tracking results were quality checked and edited manually at a coarser grid (10 x 10 samples). Roughly thirty seismic attributes were probed to establish their relevance to structural variations along the seismic horizons. The attributes were based on different input data (pre- and post-stack seismic amplitudes), computational algorithms (instantaneous, windowed, etc.), and the nature of investigation (morphological vs. physical). Seven out of thirty attributes were chosen for the continuity analysis of sealing horizons (pre- and post-stack coherency, most positive and most negative curvature, dip azimuth and dip magnitude, and coherent amplitude gradients). A special 3-D directional filter (producing the Rock Integrity attribute) was developed to allow for separation of sub-horizontal, stratigraphic discontinuities from near vertical, structural ones. Thirty-five horizon maps were prepared using the above-mentioned seven attributes to investigate their variations along the Chugwater, Dinwoody, Weber, Amsden, and Madison seismic horizons. Besides, the seven attribute volumes were loaded into the OpendTect 3-D interpretation software for seal characterization in interactive environment.

*Hydrologic confinement*- The isotopic compositions of fluids and dissolved gases were found to be unique to each formation on either side of sealing strata. Rare earth element concentrations further establish distinctive fluid concentrations. Though these fluids share a similar evolution, we suggest that dissimilarities in the isotopic compositions of the brines, dissolved gases and rare earth element concentrations indicate that the target formation fluids are isolated from each other.

*Determining seal lateral continuity*- Regional cores that penetrated potential sealing lithologies were identified at the USGS Core Facility in Golden, Co. Samples were collected for petrographical analysis. Regional well logs were analyzed to identify the lateral continuity of sealing facies. Sealing lithologies form the upper Madison Limestone, the Amsden Formation, the Weber Sandstone and the Chugwater Group were found to be laterally continuous. Regional logs were used to develop regional seal cross sections and isopach maps.

*Assessment of seal bypass systems*- Two groups of potential seal bypass systems were interpreted within the seismic survey bounds on the Rock Springs Uplift. These are (1) widely spread orthogonal sets of deformation bands and faults, and (2) fractures associated with karst collapse features southwest of the RSU #1 test well. The deformation bands interpreted on the most negative seismic attribute are associated with folding of the Paleozoic strata and are arranged in patterns related to structural position. Our fracture analysis study reveals that lineaments within the study area strike northeast-southwest and northwest-southeast. These orientations are perpendicular and parallel to the fold hinge. Isolated vertically oriented discontinuities (pipes) that originate at the Madison paleokarst surface were interpreted on coherency horizon slices and within the Rock Integrity attribute volume. The associated fractures may result from sub-aerial karst processes, cavern collapse, hydrothermal alteration and dissolution, fault tectonism, or a combination of these processes.

*Geochemical $CO_2$ injection models*- Reaction path models were created to estimate the geochemical reactions in response to $CO_2$ injections into each formation. The pH of all basis compositions is expected to decrease significantly in response to $CO_2$ injection. The largest changes in pH occur immediately after simulated injection begins. The concentration of total

dissolved solids (TDS) may increase by more than 60,000 mg/L according to the modeling results. All geochemical models indicate carbonate mineral dissolution and some anhydrite precipitation. The net porosity gain from precipitation and dissolution process is expected to be 1-3%, indicating that $CO_2$ injection will have a positive effect of reservoir porosity.

*Geochemical evaluation of seal failure-.* The modeling results suggest changes in fluid composition in the event of seal failure. These include an increase in pH from 4.5 to >7. Saturation states for reactive minerals change; most notably are dolomite, calcite and antigorite become supersaturated and undersaturated with respect to quartz. Dolomite and aragonite remain under-saturated. The model suggests that calcite precipitation may increase the original calcite volume by as much as 200%. This is dependent on fluctuations in $pCO_2$ and temperature. Indicating that fractures in the seal will be self-healing.

*Geochemical evaluation of brine production*- The wellbore scale modelling showed that calcite dominated mineral scale, with minimal amounts of iron-sulfide.

*Corrosion risk wellbores and water treatment facilities*- Corrosion modelling showed that 2205 duplex steel performed best with low corrosion rates and no localized corrosion potential. However, the 13-chrome and 304 stainless alloys both performed better than mild steel and a cost benefit analysis should be conducted. Subsurface well models were extended to surface water processing equipment. Surface model results were very similar to well model results, and brine and corrosion models developed all equipment are correlative. The results of the corrosion modeling indicate introducing oxidizing agents to the reservoir fluids increases corrosion. Engineering scenarios suggest that the dolostone within the Mississippian Madison Limestone is the site's best injection/production target by two orders of magnitude, and that commercial well equipment would meet all performance requirements.

*Numerical Simulation*- Diverse injection scenarios were generated using the 3-D numerical computation models to create performance assessments and to evaluate seal integrity, reservoir injection feasibility and storage capacity, and to evaluate displaced fluid and pressure responses for management. Simulations of $CO_2$ injection volumes were run on the LANL multiphase porous flow simulator FEHM. The 3-D fluid flow simulation models include detailed calculations of subsurface fluid movement, including flow through injection wellbores, faults, and fractures under variable scenarios. We developed a probability-based PA model to evaluate the confining layer sealing capacity and integrity, and to evaluate the importance of parameters for numerical simulation of confining layers. Monte Carlo simulations was used to optimize $CO_2$ injection feasibility, storage capacity, and reservoir pressure and displaced fluid management scenarios. The importance and effects of the simulation input parameters were prioritized. These methods were evaluated to choose crucial input parameters for $CO_2$ injection numerical simulations using 3-D property model constructions relative to sealing capacities.

The majority of injected $CO_2$, over 90% in first few hundred years, will remain at free-supercritical phase and rise buoyantly and accumulate beneath low-permeability confining layers. Migration through the water saturated pore network of a confining layer may occur if the $CO_2$ fluid pressure in the reservoir exceeds the capillary entry pressure of the confining layers.

*Critical parameters for sealing capacity simulation*- Sensitivity analysis shows that the sealing capacity of the most upper portion of the Madison Limestone is most sensitive to changes in the $CO_2$-water interfacial tension in the reservoir condition and variation in laboratory measurements. $CO_2$ column heights are most sensitive to the $CO_2$-water interfacial tension, and $CO_2$ and water density differences.

*Sealing capacity*- The entries pressures in the $CO_2$-brine system for RSU seals range from 7 to 122 psi, about half of entry pressures in the oil-brine system, and one-fourth of the entry pressures gas-brine system. Generally, entry pressures increase with depth. The primary seals at the storage site are the limestone facies in the upper Madison Limestone (122 psi), the Triassic Red Peak siltstone (91 psi), the Amsden Formation (51 psi), and marine facies at the base of the Weber Sandstone (35 psi). Total $CO_2$ column heights that the various confining layers at the RSU could competently retain range from 53 ft. to 994 ft. The low permeability (>0.001 md) limestone facies at the most upper portion of the Madison Limestone could hold over 900 ft. of injected $CO_2$ column in the reservoir portion, far thicker than the total unit. The Amsden Formation could hold a $CO_2$ column of approximately 375 ft., and the Triassic Red Peak Formation could hold a $CO_2$ column of approximatley740 ft. The $CO_2$ column height sealing capacity overlying redundant seals range from 54 ft. to 279 ft.

This study shows that the sealing capacity calculations using constants for $CO_2$-water-rock are significantly lower the sealing capacity calculations using hydrocarbon-water-rock constants. However, $CO_2$ injection simulations indicate that the confining layers at the RSU site have adequate sealing capacity to conservatively retain 25MT of injected $CO_2$ over a 50-year injection period with no risk to confinement.

# REPORT DETAILS

## Introduction

The goal of this project was to improve estimates of $CO_2$ storage reservoir storage capacity, evaluate the long-term integrity and performance of confining layers, and manage injection pressures and brine production to optimize $CO_2$ storage efficiency for the Rock Springs Uplift (RSU), Wyoming - Wyoming's highest-priority $CO_2$ storage site containing the most promising storage reservoirs.

In addition to a Project Management task, the project was structured into six technical tasks to achieve the goals and objectives:

- *Task 2:* Geophysical assessment of Rock Springs Uplift based on seismic analyses
- *Task 3:* Geological and mechanical characterization of confining lithologies using laboratory measurements
- *Task 4:* Characterize formation fluids to determine hydraulic isolation of target formation
- *Task 5:* Simulations to evaluate seal integrity, injection rate, and pressure management
- *Task 6:* Simulations of formation brine production to assess wellbore scaling/well integrity and surface treatment
- *Task 7:* Rock Springs Uplift integrated geological and geophysical $CO_2$ storage assessment

The remainder of the report describes the research conducted and results for these tasks. This is followed by a Project Summary section at the end of the report.

## Task 1: Project Management and Planning

All duties related to project management were duly met. This task was designed to maintain a constant workflow and consistent communications between researchers. This task met all the reporting and documentation requirements, and helped to keep the project on-time and on-budget. Aside from rescheduling the completion date of some Milestones, there are no complications to report with the project's timeline.

## Task 2: Geophysical assessment of Rock Springs Uplift based on seismic analyses

## Overview

Task 2 objectives were to evaluate potential seals associated with Paleozoic reservoirs (eolian sands of the Weber Sandstone and dolostones in the Madison Limestone) at a distance from the University of Wyoming stratigraphic test well (RSU #1 049-047-07154) with geophysical methods integrated with geologic and petrophysical data. To complete this task, CMI researchers utilized core plugs and wireline log data from the RSU #1 well, the 3D surface seismic data acquired in the vicinity of this well, and digital elevation and aerial photography data available online for the Rock Springs Uplift. The data were analyzed for the cap rock integrity relative to the proposed $CO_2$ storage formations within the seismic survey bounds and for the presence and character of possible seal bypass systems. CMI researchers put special emphasis on using seismic coherency, curvature, and reflector amplitude gradients for detection, mapping, and analysis of subtle structural features (seal bypass systems). Geologic interpretations were completed using in-house developed software and 'OpendTect', an open source seismic interpretation platform. Specially developed attributes, extracted from seismic amplitude volume, indicated northwest-northeast lineaments that can be interpreted as structural features. Another set of isolated anomalous features with vertical orientation can be observed in the rock-integrity attribute that we interpret as dissolution pipes originating at the Madison Limestone stratigraphic level that upward through lower confining zones. Lower Triassic units of the Chugwater Group were shown to have lateral seismic continuity.

## Executive Summary

The following results provide a brief summation of methods and major findings for the five subtasks of Task 2.

- *Subtask 2.1—Identify seismic horizons within the Jim Bridger 3-D survey that correspond to the target formation tops based on the RSU #1 VSP and log data.* Joint analysis of well logs, VSP, and surface seismic identified five seismic horizons corresponding to the Chugwater, Dinwoody, Weber, Amsden, and Madison Formations.
- *Subtask 2.2—Track the identified seismic horizons throughout the whole seismic amplitude volume.* The above-mentioned five horizons were tracked automatically within the 5 x 5 x 3-mile seismic amplitude volume at every grid sample, and the auto-tracking results were quality checked and edited manually at a coarser grid (10 x 10 samples).
- *Subtask 2.3—Prepare volumetric seismic attributes for the Jim Bridger 3-D survey.* Roughly thirty seismic attributes were probed to establish their relevance to structural variations along the seismic horizons. The attributes were based on different input data (pre- and post-stack seismic amplitudes), computational algorithms (instantaneous, windowed, etc.), and the nature of investigation (morphological vs. physical).
- *Subtask 2.4—Investigate and identify seismic attributes most appropriate for seal characterization.* Seven out of thirty attributes were chosen for the continuity analysis of sealing horizons (pre- and post-stack coherency, most positive and most negative curvature, dip azimuth and dip magnitude, and coherent amplitude gradients). A special 3-D directional filter (producing the Rock Integrity attribute) was developed to allow for

separation of sub-horizontal, stratigraphic discontinuities from near-vertical, structural ones.

- *Subtask 2.5—Prepare horizon maps showing seismic attribute variations along the confining layers.* Thirty-five horizon maps were prepared using the above-mentioned seven attributes to investigate their variations along the Chugwater, Dinwoody, Weber, Amsden, and Madison seismic horizons. Besides, the seven attribute volumes were loaded into the OpendTect 3-D interpretation software for seal characterization in interactive environment.

## Methods

*Seismic data-* The Jim Bridger 3D is a wide-azimuth seismic data set acquired in Sweetwater County, southwestern Wyoming, using vibroseis as a source and three-component digital sensors covering an area of about 25 $mi^2$. The survey was designed as a baseline study of possible $CO_2$ injection and was acquired by Geokinetics Service Co., Houston, Texas, in November 2010. The common-midpoint (CMP) bin, 110 foot in both the X and Y directions, is less than one-quarter the minimum wavelength ($\lambda_{min}$ = 500 ft.) and ensures that the data is not spatially aliased. The maximum CMP fold coverage of 48× and maximum source-to-receiver offset of 19,800 foot are adequate acquisition parameters for imaging geological targets in 10,000–15,000-foot depth range. Geokinetics did the basic preprocessing of the reflection seismic data. The purpose of data preprocessing was twofold, (1) pre-stack data conditioning for an automated, high-density velocity analyses on CMP gathers and (2) stacked amplitude volume preparation that is suitable for volumetric and horizon attribute analyses. Echo Geophysical Co., Denver, Colorado, did a good job on data enhancement including acquisition footprint removal and bringing out the higher frequency content. The quality of the resultant PSTM stacked amplitude volume is illustrated in **Figure 2.1**. A relatively high signal-noise ratio and overall lateral continuity characterize reflections in the time range 1.4 to 2.2 s that correspond to geological interfaces in the depth range approximately from 7,000 to 13,000 feet below the ground surface at the RSU #1 well location.

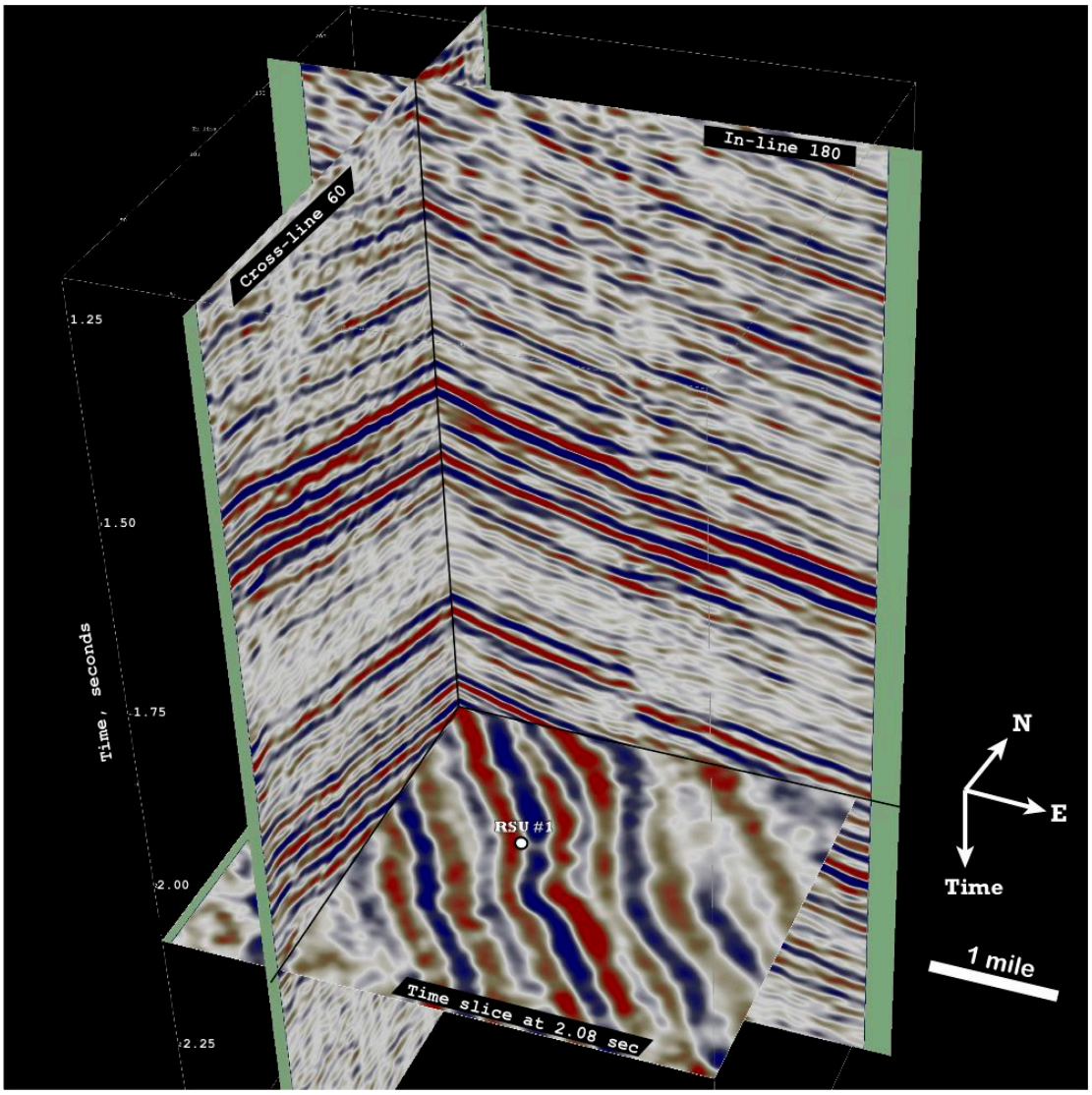


**Figure 2.1:** 3-D seismic amplitude volume after reprocessing at Echo Geophysical Co. Note an overall northeast dip of seismic reflections. Projection of the RSU 31 well (white circle) is shown on the horizontal time slice.

## Results and Discussion

*Assessing seals and seal bypass systems*- Leakage of $CO_2$ out of designated subsurface storage volumes, whether oil and gas fields or saline aquifers, is one of the main concerns regarding geologic carbon storage. Any low-permeability lithology can serve as a seal for sequestration purposes. A few inches of ordinary clay shale are theoretically adequate to trap very large column heights of injected gas. Unfortunately, there is a low probability that a zone only a few inches thick would be continuous, unbroken, and maintain stable lithic character over a sizable reservoir. CMI researchers used seismic attribute anomalies to derive the distribution of anomalous features at a regional scale around the test well. Volumetric seismic attributes, primarily coherence and curvature, were utilized to characterize subtle features such as collapse

features and folding and fracturing within the Mississippian carbonate reservoirs and Triassic and Pennsylvanian confining layers. The term seal bypass refers to any process or sequence that allows fluid to flow vertically or sub-vertically through a low-permeability caprock. The primary focus of this study is to analyze the possibility of seal bypass systems occurrence in the vicinity of the RSU #1 well. Based on seismic interpretation criteria, the following two groups of the seal bypass systems were observed in the study area: (1) fault/fracture related and (2) pipe related.

*Interpreted fracture zones and faults*- Faults and fractures are the dominant seal bypass mechanisms in potential injection sites. Fractures, deformation bands, and faults have been shown to increase or decrease permeability in certain directions and, thus, introduce permeability anisotropy and heterogeneity. Faulting and fracturing can also act as fluid flow barriers creating compartmentalization when they are shale filled or hydrothermally altered. In other situations, the faults and fractures that cause heterogeneity can act as a fluid-flow conduit, effectively bypassing the top sealing formations. Additionally, unidentified faults within potential injection sites represent significant risk factor for induced seismicity.

The structural configuration mapped from 3-D seismic data clearly depicts a northeast-dipping monocline at all stratigraphic levels within the survey bounds. The strata are almost flat in the northeastern part of the study area, but their dip steepens to about 8˚ in the southwest part. Minor folding with the fold axes plunging northeast complicates the monocline. In the vicinity of the RSU #1 well, the implied general dip changes from roughly northeast to east-northeast (**Figure 2.2**).

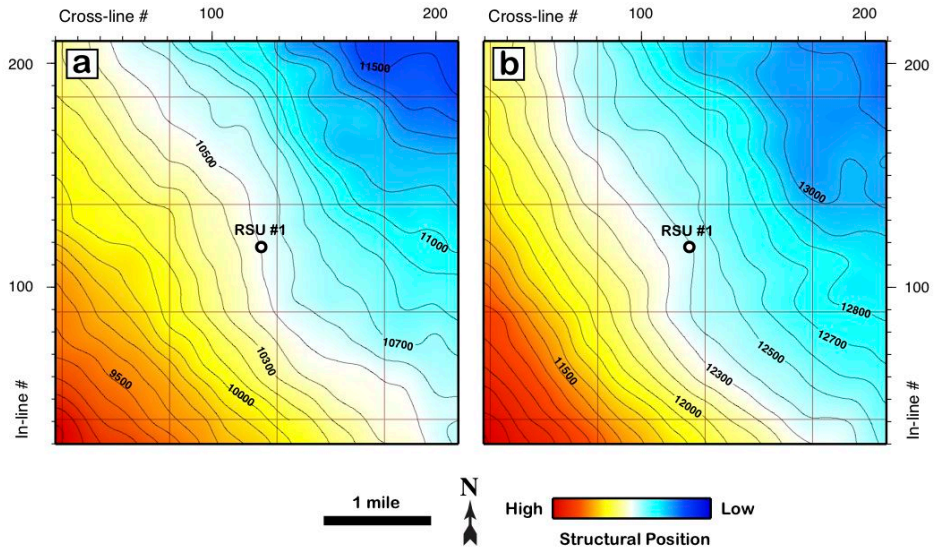


**Figure 2.2:** Color-coded structure maps of the interpreted horizons: (a) lower Triassic and (b) Madison Limestone. Contour interval is 100 feet for all maps. The depth reference point is the Kelly bushing (KB) at RSU #1 well.

**Figure 2.3** shows the most negative curvature horizon slice on top of the Madison reservoir that delineates polygonal-shaped features, which we interpret to be fractures and faults. We manually mapped the azimuth of these curvature lineaments and plotted them on a rose diagram. The rose diagram plot in **Figure 2.3b** indicates two sets of orthogonal lineaments (northwest-southeast and northeast-southwest). The same mapping technique was used on top of the Lower Triassic sealing horizon. At this stratigraphic level, the mapped lineaments strike mostly northwest-southeast, and only a few of them strike northeast-southwest (**Figure 2.4**). It is a relatively lower signal-noise ratio of seismic reflections at the lower Triassic level that do not allow a clear separation of the two orthogonal directions in the rose diagram (**Figure 2.4b**).

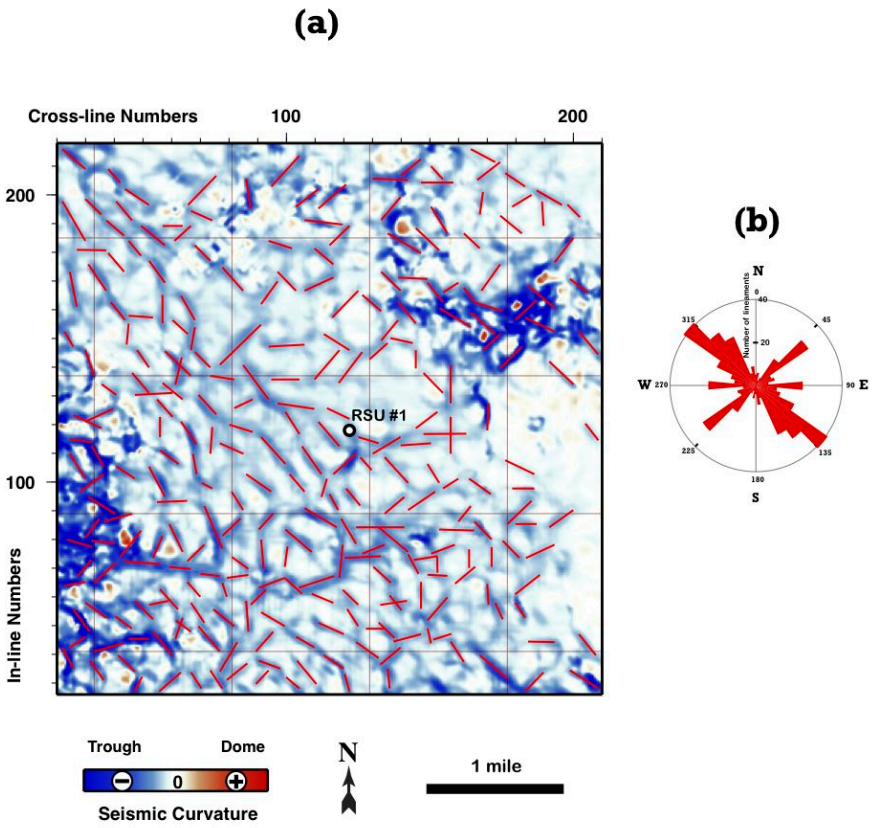


**Figure 2.3:** Horizon slice through the top of the Madison reservoir from a most-negative curvature volume generated from post-stack migrated seismic data (a). Azimuths of interpreted lineaments (red segments) are displayed in the rose diagram (b), according to relative frequencies (number of occurrences).

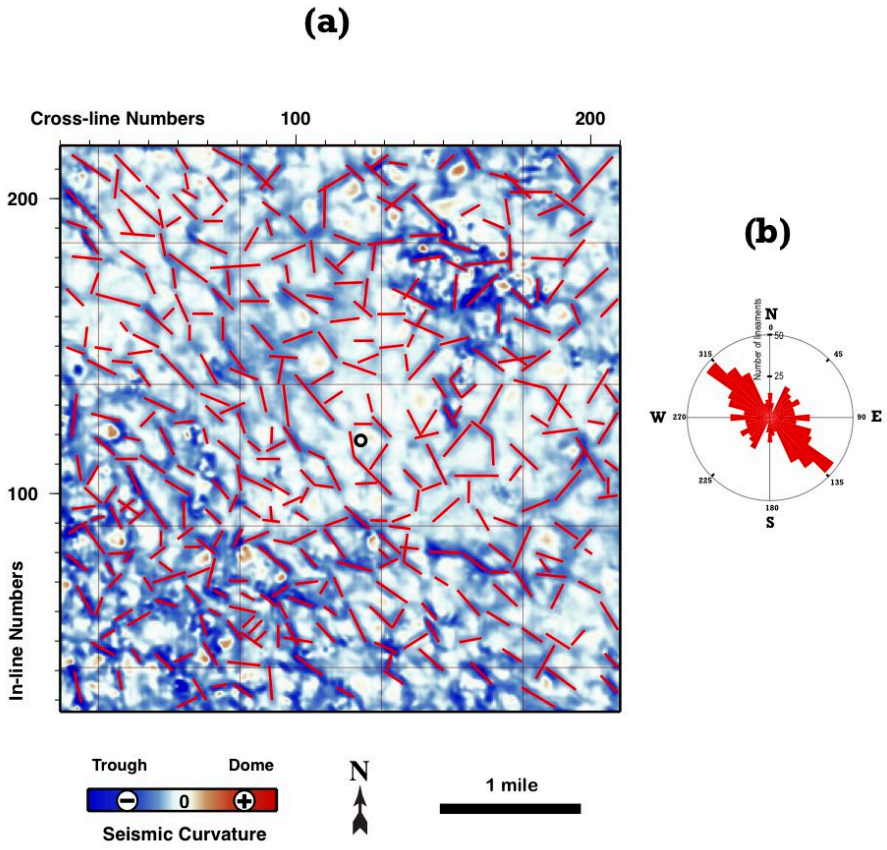


**Figure 2.4:** Horizon slice through the top of the Lower Triassic level from a most-negative curvature volume generated from post-stack migrated seismic data (a). Azimuths of interpreted lineaments (red segments) are displayed in the rose diagram (b), according to relative frequencies (number of occurrences).

The curvature lineaments mapped within the subsurface layers strike roughly parallel and perpendicular to the regional fold hinge, suggesting that they are related a regional compressional event. The orientations of curvature lineaments at study area correlate with the known structures throughout the Laramide foreland. The structures described by Cooper et al. (2003 and 2006) at Teapot Dome and at Oil Mountain (Hennings et al., 2000) in central Wyoming, are similar to those at Rock Springs Uplift.

The curvature lineaments were further compared to geologic data to determine if a relationship can be identified with the surface-exposed fracture network existing on the Rock Springs Uplift. Evidence for the presence of northwest- and northeast-oriented joints in the Cretaceous Rock Springs sandstone is found in several aerial photographs from the GeoMAC Viewer. In order to determine whether the observed fracture network is related to either of the two dominant curvature lineament trends, we manually mapped the azimuth of the outcropping joints. The mapped joints and corresponding rose diagram are shown in **Figures 2.5a** and **2.5b** respectively. The northwesterly trend observed in the outcropping joints is consistent with the seismically derived curvature lineaments in the subsurface.

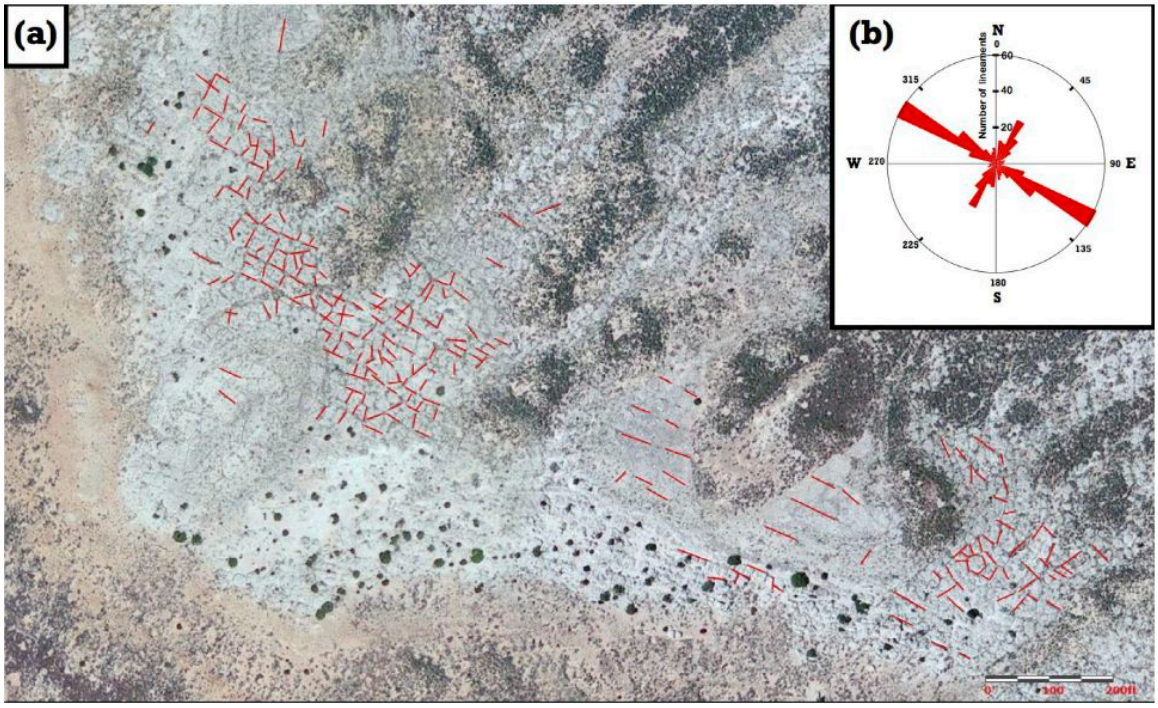


**Figure 2.5:** (a) Sandstone outcrop four miles southwest of the RSU #1 well (aerial photograph from GeoMAC Viewer). Joints in the Cretaceous Rock Springs Formation are marked as red segments, (b) orientations of the marked joints in (a) combined in the form of Rose diagram.

Seismically resolvable faults were interpreted in vertical sections through the seismic amplitude and coherency volumes. **Figure 2.6** shows southwest-northeast section with interpreted stratigraphic horizons and discontinuities. The section cuts seismic volume just north from the test well location. Several interpreted faults produce a noticeable displacement in the reflectivity patterns (**Figures 2.6** and **2.8)**. The fault planes orientation becomes more obvious when using gray-scale coherency image (**Figure 2.7**).

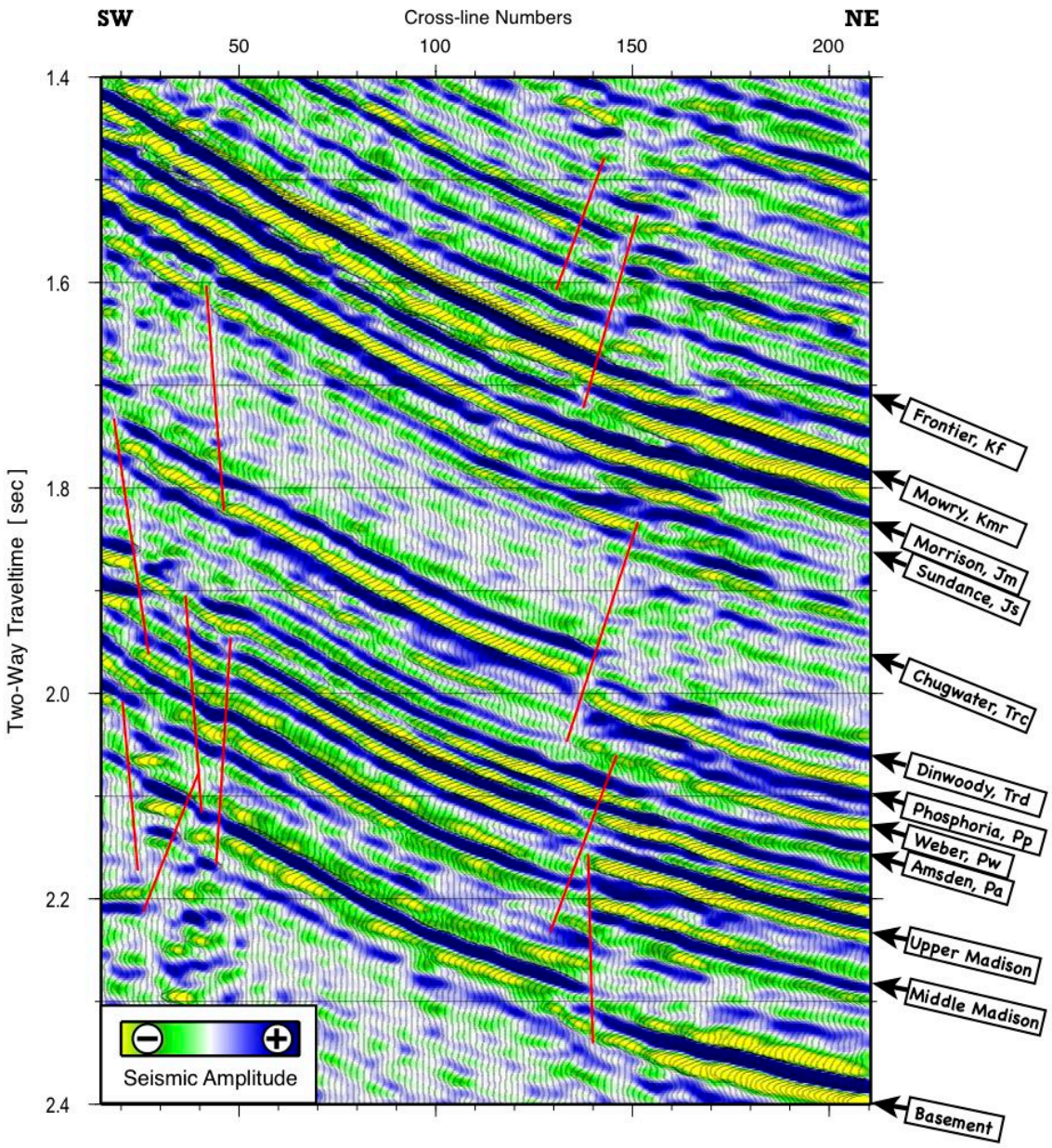


**Figure 2.6:** Interpreted southwest-northeast section through the seismic amplitude volume (north from the RSU #1 well). Red segments indicate interpreted discontinuities in a reflectivity pattern.

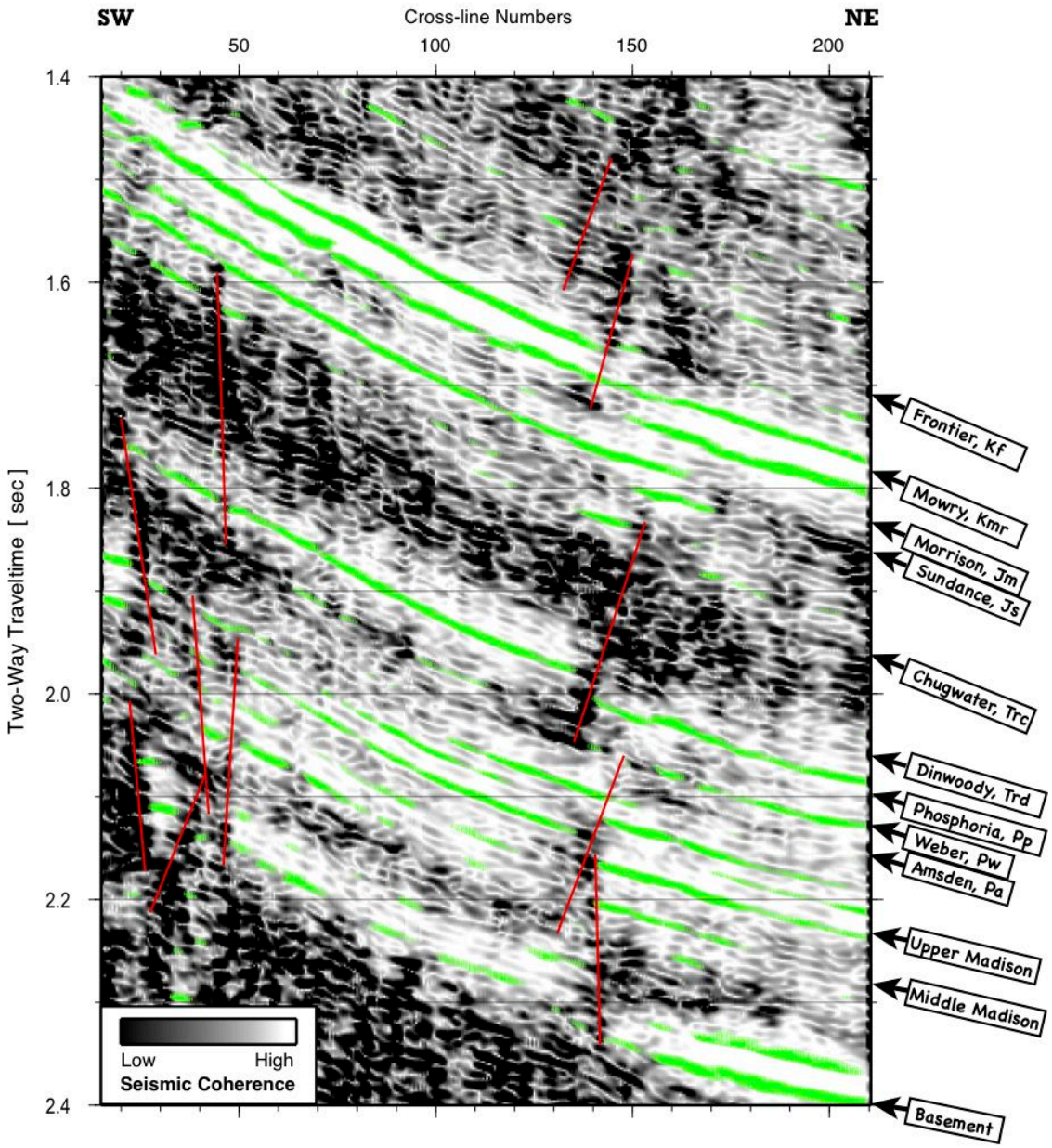


**Figure 2.7:** Interpreted southwest-northeast section through the seismic coherence volume (energy-normalized amplitude gradients). Red segments indicate interpreted discontinuities in a reflectivity pattern.

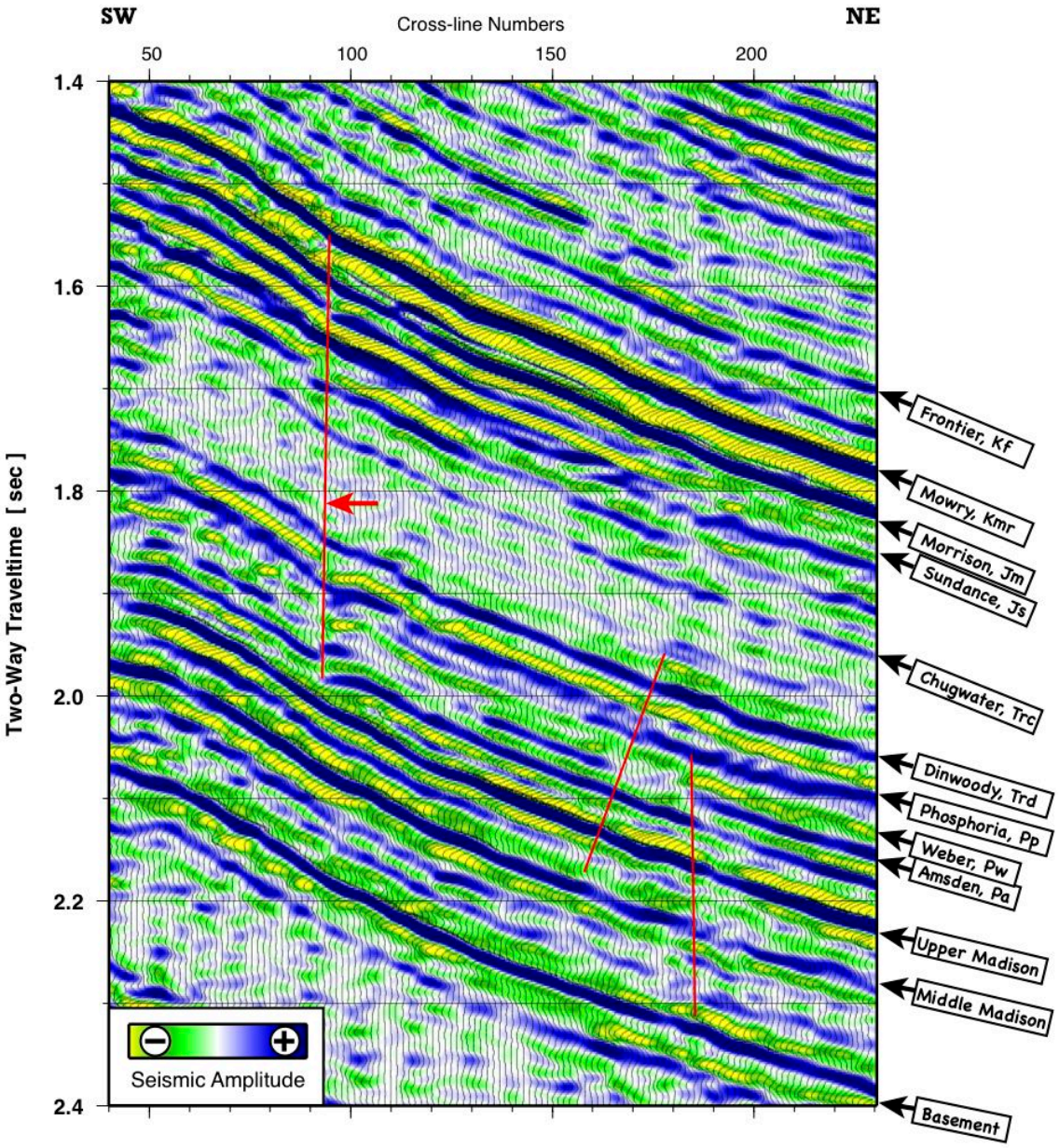


**Figure 2.8:** Interpreted southwest-northeast section through the seismic amplitude volume. Red segments indicate interpreted discontinuities in a reflectivity pattern.

Using coherency slices along the dominant seismic reflections facilitates mapping of discontinuities observed in vertical sections. Seismic coherency maps on top of the Madison, Amsden, and Dinwoody stratigraphic units are shown in **Figures 2.9** through **2.11** respectively. The figures also outline location of the vertical sections in **Figures 2.6** through **2.8**. The basement-involved faults identified in vertical sections (**Figures 2.6** and **2.7**) appear to produce a broad zone of reflections discontinuity on top of the Madison horizon northeast of the RSU #1 well (**Figure 2.9**). The configuration of this zone suggests that there are two orthogonal faults in the coherence data. One of them, subparallel to the strike of bedding, is terminated within the study area by a smaller fault that is roughly orthogonal to the first one (**Figure 2.9)**. The area southwest of the RSU #1 well (the up-dip direction) seems to be laterally continuous and does not contain traceable fault planes along the Madison horizon.

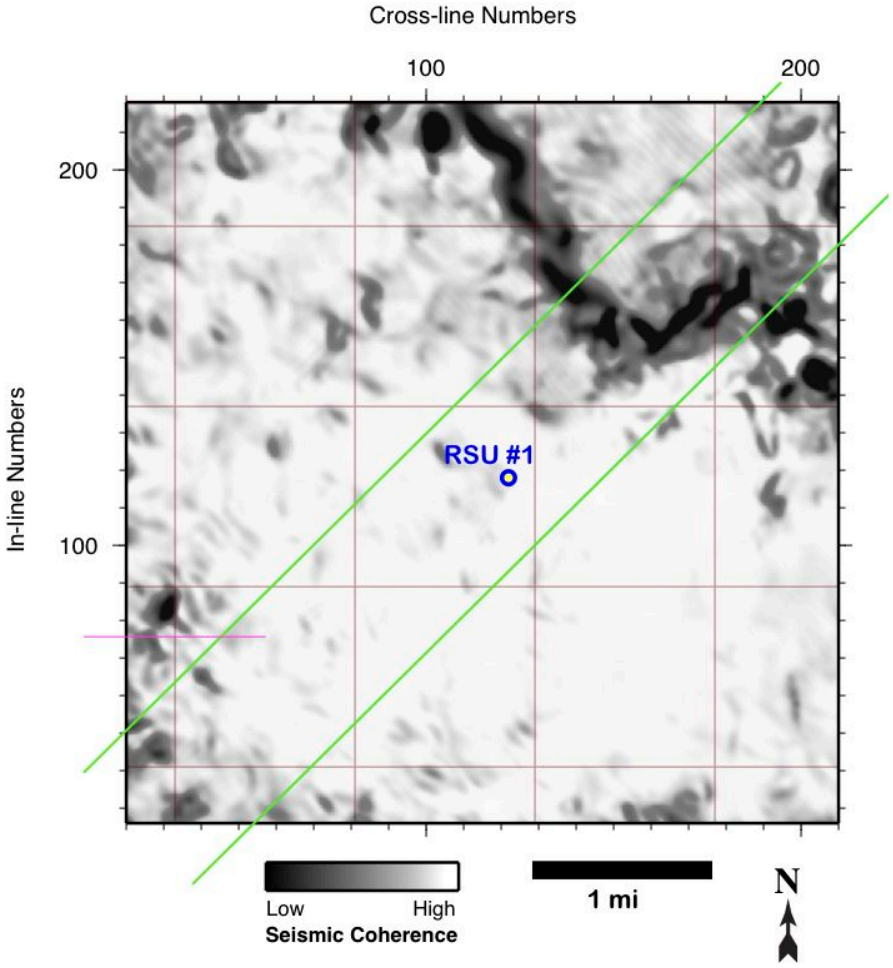


**Figure 2.9:** Seismic coherency map on top of the Middle Madison unit. Coherence changes from high (light color) in areas with continuous reflections to low in areas of intense fracturing, faulting (dark elongated features), and dissolution pipes development (dark, isolated oval features). Green lines indicate locations of vertical sections shown in **Figures 2.6-8**. Note an overall high coherency of seismic reflections in the updip direction (south and west from the RSU #1 well).

*Interpreted karst collapse features (pipes)*- Lateral continuity of reflections up-dip of the test well ceases along stratigraphically higher beds. Coherency analysis along the Amsden stratigraphic unit indicates a network of fractures with chaotic orientation and also several circular features with extremely low coherency (**Figure 2.10**). We interpret these circular discontinuities to be related to carbonate karst development within the Madison reservoir. Stratigraphically higher beds show more evidence for this interpretation. The occurrence of low-coherent, oval planforms on top of the Lower Triassic stratigraphic unit becomes invasive southwest of the RSU #1 well (**Figure 2.11**). We hypothesize that a relationship exists between the highly karsted, cavernous Madison reservoir and the overlying Pennsylvanian, Permian, and Triassic sealing sequences. We speculate that the Middle Madison reservoir was likely impacted by dissolution, resulting in the karst collapse features in the overlaying strata.

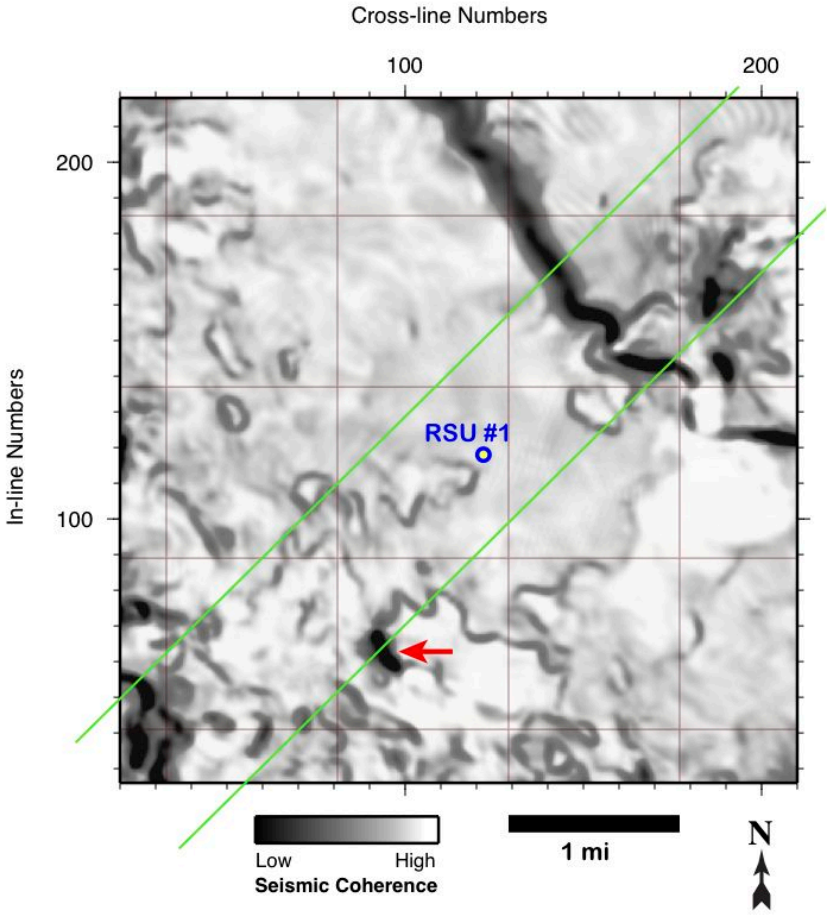


**Figure 2.10:** Seismic coherency map on top of the Amsden stratigraphic unit. Coherence changes from high (light color) in areas with continuous reflections to low in areas of intense fracturing, faulting (dark elongated features), and dissolution pipes development (dark, isolated oval features). Green lines indicate locations of vertical sections shown in **Figures 2.6-8**. Red arrowhead indicates interpreted dissolution pipe outlined in **Figure 2.8**.

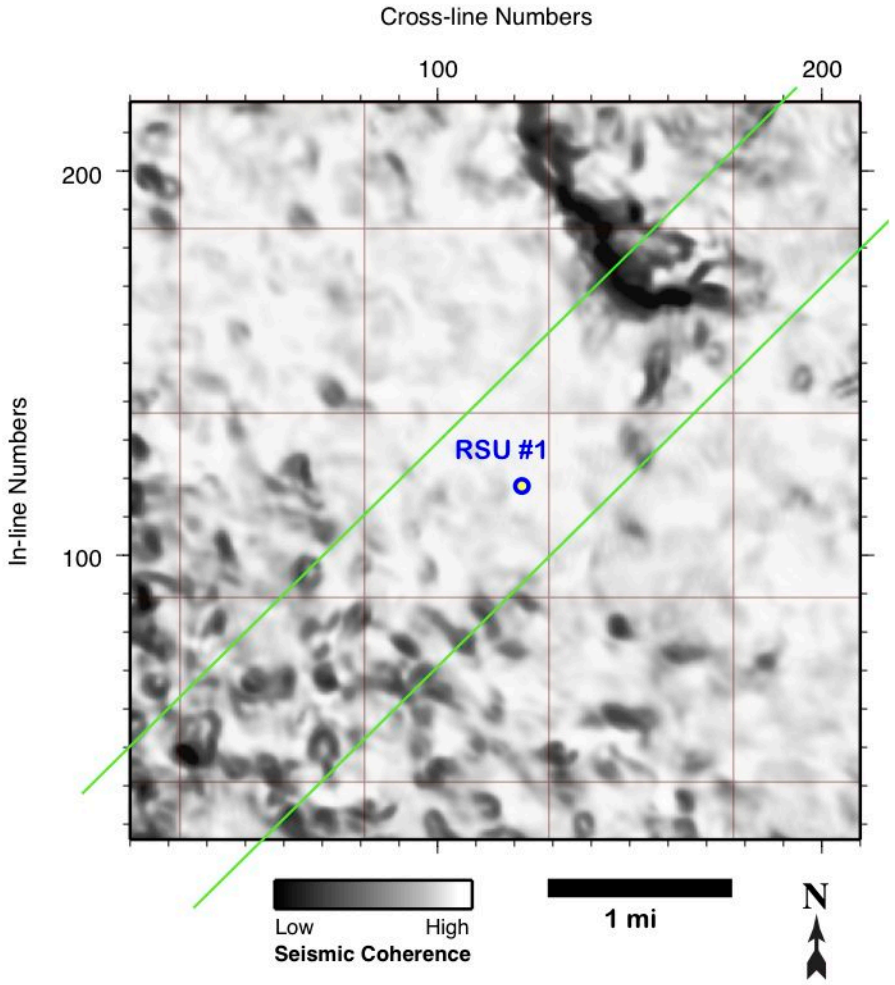


**Figure 2.11:** Seismic coherency map on top of the Dinwoody stratigraphic unit. Coherence changes from high (light color) in areas with continuous reflections to low in areas of intense fracturing, faulting (dark elongated features), and dissolution pipes development (dark, isolated oval features). Green lines indicate locations of vertical sections shown in **Figures 2.6-8**. Note an increased amount of isolated oval features that we interpret as dissolution pipes.

To get more confidence in our interpretation, we have developed a special 3-D directional filter allowing separation of sub-horizontal, stratigraphic discontinuities from near-vertical, structural ones. We used coherency volume that measures seismic amplitude variability in the way similar to energy-weighted coherent-amplitude gradients (Chopra and Marfurt, 2007). This volume was further filtered in 3-D to reject all sub-horizontal objects that are largely associated with lithological bedding and/or seismic facies boundaries. We called the resultant volume a Rock Integrity attribute that correlates best with near-vertical, structural discontinuities. We loaded the Rock Integrity attribute volume into the OpendTect, a free, open source seismic interpretation platform (http://opendtect.org) to allow the 3-D visualization of this attribute. The above-described methodology allowed obtaining displays with clear images of vertically aligned discontinuities that we interpret as karst collapse features (**Figures 2.12** and **2.13**).

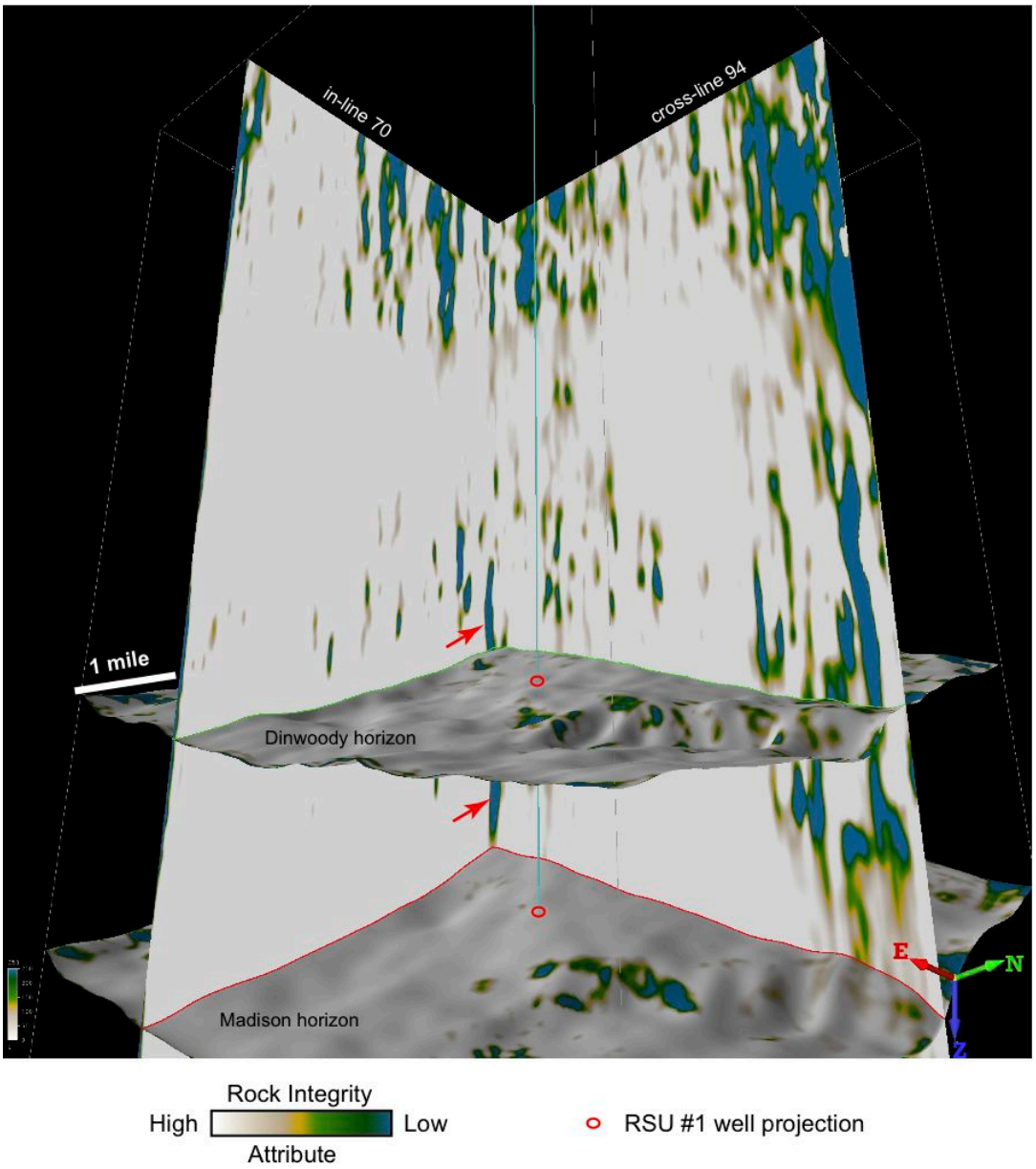


**Figure 2.12:** 3-D perspective display made of two orthogonal vertical sections (in-line 70 and cross-line 94) and two stratal slices at Madison and Triassic stratigraphic levels. Data selection is done over the volume of Rock Integrity attribute: a view from the northeast. Note a karst collapse feature (marked with red arrowheads) that originates at the top of the Madison reservoir and cuts through the rock sequence well above the Triassic horizon.

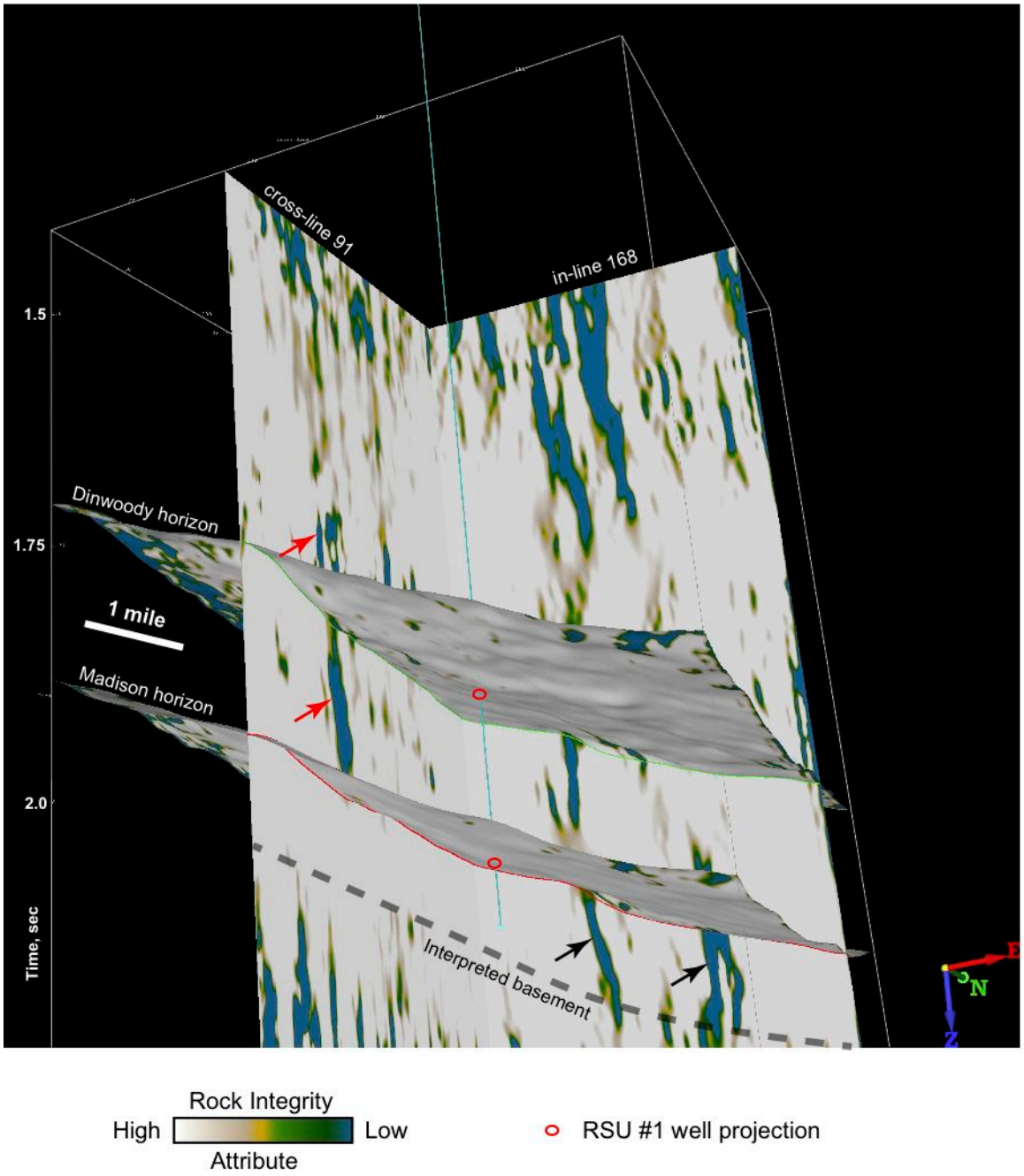


**Figure 2.13:** 3-D perspective display made of two orthogonal vertical sections (in-line 168 and cross-line 91) and two stratal slices at Madison and Triassic stratigraphic levels. Data selection is done over the volume of Rock Integrity attribute: a view from the southeast. Note a karst collapse feature (marked with red arrowheads) that originates at the top of the Madison reservoir and cuts through the rock sequence well above the Triassic horizon. The basement-rooted reverse faults are marked with black arrowheads.

*Porosity heterogeneity from well logs*- Definition and interpretation of sedimentary facies and lithologic rock properties often involves the examination of well logs to assess trends, variance, and sudden changes in recorded values. Using continuous spectral analysis could enhance the procedure, which often includes only visual inspection of the log records. In particular, spectral decomposition of logs provides an easily interpretable visual representation of signals at different spatial frequencies and is an efficient tool for supporting stratigraphic analysis.

**Figure 2.14** shows the density log and its spectrogram for the lowermost part of the RSU #1 section that includes the targeted saline reservoir, - the Mississippian Madison Limestone. Based on the cores and well log data analysis, we place one paleokarst surface at the top of the Madison Limestone. Core samples from the Middle Madison unit (from 12,340 to 12,550 feet depth) are characterized by intense dolomitization and solution cavities. Correspondingly, the density log in this depth interval exhibits reduced values while its spectrogram demonstrates several amplitude peaks within the range of wavelengths from 10 to about 50 feet (**Figure 2.14**). This range of numbers matches the observations of Madison paleokarst outcrops in north-central Wyoming done by Sando (1988). He estimates dimension of irregularly shaped solution cavities in dolostone to range from less than a foot to tens of feet. The upper 100 feet of the Madison Limestone lacks heterogeneity within the analyzed spatial scale (1.5 – 150 feet) and looks more uniform and dense (**Figure 2.14**). This is also consistent with the observations of Sando (1988), who identifies only small (few inches) joint passages in the limestone. Depth interval corresponding to the Amsden Formation appear to be composed of relatively dense and homogeneous rocks with the exception of the upper 100-feet thick interval. This depth interval appears to be complicated with cyclic events having period of 10 and 25 feet (**Figure 2.14**). Abrupt terminations of these cycles at approximately 11,800, 11,840, and 11,910 feet depth may indicate dolomitization and/or discontinuity on top of the Amsden unit. Hence, there is a 400 feet thick continuous section of low-porosity rocks with uniform properties (the upper Madison limestone and the lower part of the Amsden Formation, comprised of shale, dolomite, and sandstone) overlying the Middle Madison aquifer at the RSU #1 well.

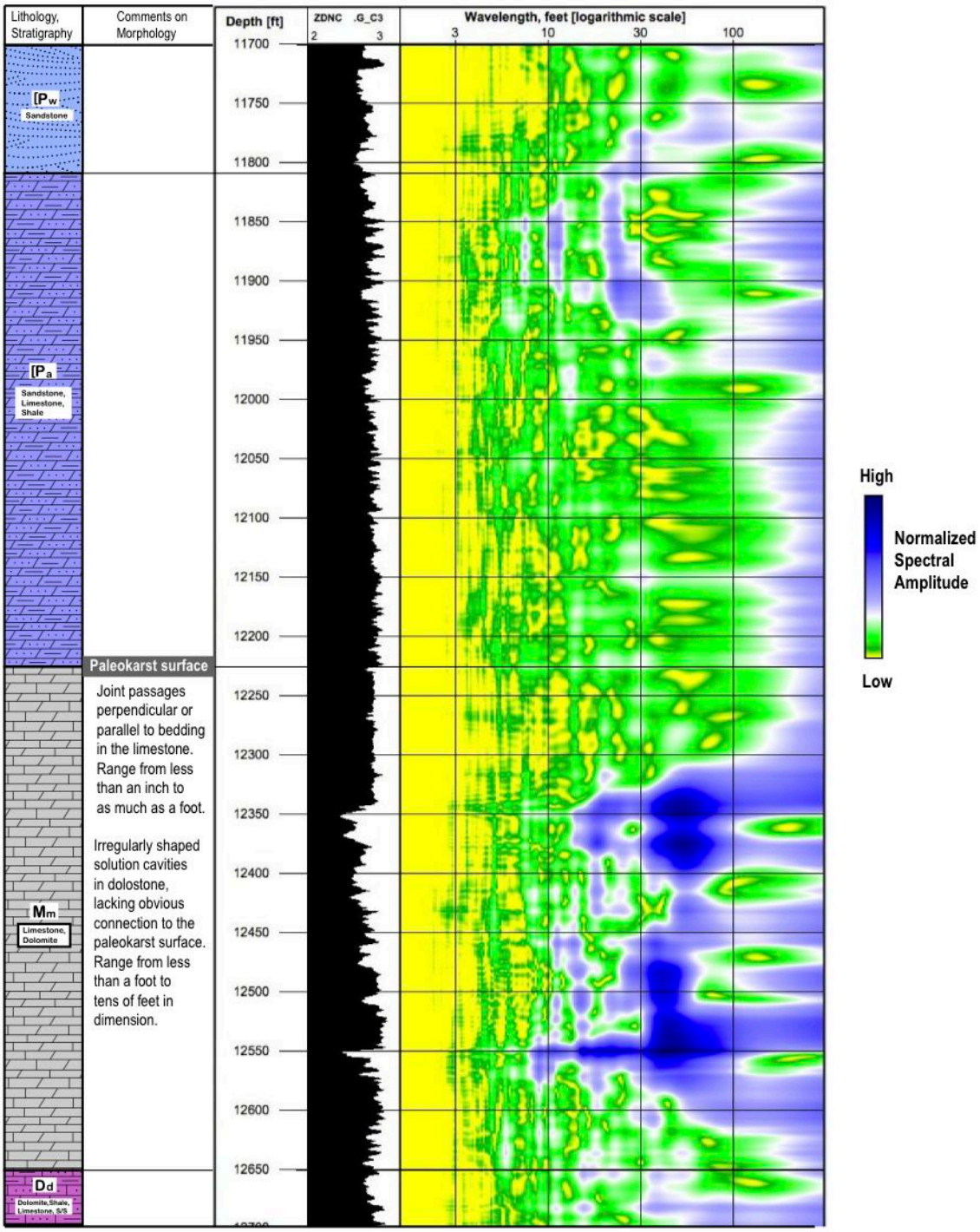


**Figure 2.14:** Density log from the bottom part of the RSU #1 well (black bar graph in the middle panel) and its spectrogram (right-most panel). Spectral amplitude intensifies from yellow to blue color. Note peak amplitudes with wavelengths ranging from 10 to about 50 feet in the Middle Madison unit that correlate with the area of dolomitization and solution cavities development. Morphological observations are from Sando (1988) for north-central Wyoming throughout the outcrop area of the Madison paleokarst.

## Conclusion

Leakage of $CO_2$ along faults and fracture networks in the subsurface is a major concern that must be considered when designing injection plans. Upward migrating $CO_2$ along a fault zone could potentially leak from the injection reservoir to the surface, or, could leak along a fault into an overlying reservoir. In both cases, $CO_2$ would be leaving the reservoir that it was intended to remain in and, the storage project would be compromised. It is therefore crucial to define seal bypass systems at the study site to help identify these risks.

Two groups of potential seal bypass systems were interpreted within the seismic survey bounds on the Rock Springs Uplift. These are (1) widely spread orthogonal sets of deformation bands and faults, and (2) fractures associated with karst collapse features southwest of the RSU #1 test well. The deformation bands interpreted on the most negative seismic attribute are associated with folding of the Paleozoic strata and are arranged in patterns related to structural position. Our fracture analysis study reveals that lineaments within the study area strike northeast-southwest and northwest-southeast. These orientations are perpendicular and parallel to the fold hinge. Isolated vertically oriented discontinuities (pipes) that originate at the Madison paleokarst surface were interpreted on coherency horizon slices and within the Rock Integrity attribute volume. The associated fractures may result from sub-aerial karst processes, cavern collapse, hydrothermal alteration and dissolution, fault tectonism, or a combination of these processes.

Continuous spectral analysis of wireline logs from the RSU #1 well were used to quantitatively describe the porosity heterogeneity in the borehole section at an intermediate scale of several feet to tens of feet. We found that spectrograms generate useful information from well-log responses that can be utilized for identification of intervals with variable reservoir/sealing capacity within a formation. The amplitude and distribution of spectral peaks appear to correspond with the relative importance of confining layers.

Based on petrological analysis of cores and spectral analyses of RSU #1 well logs, we observe at least 1,000-feet thick interval composed of sealing lithologies within the lower Triassic siltstone sequence. As the seal thickness increases, its leakage probability decreases even within an area affected by fracturing and faulting. However, faults and fracture networks that break these reservoirs into compartments might cause unintended pressure increases during $CO_2$ injection or migration in locations adjacent to compartment boundaries. Hence, it is of great importance to choose reliable rock properties for the flow simulation model when assessing compartmentalized reservoirs with highly variable porosity and permeability. Drilling additional stratigraphic test wells in the study area would bring more information on the origins of those compartment boundaries that could play an important role in adding crucial details to flow-simulation models.

## Task 3: Geological and mechanical characterization of confining lithologies using laboratory measurements

### Overview

Task 3 objectives were to evaluate geologically and characterize potential sealing lithologies in the study area. To complete this task, CMI researchers utilized core and cuttings from the RSU#1 well (funding for core and cutting retrieval was partially provided by DOE grant FE0002142). Samples were analyzed for mechanical, mineralogical, geochemical, depositional, diagenetic, pore, fluid flow, and displacement properties.

The overall goal of Task 3 was to identify the physical properties of the best seals and to characterize their geologic and lithologic nature. Potential seals associated with Paleozoic reservoirs include—from oldest to youngest—the upper limestone facies of the Madison Limestone, the Amsden Formation, a marine facies of carbonate and shale layers in the basal section of the Weber Sandstone, and the Chugwater Group and of the Dinwoody Formation (both Triassic). Also, several Mesozoic and Cenozoic formations were identified and analyzed and were found to be able to serve capably as secondary seals. In total, up to 12 seals were identified at the study site using various analyses, though only those mentioned above, 5 were studied in-depth due to the availability of core. All of the five lithologies were determined to be able to retain fully injected $CO_2$ volumes at the necessary column heights. The micritic limestone facies of the upper Madison Limestone is identified as the primary seal and has the best sealing capacity. However, it is our opinion that the Triassic Chugwater Group siltstones provide the most reliable, lateral seal at the study site due to a unique set of depositional and diagenetic properties.

### Executive Summary

The following results provide a brief summation of methods and major findings for the seven subtasks of Task 3.

- *Subtask 3.1*—Perform shear strength tests – Shear strength tests were performed on potential sealing lithologies and associated reservoirs. The compressive strength of all targeted seals was greater than the best injection interval in the Madison dolostone, suggesting initial mechanical pressure failure would be limited to the reservoir.
- *Subtask 3.2*—Perform capillary pressure tests for displacement pressure and sealing capacity – Capillary pressure entry tests were analyzed from core plugs and cuttings from potential sealing lithologies, and compared to reservoir data. A total of nine lithologies/formations had measured entry pressures that would competently retain the predicted $CO_2$ volumes. The primary seal, the upper Madison Limestone, had the highest measured entry pressures (>1250 psi). These data prove the study site has competent primary seals and multiple redundant seals.
- *Subtask 3.3*—Measure porosity and permeability – Porosity and permeability of the targeted sealing lithologies is within an expected range for seals, further supporting the displacement pressure data. The upper limestone facies of the Madison Limestone has the lowest overall porosity and permeability, which is ideal for the primary seal.
- *Subtask 3.4*—Analyze and define petrographic, geochemical, and mineralogical properties – Numerous analyses were performed to determine the geologic and

geochemical characteristics of the sites best seals. The sealing capabilities of the upper limestone facies of the Madison formation were largely related to its deposition. It is primarily a tightly-cemented, micritic limestone with little evidence of diagenetic alteration. Similar micritic carbonates are found to be sealing lithologies in the Amsden and basal unit of the Weber formations. The siltstones of the Chugwater Group are matrix dominated, with abundant carbonate and evaporate cements. The Amsden Formation is composed of multiple, stacked marine facies, some of which have a relatively high amount of diagenetic alteration.

- *Subtask 3.5*—Locate and evaluate other available core samples – Regional cores that penetrated potential sealing lithologies were identified at the USGS Core Facility in Golden, Co. Samples were collected for petrographical analysis.
- *Subtask 3.6*—Perform petrophysical analyses of well logs – Regional well logs were analyzed to identify the lateral continuity of sealing facies. Sealing lithologies form the upper Madison Limestone, the Amsden Formation, the Weber Sandstone and the Chugwater Group were found to be laterally continuous. Regional logs were used to develop regional seal cross sections and isopach maps.
- *Subtask 3.7*—Prioritize rock evaluation criteria for Best Practices Manual – Conclusions from this task were collected for input into the BPM.

## Methods

Over 70 samples were selected for thin section analysis. These samples were used to characterize the mineralogy, depositional history diagenesis, porosity, and facies of potential sealing lithologies. In addition, thin section analysis provided the data to identify strategic samples for further analysis (mechanical testing, mercury displacement testing, geochemical analysis, etc.), and was used to help define the lateral extent of potential sealing lithologies (Subtasks 3.5 and 3.6). The lithology of targeted seals relative to sealing potential is generalized in **Figure 3.1**.

## Results

Petrographic analysis identified multiple lithologies within sealing formations, as well as distinct burial and alteration histories. Primary sealing lithologies are defined as tight, micritic carbonate (limestone and/or dolostone), clastic carbonate, shale, or matrix-dominated siltstone. All evaluated sealing lithologies had thin section porosities less than 3%, and most were too minute to measure accurately with commercial petrographic software. Thin section analysis identified micritic limestones as having both the lowest overall porosity and minor diagenetic alteration. However, petrographic and geochemical analysis was also able to identify the primary controls of sealing within the siltstones of the Chugwater Group, a lithology that are typically not recognized as low-risk seals.

*Lithologic Character of Confining Layers*- The Chugwater Group is primarily siltstones composed of varying degrees of clastic, detrital grains and cements. Detrital grains are mostly quartz, with minor feldspar and heavy minerals. Detrital grains are commonly subangular and have a bimodal distribution with a higher percentage of smaller grains. Mudstone, shale and carbonate intraclasts are common, as is glauconite and oolites, suggesting some facies were deposited in near-shore high-energy environments. Other siltstones have an abundance of

anhydrite cements, signifying evaporitic concentration of shallow water: anhydrite is found to be associated with mudstone rip-up clasts in several samples. Varying percentage and character of clastic material also support an interpretation of multiple transgressions and regressions of water level. Bedding is typically consistent across the core though there is evidence of soft-sediment deformation and erosional surfaces.

Chugwater Group siltstones are notable for a high degree of oxidation (hematite), indicative of subaerial exposure, though there are remnant areas of reduction commonly with increased percentage of heavy minerals indicative of rapid burial, and/or carbonate rip-up clasts indicative of deeper water transgressions. Thin section analysis shows that areas of reduction are also commonly associated with intraclasts, suggesting that post-burial maturation of organics within the intraclasts provided localized reducing fluids. Thin section porosity was low, commonly <1%. Multiple episodes of carbonate and/or anhydrite cementation, associated with both depositional and diagenesis were major factors in the low porosity of this unit. Though a clastic siltstone with episodic alterations in water levels, the formation as a whole was rather homogenous with the only major variance observed in clastic to cement/matrix ratios. Also of importance to the character of the seal is that all evidence points to a matrix-dominated clastic system; detrital grains are supported in a matrix of clays, carbonate, and/or anhydrite, resulting in minimal porosity and increased sealing capacity. Collaborating thin sections can be found in the ***Appendix, Figures A.7, 8, 12a, 13a, 14a, 15-20***.

The basal unit of the Weber Sandstone includes several marine facies; limestone, dolostone, clastic carbonates, and minor clay/siltstones. The deposition was shallow and near-shore though some of the clastic carbonates could a represent flooded sabkha environment. Both dolostone and carbonate facies show little to no porosity, and minor post-burial alteration aside from pressure dissolution. Based on facies relations in this unit, it is likely that low porosity carbonate and shale are laterally continuous. At least one clastic carbonate sample had a secondary porosity (thin section) greater than 1% though it was uncharacteristic of the unit as a whole.

The Amsden Formation is a complicated mix of siltstone, shale, carbonate (limestone and dolostone), and even includes collapse breccias and a paleosol. Deposition initiated subareally on unconformable, karsted limestones, and progressed into a mixed-energy, cyclic, submarine environment. As a result of this depositional history, the Amsden Formation is lithologically heterogeneous, laterally variant, and has recorded differing impacts from diagenesis.

Diagenetic events include near-surface and deep-burial dolomitization, compaction, thermal chemical sulfate reduction, matrix dissolution, and pyritization. However, thin section porosity was low, commonly <1%, and the low porosity was commonly a by-product of diagenesis. Several vertical fractures, annealed with calcite and silica, were noted in the formation. Fractures were largely restricted to carbonate facies and rarely exceeded 200μm.

Limestone facies in the upper Madison formation include micrite, biomicrite, and pelmicrite. Facies can be sequential, evidence of higher order responses to eustatic seas. Also, there are two thin collapse breccias that had largely recrystallized. Nearly all of the micritic facies display primary textures, aside from localized zones of pressure solution and secondary infilling of calcite, biotite, and anhydrite in some molds and peloids. Additionally, this unit showed evidence

of fracturing and brittle deformation, though fracture aperture was small, the fractures were annealed with calcite. Collapse breccias commonly display secondary minerals associated with thermochemical sulfate reduction, though there is no evidence of remnant porosity. Porosity was nearly nonexistent in thin section analyses. Though this unit was tight and recorded minimal alteration, its relation to underlying dolostones, karsted surface and interlayered collapse breccias suggest a high degree of regional heterogeneity relative to lateral continuity and thickness.

*Diagenetic Summary*- Of the seals associated with reservoirs, the Amsden Formation records the most evidence of burial-related diagenetic alteration (*see* ***Appendix, Figures A.1, 2, 5, 6***). However, a diagenetic alteration within the Amsden has resulted in lower porosity. Siltstones, found in the red beds of the Chugwater Group and as facies in the Amsden formation, are generally cemented by a tight matrix of anhydrite, calcite, and dolomite (*see* ***Appendix, Figures A.7, 8, 12a, 13a, 14a, 15-20***). Limestone in the Amsden, upper Madison, and lower Weber are commonly unaltered and micritic, with secondary mineralization confined to molds. Unlike the Madison, dolomitization of limestone in the Amsden was selective and did not enhance porosity.

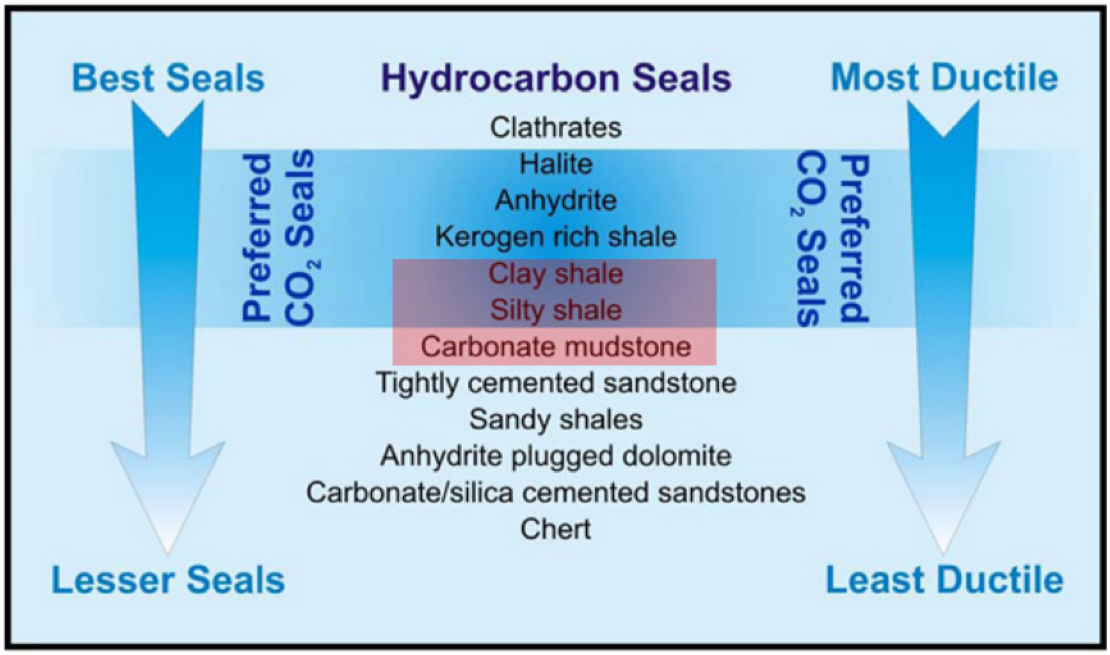


**Figure 3.1** Idealized seal chart by lithology. Lithology types from this study are highlighted by red box. Figure modified from IEAGHG, March 2009

Thin section analysis, correlated to petrophysical data, shows that the Amsden Formation has the most geologic heterogeneity, resulting in introduced uncertainty from low- lateral continuity of distinct lithofacies. Microphotographs depicting potential seals can be found in the ***Appendix, Figures A.1-20***.

*Mechanical analysis*- Triaxial shear tests were performed on seals and reservoirs to determine mechanical properties. Vertical plugs for triaxial shear analysis were acquired from potential sealing lithologies in the Chugwater Group, the Amsden Formation, and the upper limestone facies in the upper Madison Limestone as well as from reservoir intervals in the Weber and Madison formations (**Table 3.1**). Both the Chugwater Group and the Amsden Formation samples

recorded compressive strengths that were greater than reservoir dolostones in the Madison (**Table 3.1**). The Amsden Formation sample had a compressive strength that was nearly double that of the best injection interval. The Amsden sample also had the highest recorded Young's Modulus, suggesting a relatively high degree of rigidity.

Samples of the Chugwater Group vary though some have a high degree of ductility/elasticity relative to reservoir rocks. This is known to increase the overall mechanical competency of the formation, as it allows a formation a modicum of elasticity and the capability to flex under stress (**Figure 3.2** and **3.3**). The elastic rebound was evidenced in core analysis of the Chugwater Group; horizontal decompressure fractures were common. Thin section analysis would suggest the ductility of the Chugwater Group samples are associated with evaporites such as anhydrite and gypsum as well as carbonate cements.

The relatively low Poisson's Ratio of these samples further verifies unique compressibility, as neither recorded much lateral expansion relative to the reservoir sample. These tests indicate that pressure-related mechanical failure would initially be limited to the reservoir, and seals have the capacity to retain their mechanical integrity during injection.

**Table 3.1:** Triaxial shear analysis of potential seals and associated reservoirs from the RSU#1 well.

| Depth ft. (m) | Formation | Confining Pressure (psi) | Bulk Density ($g/cm^3$) | Compressive Strength (psi) | Young's Modulus ($10^6$ psi) | Poisson's Ratio |
|---|---|---|---|---|---|---|
| 10,602.6 (3,232) | Chugwater Group | 2490 | 2.69 | 49,378 | 7.96 | 0.17 |
| 10,630.7 (3,240) | Chugwater Group | 2490 | 2.78 | 38,504 | 6.11 | 0.20 |
| 10,683.2 (3,256) | Chugwater Group | 2490 | 2.65 | 41,146 | 5.04 | 0.19 |
| 11,417.2 (3,480) | Weber | 2490 | 2.48 | 61,867 | 8.23 | 0.16 |
| 12,182 (3,713) | Amsden | 5500 | 2.75 | 97,693 | 10.35 | 0.23 |
| 11416.90-11417.10 | Weber | 1000 | 2.51 | 45,883 | 8.65 | 0.16 |
| 11417.50-11417.70 | Weber | 2000 | 2.52 | 51,083 | 9.30 | 0.13 |
| 11521.35 | Weber | 2490 | 2.56 | 72,048 | 9.56 | 0.19 |

| | | | | | | |
|---|---|---|---|---|---|---|
| 11535.00-11535.15 | Weber | 4000 | 2.80 | 73,297 | 10.56 | 0.29 |
| 12382.90-12383.10 | Madison | 1000 | 2.53 | 22,046 | 6.25 | 0.31 |
| 12383.80-12384.00 | Madison | 2000 | 2.62 | 31,741 | 7.72 | 0.31 |
| 12,384 (3,773) | Madison | 2490 | 2.53 | 36,400 | 6.91 | 0.26 |
| 12512.00 | Madison | 2490 | 2.48 | 12,870 | 2.62 | 0.29 |
| 12244.00-12244.10 | Madison | 5500 | 2.73 | 47,677 | 4.75 | 0.31 |

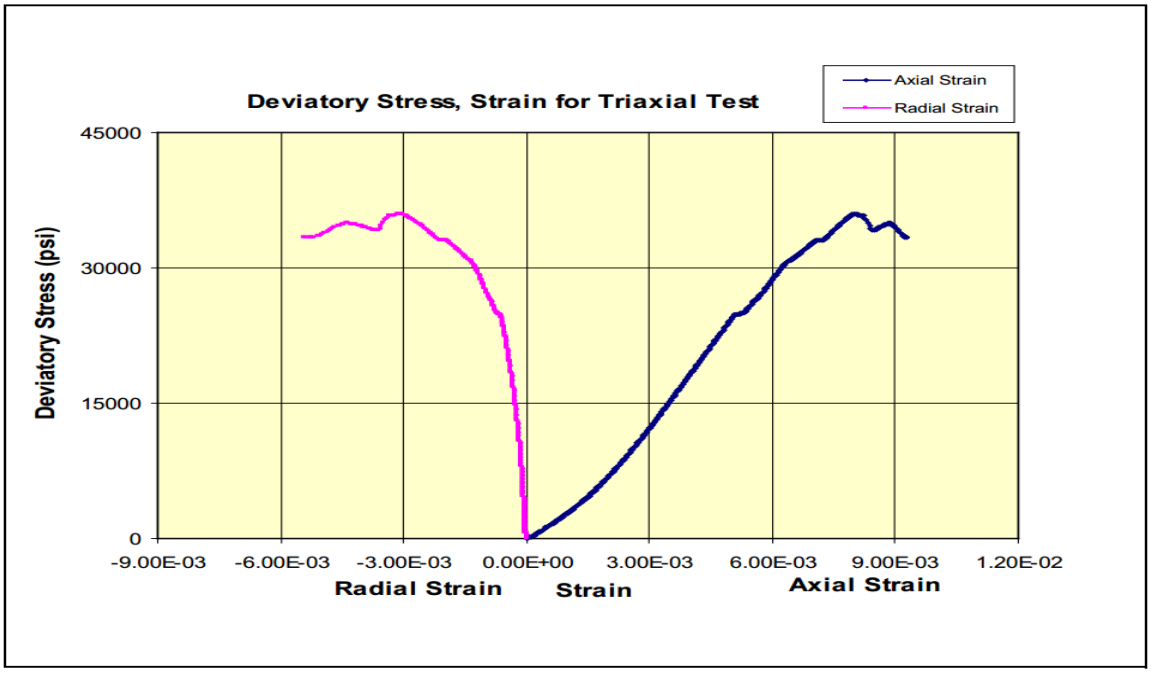


**Figure 3.2:** Stress diagram for sample 2V, from the Chugwater Group. The "warble" at the beginning of measured axial and radial strain indicates ductility and elasticity.

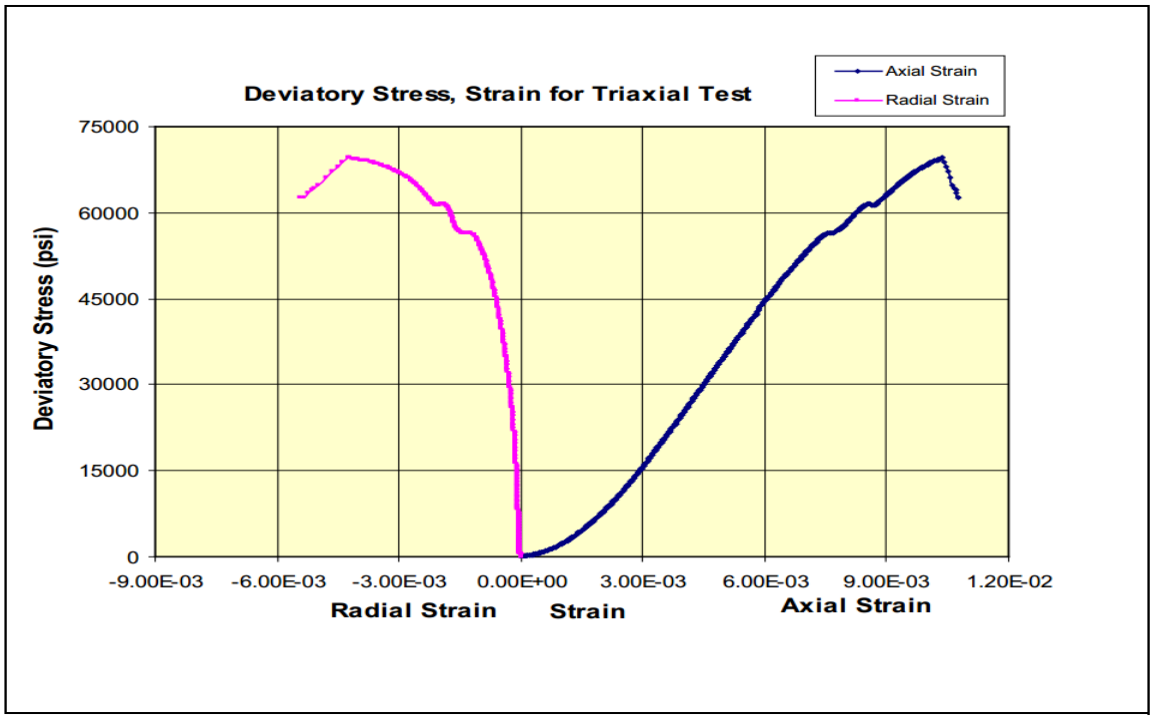


**Figure 3.3:** Stress diagram for sample 31V from the Weber Sandstone showing near instantaneous depletion of axial and radial strain at failure, indicating a relatively brittle formation.

*Displacement pressure analysis*- Mercury capillary displacement analysis was performed on selected seals and associated reservoirs. These tests are crucial in evaluating the holding capacity of a potential seal relative to an injected gas column, as well as pressures associated with infiltration and leakage. Two suites of testing were performed, and results from one example are shown in **Table 3.2**. It should be noted that these results only include competent samples. Several core plug samples were fractured during the retrieval process and recorded artificially low displacement pressures.

Data from the lab indicates that red beds from the Chugwater Group have displacement pressures that range between 939 and 2,718 psi, and the formation averages 1,580 psi (n=4). Two additional Amsden Formation samples from this analysis recorded displacement pressures of 1,254 and 1,381 psi. Data also shows that the Mowry, Baxter, Gypsum Springs, and Phosphoria formations have displacement pressures that are greater than 350 psi and up to 1,030 psi. In addition to measured displacement pressures, the pore throat distributions are characterized as micropores and both brine and air permeabilities are minor (**Table 3.2**).

This testing indicates that the study site has multiple, stacked seals including those adjacent to targeted reservoirs. These formations with the ability to retain injected fluids include—from oldest to youngest—the limestone facies of the upper Madison, the Amsden Formation, a clastic shale facies (and possibly some of the laterally extensive carbonates) at the base of the Weber Sandstone, the Phosphoria Formation, the Dinwoody Formation, the Chugwater Group, the Gypsum Springs Formation, the Mowry Shale, and the Baxter Shale.

Displacement pressure analysis shows that micritic carbonate facies have the greatest overall holding capacity. Petrographic analysis has identified this facies-type in numerous formations. It is also likely, based on similar petrophysical properties that portions of the Sundance, Morrison, Thermopolis, Frontier, Blair, and Rock Springs formations would act as potential seals at the study site.

**Table 3.2:** Results of mercury displacement pressure testing of potential seals (samples out of the RSU#1 well). Sample 206 is from the upper Madison limestone at 12,300'. Five samples, one shale, and four carbonates did not allow for mercury injection, indicating displacement pressures are higher than the upper analytical limit.

| | | | | Mercury/Air | Pore Throat Distribution | | | Swanson | |
|---|---|---|---|---|---|---|---|---|---|
| Interval Depth (ft) | Formation ID | Sample Type | Grain Density g/cc | Displacement Pressure (psi) | Micropores < 0.1 micron (%PV) | Intermediate 0.1-3 micron (%PV) | Macropores > 3 micron (%PV) | Brine Permeability (mD) | Air Permeability (mD) |
| 6300-6330 | Baxter 1 | Cuttings | 2.59 | 390.424 | 87.3 | 12.7 | 0.0 | 0.003 | 0.022 |
| 7680-7710 | Baxter 2 | Cuttings | 2.57 | 217.251 | 78.8 | 23.7 | 0.0 | 0.006 | 0.040 |
| 7590-7620 | Baxter 3 | Cuttings | 2.49 | 430.624 | 85.3 | 14.7 | 0.0 | 0.003 | 0.018 |
| 8130-8160 | Mowry 1 | Cuttings | 2.51 | 701.029 | 92.2 | 7.8 | 0.0 | 0.004 | 0.026 |
| 8220-8250 | Mowry 2 | Cuttings | 2.50 | 1032.419 | 100.0 | 0.0 | 0.0 | 0.002 | 0.013 |
| 9190-9200 | Gypsum Springs 1 | Cuttings | 2.59 | 850.344 | 100.0 | 0.0 | 0.0 | 0.003 | 0.023 |
| 10601.9 | Chugwater 1 | Core Plug | 2.71 | 939.710 | 90.2 | 9.8 | 0.0 | 0.000 | 0.005 |
| 10605.8 | Chugwater 2 | Core Plug | ND | 1140.440 | 82.1 | 17.9 | 0.0 | 0.000 | 0.000 |
| 10653.4 | Chugwater 3 | Core Plug | ND | 2718.728 | 54.8 | 45.2 | 0.0 | 0.000 | 0.000 |
| 10682.1 | Chugwater 4 | Core Plug | 2.69 | 1521.419 | 86.8 | 13.2 | 0.0 | 0.000 | 0.003 |
| 10820-10840 | Dinwoody 1 | Cuttings | 2.73 | 412.720 | 65.9 | 34.1 | 0.0 | 0.052 | NA |
| 10840-10860 | Dinwoody 2 | Cuttings | 2.74 | 405.954 | 67.9 | 32.1 | 0.0 | 0.044 | NA |
| 11040-11050 | Phosphoria 1 | Cuttings | 2.71 | 354.480 | 73.7 | 26.3 | 0.0 | 0.024 | 0.121 |
| 11140-11150 | Phosphoria 2 | Cuttings | 2.65 | 389.745 | 76.9 | 23.1 | 0.0 | 0.020 | 0.105 |
| 11725.9 | Weber 1 | Core Plug | 2.70 | No Injection | ND | ND | ND | ND | ND |
| 11,766.8 | Weber marine | Core Plug | 2.65 | 1034.229 | 83.0 | 17.0 | 0.0 | 0.000 | 0.016 |
| 12,178.1 | Amsden 1 | Core Plug | 2.91 | No Injection | ND | ND | ND | ND | ND |
| 12,197.4 | Amsden 2 | Core Plug | 2.85 | 1381.100 | 83.3 | 16.7 | 0.0 | 0.001 | 0.005 |
| 12,227.3 | Amsden 3 | Core Plug | 2.85 | No Injection | ND | ND | ND | ND | ND |
| 12,250.0 | Madison | Core Plug | 2.70 | 1253.697 | 15.3 | 84.7 | 0.0 | 0.000 | 0.001 |
| 12333.9 | Madison 1 | Core Plug | 2.83 | 3630.110 | 100.0 | 0.0 | 0.0 | 0.000 | 0.000 |
| 12300.0 | Madison 2 | Core Plug | 2.74 | No Injection | ND | ND | ND | ND | ND |

| Company: | University of Wyoming | | Sample: | D1m | un- | Host Plug | |
|---|---|---|---|---|---|---|---|
| Well: | Dinwoody | | Depth, feet: | 10820.00-10840.00 | stressed | n/a | n/a |
| File: | HOU-131093 | | Klinkenberg Permeability, md: | | N/A | - | - |
| | | | Permeability to Air, md: | | N/A | - | - |
| | | | Swanson Permeability, md: | | 0.0526 | - | - |
| | | | Porosity, fraction: | | 0.117 | - | - |
| | | | maximum Sb/Pc, fraction: | | 0.00508 | | |
| | | | R35, microns: | | 0.0961 | | |
| | | | R50 (median pore throat radius): | | 0.0549 | | |

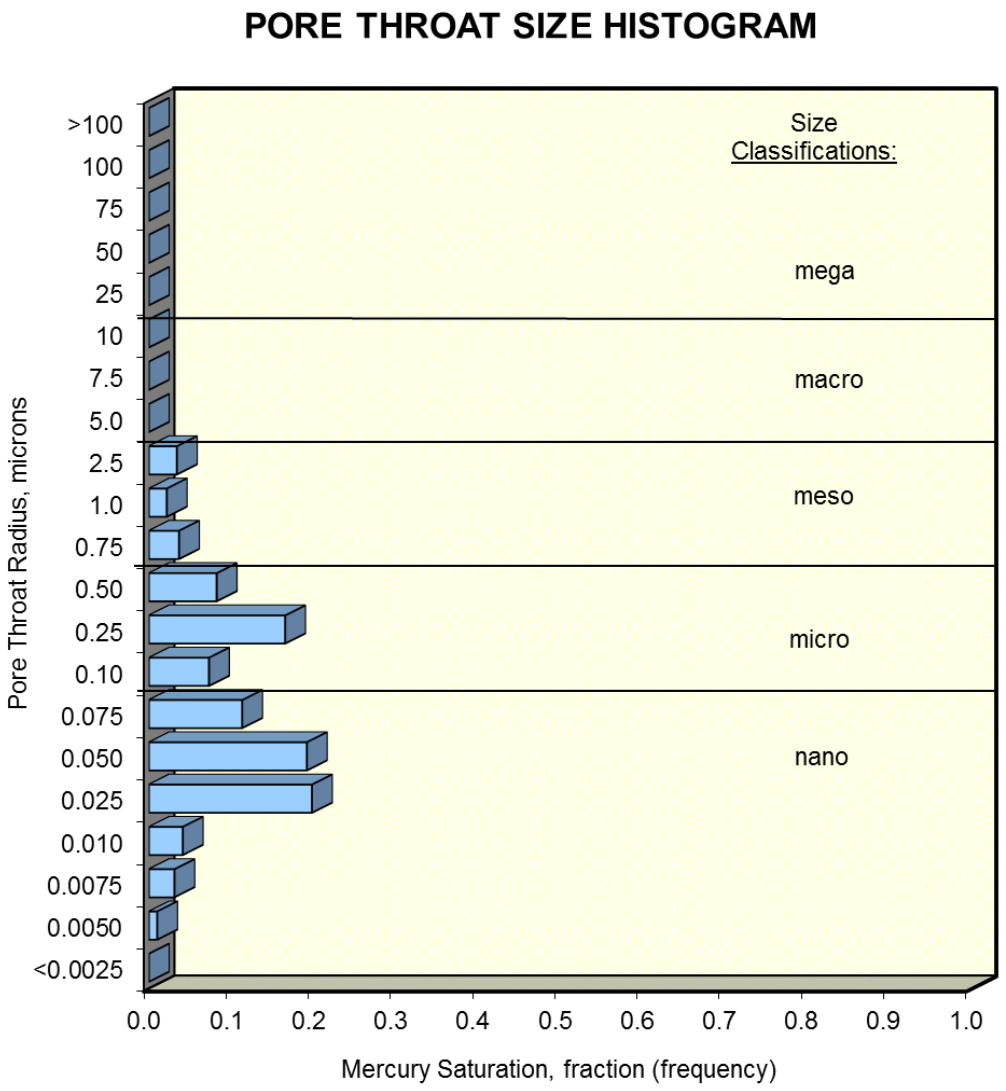


**Figure 3.4:** Histogram of pore throat sizes from cuttings form the Dinwoody Formation (from 10,820 to 10,840 ft.). Pore throat sizes are dominantly micro to nano size.

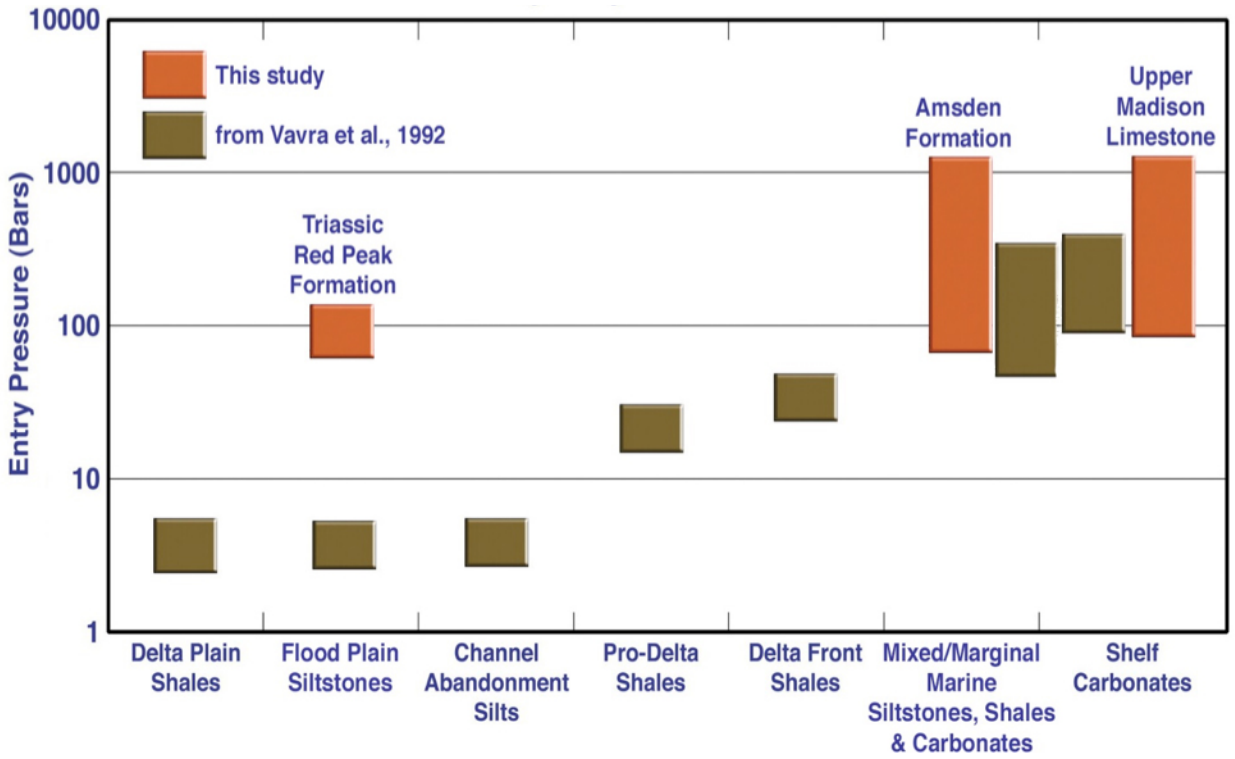


**Figure 3.5:** Previous studies have identified a correlation between specific lithology and sealing potential. This study shows comparable (and the highest) sealing potential between marine sediments, but continental sediments (i.e. the Red Peak Formation) at our study site has enhanced sealing potential relative to other investigated siltstones.

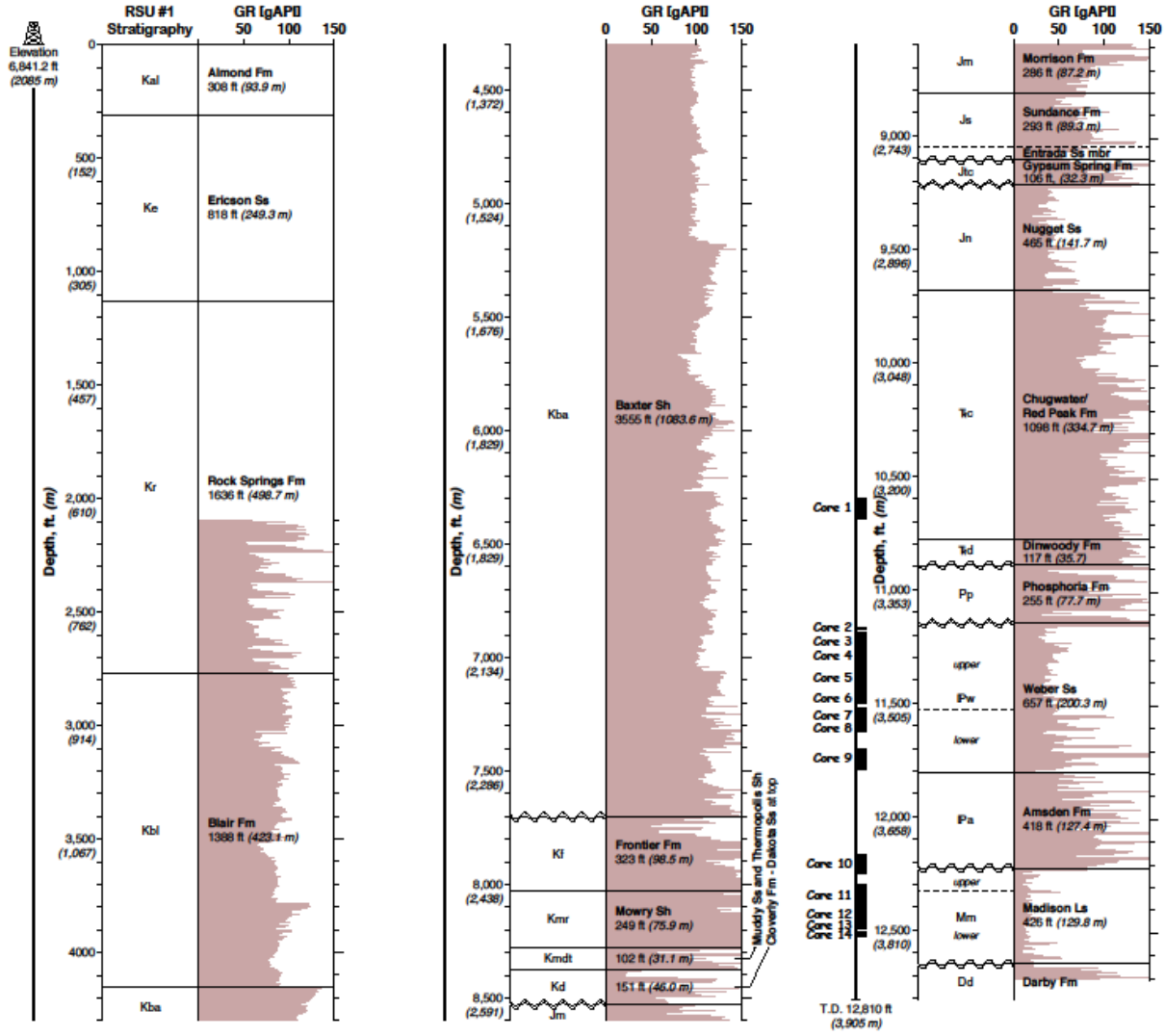


**Figure 3.6:** Gamma log showing formation tops, thicknesses, depths, and cored intervals for the RSU#1 well. This data suggests that there are multiple units with lithological characteristics similar to analyzed seals.

*Porosity and Permeability of Sealing Lithologies*- Permeability and porosity were measured in intervals identified as potential seals. These analyses were performed to augment the displacement pressure analyses at reservoir conditions. Nearly all samples had minimal permeability and porosity, indicative of sealing capabilities (**Table 3.3**). The upper carbonate facies of the Madison Limestone has the lowest porosity and permeability, which is corroborated by petrographic analyses and published data of unaltered shelf carbonates (**Table 3.3**).

**Table 3.3:** Porosity and permeability measurements of potential sealing lithologies. Note that sample 122 was fractured during testing (indicated by Fr). Triassic Redbeds denotes samples taken from the Chugwater Group. *

| Sample No. | Sample Depth | | Permeability | | | | Porosity | | Density |
|---|---|---|---|---|---|---|---|---|---|
| | | | 800 psi NCS | | Reservoir NCS | | 800 NCS | Res. NCS | |
| | | | to Air | Klinkenberg | to Air | Klinkenberg | Porosity | Porosity | |
| | (ft) | (m) | (mD) | | (mD) | | (percent) | | (g/cm$^3$) |
| **Triassic Redbeds** | | | | | | | | | |
| 1 | 10,601.9 | 3,231.5 | 0.005 | 0.002 | 0.001 | 0.000 | 1.64 | 1.00 | 2.71 |
| 120 | 10636.3 | 3,241.9 | 0.11 | 0.075 | 0.001 | 0.000 | 1.79 | 0.62 | 2.73 |
| 122 | 10649.10 | 3,245.8 | Fr | Fr | 0.438 | 0.342 | 2.2 | 1.0 | 2.71 |
| 125 | 10671.8 | 3,252.8 | 0.01 | 0.005 | 0.001 | 0.000 | 2.54 | 1.43 | 2.67 |
| 18 | 10,682.1 | 3,255.9 | 0.003 | 0.001 | 0.001 | 0.000 | 1.24 | 0.79 | 2.69 |
| **Shale at base of Weber** | | | | | | | | | |
| 175 | 11,725.0 | 3,573.8 | 0.007 | 0.002 | 0.002 | 0.001 | 1.198 | 0.402 | 2.72 |
| **Amsden Formation** | | | | | | | | | |
| 186 | 12170.3 | 3,709.5 | 0.016 | 0.008 | < .001 | < .001 | 2.05 | 0.59 | 2.68 |
| 190 | 12198.95 | 3,718.2 | 0.159 | 0.21 | 0.028 | 0.045 | 3.62 | 2.04 | 2.80 |
| 195 | 12215.6 | 3,723.3 | 0.183 | 0.129 | < .001 | < .001 | 2.90 | 1.27 | 2.64 |
| 199 | 12224.6 | 3,726.1 | 0.002 | < .000 | < .001 | < .001 | 4.98 | 2.58 | 2.83 |
| **Madison Carbonate** | | | | | | | | | |
| 201 | 12240.00 | 3,730.8 | 0.043 | 0.026 | 0.003 | 0.001 | 2.9 | 1.8 | 2.69 |
| 59 | 12250.00 | 3,733.8 | 0.001 | 0.000 | 0.000 | 0.000 | 1.3 | 0.3 | 2.70 |
| 205 | 12255.90 | 3,735.6 | 0.013 | 0.006 | < .001 | 0.000 | 1.0 | 0.3 | 2.69 |
| 208 | 12309.30 | 3,751.9 | 0.008 | 0.003 | < .001 | 0.000 | 1.3 | 0.3 | 2.68 |
| 210 | 12318.00 | 3,754.5 | 0.012 | 0.005 | < .001 | 0.000 | 1.3 | 0.3 | 2.68 |
| 212 | 12323.80 | 3,756.3 | 0.003 | 0.001 | < .001 | 0.000 | 0.5 | 0.3 | 2.68 |
| 63 | 12333.00 | 3,759.1 | 0.001 | 0.000 | < .001 | 0.000 | 0.9 | 0.3 | 2.70 |

*Geochemical Analysis*- Geochemical analysis of selected sealing lithologies included trace element analysis, XRD, XRF, and radiogenic and stable isotopic analysis. These analyses were used to both evaluate geologic character and to help define models in Tasks 4 and 5. The elemental analysis will be used to characterize potential geochemical reactions between injected $CO_2$ and reactive shales and carbonates, and help to define clay species, burial, and alteration history. Preliminary elemental analysis indicates most sediment was deposited in oxidative environments, with the exception of the clastic shale near the base of the Weber (reduced environment indicated by high uranium concentrations, as well as Cr, V, Ni, and Zn) (**Table 3.4**). This data also suggests that enriched zones of evaporitic minerals, long known to enhance the sealing capacity of sediments, have had a measurable impact on trace element abundances, and possibly altered formation fluids (**Table 3.4**).

**Table 3.4:** Trace element analysis of potential sealing lithologies. Note that Red Peak corresponds to samples from the Chugwater Group. *

| RSU Sample # | Depth | | | | | | | | | | | | | | | | | | | | | | | | | | | | | | | |
|---|---|---|---|---|---|---|---|---|---|---|---|---|---|---|---|---|---|---|---|---|---|---|---|---|---|---|---|---|---|---|---|---|
| *Whole Rock Geochem (in ppm)* | | Sample | Sc | Ti | V | Cr | Mn | Ni | Cu | Zn | Ga | As | Se | Br | Rb | Sr | Y | Zr | Nb | Ag | Cd | Te | Cs | Ba | La | Ce | Nd | W | Tl | Pb | Bi | Th | U |
| *Red Peak* | | | | | | | | | | | | | | | | | | | | | | | | | | | | | | | | | |
| 3 | 10603.20 | redbed | <d.l. | 8010.5 | 61.1 | 75.7 | 542.0 | 29.3 | 14.3 | 54.2 | 14.7 | 44.7 | 8.9 | 7.2 | 79.9 | 118.3 | 29.5 | 331.3 | 12.1 | 18.3 | 16.8 | <d.l. | <d.l. | 368.9 | 36.3 | 69.7 | 36.5 | 5.3 | 14.9 | 18.9 | 15.4 | 9.1 | <d.l. |
| 12 | 10633.80 | evap | <d.l. | 5488.7 | 46.9 | 42.6 | 526.2 | 21.1 | 15.2 | 47.2 | 11.9 | 43.0 | 9.8 | 7.4 | 65.0 | 491.5 | 21.1 | 182.5 | 7.8 | 23.8 | 14.5 | <d.l. | <d.l. | 474.8 | 30.7 | <d.l. | <d.l. | 4.7 | 17.0 | 10.7 | 16.9 | 5.7 | <d.l. |
| 14 | 10645.50 | redbed | <d.l. | 4899.5 | 35.3 | 36.2 | 416.6 | 17.3 | 10.3 | 29.3 | 9.7 | 44.4 | 9.1 | 7.5 | 53.5 | 589.0 | 16.5 | 196.1 | 7.0 | 17.0 | 11.1 | 9.8 | <d.l. | 245.1 | <d.l. | <d.l. | <d.l. | <d.l. | 20.2 | 12.3 | 17.2 | <d.l. | <d.l. |
| 17 | 10680.05 | redbed | <d.l. | 6976.3 | 63.8 | 52.7 | 523.1 | 27.5 | 14.1 | 47.9 | 14.2 | 42.1 | 8.4 | 6.3 | 82.2 | 268.1 | 25.0 | 315.1 | 11.2 | 14.3 | 15.4 | <d.l. | <d.l. | 340.1 | 34.3 | 51.0 | 25.7 | 4.9 | 16.1 | 19.0 | 16.5 | 7.0 | <d.l. |
| *Weber (shale near base)* | | | | | | | | | | | | | | | | | | | | | | | | | | | | | | | | | |
| 43 | 11726.40 | shale | <d.l. | 6423.2 | 1069.2 | 1702.1 | 39.9 | 558.3 | 131.7 | 1640.0 | 20.1 | 73.1 | 23.1 | 8.4 | 172.4 | 348.7 | 110.2 | 274.8 | 9.1 | 25.2 | 40.2 | <d.l. | 47.3 | 300.2 | 102.3 | 135.8 | 50.8 | <d.l. | 23.2 | 137.2 | 17.9 | 8.4 | 81.2 |
| *Amsden Formation* | | | | | | | | | | | | | | | | | | | | | | | | | | | | | | | | | |
| 49 | 12174.45 | lime | <d.l. | 80.0 | <d.l. | 11.1 | 60.1 | <d.l. | <d.l. | 3.9 | 2.8 | 62.9 | 12.6 | 10.5 | 2.1 | 186.9 | <d.l. | <d.l. | <d.l. | 28.0 | 15.2 | <d.l. | <d.l. | 40.3 | <d.l. | <d.l. | <d.l. | 6.3 | 29.6 | 8.6 | 23.6 | <d.l. | <d.l. |
| 50 | 12178.45 | clastic | 12.0 | 8579.0 | 56.6 | 100.5 | 32.1 | 31.2 | 5.0 | 35.5 | 16.8 | 41.7 | 8.4 | 6.2 | 201.5 | 191.3 | 22.8 | 392.7 | 12.3 | 21.0 | 14.8 | <d.l. | 31.5 | 112.7 | 28.8 | 74.9 | 37.1 | 4.5 | 17.6 | 12.1 | 14.5 | 9.7 | <d.l. |
| 52 | 12187.30 | lime | <d.l. | 453.1 | <d.l. | 10.6 | 85.3 | <d.l. | <d.l. | 2.6 | 2.4 | 56.8 | 10.5 | 9.6 | 4.5 | 148.5 | <d.l. | 11.8 | <d.l. | 22.6 | 14.2 | <d.l. | <d.l. | 28.7 | <d.l. | <d.l. | <d.l. | 5.2 | 25.8 | 6.0 | 21.7 | <d.l. | <d.l. |
| 56 | 12219.15 | clastic | <d.l. | 3492.3 | 43.4 | 40.5 | 77.0 | 16.3 | <d.l. | 10.4 | 7.4 | 56.9 | 11.0 | 9.5 | 48.0 | 60.2 | 5.6 | 37.1 | 2.4 | 22.2 | 12.2 | 19.9 | <d.l. | 99.7 | <d.l. | <d.l. | <d.l. | 5.5 | 25.0 | 6.1 | 22.5 | <d.l. | <d.l. |
| *Upper limestone facies of the Madison Limestone* | | | | | | | | | | | | | | | | | | | | | | | | | | | | | | | | | |
| 57 | 12233.00 | lime | <d.l. | 72.8 | <d.l. | 8.9 | 1297.0 | 20.0 | <d.l. | 33.8 | <d.l. | 41.5 | 9.1 | 11.9 | 2.3 | 126.4 | <d.l. | <d.l. | <d.l. | 13.5 | <d.l. | <d.l. | <d.l. | 31.8 | <d.l. | <d.l. | <d.l. | 4.4 | 20.2 | 8.3 | 15.4 | <d.l. | <d.l. |

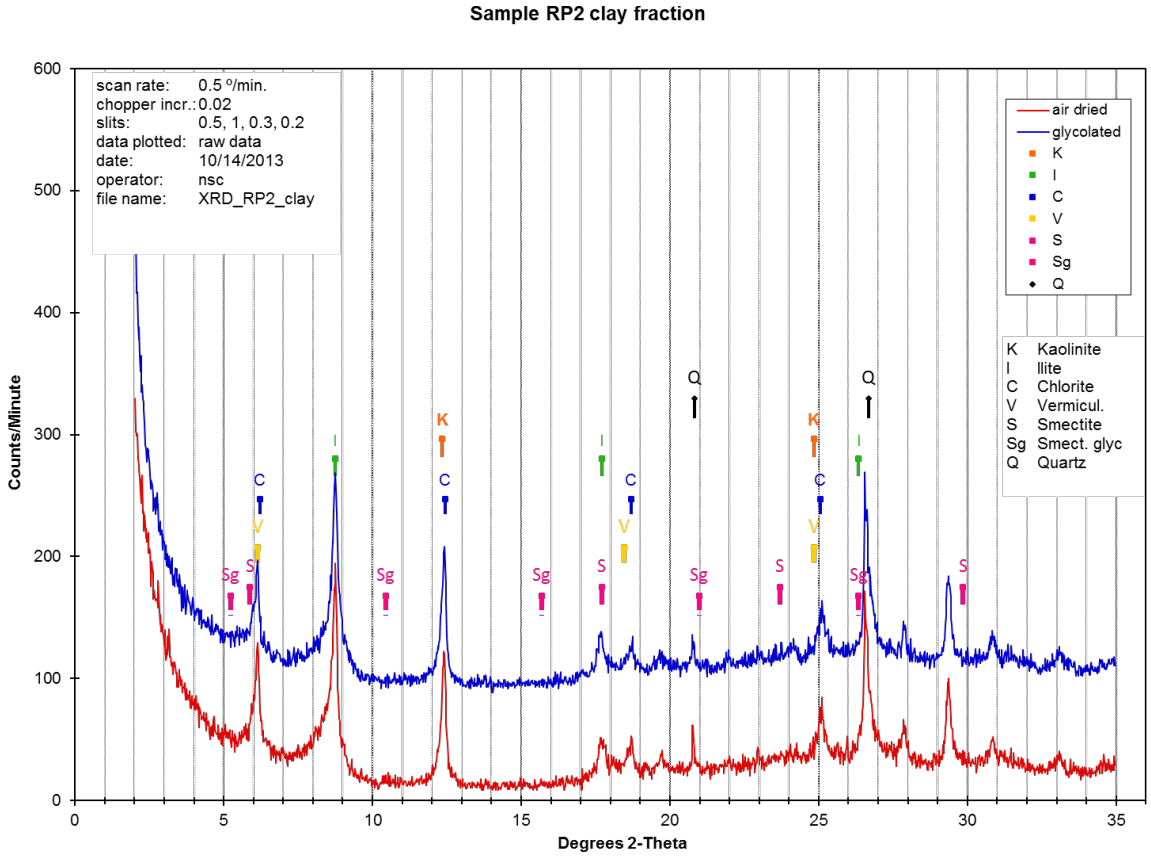


**Figure 3.7:** 10603.2 XRD clay fraction diagram. This sample had steeper peaks than other Triassic samples noticeably. Petrographic analysis suggests a high percentage of mudstone relative to other samples.

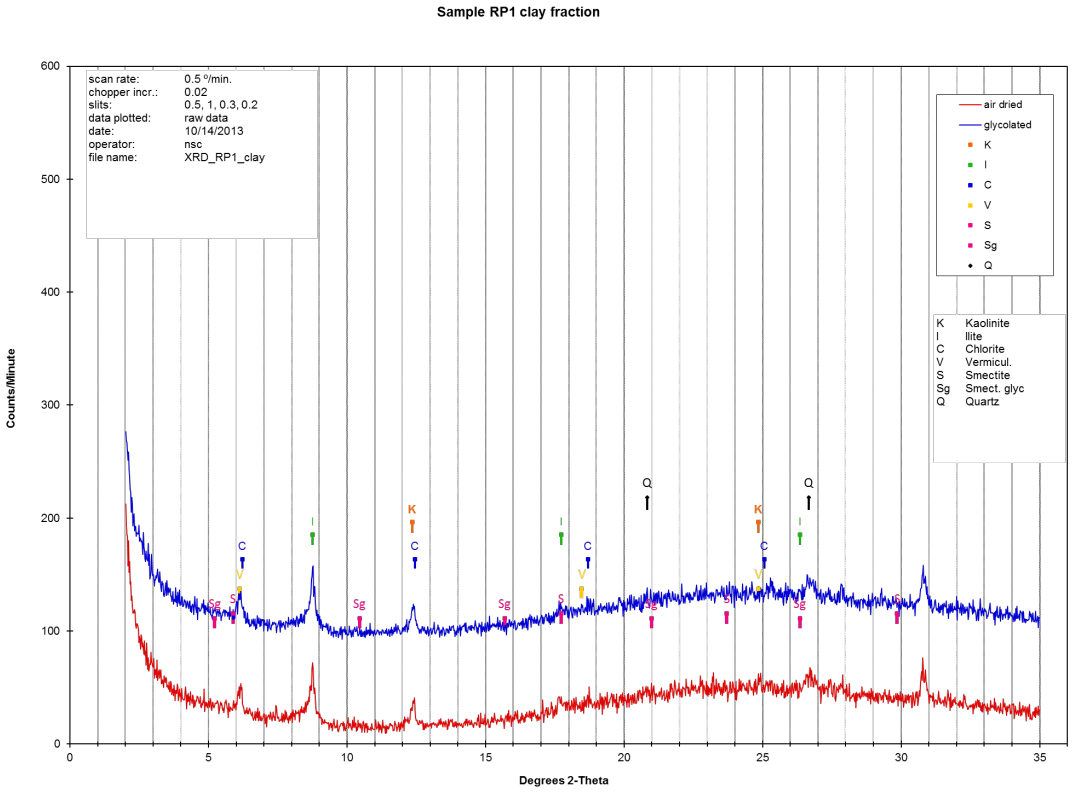


**Figure 3.8:** 10,636.3. XRD clay fraction diagram. This sample has illite as a primary clay with minimal mixed-layer clays. This supports the thin section analysis and burial history interpretations.

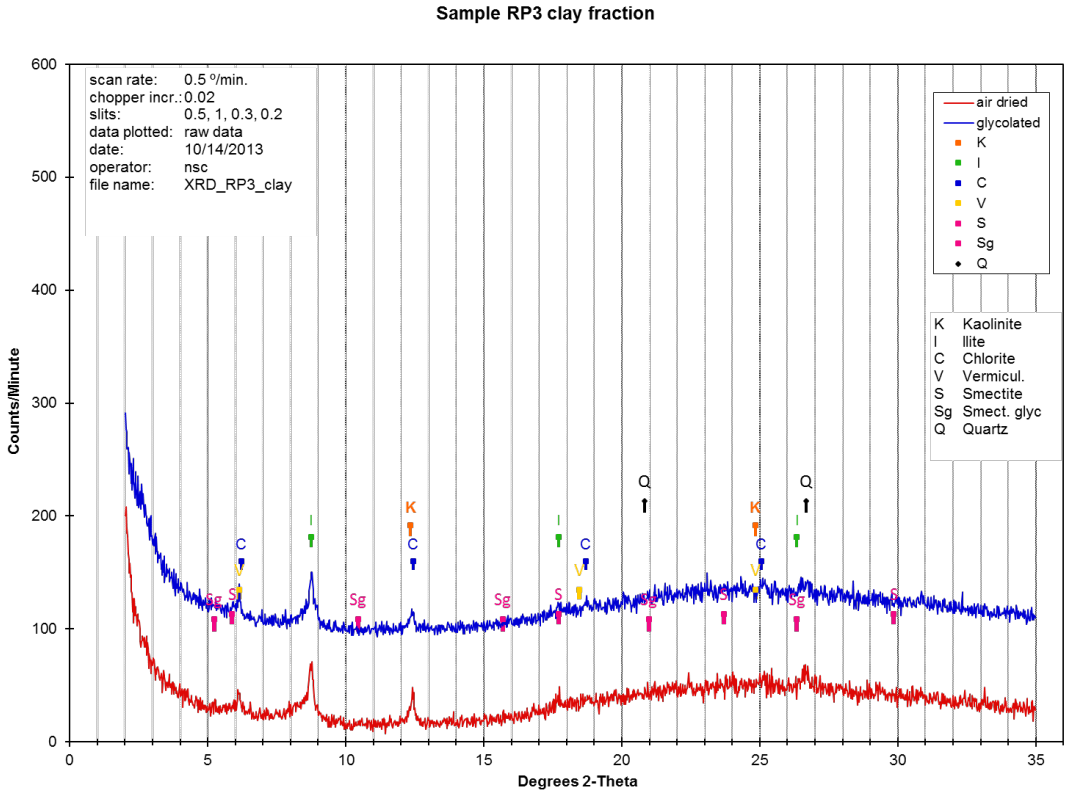


**Figure 3.9:** 10,680.05. XRD clay fraction diagram. Note the consistency with Figure 3.8.

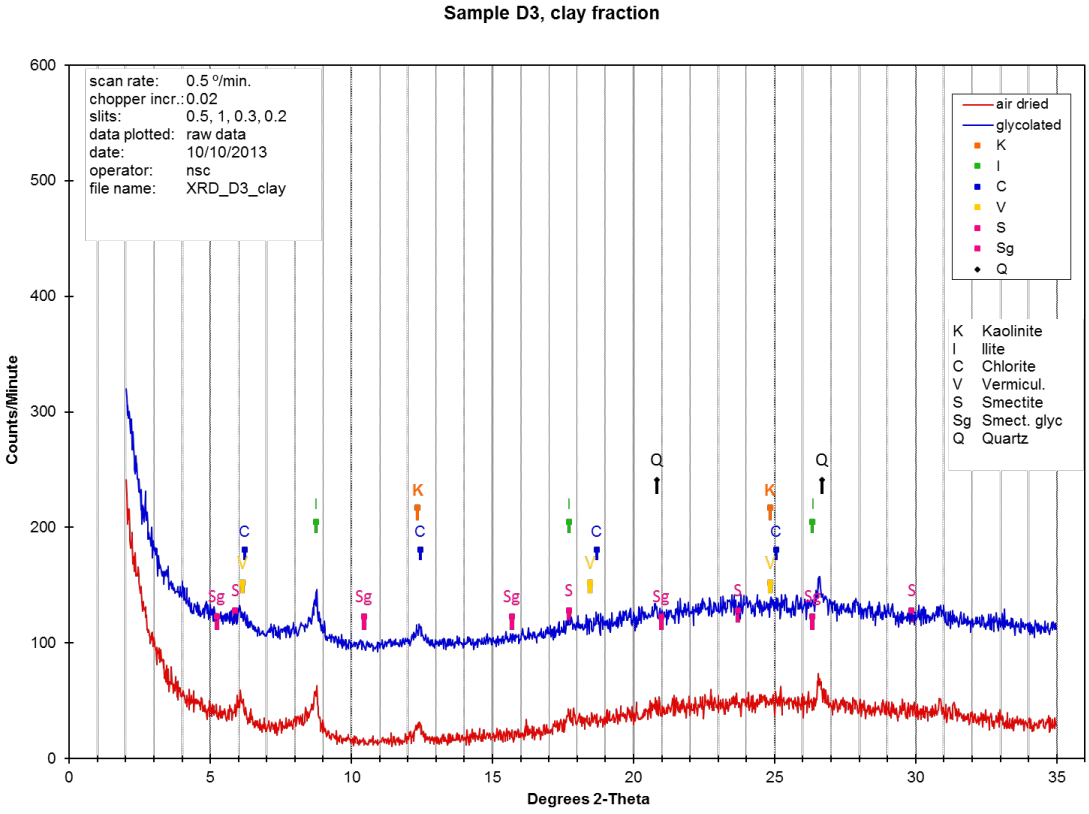


**Figure 3.10:** 10,780-10,800. XRD clay fraction diagram from cuttings. The illite and chlorite spikes are more pronounced than the Red Peak samples, indicating higher proportions of clay in the Dinwoody Formation.

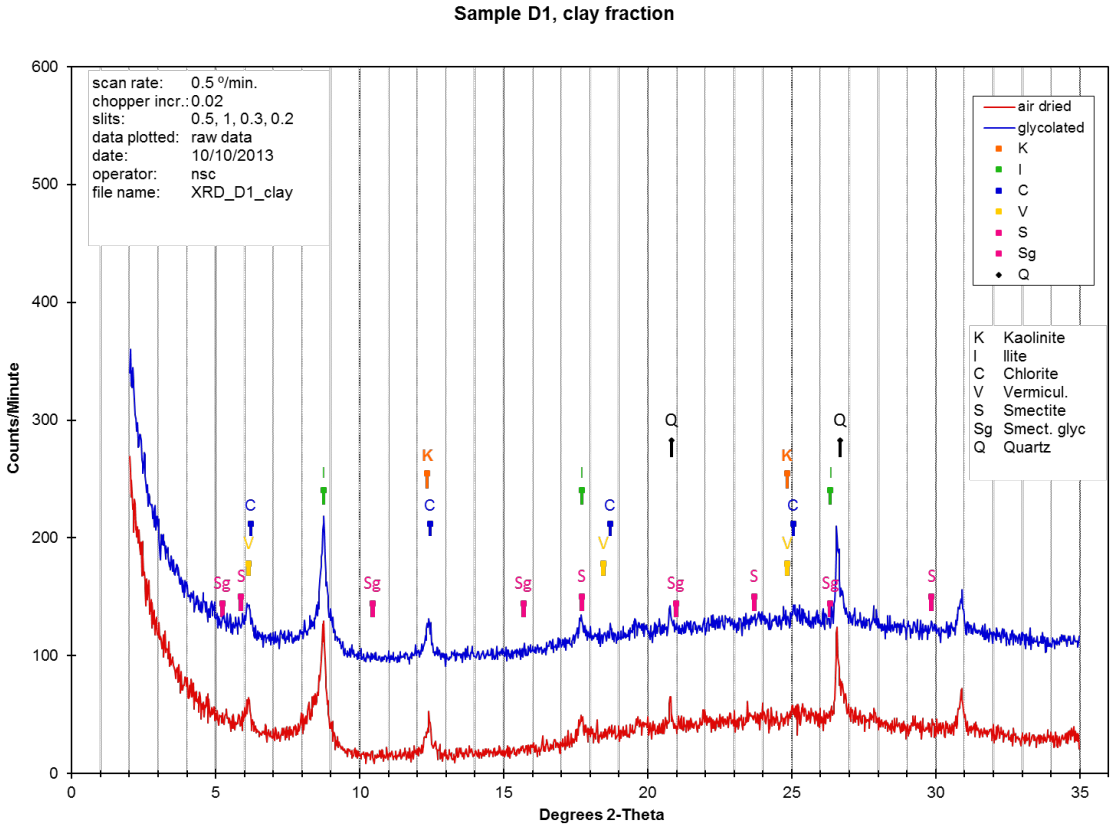


**Figure 3.11:** 10,820-10,840. XRD clay fraction diagram from cuttings. Note the consistency with Figure 3.10 indicative of the homogeneous lithology of Triassic units.

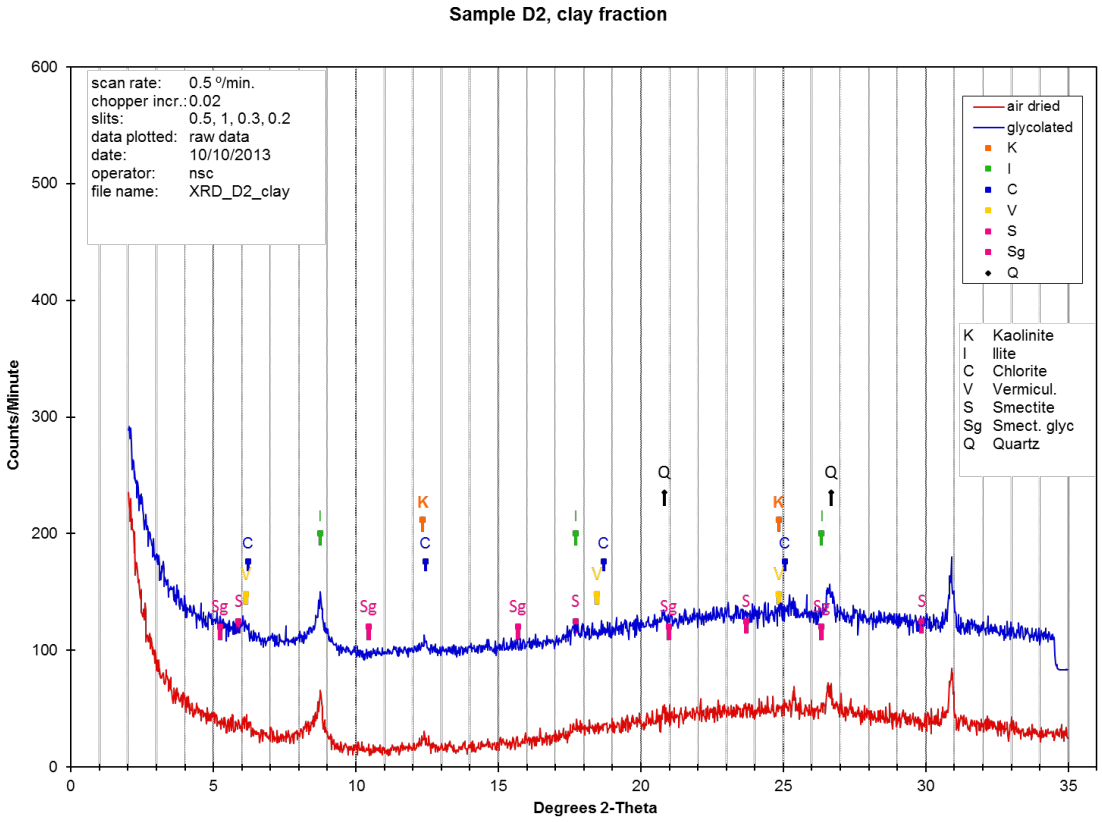


**Figure 3.12:** 10,840-10,860. XRD clay fraction diagram from cuttings. Again, this shows a high degree of similarity to other Triassic samples.

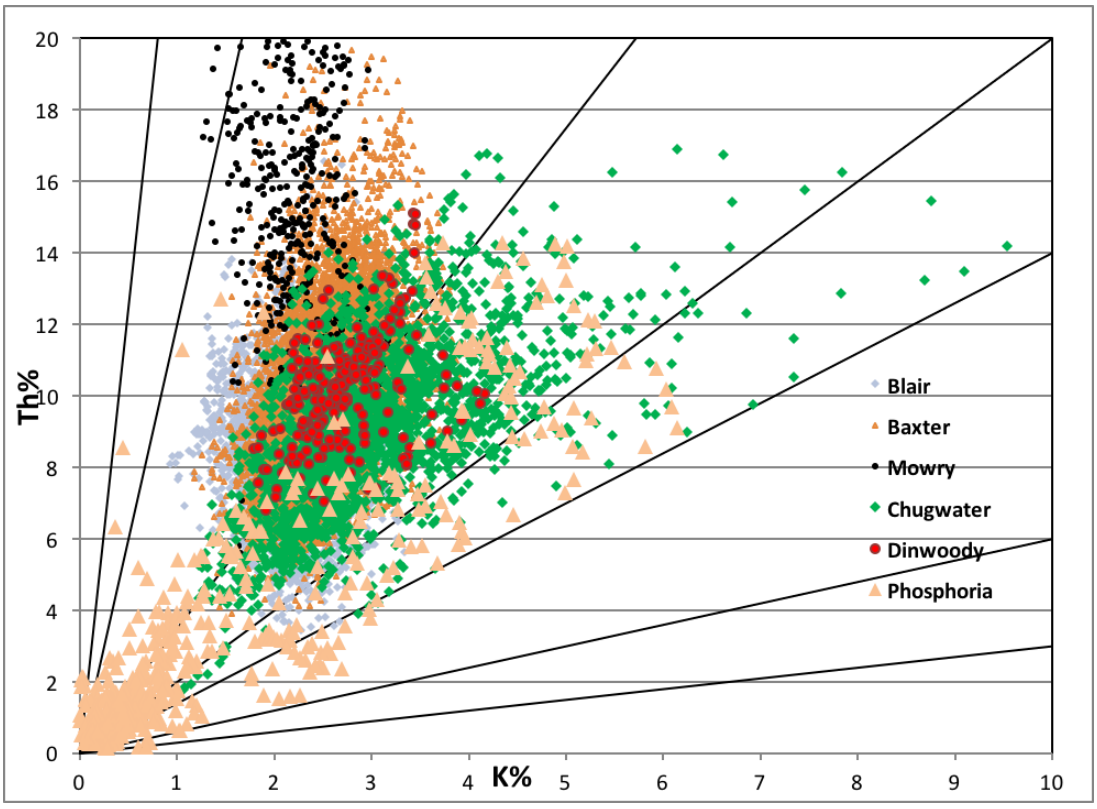


**Figure 3.13:** Spectral log analysis of clay species. Note the increasing chemical maturity of the deeper shales such as the Chugwater Group relative to the Mowry Shale.

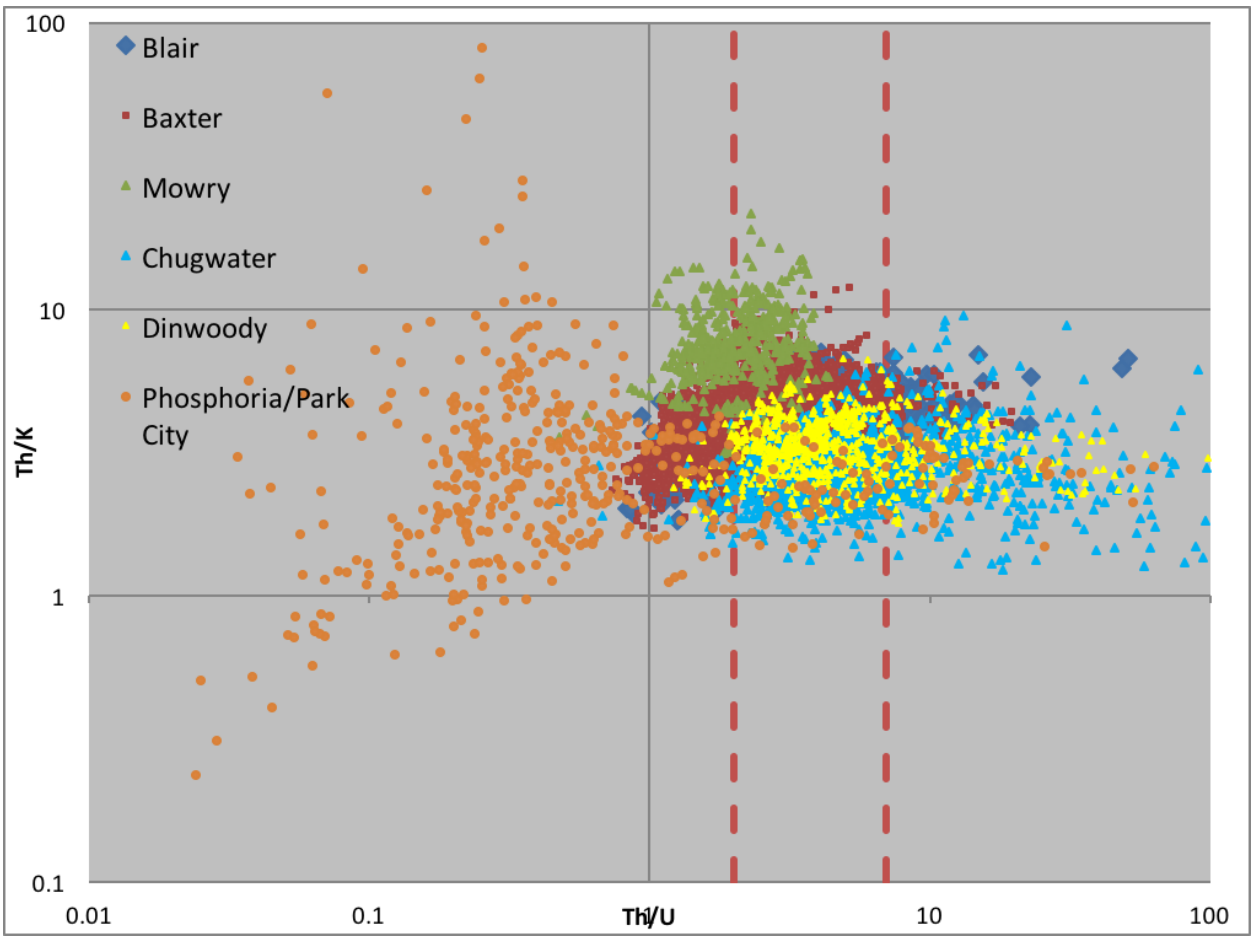


**Figure 3.14:** Advanced spectral log analysis of the oxidation states various sealing lithologies. Note that relatively organic-rich shales, such as the Phosphoria/Parky City and Mowry formations, are reduced and that the redbeds of the Chugwater Group are the most oxidized seals.

Stable isotopic analysis has distinguished the effects of diagenetic alteration on cements and carbonates. These data will help define the geochemical evolution of the seals post-deposition, impact of matrix minerals and cements, and the relative relation of alteration to lateral continuity. **Figure 3.15** shows the oxygen and carbon compositions of potential seals; alteration of primary carbonates is particularly distinct in the Madison Limestone. None of the preliminary analyses indicated high-temperature crystallization of carbonates, as seen in carbonate vugs though petrographic examination has revealed high-T mineralization in the Amsden. Differences in carbon compositions in the Triassic units relative to the Amsden and upper Madison limestone could be the result of oxidized organic matter, or related to post-burial carbonate alteration and precipitation (**Figure 3.15**).

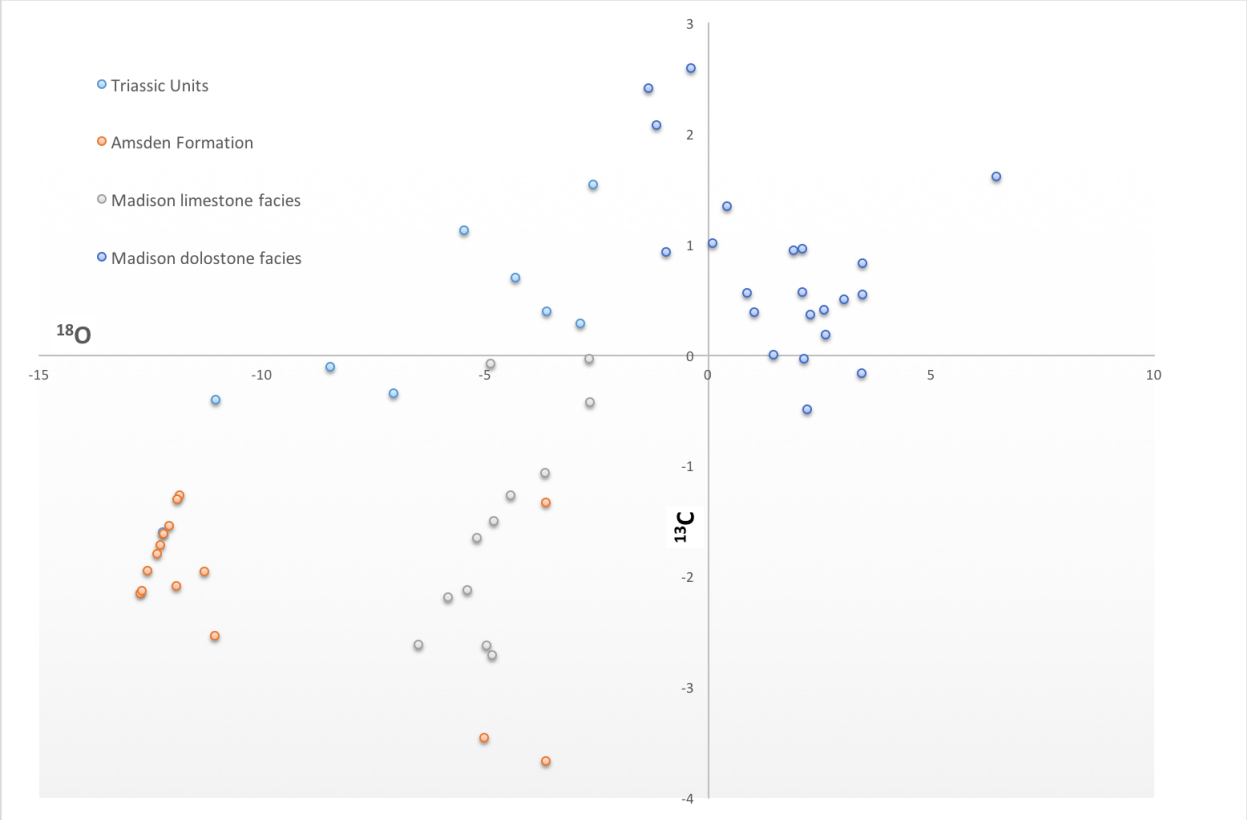


**Figure 3.15:** Stable isotopic analysis of potential seals from the RSU#1 well site. Primary, unaltered carbonates of the Madison and the Amsden record similar isotopic compositions, samples from the Red Peak (Triassic units) have enriched carbon values, similar to the dolostone in the Madison. None of the samples is similar to high-temperature calcite vugs/veins though additional Amsden samples are being tested. *

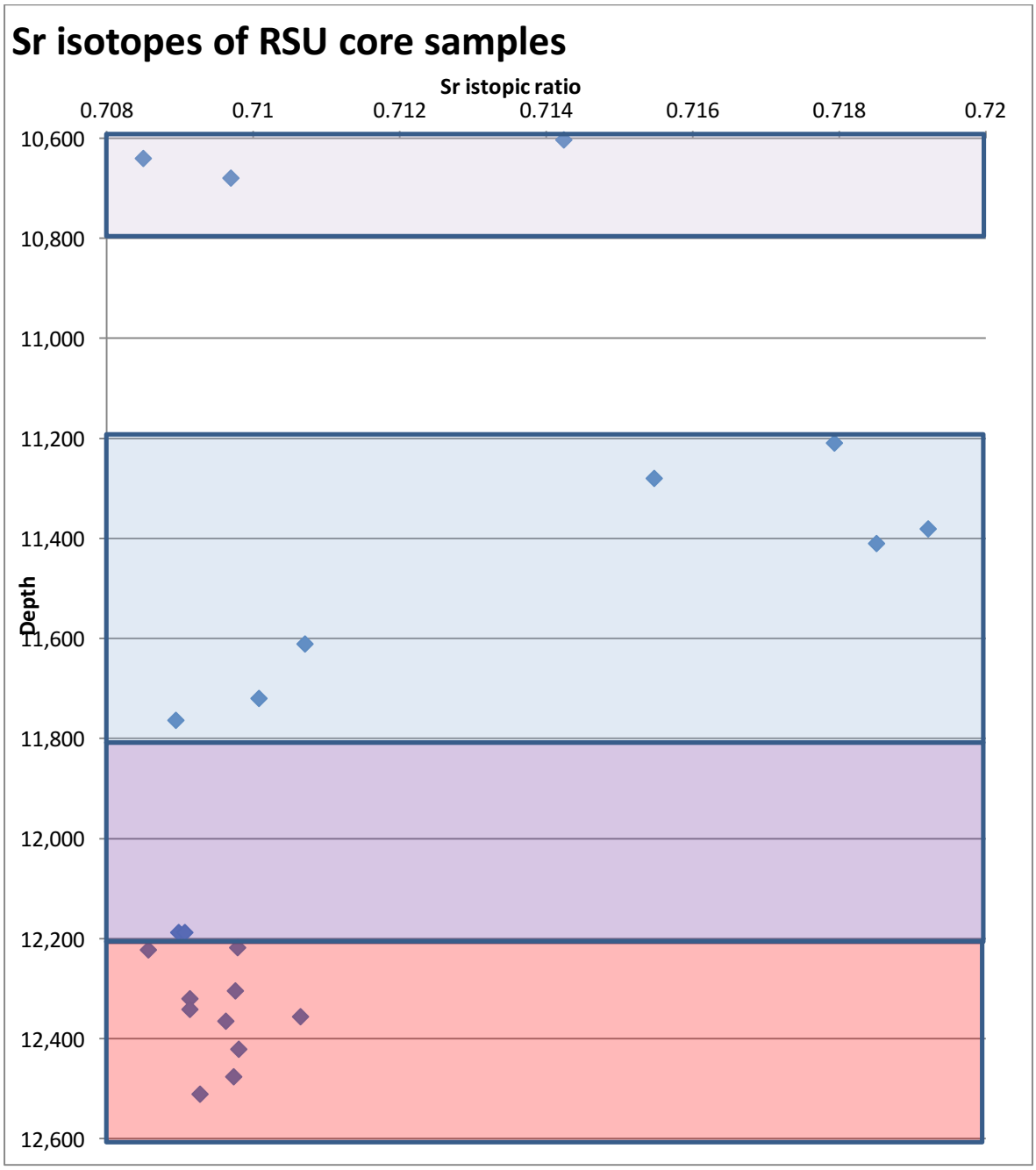


**Figure 3.16:** Strontium isotope analysis of whole rock from selected seals and reservoirs.

*Cooperative Work, related to Task 3.1*- CMI researchers and geoscientists at Idaho National Laboratories (INL) collaborated to characterize the rare earth element (REE) geology at the study site. Scientists at INL applied a new technique for REE groundwater fingerprinting and water-rock interactions. This technique (see Task 4) was utilized to augment the interpretation of basinal fluid evolution, reservoir confinement, and sealing capacity. This project allowed INL scientists to refine a new, experimental, analytical technique that will apply to the analysis of groundwater reservoirs. Results of whole rock geochemistry (**Table 3.5**) were correlated with the REE values in Task 4.

**Table 3.5:** Whole rock, trace element, and rare earth analyses from INL. *****

| Analyte Symbol | C-Organic(calc) | CO2 | SiO2 | Al2O3 | Fe2O3(T) | MnO | MgO | CaO | Na2O | K2O | TiO2 | P2O5 | LOI | Total |
|---|---|---|---|---|---|---|---|---|---|---|---|---|---|---|
| Unit Symbol | % | % | % | % | % | % | % | % | % | % | % | % | % | % |
| Detection Limit | 0.05 | 0.01 | 0.01 | 0.01 | 0.01 | 0.001 | 0.01 | 0.01 | 0.01 | 0.01 | 0.001 | 0.01 | | 0.01 |
| Analysis Method | IR | IR | FUS-ICP | FUS-ICP | FUS-ICP | FUS-ICP | FUS-ICP | FUS-ICP | FUS-ICP | FUS-ICP | FUS-ICP | FUS-ICP | FUS-ICP | FUS-ICP |
| M1Madison 1 | | 45 | 141 | 0.16 | 0.11 | 0.011 | 20.23 | 29.54 | 0.21 | 0.1 | 0.01 | 0.02 | 46.72 | 98.52 |
| M2 Madison 2 | | 46.3 | 142 | 0.09 | 0.1 | 0.015 | 20.68 | 29.95 | 0.05 | 0.02 | 0.003 | < 0.01 | 44.86 | 97.2 |
| M3 Madison 3 | | 45.3 | 1.15 | 0.15 | 0.11 | 0.016 | 17.59 | 34.93 | 0.05 | 0.06 | 0.006 | < 0.01 | 44.4 | 98.44 |
| W1Weber 1 | | 2.04 | 88.21 | 2.44 | 1.4 | 0.013 | 0.98 | 1.49 | 0.09 | 1.81 | 0.126 | 0.02 | 2.69 | 99.26 |
| W2 Weber 2 | | 2.79 | 87.33 | 1.98 | 1.39 | 0.015 | 1.25 | 2.1 | 0.15 | 1.54 | 0.055 | < 0.01 | 3.21 | 99.03 |
| W3 weber 3 | | 3.46 | 87.85 | 1.55 | 1.17 | 0.014 | 1.61 | 2.47 | 0.18 | 1.07 | 0.038 | 0.01 | 4.14 | 100.1 |

| Analyte Symbol | C-Organic(calc) | CO2 | SiO2 | Al2O3 | Fe2O3(T) | MnO | MgO | CaO | Na2O | K2O | TiO2 | P2O5 | LOI | Total | Sc | Be | V | Ba | Sr | Y | Zr | Cr | Co | Ni | Cu | Zn | Ga | Ge | As | Rb | Nb | Mo | Ag | In | Sn | Sb | Cs |
|---|---|---|---|---|---|---|---|---|---|---|---|---|---|---|---|---|---|---|---|---|---|---|---|---|---|---|---|---|---|---|---|---|---|---|---|---|
| Unit Symbol | % | % | % | % | % | % | % | % | % | % | % | % | % | % | ppm | ppm | ppm | ppm | ppm | ppm | ppm | ppm | ppm | ppm | ppm | ppm | ppm | ppm | ppm | ppm | ppm | ppm | ppm | ppm | ppm | ppm | ppm |
| Detection Limit | 0.05 | 0.01 | 0.01 | 0.01 | 0.01 | 0.001 | 0.01 | 0.01 | 0.01 | 0.01 | 0.001 | 0.01 | | 0.01 | 1 | 1 | 5 | 3 | 2 | 2 | 4 | 20 | 1 | 20 | 10 | 30 | 1 | 1 | 5 | 2 | 1 | 2 | 0.5 | 0.2 | 1 | 0.5 | 0.5 |
| Analysis Method | IR | IR | FUS-ICP | FUS-ICP | FUS-ICP | FUS-ICP | FUS-ICP | FUS-ICP | FUS-ICP | FUS-ICP | FUS-ICP | FUS-ICP | FUS-ICP | FUS-ICP | FUS-ICP | FUS-ICP | FUS-ICP | FUS-ICP | FUS-ICP | FUS-ICP | FUS-ICP | FUS-ICP | FUS-MS | FUS-MS | FUS-MS | FUS-MS | FUS-MS | FUS-MS | FUS-MS | FUS-MS | FUS-MS | FUS-MS | FUS-MS | FUS-MS | FUS-MS | FUS-MS | FUS-MS |
| M1Madison 1 | | 45 | 141 | 0.16 | 0.11 | 0.011 | 20.23 | 29.54 | 0.21 | 0.1 | 0.01 | 0.02 | 46.72 | 98.52 | <1 | <1 | 13 | 4 | 48 | 4 | 5 | <20 | <1 | <20 | <10 | <30 | <1 | <1 | <5 | 3 | 2 | <2 | 1 | <0.2 | <1 | <0.5 | <0.5 |
| M2 Madison 2 | | 46.3 | 142 | 0.09 | 0.1 | 0.015 | 20.68 | 29.95 | 0.05 | 0.02 | 0.003 | < 0.01 | 44.86 | 97.2 | <1 | <1 | 7 | <3 | 42 | 4 | 5 | <20 | <1 | <20 | <10 | <30 | <1 | <1 | <5 | <2 | <1 | <2 | <0.5 | <0.2 | <1 | <0.5 | <0.5 |
| M3 Madison 3 | | 45.3 | 1.15 | 0.15 | 0.11 | 0.016 | 17.59 | 34.93 | 0.05 | 0.06 | 0.006 | < 0.01 | 44.4 | 98.44 | <1 | <1 | 8 | 4 | 91 | 5 | 6 | <20 | <1 | <20 | <10 | <30 | <1 | <1 | <5 | <2 | <1 | <2 | 0.6 | <0.2 | <1 | <0.5 | <0.5 |
| W1Weber 1 | | 2.04 | 88.21 | 2.44 | 1.4 | 0.013 | 0.98 | 1.49 | 0.09 | 1.81 | 0.126 | 0.02 | 2.69 | 99.26 | <1 | <1 | 16 | 274 | 44 | 5 | 319 | <20 | 2 | <20 | 10 | 30 | 3 | <1 | <5 | 35 | 2 | <2 | 16 | <0.2 | <1 | <0.5 | <0.5 |
| W2 Weber 2 | | 2.79 | 87.33 | 1.98 | 1.39 | 0.015 | 1.25 | 2.1 | 0.15 | 1.54 | 0.055 | < 0.01 | 3.21 | 99.03 | <1 | <1 | 10 | 157 | 38 | 2 | 117 | 20 | 1 | <20 | 20 | <30 | 2 | <1 | <5 | 30 | <1 | <2 | 0.9 | <0.2 | <1 | <0.5 | <0.5 |
| W3 weber 3 | | 3.46 | 87.85 | 1.55 | 1.17 | 0.014 | 1.61 | 2.47 | 0.18 | 1.07 | 0.038 | 0.01 | 4.14 | 100.1 | <1 | <1 | 8 | 179 | 46 | 2 | 77 | <20 | 1 | <20 | <10 | <30 | 2 | <1 | <5 | 20 | <1 | <2 | 0.8 | <0.2 | <1 | <0.5 | <0.5 |

| Analyte Symbol | C-Organic(calc) | CO2 | SiO2 | Al2O3 | Fe2O3(T) | MnO | MgO | CaO | Na2O | K2O | TiO2 | P2O5 | LOI | Total | Sc | Be | V | Ba | Sr | Y | Zr | Cr | Co | Ni | Cu | Zn | Ga | Ge | As | Rb | Nb | Mo | Ag | In | Sn | Sb | Cs | La | Ce | Pr | Nd | Sm | Eu | Gd | Tb | Dy | Ho | Er | Tm | Yb | Lu | Hf | Ta | W | Tl | Pb | Bi | Th | U |
|---|---|---|---|---|---|---|---|---|---|---|---|---|---|---|---|---|---|---|---|---|---|---|---|---|---|---|---|---|---|---|---|---|---|---|---|---|---|---|---|---|---|---|---|---|---|---|---|---|---|---|---|---|---|---|---|---|---|---|---|---|---|---|---|
| Unit Symbol | % | % | % | % | % | % | % | % | % | % | % | % | % | % | ppm | ppm | ppm | ppm | ppm | ppm | ppm | ppm | ppm | ppm | ppm | ppm | ppm | ppm | ppm | ppm | ppm | ppm | ppm | ppm | ppm | ppm | ppm | ppm | ppm | ppm | ppm | ppm | ppm | ppm | ppm | ppm | ppm | ppm | ppm | ppm | ppm | ppm | ppm | ppm | ppm | ppm | ppm | ppm | ppm | ppm | ppm | ppm |
| Detection Limit | 0.05 | 0.01 | 0.01 | 0.01 | 0.01 | 0.001 | 0.01 | 0.01 | 0.01 | 0.01 | 0.001 | 0.01 | | 0.01 | 1 | 1 | 5 | 3 | 2 | 2 | 4 | 20 | 1 | 20 | 10 | 30 | 1 | 1 | 5 | 2 | 1 | 2 | 0.5 | 0.2 | 1 | 0.5 | 0.5 | 0.1 | 0.1 | 0.05 | 0.1 | 0.1 | 0.1 | 0.1 | 0.1 | 0.05 | 0.1 | 0.1 | 0.1 | 0.1 | 0.1 | 0.05 | 0.1 | 0.04 | 0.2 | 0.1 | 1 | 0.1 | 5 | 0.4 | 0.1 | 0.1 |
| Analysis Method | IR | IR | FUS-ICP | FUS-ICP | FUS-ICP | FUS-ICP | FUS-ICP | FUS-ICP | FUS-ICP | FUS-ICP | FUS-ICP | FUS-ICP | FUS-ICP | FUS-ICP | FUS-ICP | FUS-ICP | FUS-ICP | FUS-ICP | FUS-ICP | FUS-ICP | FUS-ICP | FUS-ICP | FUS-MS | FUS-MS | FUS-MS | FUS-MS | FUS-MS | FUS-MS | FUS-MS | FUS-MS | FUS-MS | FUS-MS | FUS-MS | FUS-MS | FUS-MS | FUS-MS | FUS-MS | FUS-MS | FUS-MS | FUS-MS | FUS-MS | FUS-MS | FUS-MS | FUS-MS | FUS-MS | FUS-MS | FUS-MS | FUS-MS | FUS-MS | FUS-MS | FUS-MS | FUS-MS | FUS-MS | FUS-MS | FUS-MS | FUS-MS | FUS-MS | FUS-MS | FUS-MS | FUS-MS | FUS-MS | FUS-MS |
| M1Madison 1 | | 45 | 141 | 0.16 | 0.11 | 0.011 | 20.23 | 29.54 | 0.21 | 0.1 | 0.01 | 0.02 | 46.72 | 98.52 | <1 | <1 | 13 | 4 | 48 | 4 | 5 | <20 | <1 | <20 | <10 | <30 | <1 | <1 | <5 | 3 | 2 | <2 | 1 | <0.2 | <1 | <0.5 | <0.5 | 5.3 | 8.7 | 1.17 | 4.5 | 0.8 | 0.16 | 0.7 | <0.1 | 0.3 | <0.1 | 0.2 | <0.05 | 0.2 | <0.04 | <0.2 | <0.1 | <1 | <0.1 | <5 | <0.4 | 16 | 0.5 |
| M2Madison 2 | | 46.3 | 142 | 0.09 | 0.1 | 0.015 | 20.68 | 29.95 | 0.05 | 0.02 | 0.003 | < 0.01 | 44.86 | 97.2 | <1 | <1 | 7 | <3 | 42 | 4 | 5 | <20 | <1 | <20 | <10 | <30 | <1 | <1 | <5 | <2 | <1 | <2 | <0.5 | <0.2 | <1 | <0.5 | <0.5 | 13 | 0.9 | 0.17 | 0.6 | 0.1 | <0.05 | 0.1 | <0.1 | 0.2 | <0.1 | 0.1 | <0.05 | 0.1 | <0.04 | <0.2 | 0.1 | <1 | <0.1 | <5 | <0.4 | <0.1 | 0.1 |
| M3Madison 3 | | 45.3 | 1.15 | 0.15 | 0.11 | 0.016 | 17.59 | 34.93 | 0.05 | 0.06 | 0.006 | < 0.01 | 44.4 | 98.44 | <1 | <1 | 8 | 4 | 91 | 5 | 6 | <20 | <1 | <20 | <10 | <30 | <1 | <1 | <5 | <2 | <1 | <2 | 0.6 | <0.2 | <1 | <0.5 | <0.5 | 3.8 | 6.1 | 0.92 | 3.7 | 0.5 | 0.17 | 0.4 | <0.1 | 0.3 | <0.1 | 0.2 | <0.05 | 0.2 | <0.04 | <0.2 | 0.3 | <1 | <0.1 | <5 | <0.4 | 0.8 | 0.5 |
| W1Weber 1 | | 2.04 | 88.21 | 2.44 | 1.4 | 0.013 | 0.98 | 1.49 | 0.09 | 1.81 | 0.126 | 0.02 | 2.69 | 99.26 | <1 | <1 | 16 | 274 | 44 | 5 | 319 | <20 | 2 | <20 | 10 | 30 | 3 | <1 | <5 | 35 | 2 | <2 | 16 | <0.2 | <1 | <0.5 | <0.5 | 5.1 | 9.1 | 0.87 | 3.5 | 0.7 | 0.16 | 0.6 | 0.1 | 0.8 | 0.2 | 0.6 | 0.1 | 0.7 | 0.14 | 0.5 | 0.3 | <1 | 0.5 | 8 | <0.4 | 17 | 12 |
| W2Weber 2 | | 2.79 | 87.33 | 1.98 | 1.39 | 0.015 | 1.25 | 2.1 | 0.15 | 1.54 | 0.055 | < 0.01 | 3.21 | 99.03 | <1 | <1 | 10 | 157 | 38 | 2 | 117 | 20 | 1 | <20 | 20 | <30 | 2 | <1 | <5 | 30 | <1 | <2 | 0.9 | <0.2 | <1 | <0.5 | <0.5 | 3.6 | 6.2 | 0.74 | 2.6 | 0.5 | 0.13 | 0.5 | <0.1 | 0.4 | <0.1 | 0.3 | <0.1 | 0.2 | <0.05 | 0.2 | 0.04 | 3 | 0.1 | <1 | 0.4 | <5 | <0.4 | 1 | 0.5 |
| W3 weber 3 | | 3.46 | 87.85 | 1.55 | 1.17 | 0.014 | 1.61 | 2.47 | 0.18 | 1.07 | 0.038 | 0.01 | 4.14 | 100.1 | <1 | <1 | 8 | 179 | 46 | 2 | 77 | <20 | 1 | <20 | <10 | <30 | 2 | <1 | <5 | 20 | <1 | <2 | 0.8 | <0.2 | <1 | <0.5 | <0.5 | 3.3 | 5.9 | 0.73 | 2.8 | 0.4 | 0.13 | 0.4 | <0.1 | 0.3 | <0.1 | 0.2 | <0.05 | 0.2 | 0.04 | 18 | <0.1 | <1 | 0.3 | <5 | <0.4 | 0.8 | 0.3 |

- *Subtask 3.5—Locate and evaluate other available core samples.* CMI located 40 cores stored at the USGS Core Research Center in Denver, Colorado that were deemed regionally relevant to the scope of this project (*see* ***Appendix, Table A.1***). These cores were located within the general boundaries of the greater RSU and included strata targeted for this study. Examinations of the core suggested the need for sampling. In all, CMI collected 17 plugs from the USGS cores for petrographic evaluation (**Table 3.6**). Samples included targeted seals and associated reservoirs, but also include overlying seals and reservoirs with little data control at the study site. It was noted that few cores contained primary seals; most core samples were of reservoir strata. The analysis focused on identifying lithologic and diagenetic similarities between regional samples and targeted sealing strata from the RSU#1 well.

**Table 3.6:** List of sampled core for petrographic analysis.

| Operator | Well Name | Library Number | Depth (ft.) | Core Box # | |
|---|---|---|---|---|---|
| General American Oil | 1-6 Olsen Springs | B087 | 5,944.6 | (1/5) | Nugget |
| General American Oil | 1-6 Olsen Springs | B087 | 5,948.6 | (1/5) | Nugget |
| General American Oil | 1-6 Olsen Springs | B087 | 5,977.0 | (3/5) | Nugget |
| General American Oil | 1-6 Olsen Springs | B087 | 5,987.6 | (4/5) | Nugget |
| General American Oil | 1-6 Olsen Springs | B087 | 7,500.5 | (3/5) | Phosphoria |
| General American Oil | 1-6 Olsen Springs | B087 | 7,822.1 | (3/5) | Tensleep |
| Texaco INC. | #15 Unit Table Rock | A544 | 15,696.0 | (1/14) | Chugwater |
| Texaco INC. | #15 Unit Table Rock | A544 | 15,708.0 | (4/14) | Chugwater |
| Texaco INC. | #15 Unit Table Rock | A544 | 16,975.0 | (4/14) | Phosphoria |
| Texaco INC. | #15 Unit Table Rock | A544 | 16,988.0 | (4/14) | Phosphoria |
| Enscource INC. | 2-31 Ensource Federal | C842 | 4,776.0 | (3/9) | Mowry |
| Enscource INC. | 2-31 Ensource Federal | C842 | 5,214.0 | (3/9) | Mowry |
| Mountain Fuel Supply | 4UPRR-11-19-104 | D037 | 6,568.0 | (13/225) | Weber |
| Mountain Fuel Supply | 4UPRR-11-19-104 | D037 | 7,480.5 | (84/225) | Amsden |
| Mountain Fuel Supply | 4UPRR-11-19-104 | D037 | 7,491.3 | (85/225) | Madison |
| Mountain Fuel Supply | 1 Agnes Fay | R616 | 4,210.0 | 29 | Jelm |
| Mountain Fuel Supply | 1 Agnes Fay | R616 | 4,170.0 | 23 | Jelm |

*Petrography of regional cores samples*- Comparative petrographic analysis of regional seals was performed to reduce the uncertainties associated with lateral continuities, regional diagenetic variance, and to investigate regional depositional trends. Plugs were collected from core extracted from regional hydrocarbon fields, and samples include both reservoir and sealing units (**Table 3.6**).

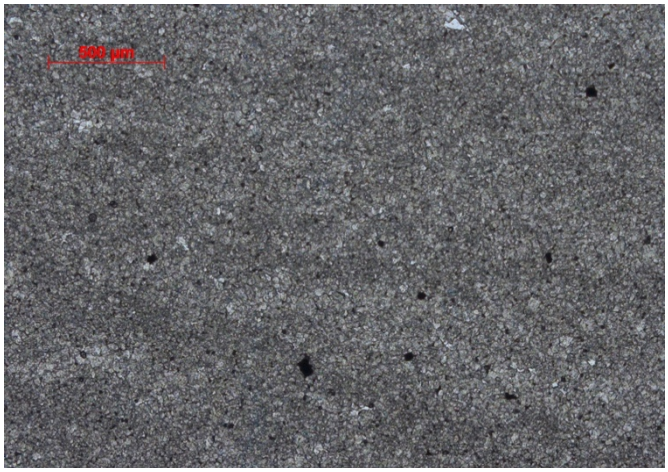

**Figure 3.17:** Tight, micritic dolostone from the Amsden Formation at well 4 UPRR-11-19-104 (7,491').

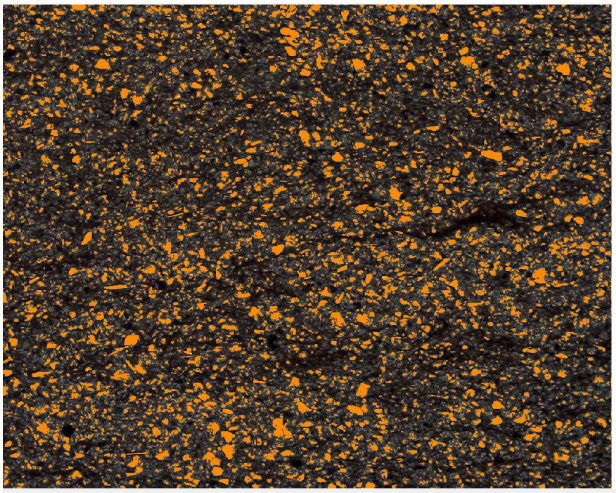

**Figure 3.18:** Clastic grain distribution, #15 Table Rock Unit, 15,696'

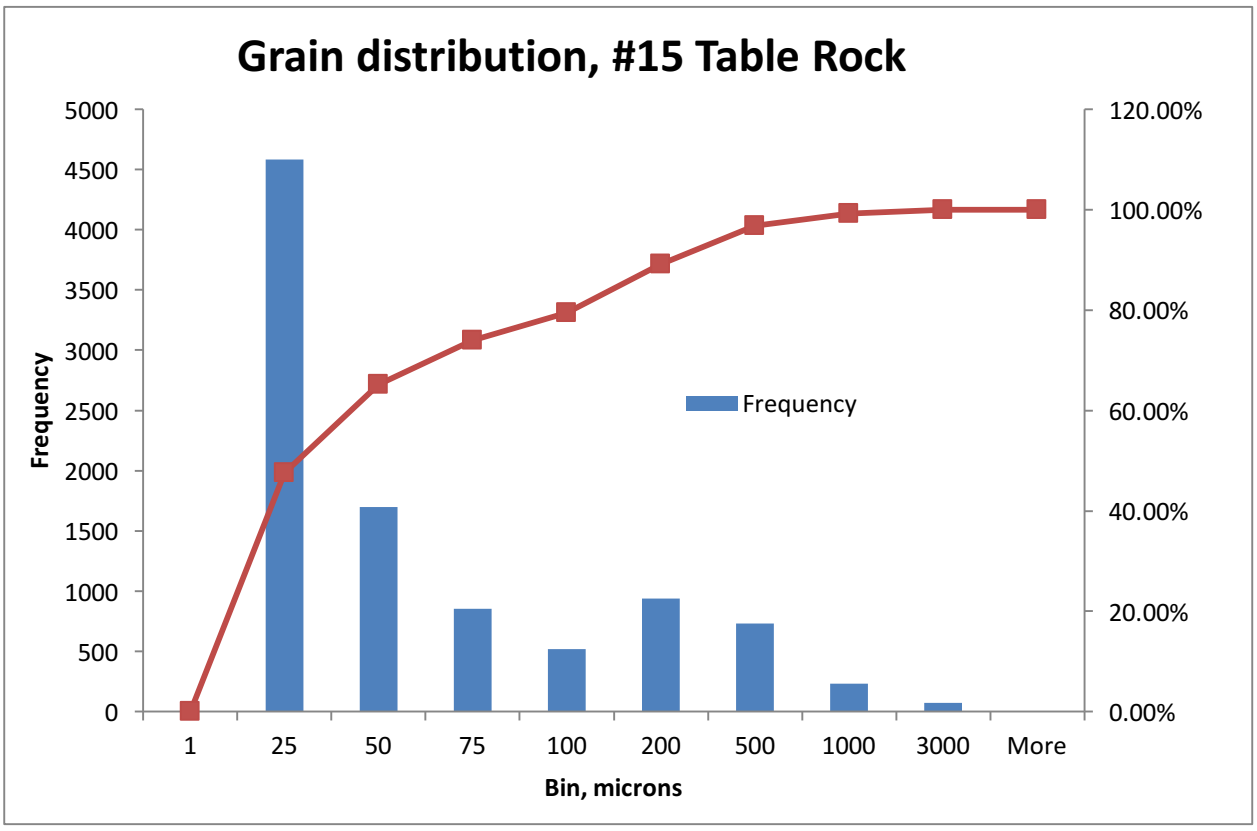


**Figure 3.19:** Grain distribution histogram of the #15 Table Rock Unit, 15,696' slide.

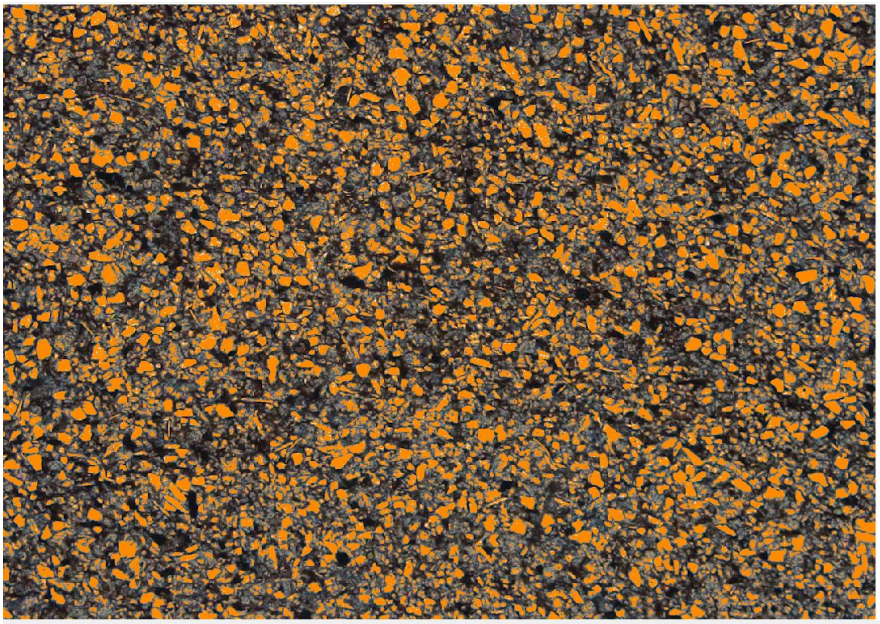

**Figure 3.20:** Clastic grain distribution, Agnes Fay 4,170'.

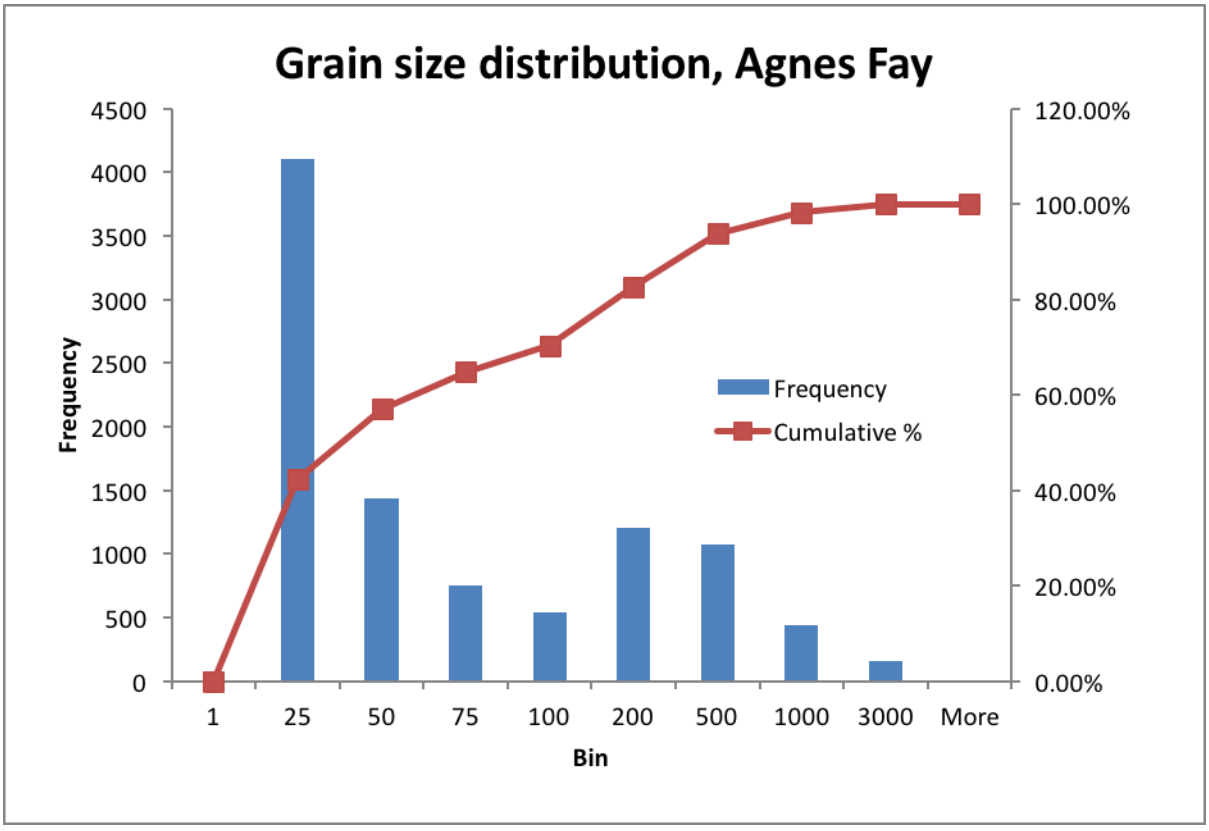


**Figure 3.21:** Grain distribution histogram of the Agnes Fay 4,170' slide.

- *Subtask 3.6*—Investigation of sealing formations at the RSU #1, and in the region surrounding the well, including the Greater Green River Basin and northern Colorado.

  Well logs, published oil and gas field synopses, and United States Geological Survey (USGS)publications have been studied to confirm the effectiveness of the sealing formations encountered in the RSU #1, and in the region as a whole (WOGCC 2015, WGA 2010, USGS 2005). The Rock Springs Uplift is host to 45 distinct oil and gas fields (WSGS). On the basis of reported fluid characteristics of many of the oil and gas fields in the area, it is evident that each formation has a particular mix of formation fluids. These fluids vary from one oil and gas field to another depending on the local structural setting, subsurface fluid flow, and stratigraphic facies changes. What is evident on the Rock Springs Uplift, as well as regionally, is differences in fluid composition between the Weber Sandstone and the Madison Limestone and between the Weber and overlying Phosphoria Formation. It is apparent that each formation has a competent seal of its own. The upper Madison limestone lithofacies caps the dolomitic reservoir rock of the middle Madison. The Amsden caps the Madison as well, adding to seal competence. The Phosphoria caps the Weber, providing an effective seal. Above the Phosphoria the combined Dinwoody/Chugwater rocks provide additional sealing competence, as do the thick section of Cretaceous shales further up-section. This combination of seals stacked multiple seals leads to great confidence in the premise that injected $CO_2$ will remain within the Weber and the Madison on the Rock Springs Uplift if they are developed for storage.

  Most production on the Rock Springs Uplift is from Upper Cretaceous Mesaverde Group reservoirs (Almond, Ericson, Rock Springs, and Blair Formations) (Surdam and Jiao 2007). Several oil and gas fields produce from the Pennsylvanian Weber Sandstone and the Mississippian Madison Limestone, and these fields lay within approximately 20 mi of the RSU #1 well site. The North Brady and South Brady fields lie about 20 mi southeast of the well site; both produce prolifically from the Weber (among other, shallower zones). About 20 mi east-southeast of the well site lays Table Rock field, where both the Weber and Madison are prolific hydrocarbon producers. Both the Brady North/South and Table Rock field areas are developed along faulted anticlines located on the east and southeast flanks of the Rock Springs Uplift. North Baxter Basin field is located approximately 14 mi west of the RSU #1 well site on the crest of the RSU. Several deep wells drilled at North Baxter during field development tested significant amounts of $CO_2$ from both the Weber and the Madison. Although they are distant from the RSU #1 drill site, these fields, as well as others in the GGRB, are evidence that the target reservoir rocks at the RSU #1 well site are valid for storage, and that the sealing units are fully competent and continuous over the region.

  Petrophysical log characteristics offer a high level of correlation across the region as a whole, and further support the great lateral extent of the sealing formation units discussed above. These log characteristics further attest to seal effectiveness. A west to east cross-section A-A' (**Figure 3.22**) is color-coded to key in on the individual seal units to illustrate the continuous nature of these sealing units. **Figure 3.23** illustrates the RSU #1 gamma ray, resistivity, and porosity curves from the well's petrophysical log, correlated

with a general lithology panel. The 115-foot-thick upper Madison limestone unit in the RSU #1 has log characteristics typical of a limestone with low porosity and low permeability. The low gamma ray curve is indicative of a limestone. This coupled with high resistivity and near zero porosity (both the combined neutron-density curves and the acoustic (sonic) porosity curve) readings attest to seal effectiveness. Low permeability is indirectly indicated by limited separation of the different resistivity curves (little difference in the different depth of penetration curves). The upper Madison unit thins away from the RSU #1, particularly to the west in the UP #4 well shown on the A-A' cross-section. Although only just less than 30 feet thick, drill stem tests in the Madison indicate a substantial $CO_2$ reservoir. The presence of this reservoir indicates a competent seal at the site, probably the upper Madison limestone, although the overlying Amsden may be providing additional sealing competence. The 418-foot thick Amsden is highly variable lithologically as indicated by the varying nature of the gamma ray log readings. The Amsden is comprised of interbedded limestone, shale, sandstone and dolomite, all with porosity readings of zero to 3%, and resistivity readings indicating low permeability with limited separation of the different curves. The combined Dinwoody-Chugwater at 1215-feet thick, is also lithologically variable, comprised of mainly siltstone and shale. Porosity hovers around 3% throughout most of this section, and resistivity curves show almost no separation, indicating very low permeability. Thickness isopach maps of the three main seal units are presented (*see* ***Appendix, A.34-36***) and supported by the Excel sheet database (*see* ***Appendix, Table A.2***). Thicknesses for the seals are based on in-house formation top/unit picks and these correlate with those shown on the log cross-sections. While the thickness of a seal can be an indication of competence, lateral extent is important as well, and this is the case at the Rock Springs Uplift and throughout the Greater Green River Basin.

Another zone of interest is an approximately 10-foot thick very fine-grained unit within the lower Weber Sandstone. This unit can be seen on the cross-section and appears to be present across the Rock Springs Uplift (as well as regionally) with a fairly uniform thickness. It appears at a depth of 11,712-11,720 in the RSU #1, and can be seen in the Amoco-Texas #1 at A on the cross-section, in the RSU #1, and in the Table Rock #23 at A'. Its presence is not as prominent in the UP #4 log presented in the cross-section, but it is prominent on the Gamma Ray-Neutron log from that well. The apparent regional nature of this unit points to a brief period of possible transgression, in which an influx of fine sediment covered the area. Core plug tests of this sequence in the RSU #1, indicate that it has very low permeability and is most likely a regional seal. The nature of the unit is evidence that seals do not necessarily need to be thick to be effective barriers to fluid movement but rely more on lithologic characteristics and lateral extent.

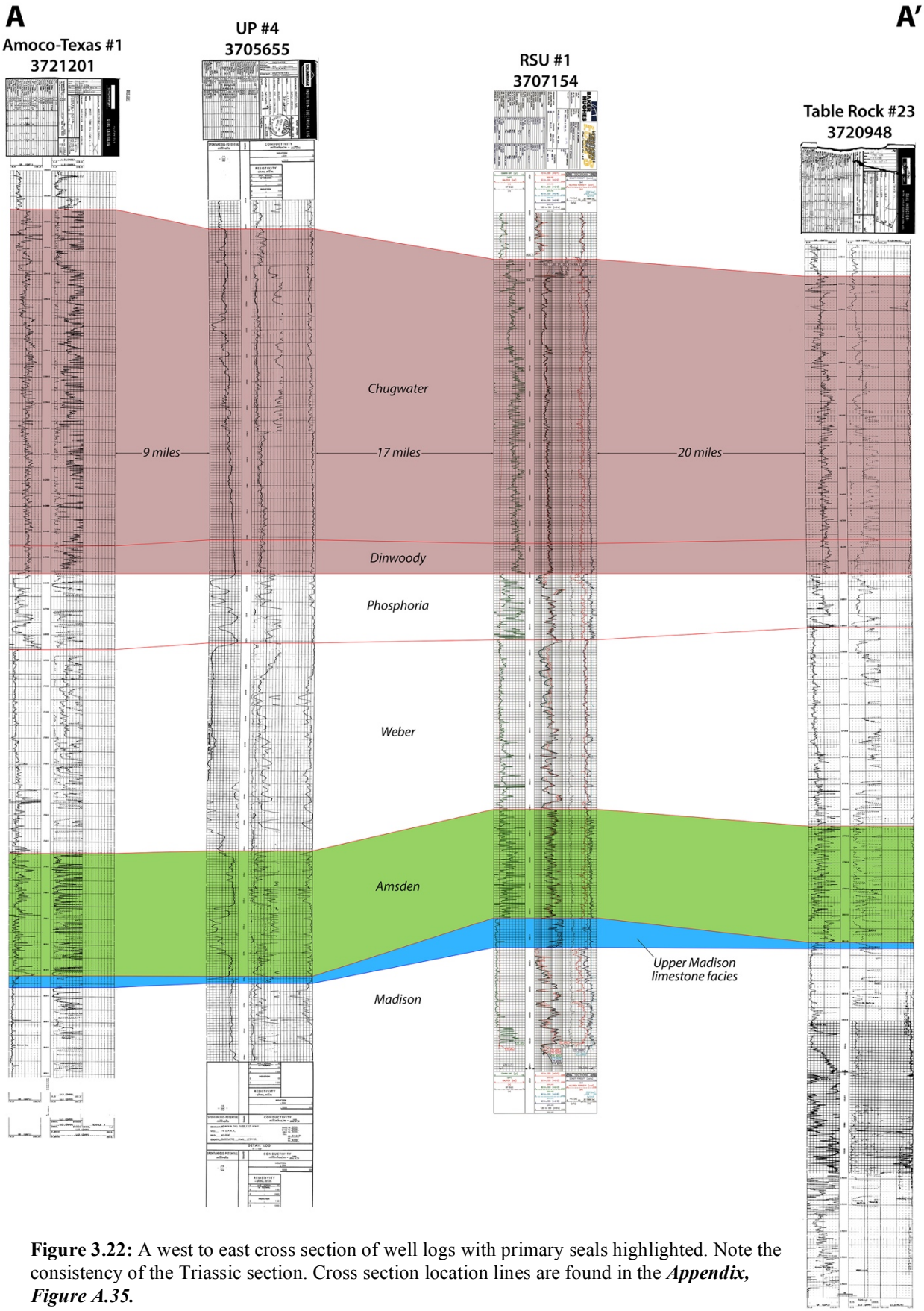


**Figure 3.22:** A west to east cross section of well logs with primary seals highlighted. Note the consistency of the Triassic section. Cross section location lines are found in the ***Appendix, Figure A.35.***

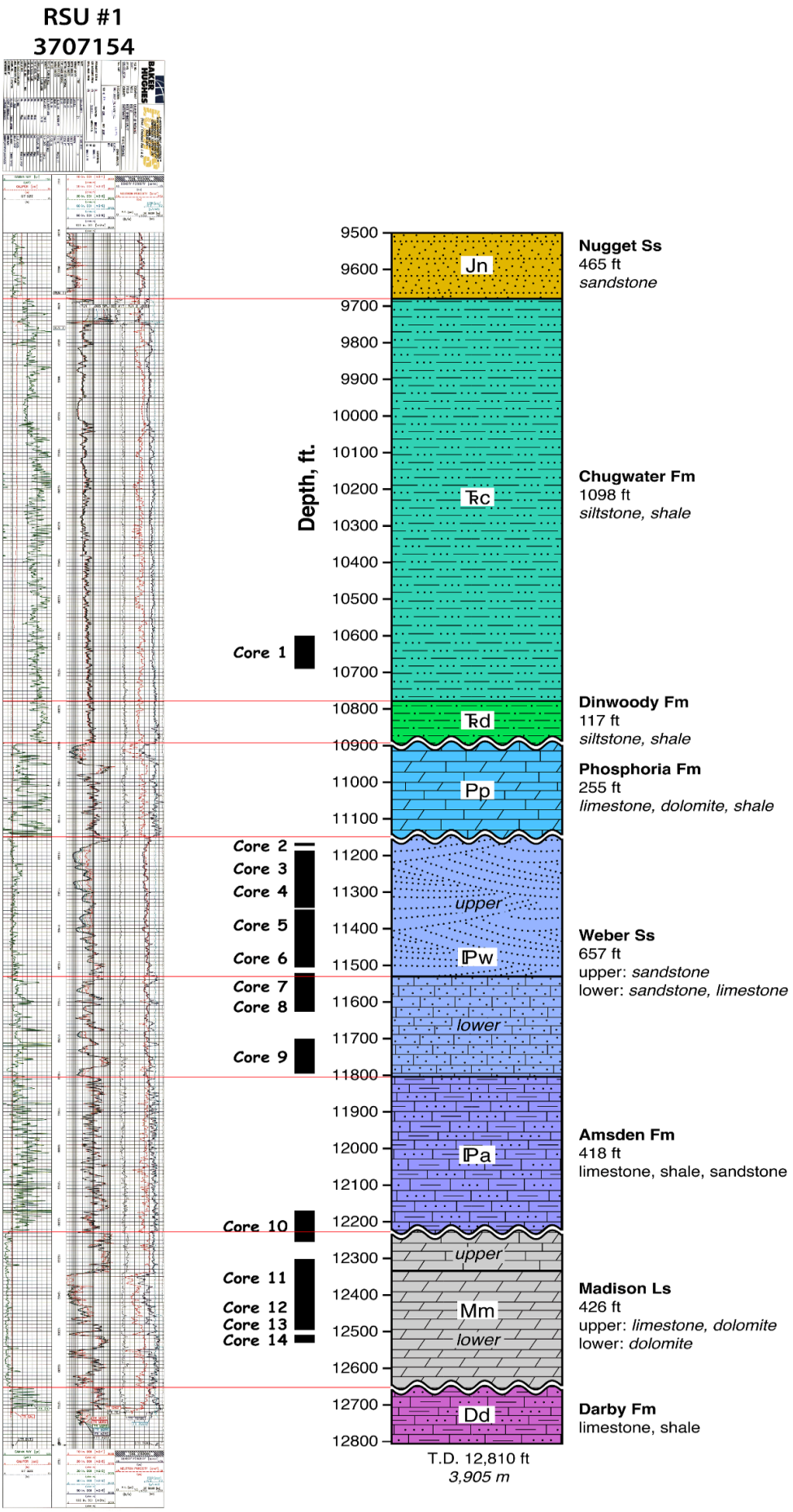


**Figure 3.23:** Lithologic log and corresponding petrophysical data for the RSU#1 well. These data were used to correlate regional petrophysical data of primary confining layers.

## Discussion

There have been numerous studies on the sealing capacities of different lithofacies involving both hydrocarbons and $CO_2$ (Vavra et al., 1992; Al-Bazali et al., 2005; Busch et al., 2008; Wollenweber et al., 2010). One thing these studies all call attention to is the variation in sealing response relative to lithology. Though shale is deemed a confining layer, true sealing capacity can be highly variable.

The conclusions from Task 3 demonstrate the need for site-specific analysis of potential confining layers. For instance, siltstones analyzed in other studies were deemed less ideal confining layers in a sedimentary package (Vavra et al., 1992). However, the Triassic siltstones of southwest Wyoming were found to be superior seals due to a combination of their depositional and diagenetic history. These are parameters that are not always studied in confining layer investigations (Busch et al., 2008; Wollenweber et al., 2010), though this study shows that they are crucial to reducing the uncertainty of regional/lateral continuity. This task has helped identify the importance of defining geologic controls on sealing capacity; the lithologic response to regional tectonism, cementation, diagenesis, sequence stratigraphy, depositional environment, deformational history, fluid history, and mechanical properties. These are all recognized as crucial to reducing the uncertainty of confining capacities at potential CCUS sites.

## Conclusion

Task 3 has identified seven formations that have the capacity to hold and retain $CO_2$ injected into targeted reservoirs. These reservoirs include those in contact with reservoir rocks, as well as multiple younger seals. Limestones with little diagenetic alteration have the best overall holding capacity though Triassic red beds are more ductile (and, therefore, have preferential mechanical properties). Petrographic, geochemical and isotopic analyses helped to provide the base data for a full geological characterization, which were then used to populate geochemical, seismic, and geological models to help define the lateral continuity of potential seals and response to $CO_2$ injection.

## Task 4: Characterize formation fluids to determine hydraulic isolation of target formation

### Overview

Target formation brines were collected and analyzed under DOE-FE0002142. These data provided the regulatory-required baseline data to classify the groundwater and move forward with permitting. These data were further evaluated under this project to investigate evaluate brine evolution, calculate thermodynamic equilibrium, estimate geochemical reactions with respect to $CO_2$ injection, evaluate geochemical reactions in case of seal failure, and to investigate stacked reservoir confinement.

CMI collected water samples in August 2011 from the wellbore using the Baker Atlas RCI (Reservoir Characterization) tool. We collected a second set of samples in December 2012 using a bailer and an additional set of pressurized samples to be analyzed for isotopic compositions of the brine (**Milestone 4-5**). These samples were collected for measurement of minor and major elements, radionuclides, organic acids, volatile organics, organic characteristics, and flash gas compositions using the methods described by Brown et al. (1970). The results of these analyses are presented in ***Appendix, Table A.3***.

Analyte and dissolved gas concentrations of formation fluids and compositions were characterized and evaluated. Conservative analyte analysis was used to characterize the water-rock interaction and as a proxy for long-term storage potential. Comparative analyses of dissolved gases, along with geochemical analysis, were used to determine reservoir confinement and the influence of extraneous fluids.

The evolution of solutes within Madison and Weber formation fluids was evaluated by comparing conservative and non-conservative ions (Rittenhouse 1967, Carpenter 1978, Macaffrey 1987, Walters et al. 1990). The concentrations and molarity of Br were compared with those of TDS, Ca, Mg, Cl, K, Na, and Li. Aside from Mg and Ca, all ions were enriched with respect to seawater evaporation (**Figures 4.1a–h**). There were also quantitative differences between the first sample set and the second sample set, as well as differences between the two formations (**Figures 4.1a–h**). Thermodynamic calculations on the basis of analytical results from the pressurized samples were computed using Geochemists Workbench (Bethke 1996).

### Executive Summary

The following results provide a brief summation of methods and major findings for six subtasks for Task 4.

- *Subtask 4.1—Perform isotopic analyses*. Isotopic compositions were measured by Sandia National Laboratories, for strontium, carbon of dissolved methane and carbon dioxide, oxygen in carbon dioxide, and sulfur of sulfate. The results were used to inform Subtask 4.3 to define the degree of hydraulic isolation between reservoirs.
- *Subtask 4.2—Perform geochemical analyses*. The results for the geochemical analyses are presented in ***Appendix, Table A.3***. The results are used as the basis of the geochemical models in Subtasks 4.4 and 4.5.

- *Subtask 4.3—Define hydraulic isolation of the target reservoir.* On the basis of the isotopic and geochemical analysis, we find that the target reservoirs are hydraulically isolated from one another. Thus, the Amsden and Upper Madison Limestone facies are found to seal effectively the Madison Dolostone facies.
- *Subtask 4.4—Perform reaction path modeling.* Reaction path models were created using the calculated speciation models and reactive minerals that were identified using petrographic analysis of core retrieved from the well. Simulations were modeled at 100 degrees Celsius, a pressure of 1 bar, and simulate the continuous injection of $CO_2$ into the basis compositions for one year. Results indicate that the pH of all basis compositions is expected decrease significantly in response to $CO_2$ injection. The largest changes in pH occur immediately after simulated injection begins. The salinity of each reservoir fluid is expected to increase significantly as a result of $CO_2$ injection. This is due in part to an increasing reservoir $pCO_2$ and in part to the dissolution of pH-sensitive minerals. The concentration of total dissolved solids (TDS) may increase by more than 60,000 mg/L according to the modeling results. All geochemical models indicate carbonate mineral dissolution and some anhydrite precipitation. The net porosity gain from precipitation and dissolution process is expected to be 1-3%, indicating that $CO_2$ injection will have a positive effect of reservoir porosity.
- *Subtask 4.5—Evaluate geochemical reactions associated with seal failure*. In the event of mechanical seal failure, geochemical models of the brine suggest that calcite precipitation would rapidly occur within fractures. This suggests that failures within the seal are self-healing, if exposed to formation fluids containing high $pCO_2$.
- *Subtask 4.6—Evaluation of technique for use in Best Practices Manual*. The evaluations of these techniques are found in the Best Practices Manual.

## Methods

Formation fluids were collected from each target formation on two occasions. CMI collected water samples on August 27th, 2011 from the wellbore using the Baker Atlas RCI (Reservoir Characterization Instrument). Samples were then transferred to two laboratories for analyses, (Energy Laboratories, Inc. in Casper, Wyoming and Core Labs in Broussard, Louisiana). A second set of samples was collected in December 2012. During the second sampling event, fluid samples were collected using two methods: first they were collected from a wireline bailer and second in-situ using a Type 5 Double End Hydrocarbon Sample Cylinder (pt. no. 850669, ***Appendix, Figure A.37***). This tool allowed samples to be collected at reservoir temperature and pressure. Samples were then shipped to separate laboratories for analysis. The bailer samples were sent to Energy labs, and the pressurized samples were sent to Sandia National Laboratories, in Albuquerque, New Mexico. Remaining samples being stored at Core Labs from the initial sample were also sent to Sandia National Laboratories for final analysis.

Fluid samples were measured for minor and major elements (**Figure 4.1**), radionuclides, organic acids, volatile organics, organic characteristics, and flash gas compositions using the methods described by Brown et al. (1970). Isotope ratios were measured at Sandia National Laboratories. Six water samples were submitted for analysis by ICP-MS to determine the isotope ratio of strontium 87 to strontium 86. Samples were diluted in 2.5% nitric acid solution and then

analyzed using the isotope ratio method of the Perkin Elmer 350D ICP-MS. Each value is the result of 240 measurements of each isotope.

## Results

*Brine Compositions*- Brines from both formations are sodium-chloride-type with measured total dissolved solids concentrations of 89,000 mg/L–109,000 mg/L in the Weber Sandstone and 75,000 mg/L–95,000 mg/L in the Madison Limestone. The brine densities are calculated to be 1.06 g/cm$^3$ (Weber) and 1.05 g/cm$^3$ (Madison). Ionic strength ranges from 1.77 molal – 2.03 molal (Weber) and 1.44 molal – 1.61 molal (Madison). Brine temperatures range from 92°C (Weber) to 95°C (Madison), with a formation pressure of 4,800 psi (Weber) and 5,900 psi (Madison). Water quality analyses revealed some constituents that could be economically extracted from the brine. These include lithium (90 mg/L to 105 mg/L), boron (61 mg/L to 101 mg/L), and potassium (1,940 mg/L to 3,3780 mg/L).

Comparison of the study-site brines with the USEPA maximum contaminant level (MCL) shows that the formation brines greatly exceed the standards for TDS. In addition, MCLs are exceeded with respect to chloride, fluoride, sulfate, aluminum, barium, iron, lead, manganese, and gross beta.

Formation fluids were analyzed for 63 volatile organic compounds (*see **Appendix, Table A.3**, Lines 70–132*). The first sample set (August 2011) detected six volatile organic compounds in both Weber, and Madison brines. This increased to fourteen in the second round of sampling (December 2012). With the exception of BTEX compounds, when a VOC was detected similar concentrations were measured in both reservoirs. This indicates that some VOC's were contaminants likely introduced during later work in the wellbore. Benzene, toluene, and xylenes were not detected in the first round of sampling but were measured in the second round; concentrations were much higher in the Weber. Ethylbenzene was found in equal concentrations in both formations in the first sample set (20 µg/L), but more than doubled in the Weber in the second round (50 µg/L).

Thermodynamic calculations and reaction path models were built on the basis of the analytical results and were computed using Geochemists Workbench (Bethke 1996).

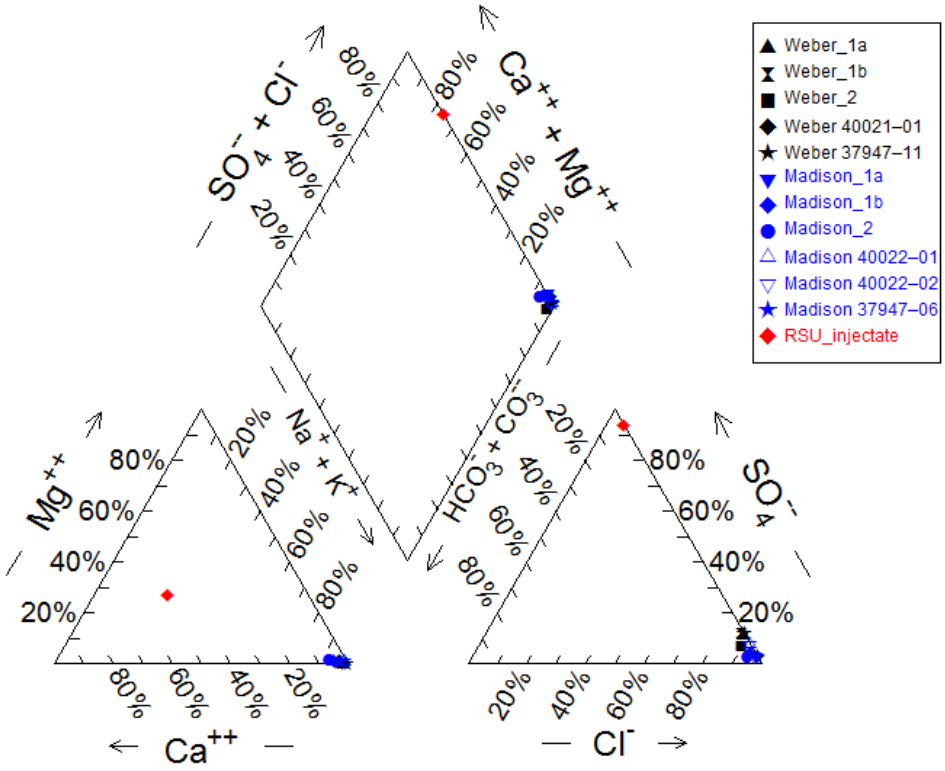


**Figure 4.1:** Piper diagram illustrating the relative brine compositions of each sample.

*Aqueous Species*- Species activities and saturation states were calculated to characterize thermodynamic controls on the water-rock system. Speciation models were calculated for each of the three samples recovered from each reservoir. The Aqueous species with a molar concentration above 1 x 10-8 are listed in **Table 4.1**. The activities of the aqueous species were calculated using Debye-Hückel equations. Dominate aqueous species for all samples collected from the Weber Sandstone include sodium (act. coef. -0.0171 to .0278), chloride (act. coef. -0.0818 to -0.0157), sodium chloride (act. coef. -1.0845 to -.9411), sodium sulfate (act. coef. -1.3987 to -1.6935) and potassium (act. coef. -1.5776 to -1.5713). Potassium and strontium concentrations were only analyzed for in two of the three samples. Dominate aqueous species for samples collected from the Madison Limestone include chloride (act. coef. -0.1616 to -0.0678), sodium (act. coef. -0.1341 to -0.0573), potassium (act. coef. -1.2236 to -1.2722), sodium chloride (act. coef. -1.2512 to -1.1106) and carbon dioxide (-1.4930 to -2.0118).

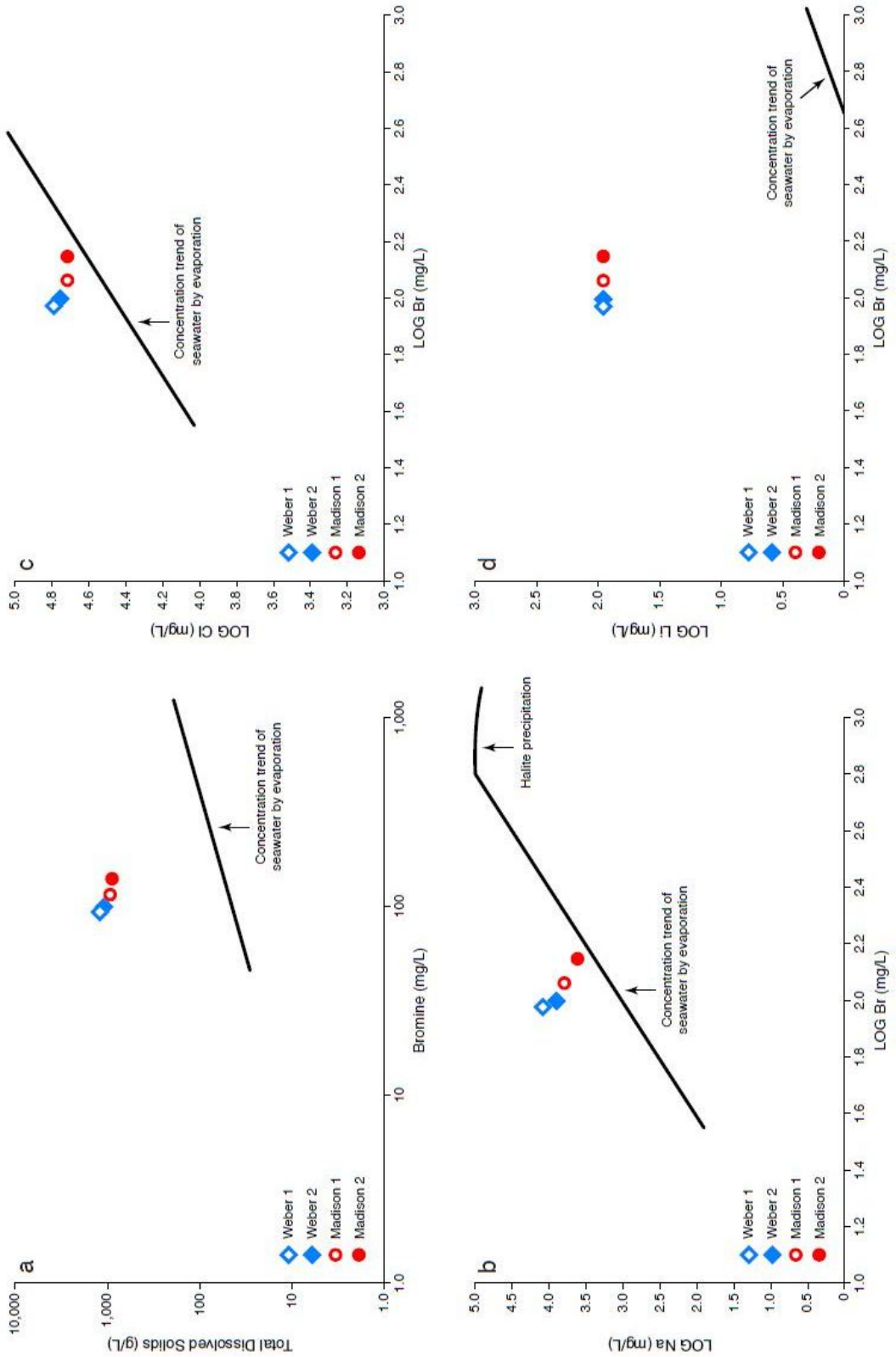


**Figure 4.2:** Plots of log constituent concentrations versus log bromine concentration relative to the seawater evaporation pathway described by Rittenhouse 1967. (a) TDS (b) Sodium (c) Chlorine (d) Lithium

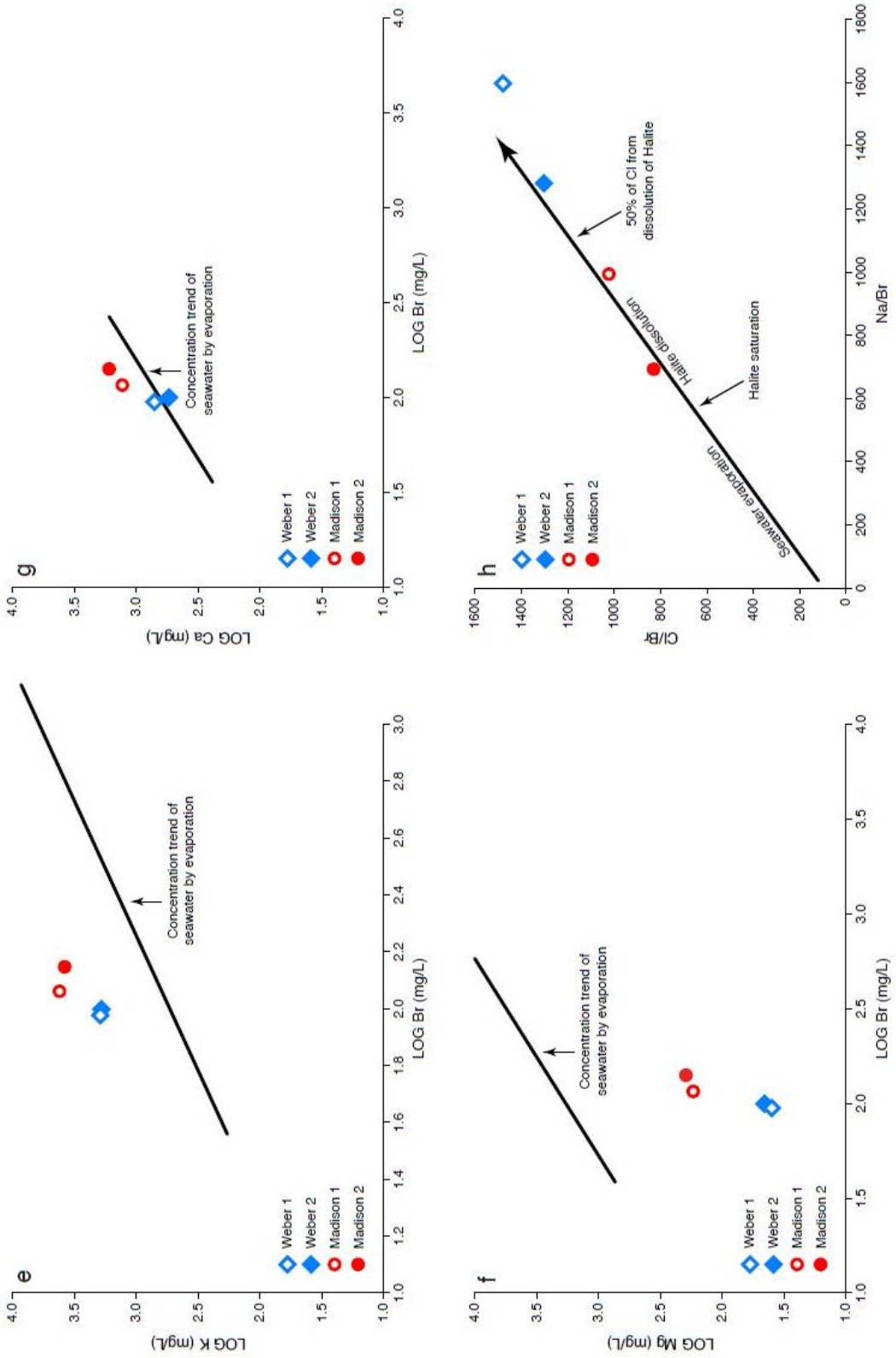


**Figure 4.3:** Plots of log constituents concentrations versus log bromine concentration relative to the seawater evaporation pathway described by Rittenhouse 1967. (e) Potassium (f) Calcium g) Magnesium (h) Na/Br versus Cl/Br molar ratio plot adapted from Engle and Rowan 2013.

## Discussion

*Comparative Solute Analysis*- Enrichment of Na and Cl over the seawater evaporation trend is related to halite dissolution (Rittenhouse 1967, Carpenter 1978, Macaffrey 1987, Walter et al. 1990). Both the Weber and the Madison formations contain evaporites, and dissolution of evaporites that has enriched the formation waters with respect to Na and Cl (**Figure 4.2** and **4.31b, c, h**). Molar ratio analysis of Br-Na-Cl, proposed by Walter et al. (1990) highlights the effect of halite dissolution on formation fluids (**Figure 4.3h**). Though both formations have Na-Cl concentrations that are enriched by halite dissolution, it is more pronounced in fluids from the Weber Sandstone (**Figure 4.3h**).

Dissolution of minerals is further evidenced by comparison of Li-Br and K-Br systematics, both of which are enriched with respect to seawater evaporation trends (**Figure 4.2 d,** and **4.3 e**). The enrichment suggests that post-burial dissolution or alteration of minerals, such as feldspars and clays, has influenced solute concentrations in these formation fluids. Mg is depleted with respect to evaporative seawater, particularly in Weber fluids (**Figure 4.3f**). Mg depletion is most likely a byproduct of dolomitization though the timing of Mg depletion in the fluids (near the surface or at depth) is indeterminable from these data. Ca is slightly enriched with respect to evaporative seawater in Madison fluids; Weber fluids straddle the trend line (**Figure 4.3g**). The abundance of secondary Ca-minerals, such as calcite and anhydrite, and the reactive nature of these minerals make interpretation of Ca solute concentrations difficult. However, enrichment of Ca in the Madison suggests that dissolution of Ca-minerals has impacted the water chemistry of the formation.

Comparative analysis of solutes in Weber and Madison formation fluids suggests that the interaction of reservoir rocks and formation fluids, via dissolution of evaporite and other minerals, has had a large influence on the evolution of the formation fluids. It has increased the overall TDS of the formation fluids post-burial, resulting in some of the most saline formation fluids collected in Wyoming (WOGCC 2013, USGS 2013). Though potential reaction rates and ionic strengths can vary, the evidence of mineral dissolution and high TDS suggests that the formation fluids and the reservoir rock at the study site have been in contact for a relatively long period of time. The differences in solute concentrations between formation fluids suggest that the fluids from the Weber and the Madison are in equilibrium with the reservoir rock and are not likely mixed or mixing. This indicates that both reservoirs are reasonably stable, and both exhibit the ability to hold and retain fluids; these conditions are ideal for CCS, as they indicate a low likelihood of unforeseen migrations or leakage, which reduces the overall potential risk.

*Differences Between Sample Sets*- It is important to note the molar ratios of Br-Na-Cl record a noticeable decrease between the first and the second sample sets (**Figure 4.1h**), mostly are decreased in the concentrations of Na and Cl (*see* ***Appendix, Table A.3***). The differences of solute concentrations between the two samples could be attributable to several factors. The first set of samples was maintained at reservoir pressure by capture cylinders, whereas the second set was collected using a bailer, so pressure was not maintained. The second sampling method could have led to the precipitation of some solutes.

The first set of samples collected had very low concentrations of $H_2S$ (Madison, 29 mg/L; Weber, 0.04 mg/L). The second set of samples measured much higher concentrations of $H_2S$ (Madison 87 mg/L, Weber 127 mg/L). Interestingly, the sulfate concentrations decreased between the first and second sample set (*see **Appendix, Table A.3***). This may suggest that perhaps water circulated during drilling, completion, and work-over of the well may have introduced sulfate-reducing bacteria (SRB). SRB ingest sulfate and organic acids and generate $H_2S$. Mixing these drilling waters with highly saline reservoir fluids could sour the reservoir in these mixing zones (Ligthelm et al. 1991). Another possibility is that work within the wellbore oxidized sulfide-bearing minerals, such as pyrite. The increase in Fe concentrations between sample sets supports this theory. Though it is uncertain which process or processes generated the $H_2S$, one thing remains certain: if targeted reservoirs and associated fluids are highly sensitive to redox reactions or non-native fluids, fluids injected during CCS must be closely monitored to avoid degrading the reservoir and formation fluids.

It is also advisable to design the downhole data collection program carefully, particularly concerning alteration of formation fluids or the potential for borehole-adjacent reservoir degradation. While it is foolhardy to omit collection of all downhole data, identifying the most invasive tests and the potential consequences associated with testing should be carefully considered.

*Dissolved Gas Analysis*- The composition of dissolved gases in Weber and Madison formation fluids is unique to each formation. Though the total abundance of gas in both formations is dominated by three species – nitrogen, carbon dioxide, and alkanes – the concentrations are markedly different. Nitrogen is the dominant gas species (approximately 79%) in fluids from the Weber Sandstone, followed by carbon dioxide (approximately 15%) and alkanes, mostly methane and hexane (approximately 6%). Carbon dioxide is the dominant gas species (approximately 83%) in fluids from the Madison Limestone, followed by nitrogen (approximately 17%) and a minor alkane component (<1%).

*Equilibrium Calculations*- We calculated species activities and saturation states to characterize thermodynamic controls on the water-rock system. Calculations provide saturation indices for the potentially reactive minerals – dolomite, calcite, and anhydrite. Both the Weber and the Madison are supersaturated with respect to dolomite and calcite. With respect to anhydrite, the Weber is saturated or slightly under-saturated, and the Madison is undersaturated (**Table 4.1**).

*Aqueous Species*- Species activities and saturation states were calculated to characterize thermodynamic controls on the water-rock system. Speciation models were calculated for each of the three samples recovered from the wellbore. The complete results of these speciations will be reported in the quarterly and final reports. The Aqueous species with a molar concentration above 1 x 10-8 are listed in **Table 4.1**. The activities of the aqueous species were calculated using Debye-Hückel equations. Dominate aqueous species for all samples collected from the Weber Sandstone include sodium (act. coef. -0.0171 to .0278), chloride (act. coef. -0.0818 to -0.0157), sodium chloride (act. coef. -1.0845 to -.9411), sodium sulfate (act. coef. -1.3987 to -1.6935) and potassium (act. coef. -1.5776 to -1.5713). Potassium and strontium concentrations were only analyzed for in two of the three samples. Dominate aqueous species for samples collected from the Madison Limestone include chloride (act. coef. -0.1616 to -0.0678), sodium

(act. coef. -0.1341 to -0.0573), potassium (act. coef. -1.2236 to -1.2722), sodium chloride (act. coef. -1.2512 to -1.1106) and carbon dioxide (-1.4930 to -2.0118).

*Minerals in the system*- Supersaturated minerals in the basis composition of the Weber Sandstone include anhydrite, calcite, dolomite, fluorite, quartz, strontianite, and barite are super-saturated. Petrographic analysis of the Weber Sandstone has identified late-stage anhydrite, calcite, dolomite, and quartz, supporting the modeling results. Fluorite, strontianite, and barite were not found in thin section samples.

The modeling results suggest that minerals precipitating from the Madison Limestone fluids are dolomite, fluorite, quartz, and strontianite. Calcite and anhydrite are slightly undersaturated. Thin section analysis of the sampled interval from Madison Limestone shows mineralogy comprised primarily of dolomite with late stage anhydrite and calcite veins. Although modeling results suggest that fluorite and strontianite are supersaturated these minerals have not been identified during petrographic analysis.

**Table 4.1:** Speciation model results

| System parameters | Weber 1a | Weber 1b | Weber 2 | Madison 1a | Madison 1b | Madison 2 |
|---|---|---|---|---|---|---|
| pH | 6.24 | 6.37 | 5.97 | 5.51 | 5.80 | 5.53 |
| Temperature (°C) | 100.00 | 100.00 | 100.00 | 100.00 | 100.00 | 100.00 |
| Ionic strength | 1.95 | 1.79 | 1.64 | 1.62 | 1.32 | 1.39 |
| Activity of water | 0.94 | 0.95 | 0.95 | 0.95 | 0.96 | 0.96 |
| Solvent mass (kg) | 1.00 | 1.00 | 1.00 | 1.00 | 1.00 | 1.00 |
| Solution mass (kg) | 1.13 | 1.11 | 1.11 | 1.10 | 1.08 | 1.09 |
| Solution density ($g/cm^{3)}$ | 1.02 | 1.01 | 1.01 | 1.01 | 1.00 | 1.00 |
| Chlorinity (molal) | 1.85 | 1.65 | 1.58 | 1.64 | 1.30 | 1.40 |
| Total Dissolved Solids (mg/kg) | 111483.00 | 102325.00 | 95841.00 | 92653.00 | 75300.00 | 81239.00 |
| Hardness mg/kg) | 1289.79 | 1095.07 | 537.48 | 3364.01 | 2526.08 | 3351.56 |
| Carbonate alkalinity (mg/kg) | 202.85 | 180.80 | 824.75 | 167.53 | 170.85 | 295.64 |
| Water Type | Na-Cl | Na-Cl | Na-Cl | Na-Cl | Na-Cl | Na-Cl |
| Aqueous Species (mg/Kg) | | | | | | |
| $B(OH)_3$ | 75.63 | 326.50 | 386.20 | 113.60 | 517.50 | 547.90 |
| $B(OH)^{-4}$ | 0.40 | 2.31 | 1.07 | 0.11 | 0.92 | 0.53 |
| Ba+2 | * | * | 0.11 | <0.1 | 0.21 | 0.34 |
| $Br^-$ | 88.14 | * | 93.30 | 109.00 | * | 132.90 |
| $Ca^{+2}$ | 232.00 | 197.30 | 103.60 | 636.70 | 550.20 | 753.20 |

| | | | | | | |
|---|---|---|---|---|---|---|
| $CaCl^{+}$ | 327.60 | 251.00 | 128.80 | <0.1 | 589.20 | 852.10 |
| $CaCO_3$ | 0.16 | 0.16 | 0.16 | <0.1 | 589.20 | 0.16 |
| $CaF^{+}$ | 0.85 | 0.79 | 0.44 | 1.45 | 1.20 | 1.27 |
| $CaHCO_3^{+3}$ | 12.11 | 9.14 | 23.30 | 29.71 | 26.26 | 63.06 |
| $CaSO_4$ | 299.10 | 302.20 | 89.90 | 198.00 | 251.00 | 206.30 |
| $Cl^{-}$ | 54590.00 | 49230.00 | 47920.00 | 49670.00 | 40690.00 | 43130.00 |
| CO2(aq) | 163.80 | 106.20 | 1281.00 | 776.10 | 396.00 | 1299.00 |
| $CO3^{-2}$ | 0.12 | 0.14 | 0.26 | <0.1 | <0.1 | <0.1 |
| $F^{-}$ | 3.87 | 4.27 | 4.47 | 2.42 | 2.29 | 1.77 |
| $Fe^{+2}$ | 0.12 | <0.1 | 0.92 | 0.50 | <0.1 | 2.24 |
| $FeCl^{+}$ | 2.44 | 1.06 | 16.43 | 9.35 | 0.64 | 36.50 |
| $FeCl_2$ | 0.97 | 0.37 | 5.52 | 3.24 | 0.18 | 10.80 |
| FeSO4 | <0.1 | <0.1 | 0.30 | <0.1 | <0.1 | 0.23 |
| $HCO_3$ | 207.50 | 184.80 | 896.00 | 186.10 | 188.70 | 331.50 |
| $HSO_4$ | 0.56 | 0.50 | 0.72 | 0.75 | 0.57 | 0.63 |
| $K^{+}$ | 1675.00 | * | 1687.00 | 3826.00 | * | 3460.00 |
| KCl | 108.30 | * | 93.25 | 218.30 | * | 169.70 |
| $KSO_4$ | 301.40 | * | 203.50 | 165.30 | * | 130.30 |
| $Li^{+}$ | 91.87 | 85.12 | 84.14 | 98.99 | 86.86 | 86.58 |
| $LiSO_4$ | 28.23 | 30.78 | 17.04 | 7.17 | 8.91 | 5.39 |
| $Mg^{+2}$ | 5.41 | 4.64 | 2.45 | 79.65 | 25.39 | 20.31 |
| $MgCl^{+}$ | 6.44 | 4.93 | 2.53 | 84.98 | 22.10 | 18.77 |
| $MgF^{+}$ | 0.17 | 0.16 | <0.1 | 1.52 | 0.46 | 0.28 |
| $MgHCO3^{+}$ | 0.36 | 0.27 | 0.68 | 4.60 | 1.46 | 2.06 |
| $MgSO_4$ | 10.68 | 10.79 | 3.21 | 37.29 | 17.10 | 8.25 |
| Mn+2 | <0.1 | <0.1 | 0.47 | 0.28 | <0.1 | 6.26 |
| MnHCO3+ | <0.1 | <0.1 | <0.1 | <0.1 | <0.1 | 0.42 |
| $MnSO_4$ | <0.1 | <0.1 | 0.59 | 0.13 | <0.1 | 2.47 |
| $Na^{+}$ | 37020.00 | 34960.00 | 31930.00 | 29240.00 | 26150.00 | 25110.00 |
| NaCl | 5948.00 | 4963.00 | 4350.00 | 4110.00 | 2939.00 | 3011.00 |
| NaF | 2.46 | 2.51 | 2.37 | 1.16 | 0.96 | 0.72 |
| $NaH_3SiO_4$ | 0.94 | <0.1 | 0.44 | 0.14 | <0.1 | 0.12 |
| $NaHCO_3$ | 81.95 | 67.15 | 291.60 | 55.16 | 48.18 | 82.11 |
| $NaSO_4$ | 6075.00 | 6781.00 | 3484.00 | 1142.00 | 1461.00 | 848.30 |
| $NH_3^{+}$ | <0.1 | 1.21 | 0.49 | <0.1 | 0.43 | 0.21 |

| | | | | | | |
|---|---|---|---|---|---|---|
| $NH_4^+$ | <0.1 | 30.10 | 30.67 | <0.1 | 39.52 | 36.79 |
| PbCl4-- | <0.1 | <0.1 | 0.34 | <0.1 | <0.1 | <0.1 |
| PbCO3 | <0.1 | <0.1 | 2.98 | <0.1 | <0.1 | 0.15 |
| Rb+ | * | * | 8.39 | * | * | 14.52 |
| $SiO_2$ | 30.07 | * | 32.37 | 32.64 | * | 34.44 |
| $SO_4^{-2}$ | 4079.00 | 4760.00 | 2634.00 | 941.30 | 1286.00 | 786.70 |
| $Sr^{+2}$ | 6.21 | * | 2.74 | 38.58 | * | 20.79 |
| $SrHCO_3^+$ | 0.67 | * | 1.28 | 3.75 | * | 3.65 |
| $SrSO_4$ | 3.92 | * | 1.18 | 5.96 | * | 2.86 |
| ZnCl+ | <0.1 | <0.1 | 0.50 | <0.1 | <0.1 | 0.29 |
| ZnCl2 | <0.1 | <0.1 | 0.72 | <0.1 | <0.1 | 0.37 |
| ZnCl3- | <0.1 | <0.1 | 1.52 | <0.1 | 0.15 | 0.69 |
| $ZnCl_4$ | <0.1 | 0.54 | 8.46 | <0.1 | 0.63 | 3.20 |

* Ba, Br-, K+, Hg, SiO2 and Sr+2 were not measured in all samples

| Mineral saturation states (log Q/K) | Weber 1a | Weber 1b | Weber 2 | Madison 1a | Madison 1b | Madison 2 |
|---|---|---|---|---|---|---|
| Albite | – | * | -0.51 | – | * | -1.0155 |
| Amorphous silica | -0.89 | * | -0.8939 | -0.8939 | * | -0.8939 |
| Analcime | – | * | -0.72 | – | * | -1.2256 |
| Anhydrite | Saturated | Saturated | -0.5296 | -0.1882 | -0.0936 | -0.1759 |
| Aragonite | -0.16 | -0.1602 | -0.1602 | -0.5213 | -0.3005 | -0.1850 |
| Bassanite | -0.65 | -0.6523 | -1.1815 | -0.8404 | -0.7435 | -0.8265 |
| Barite | * | – | Saturated | * | Saturated | Saturated |
| Boric Acid | -1.65 | -1.04 | -0.98 | -1.5105 | -0.8838 | -0.8505 |
| Calcite | Saturated | Saturated | Saturated | -0.3611 | -0.1403 | -0.0248 |
| Celesite | -0.4309 | * | -0.96 | -0.2580 | * | -0.5820 |
| Chalcedony | -0.22 | * | -0.2168 | -0.22 | * | -0.2168 |
| Cristobalite | -0.42 | * | -0.4177 | -0.42 | * | -0.4177 |
| $CuFeO_2$ | – | – | Saturated | – | – | Saturated |
| Dawsonite | – | – | -0.69 | – | – | -1.1955 |
| Dolomite | Saturated | Saturated | Saturated | Saturated | Saturated | Saturated |
| Dolomite-ord | Saturated | Saturated | Saturated | Saturated | Saturated | Saturated |
| Fluorite | Saturated | Saturated | -0.2485 | Saturated | -0.1246 | -0.2083 |
| Gibbsite | – | – | -1.04 | – | – | -0.9862 |
| Gypsum | -0.53 | -0.5253 | -1.0534 | -0.7134 | -0.61 | -0.69 |

| | | | | | | |
|---|---|---|---|---|---|---|
| Halite | -1.54 | -1.6203 | -1.6807 | -1.7068 | -1.86 | – |
| Illite | – | – | -1.46 | – | – | -1.42 |
| Kaolinite | – | – | -1.09 | – | – | -0.98 |
| K-feldspar | – | – | -0.01 | – | – | -0.10 |
| Magnesite | -1.27 | -1.2675 | -1.2675 | -0.91 | -1.13 | -1.24 |
| Monohydrocalcite | -1.37 | -1.3622 | -1.3614 | – | -1.50 | -1.38 |
| Muscovite | – | – | -0.02 | – | – | Saturated |
| Paragonite | – | – | -1.29 | – | – | – |
| PbSe | – | – | Saturated | – | – | Saturated |
| Quartz | Saturated | * | Saturated | Saturated | * | Saturated |
| Rhodochrosite | – | – | -0.69 | – | – | -0.46 |
| Siderite | -1.23 | -1.48 | Saturated | -1.4099 | | -0.50 |
| Strontianite | Saturated | * | Saturated | Saturated | * | Saturated |
| Thenardite | -1.59 | -1.5858 | – | – | – | |
| Tridymite | -0.11 | * | -0.1129 | -0.1129 | * | -0.11 |
| $V_2O_3$ | – | – | Saturated | – | – | 0.00 |
| Witherite | * | * | – | – | -0.90 | -0.70 |
| $ZnCr_2O_4$ | – | – | Saturated | – | Saturated | Saturated |
| ZnSe | – | -1.11 | – | – | -0.72 | – |

* Ba, Br-, K+, Hg, SiO2 and Sr+2 were not measured in all samples

– Minerals with log Q/K greater than -1.7 are listed

*Reaction path modeling*- Reaction path models were created using the speciation models above and reactive minerals identified using petrographic analysis of core retrieved from the well. Simulations were modeled at 100 degrees Celsius, a pressure of 1 bar and simulate the continuous injection of $CO_2$ into the basis compositions for one year.

- *pH*- The pH of all basis compositions is expected decrease significantly in response to $CO_2$ injection. The largest changes in pH occur immediately after simulated injection begins. The $CO_2$ injection simulations into the Madison Limestone fluids suggest a rapid drop in pH from the initial value to a value below 5.5. Simulations of $CO_2$ injection into the Weber Sandstone fluids suggest an initial pH drop to about 5.5. Although in all simulations the starting pH differed, in each simulation the ending pH was 4.5 (**Figure 4.4** and **4.9)**.
- *Total dissolved solids*- The salinity of each reservoir fluid is expected to increase significantly as a result of $CO_2$ injection. This is due in part to an increasing reservoir $pCO_2$ and in part to the dissolution of pH-sensitive minerals. The concentration of total dissolved solids (TDS) may increase by more than 60,000 mg/L according to the modeling results. TDS concentrations increase linearly in both the Madison (363 to 382 mg/L per day) and Weber fluids (333 to 346 mg/L per day; **Figures 4.5** and **4.10)**

- *Saturation indices*- Mineral saturation indices were calculated and estimated for reactive minerals that were identified during petrographic analysis. These minerals include calcite, dolomite and anhydrite in both target formations, and quartz is added to the Weber. Independent models were created for each of the base samples. All results were fairly consistent between base samples, although the reaction paths were slightly different (**Figures, 4.6, 7, 8** and **4.11, 12, 13)**.

In the models using Madison fluid compositions (Madison 1a, 1b, and 2), all showed that $CO_2$ injection will drive calcite to under saturation. In models Madison 1b and 2, dolomite becomes undersaturated and begins to dissolve. Calcite dissolution occurs early in the model, occurring sometime between day 8 (Madison 1b) and day 20 (Madison 1a). Dolomite dissolution occurs on day 314 in Madison 1b and day 306 in Madison 2. Dolomite remains supersaturated for the entire modeling interval in Madison 1a. Anhydrite remains saturated and begins to precipitate taking up excess calcium in the fluid prompted by the dissolution of calcite. It is estimated that the additional anhydrite may increase as little as .01% (Madison 1a) or as much as 1% (Madison 1b). Further study is needed to determine the net effect on permeability.

The mineral saturation indices calculated using the Weber fluid compositions is similar to the overall results of Madison fluid models. Calcite and dolomite become undersaturated. Anhydrite and quartz remain saturated. Calcite dissolution begins on day 8 of the simulations in Weber 1a and Weber 1b and day 11 in Weber 2. In contrast to the Madison, dolomite begins to dissolve much earlier in the Weber models. Dolomite begins to dissolve on day 81 in Weber 1a and Weber 1b and 124 in Weber 2. Anhydrite precipitation in the Weber may increase the mineral occurrence by 1.5%. A very small increase is also expected in quartz. Quartz occurrence may increase by .001 to .01%.

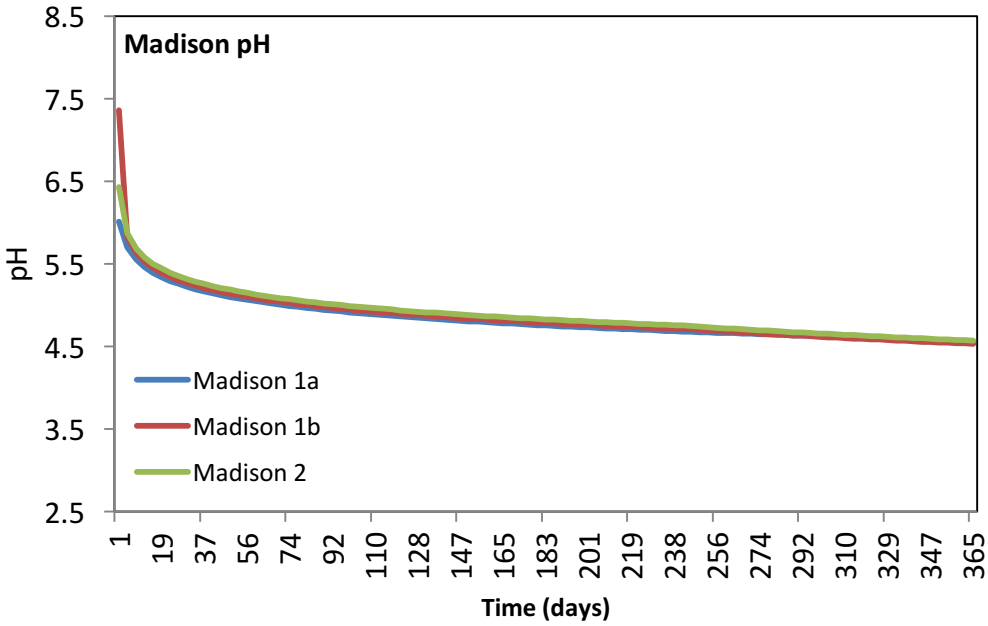


**Figure 4.4:** Estimated fluid pH values of the Madison Limestone during $CO_2$ injection

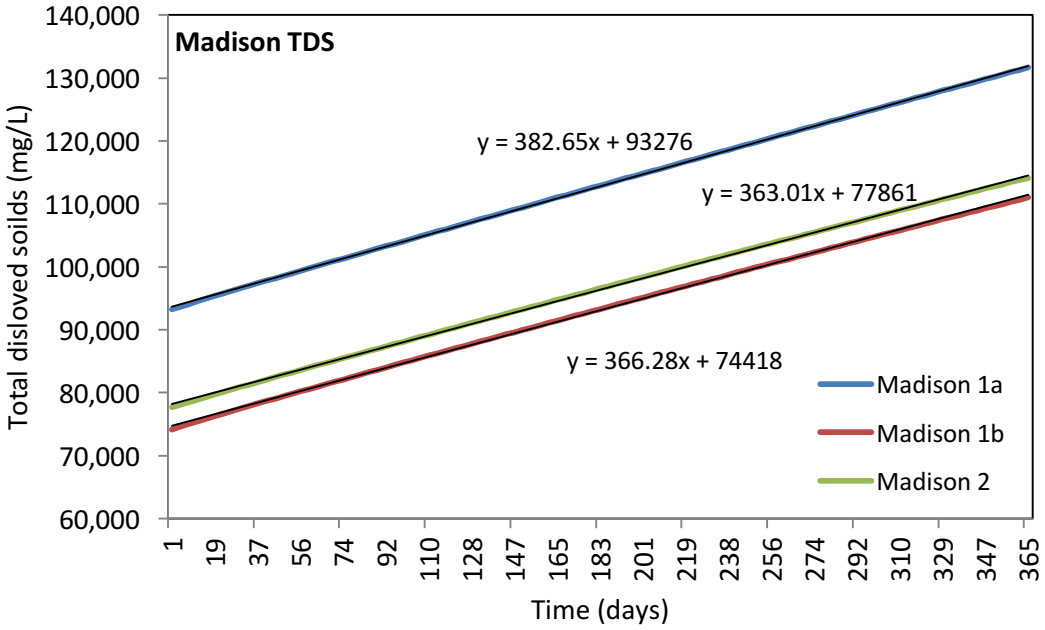


**Figure 4.5:** Estimated total dissolved solids in the fluids of the Madison Limestone in response to $CO_2$ injection

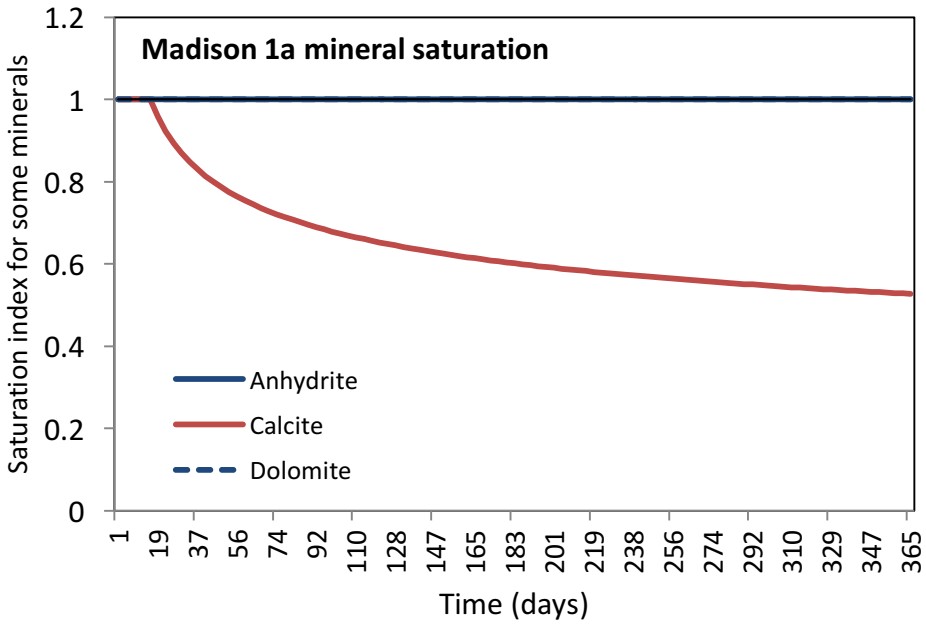


**Figure 4.6:** Modeled mineral saturation indices for reactive minerals during $CO_2$ simulations into the Madison 1a samples

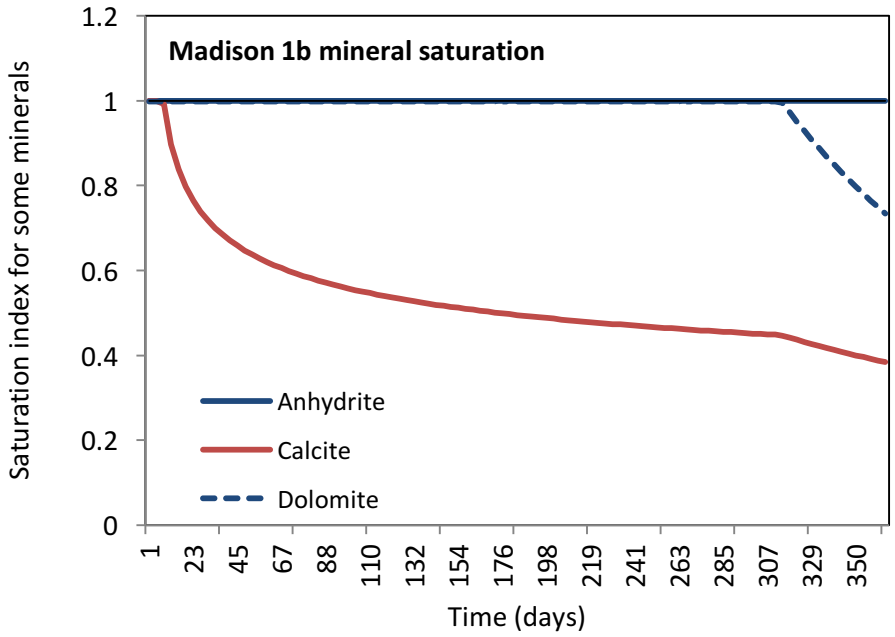


**Figure 4.7:** Modeled mineral saturation indices for reactive minerals into the Madison 1b samples

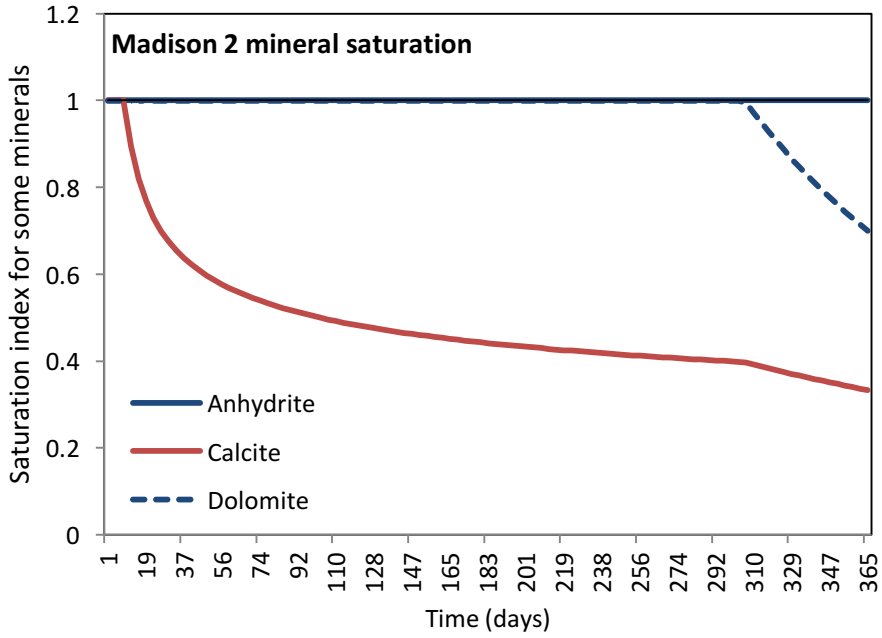


**Figure 4.8:** Modeled mineral saturation indices for during $CO_2$ injection into the Madison 2 fluid samples

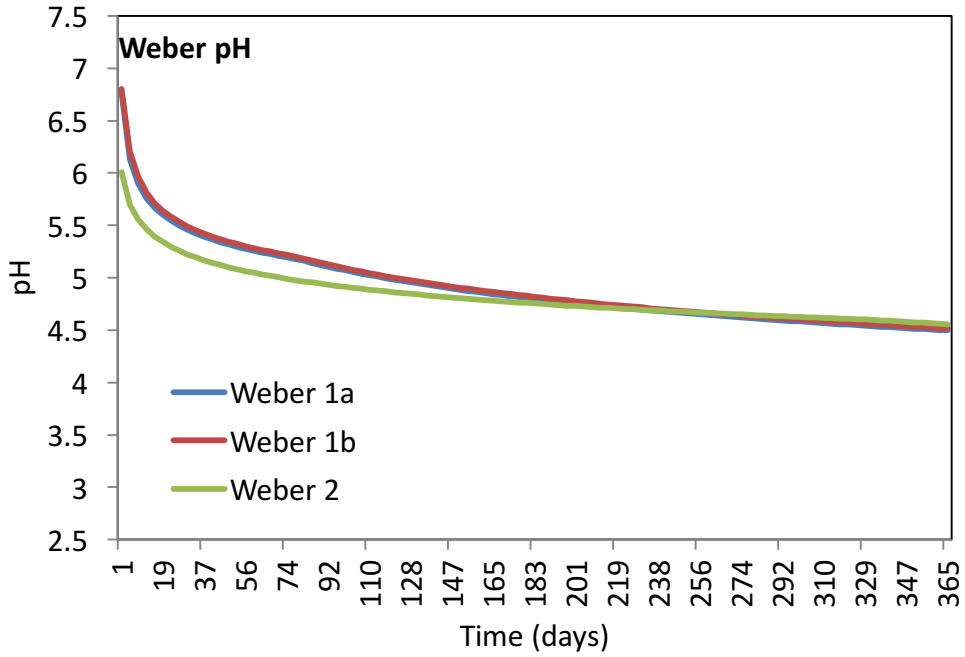


**Figure 4.9:** Estimated fluid pH values for the Weber Sandstone fluids during $CO_2$ injection simulations

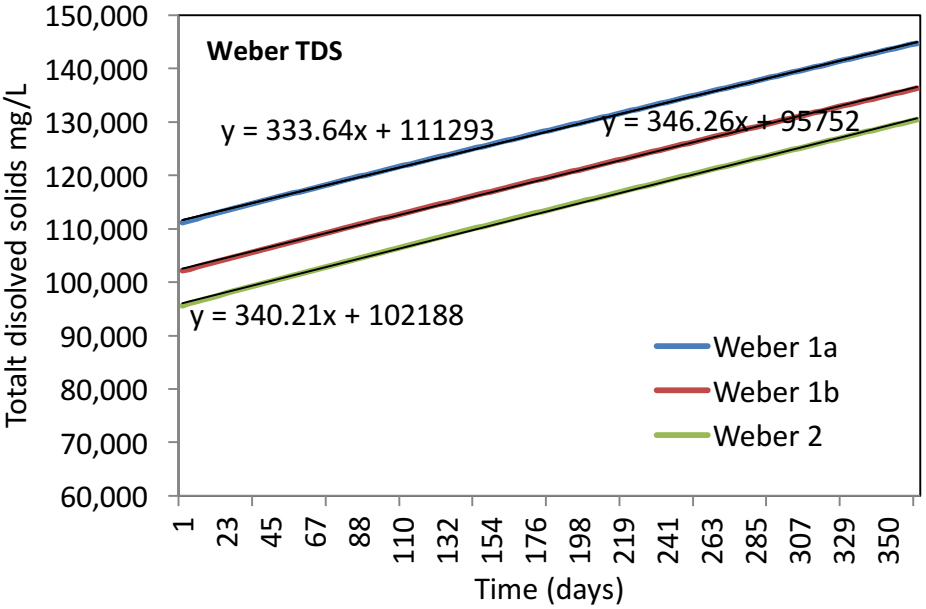


**Figure 4.10:** Estimated total dissolved solids concentrations for Weber Sandstone concentrations during $CO_2$ injection simulations

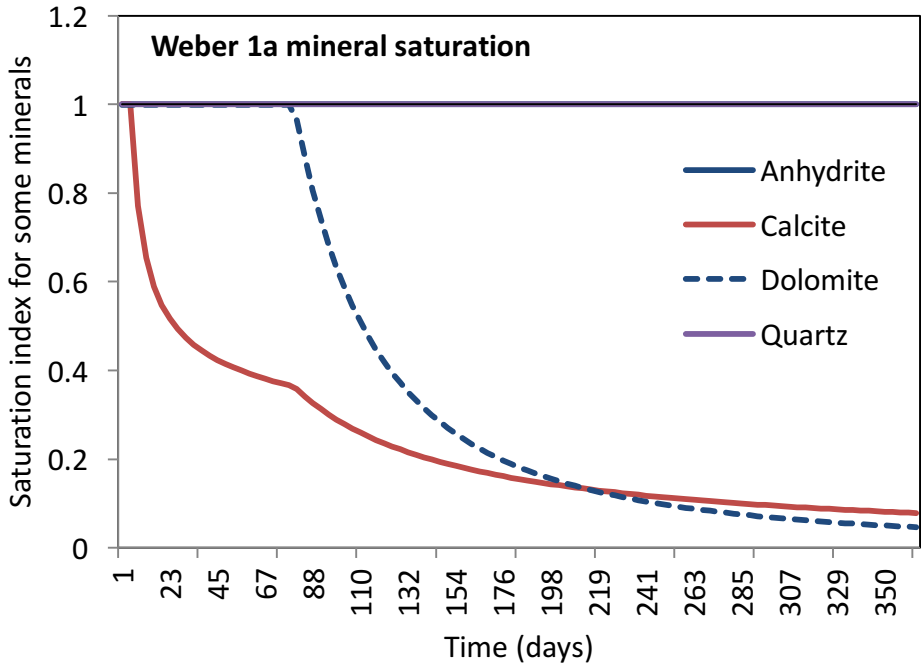


**Figure 4.11:** Modeled mineral saturation indices for reactive minerals in the Weber 1a fluid samples in response to simulated $CO_2$ injection.

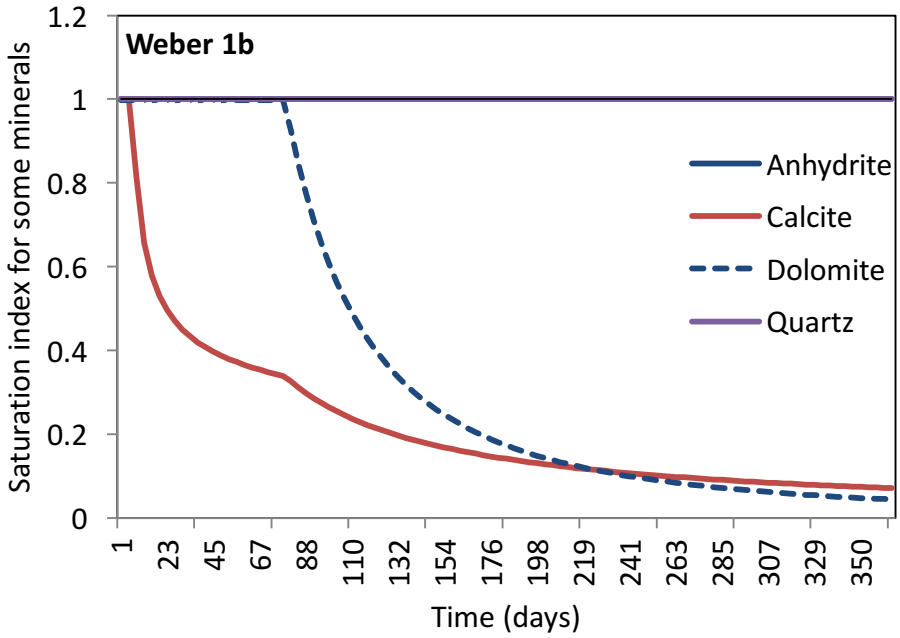


**Figure 4.12:** Modeled mineral saturation indices for reactive minerals in the Weber 1b fluid samples in response to simulated $CO_2$ injection.

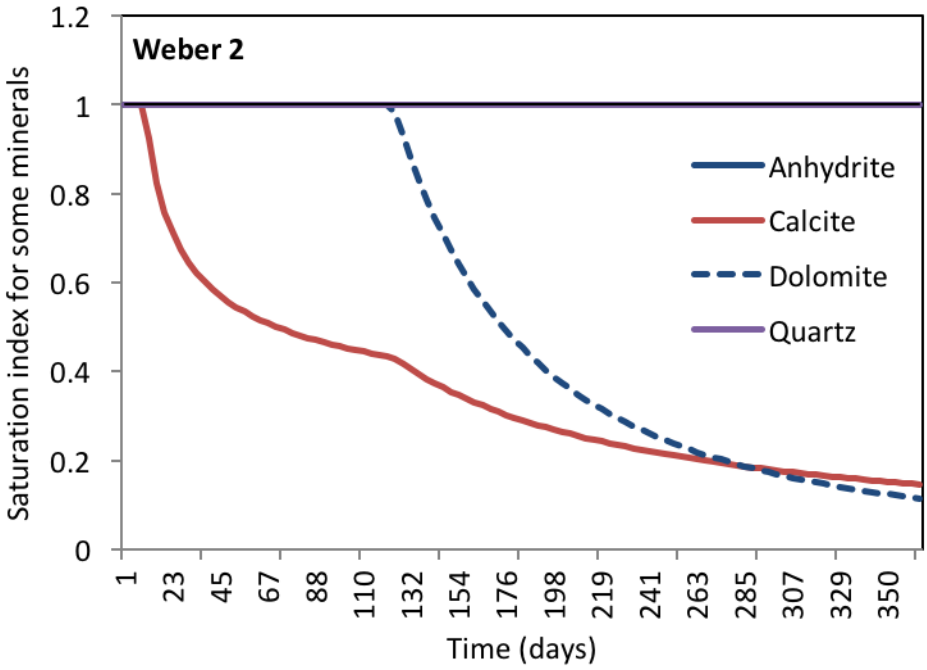


**Figure 4.13:** Modeled mineral saturation indices for reactive minerals in the Weber Sandstone 2 fluid samples in response to $CO_2$ injection.

*Define hydraulic isolation*- This analysis includes Sr isotope ratios and carbon isotope ratios from dissolved $CH_4$ and rare earth element analysis.

**Table 4.2:** Isotope results

| Sample | | δ13C $_{CO2}$ ‰ | δ$^{18}$0 $_{CO2}$ ‰ | δ$^{13}$C $_{CH4}$ ‰ | $^{34}$S |
|---|---|---|---|---|---|
| Weber 1 | 0.7505 | 28.0 | -53.7 | -22.0 | -18.8 |
| Weber 2 | 0.7424 | * | * | -21.0 | * |
| Weber 3 | 0.7454 | * | * | * | * |
| Madison 1 | 0.7262 | 35.0 | -43.9 | -46.0 | -7.1 |
| Madison 2 | 0.7236 | 46.0 | 4.9 | -41.0 | 23.5 |
| Madison 3 | 0.7267 | * | * | * | * |

*Not measured

$^{87}Sr/^{86}Sr$. The ratio of strontium 87 to strontium 86 was measured on three brine samples from the RSU #1 stratigraphic test well. The Weber Sandstone has $^{87}Sr/^{67}Sr$ values ranging from 0.7505 to .7424 and is more radiogenic than the Madison Limestone. The $^{87}Sr/^{67}Sr$ of the Madison range from 0.7236 to 0.7267. The water types are isotopically distinguishable from one another. Thus, it is likely that the target reservoirs are not mixing.

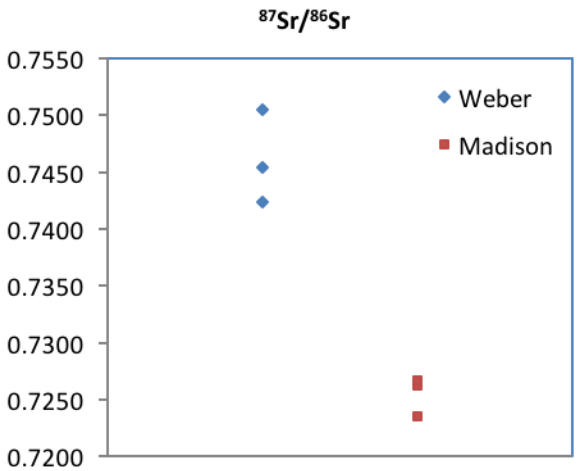


**Figure 4.14:** Strontium isotope compositions for the Weber Sandstone and Madison Limestone

$^{13}C_{CH4}$. The carbon isotopic compositions of methane for the Weber Sandstone are enriched relative to the Madison Limestone. The $\delta^{13}C_{CH4}$ of the Weber Sandstone measured in two samples are -22.0‰ and -21.0‰. The $\delta^{13}C_{CH4}$ of the Madison Limestone are -46.0‰ and -41.0‰. Both isotopic compositions are indicative of thermogenic methane. The enriched values in the Weber Sandstone should be further investigated for the potential of being mantle-sourced. Regardless of the origin of the methane, the $\delta^{13}C_{CH4}$ are unique and easily distinguishable from each other.

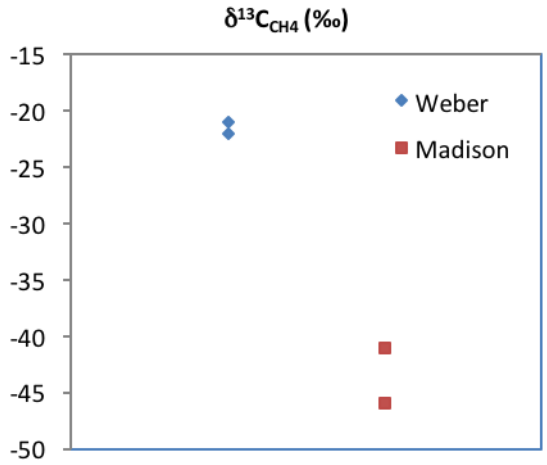


**Figure 4.15:** Carbon isotope compositions of dissolved methane in the Weber Sandstone and Madison Limestone.

*Rare Earth Element Analysis.* The REE concentrations of the fluids were measured by McLing et al., 2014. They note that there are similarities in the REE enrichment evidenced by a LREE enrichment including a slightly negative Ce anomaly and positive Gd anomalies. However, there is a large HREE enrichment in the Weber as opposed to a HREE depletion in the Madison. The Madison Limestone also has a much larger REE concentration when compared to the Weber Sandstone. McLing et al. concluded that these formations are not likely in hydraulic communication.

On the basis of this analysis, all indicate that the fluids of the target reservoirs are not mixing and suggest that the reservoirs are confined. Thus, $CO_2$ injections into the Madison Limestone are likely to be contained, and confined from the Weber Sandstone.

*Evaluation of seal failure*- There are two main mechanical failures that have been recognized to occur during $CO_2$ injection; tensile fracturing and shear slip of pre-existing fracturing (Rohmer and Seyedi, 2010). The geochemical conceptual models have been developed to represent these types of failures. Three mineral reactions were considered to represent basic dynamics of chemical transformations of seal failure (**Table 4.3**). The brine composition and calculated aqueous species (**Table 4.4, 4.5**), were calculated using the reaction path models for Weber fluids created under Milestone 4.2.

The modeling results suggest changes in fluid composition in the event of seal failure. These include an increase in pH from 4.5 to >7. Saturation states for reactive minerals change; most notably are dolomite-ord, calcite and antigorite become supersaturated and undersaturated with respect to quartz (**Table 4.6**). Dolomite and aragonite remain under-saturated (**Table 4.6**). The model suggests that calcite precipitation may increase the original calcite volume by as much as 200% (**Figure 4.16**). This is dependent on fluctuations in $pCO_2$ and temperature. However, this suggests that escaped fluids would likely drive the precipitation of calcite within the fractures.

This is consistent with observations made on the RSU core (Task 3). The presence of calcite-filled fractures in the core suggests high $pCO_2$ fluids have moved through the system, sometime in the geologic past. Thus, validating the conceptual model and also demonstrating the self - healing nature of the fractures in the presence of $CO_2$. Future work will be focused to further assimilate the conceptual models, to the measured geologic data.

**Table 4.3:** Mineral reactions present in the system

| Minerals in system | moles | log moles | grams | volume (cm3) |
|---|---|---|---|---|
| Anhydrite | 0.003673 | -2.435 | 0.5000 | 0.1687 |
| Calcite | 0.004996 | -2.301 | 0.5000 | 0.1845 |
| Dolomite | 0.005423 | -2.266 | 1.000 | 0.3490 |
| (total) | | | 2.000 | 0.7023 |

**Table 4.4:** Initial brine composition calculated from $CO_2$ injection models

| | | | |
|---|---|---|---|
| Temperature = 92.2 C | | Pressure = 1.013 bars | |
| pH = 4.500 | | | |
| Ionic strength | = | 4.298043 | |
| Activity of water | = | 0.906747 | |
| Solvent mass | = | 1.0000 | kg |
| Solution mass | = | 3.0288 | kg |
| Mineral mass | = | 0.0020000 | kg |
| Solution density | = | 7.451 | g/cm3 |
| Solution viscosity | = | 0.004 | poise |
| Chlorinity | = | 3.216108 | molal |
| Dissolved solids | = | 669838 | mg/kg sol'n |
| Hardness | = | 577.69 | mg/kg sol'n as CaCO3 |
| carbonate | = | 577.69 | mg/kg sol'n as CaCO3 |
| non-carbonate | = | 0.00 | mg/kg sol'n as CaCO3 |
| Carbonate alkalinity | = | 10948.57 | mg/kg sol'n as CaCO3 |
| Water type | = | Na-Cl | |
| Bulk volume | = | 407. | cm3 |
| Fluid volume | = | 407. | cm3 |
| Mineral volume | = | 0.702 | cm3 |
| Inert volume | = | 0.000 | cm3 |
| Porosity | = | 99.8 | % |
| Permeability | = | 93.0 | cm2 |

**Table 4.5:** Aqueous species and species activities for initial brine compositions

| Aqueous species | molality | mg/kg sol'n | act. coef. | log act. |
|---|---|---|---|---|
| CO2(aq) | 37.73 | 5.483e+05 | 1.0000 | 1.5767 |
| Na+ | 4.000 | 3.036e+04 | 0.6910 | 0.4416 |
| Cl- | 2.791 | 3.267e+04 | 0.5953 | 0.2205 |
| HCO3- | 0.5936 | 1.196e+04 | 0.7311 | -0.3625 |
| NaHCO3 | 0.5174 | 1.435e+04 | 1.0000 | -0.2862 |
| NaCl | 0.4153 | 8014. | 1.0000 | -0.3816 |
| NaSO4- | 0.4066 | 1.598e+04 | 0.6910 | -0.5514 |
| SO4-- | 0.1619 | 5134. | 0.0847 | -1.8630 |
| K+ | 0.1162 | 1500. | 0.5953 | -1.1601 |
| KSO4- | 0.01794 | 800.6 | 0.6910 | -1.9067 |
| CaHCO3+ | 0.008211 | 274.1 | 0.7805 | -2.1933 |
| KCl | 0.006710 | 165.1 | 1.0000 | -2.1733 |
| CaCl+ | 0.003122 | 77.87 | 0.6910 | -2.6660 |
| CaSO4 | 0.003004 | 135.0 | 1.0000 | -2.5224 |
| SiO2(aq) | 0.002626 | 52.08 | 1.7405 | -2.3401 |
| Ca++ | 0.002538 | 33.59 | 0.1753 | -3.3517 |
| HSO4- | 0.0007779 | 24.93 | 0.6910 | -3.2696 |
| MgHCO3+ | 0.0002962 | 8.343 | 0.6910 | -3.6890 |
| MgSO4 | 0.0001295 | 5.147 | 1.0000 | -3.8877 |
| Mg++ | 0.0001004 | 0.8056 | 0.2687 | -4.5689 |
| MgCl+ | 7.899e-05 | 1.558 | 0.6910 | -4.2630 |
| H+ | 3.300e-05 | 0.01098 | 0.9584 | -4.5000 |
| CO3-- | 7.507e-06 | 0.1487 | 0.1061 | -6.0986 |
| CaCO3 | 2.054e-06 | 0.06787 | 1.0000 | -5.6874 |
| NaH3SiO4 | 1.965e-06 | 0.07663 | 1.0000 | -5.7066 |
| NaCO3- | 1.672e-06 | 0.04581 | 0.6910 | -5.9374 |
| H3SiO4- | 9.940e-08 | 0.003121 | 0.6910 | -7.1631 |
| MgCO3 | 4.880e-08 | 0.001358 | 1.0000 | -7.3116 |
| HCl | 3.422e-08 | 0.0004120 | 1.0000 | -7.4657 |
| NaOH | 1.989e-08 | 0.0002627 | 1.0000 | -7.7013 |
| OH- | 1.918e-08 | 0.0001077 | 0.6460 | -7.9069 |

(only species > 1e-8 molal listed)

**Table 4.6:** Saturation indices of reactive minerals after seal failure.

Mineral saturation states

| | log Q/K | | | log Q/K |
|---|---|---|---|---|
| Dolomite-ord | 0.0000 | sat | Quartz | -1.9904 |
| Calcite | 0.0000 | sat | Tridymite | -2.1072 |
| Antigorite | 0.0000 | sat | Chalcedony | -2.2117 |
| Dolomite | -0.0005 | | Sylvite | -2.3050 |
| Aragonite | -0.1602 | | Enstatite | -2.3660 |
| Thenardite | -0.3353 | | Cristobalite | -2.4189 |
| Chrysotile | -0.4391 | | Talc | -2.4599 |
| Halite | -0.9106 | | Diopside | -2.6119 |
| Dolomite-dis | -1.1490 | | Pirssonite | -2.7985 |
| Magnesite | -1.2978 | | Amrph^silica | -2.9107 |
| Monohydrocalcite | -1.3341 | | Arcanite | -2.9251 |
| Brucite | -1.5593 | | | |

(only minerals with log Q/K > -3 listed)

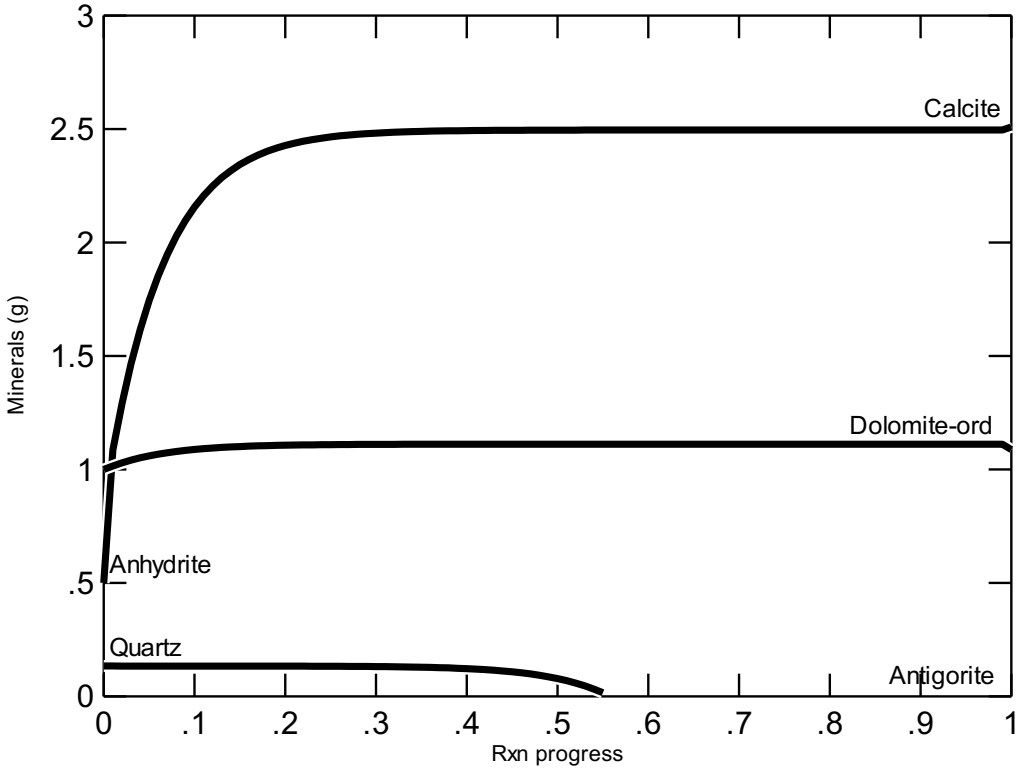


**Figure 4.16:** Mineral precipitation and dissolution in the fractures in the event of failure.

## Conclusion

Fluid characterization is a vital component of reservoir characterization projects. Geochemical and isotopic results of reservoir fluids and dissolved gases from the Mississippian Madison Limestone and Pennsylvanian Weber Sandstone were used to evaluate brine evolution, calculate thermodynamic equilibrium, estimate geochemical reactions with respect to $CO_2$ injection, evaluate geochemical reactions in case of seal failure, and to investigate stacked reservoir confinement.

The brines are Na-Cl type with total dissolved solid concentrations in excess of 85,000 mg/L. Conservative analytes indicate that the evolution of the brines in both formations have been heavily influenced by evaporite dissolution, increasing the molar ratio of Br-Na-Cl. Dolomitization at depth in each reservoir results in magnesium depletion. Comparative analysis suggests that dissolution of evaporite and other minerals have had a large influence on the evolution of the formation fluids. This has resulted in increased TDS post-burial, resulting in some of the most saline formation fluids collected in Wyoming.

Dominate aqueous species for all samples collected from the Weber Sandstone include sodium (act. coef. -0.0171 to .0278), chloride (act. coef. -0.0818 to -0.0157), sodium chloride (act. coef. -1.0845 to -.9411), sodium sulfate (act. coef. -1.3987 to -1.6935) and potassium (act. coef. -1.5776 to -1.5713). Potassium and strontium concentrations were only analyzed for in two of the three samples. Dominate aqueous species for samples collected from the Madison Limestone include chloride (act. coef. -0.1616 to -0.0678), sodium (act. coef. -0.1341 to -0.0573), potassium (act. coef. -1.2236 to -1.2722), sodium chloride (act. coef. -1.2512 to -1.1106) and carbon dioxide (-1.4930 to -2.0118).

Reaction path models were created to estimate the geochemical reactions in response to $CO_2$ injections into each formation. The pH of all basis compositions is expected decrease significantly in response to $CO_2$ injection. The largest changes in pH occur immediately after simulated injection begins. The concentration of total dissolved solids (TDS) may increase by more than 60,000 mg/L according to the modeling results. All geochemical models indicate carbonate mineral dissolution and some anhydrite precipitation. The net porosity gain from precipitation and dissolution process is expected to be 1-3%, indicating that $CO_2$ injection will have a positive effect of reservoir porosity.

In the event of mechanical seal failure, geochemical models of the brine suggest that calcite precipitation would rapidly occur within fractures. This suggests that failures within the seal would be self-healing if exposed to formation fluids.

The isotopic compositions of fluids and dissolved gases were found to be unique to each formation. Rare earth element concentrations further establish distinctive fluid concentrations. Though these fluids share a similar evolution, we suggest that dissimilarities in the isotopic compositions of the brines, dissolved gases and rare earth element concentrations indicate that the target formation fluids are isolated from each other.

## Task 5: Simulations to evaluate seal integrity, injection rate, and pressure management

### Overview

Initial investigations of the RSU CCS characterization project (DOE DE-FE0002142) identified priority saline storage reservoirs (the Mississippi Madison Limestone and Pennsylvanian Weber Sandstone) which have the capacity to store commercial volumes of supercritical $CO_2$. This study evaluated sealing potential relative to injection parameters.

Laboratory experiments and geochemical modeling show that the solubility of $CO_2$ in formation brines is low, and decreases with increasing salinity: $CO_2$ concentrations are usually less than 3 mol % (Duan et al., 2008), and only a small fraction (less than 8%) of the injected $CO_2$ could dissolve into formation brine within 200 years (Hassanzadeh et al., 2009). The low solubility and slow dissolution rate of $CO_2$ suggests that the time necessary to dissolve injected $CO_2$ into brine will be much longer than the injection period (i.e., 50 years, a typical life span for a coal-fired power plant). Subsequently the majority of injected $CO_2$, over 90% in first few hundred years, is expected to remain in a supercritical phase, rising buoyantly to the top of the reservoir along the sealing margin. Therefore, identifying caprock that possesses sufficient sealing capacity to trap injected $CO_2$ for a long term (i.e., several hundred years) becomes a critical issue for assessing the safe storage capacity of a geological $CO_2$ storage site.

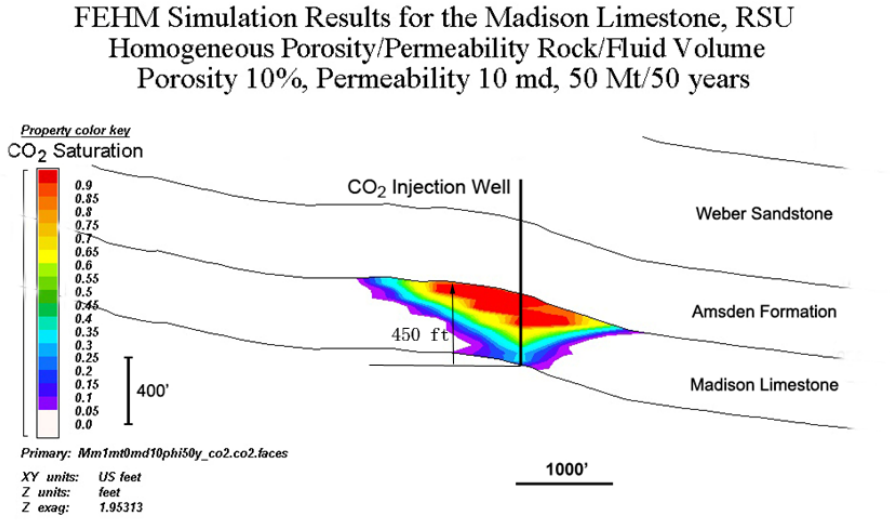


**Figure 5.1:** The injected $CO_2$ is trapped below the most upper portion of the Madison Limestone and the Amsden Formation and the $CO_2$ column can be 450 ft. of height.

The objective of Task 5 is three-fold. The first objective is to integrate data and results collected from other tasks to produce a detailed 3-D geological property models to characterize the distribution of porosity, permeability, rock mechanical strength, regional stress field, and fluid for confining formations. The second objective is to integrate the high-mercury injection test data with the $CO_2$/brine interfacial tension and analog contact angle data collected from the literature to determine the sealing capacity of various confining layers with respect to injected $CO_2$. The third objective is to perform a sensitivity analysis by varying critical effective parameters

including pore throat radii, interfacial tension, relative permeability, contact angle, and $CO_2$ and formation water density independently over natural ranges. The reservoirs at this study site have associated seals that can conservatively contain a column height of supercritical $CO_2$ of up to 400 feet within the Weber Sandstone and 700 feet within the Madison Limestone (**Figure 5.1**, modified from Jiao et al., 2013).

## Executive Summary

Task 5 is composed of five subtasks.

- *Subtask 5.1*—A refined, heterogenic 3-D geological property model was developed for the injection reservoir and associated confining formations. Data and results collected from Task 2, 3, 4, and 6 were integrated to generate model. The model included distribution of porosity, permeability, mechanical strength, regional stress fields, and fluid constants for the reservoir and confining formations using the EarthVision geospatial modeling and Petrel property modeling software. The model served as the template for all dynamic fluid modeling and injection scenarios.
- *Subtask 5.2*—Diverse injection scenarios were generated using the 3-D numerical computation models to create performance assessments and to evaluate seal integrity, reservoir injection feasibility and storage capacity, and to evaluate displaced fluid and pressure responses for management. Simulations of $CO_2$ injection volumes were run on the LANL multiphase porous flow simulator FEHM. The 3-D fluid flow simulation models include detailed calculations of subsurface fluid movement, including flow through injection wellbores, faults, and fractures under variable scenarios.
- *Subtask 5.3*— A probability-based PA model was developed to evaluate sealing capacity and integrity, and to evaluate the importance of parameters for numerical simulation of confining layers. Monte Carlo simulations were used to optimize $CO_2$ injection feasibility, storage capacity, and reservoir pressure and displaced fluid management scenarios. The importance and effects of the simulation input parameters were then prioritized from the experiments.
- *Subtask 5.4*—Conclusion and methods were evaluated to choose crucial input parameters for $CO_2$ injection numerical simulations using 3-D property model constructions relative to sealing capacities of confining layers.

The following conclusions and recommendations resulted from this study:

- The majority of injected $CO_2$, over 90% in the first few hundred years, will remain in supercritical phase and rise buoyantly beneath low-permeability confining layers. Migration through the water saturated pore network of a confining layer may occur if the $CO_2$ fluid pressure in the reservoir exceeds the capillary entry pressure of the confining layers.
- An integrated, multi-data approach is necessary to characterize the heterogeneities of porosity and permeability for containment formations. High vertical resolution core measurement data and log data were needed to constrain and generate reservoir and seal property models based on attribute analysis results from the Jim Bridger 3-D seismic survey.
- As borehole and core data were used to retrieve much of the geostatistical parameters, such as the spatial heterogeneities of porosity and permeability, a question may

reasonably arise regarding how representative the vertical data is in the lateral sense. By combining the vertical heterogeneities with regional geological information and seismic attribute analyses, we believe heterogeneities in both the vertical and horizontal directions within the modeling domains were fairly captured, reducing the lateral uncertainties outside of the wellbore.

- The entries pressures of a $CO_2$-brine system for RSU seals range from 7 to 122 psi, about half the total of entry pressures of an oil-brine system, and one-fourth the total of entry pressures gas-brine system. Generally, entry pressures increase with depth. The primary seals at the storage site are the limestone facies in the upper Madison Limestone (122 psi), the Triassic Red Peak siltstone (91 psi), the Amsden Formation (51 psi), and varying marine facies at the base of the Weber Sandstone (35 psi). Additional (redundant) seals were identified in Task 3. Total $CO_2$ column heights that the various confining layers at the RSU could competently retain range from 53 to 994 ft. The low permeability (>0.001 md) micritic limestone facies at the most upper portion of the Madison Limestone could hold over 900 ft. of injected $CO_2$ in a column, far thicker than the total formation. The Amsden Formation could a $CO_2$ column of approximately 375 ft., and the Triassic Red Peak Formation could hold a $CO_2$ column of approximatley740 ft. The $CO_2$ column height sealing capacity of overlying redundant seals range from 54 to 279 ft.
- This study suggests that the sealing capacity of a $CO_2$-water-rock system confining layer is significantly lower than similar confining layers in a hydrocarbon-water-rock system. However, $CO_2$ injection simulations indicate that the confining layers at the RSU site have adequate sealing capacity to conservatively retain 25MT of injected $CO_2$ over a 50-year injection period with no risk to confinement.
- Sensitivity analysis shows that the sealing capacity of the upper portion of the Madison Limestone is most sensitive to changes in the $CO_2$-water interfacial tension angle. $CO_2$ column heights are most sensitive to the $CO_2$-water interfacial tension, and to differences in $CO_2$ and brine densities.

## Methods

*Multi-scale heterogeneity characterization*- Previous characterization work at the RSU site (DE-FE0002142) established that obtaining reliable results from $CO_2$ injection simulations depends on thoroughly characterizing reservoir properties in three dimensions. A property model is a simplified version of real reservoir conditions that is used as a tool to describe the trend and characteristics of reservoir property distribution. A successful reservoir property model should balance realism and practicality, being neither so simplified that it is unrealistic nor so detailed that it obscures features of the reservoir property distributions. We used an integrated approach to characterize the heterogeneities of the porosity and permeability for confining layers. This was done by integrating high-vertical-resolution core measurement data and geophysical log data with attribute analysis results from the Jim Bridger 3-D seismic survey. This integrated approach allowed for the development of a realistic and geologically constrained 3-D property model of the study area.

## Results and Discussion

*Core measured porosity*- The porosity of a rock is calculated as the pore volume of the rock divided by its bulk volume. Routine core analysis was conducted on core plug samples from the Weber Sandstone and Madison Limestone (reservoirs), and the Triassic Red Peak and Amsden formations (confining layers). All tests were conducted by Intertek Westport Technology Center, following the core analysis procedures specified in API RP40 Recommended Practices for Core Analysis (1988). Pore volume and permeability measurements were made with the samples mounted in a rubber-sleeved, hydrostatically loaded overburden cell. The samples were tested at 800 psi, and a calculated reservoir net confining stress (NCS). Boyle's Law, using helium as the gas medium, was employed to determine pore volume. Unsteady-state Klinkenberg permeability was measured after each pore volume measurement. Permeability to air was calculated using the unsteady-state flow data. These data were generated in Task 3.

The porosities of the Red Peak Formation are less than 2%, measured both at confining pressure (800 psi) and in-situ reservoir pressure (>5,000 psi), and average density is 2.7 g/cm$^3$ (**Figure 5.2**). Pore throat radii are <2 μm, ranging between 0.001 to 1.6 μm. The porosity of the Amsden is 5.7 at 800 psi confining pressure, and 5.3% at reservoir pressure. Pore throat radii are <3 μm, ranging between 0.008 to 2.5 μm. The porosities of the most upper portion of the Madison Limestone confining layer range from 0.2 to 0.42%, measured both at confining pressure (800 psi) and in-situ reservoir pressure (>5,000 psi), and average density is 2.7 g/cm$^3$ (**Figure 5.2**). Pore throat radii are <3 μm, ranging between 0.005 to 0.25 μm.

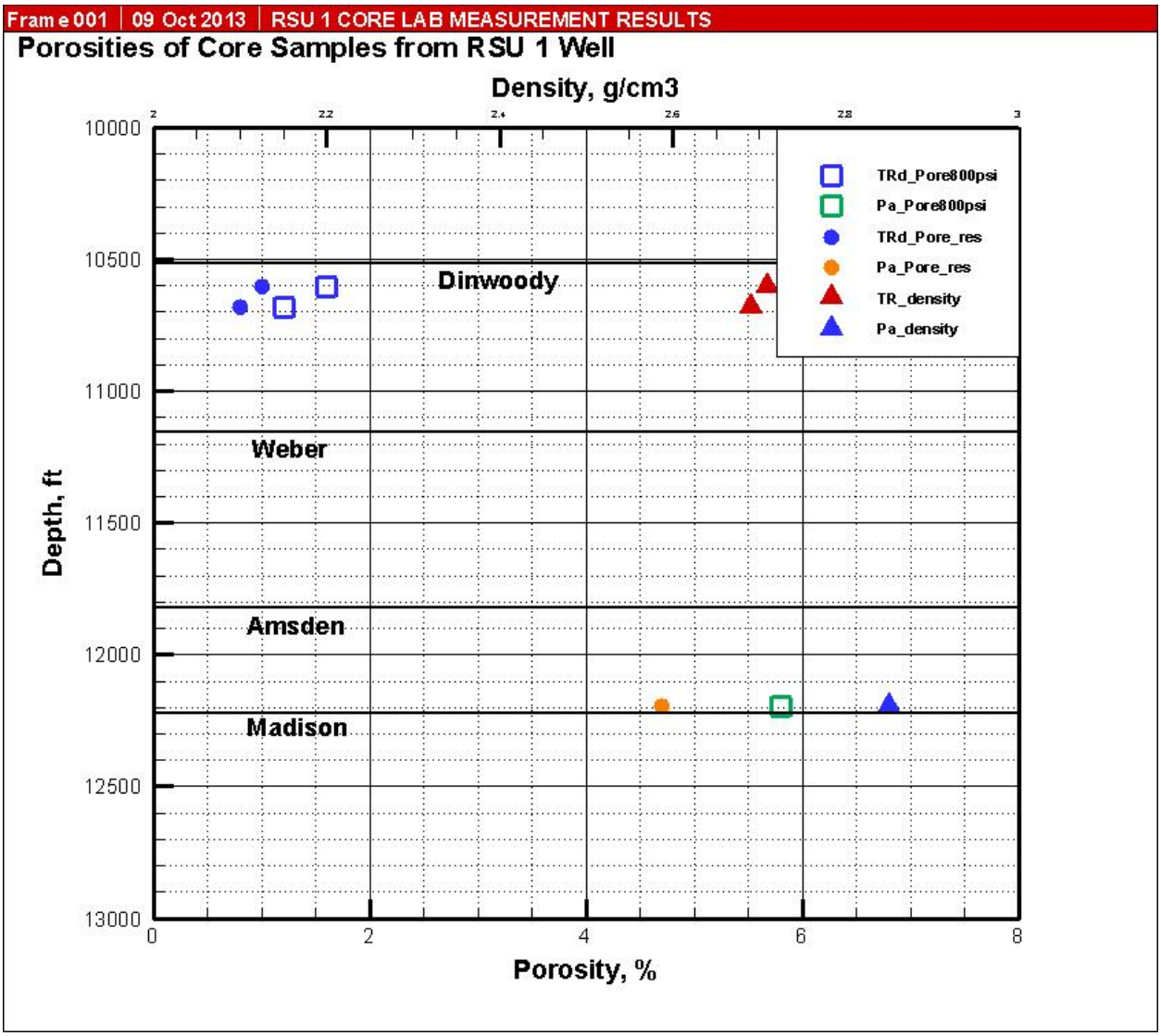


**Figure 5.2:** Plot of porosity and density versus depth for the Triassic Red Peak and Amsden formations. Both porosities measured under 800 psi NCS and reservoir NCS are shown.

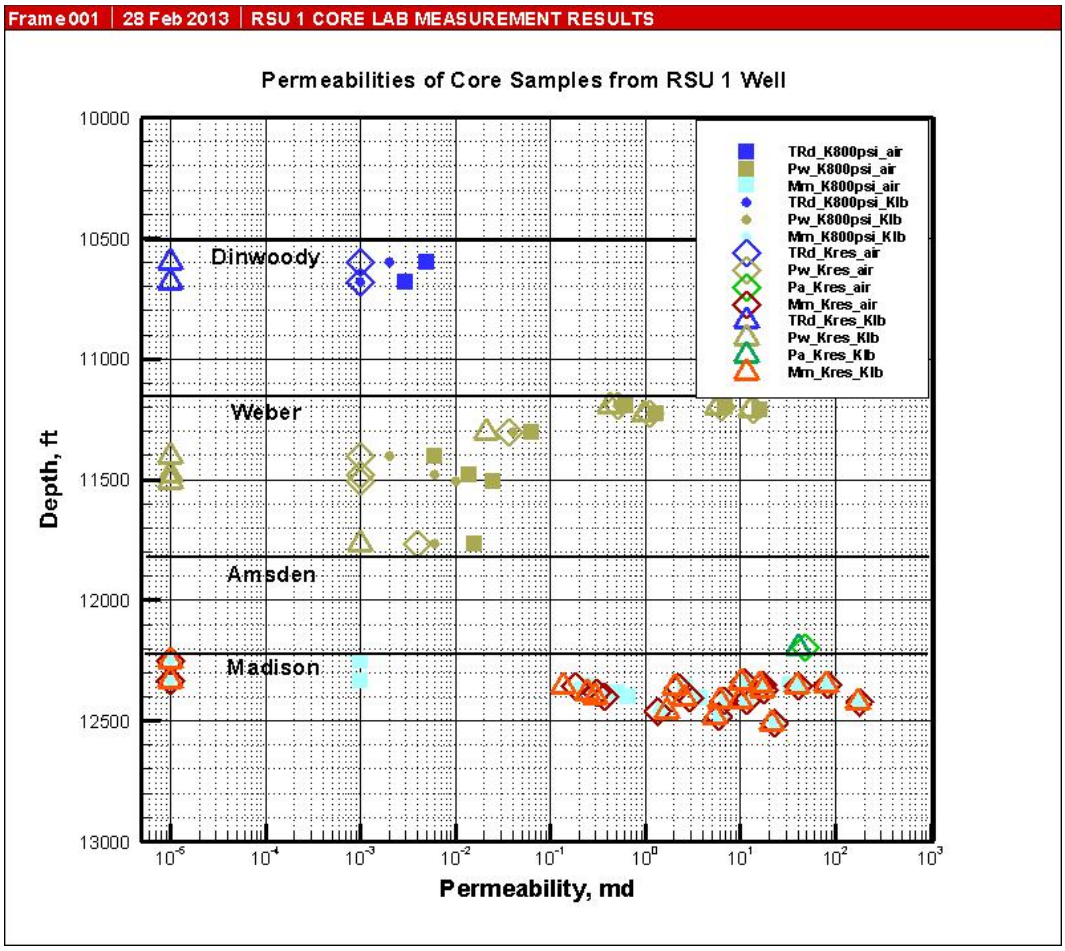


**Figure 5.3:** Plot showing the air and Klinkenberg permeability variations in targeted reservoirs and confining layers under 800 psi NCS and reservoir NCS. Klinkenberg permeability of the Dinwoody Formation is on the order of $10^{-5}$ md under reservoir conditions (5,000 psi), and on the order of $10^{-3}$ mD under 800 psi confining pressure. The laboratory reports a higher permeability for the Amsden Formation, due mainly to micro-fractures from sample retrieval rather than natural permeability. The permeability of the upper portion of the Madison Limestone is approximately $10^{-5}$ mD under reservoir conditions (5,000 psi).

*Log porosity and core porosity*- Porosity values calculated from logs were correlated with core-derived measurements from Task 3. Effective porosity is the total porosity less the fraction of the pore space occupied by clay-bound water. Since it is not possible to measure effective porosities in a reliable and repeatable manner, calibration with core analyses is best achieved by estimating total porosities from logs and comparing these with measured total porosities from core plugs.

Total porosity was calculated by using the density log, corrected for lithology (using grain density) and fluid density (using invaded zone resistivity or neutron logs). Formation bulk density is a function of matrix density, porosity, and density of the fluid in the pores. To determine the density porosity from the bulk density log, the matrix density and density of fluid in the pores must be known. Measured densities of confining layers are 2.7 g/cm$^3$ for the Red Peak Formation, 2.64 g/cm$^3$ for the Weber Sandstone, 2.70 g/cm$^3$ for the limestone facies in the Madison Limestone, and 2.84 g/cm$^3$ for dolostone facies in the Madison Limestone. These densities were used for the porosity estimation from the bulk density log in this study. The cross

plots of the laboratory measured porosities under reservoir conditions with log derived porosity show that neutron porosity overestimates the porosity of carbonate and carbonaceous shale (**Figure 5.4a**), whereas the density porosity log underestimates the porosity of carbonate (**Figures 5.4b**). As indicated by Asquith and Gibson (1982), true porosity could be calculated from neutron porosity and density porosity using the root mean square formula (gas-bearing formation) or mathematic mean formula (oil and water bearing formation). The heavy magenta line shown in **Figure 5.5** represents the total porosity estimated from the neutron and density porosity log from the RSU#1 well. These neutron-density porosities are a good match for core sample porosity (**Figure 5.6**). The neutron-density porosity still overestimates the carbonaceous shale and limestone samples. This may be caused by the high clay content of the shale and vugs in the limestone, which would increase the porosity on the well logs.

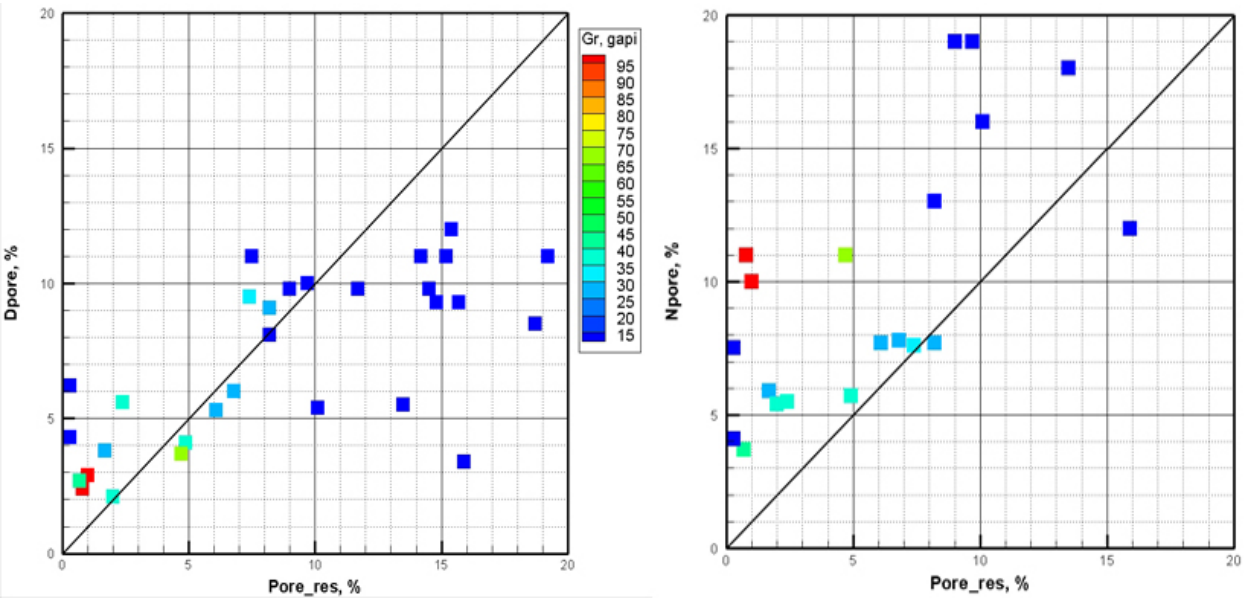


**Figure 5.4:** Cross plot of the laboratory measured porosity at reservoir conditions with the log derived bulk density porosity (A) and neutron porosity (B).

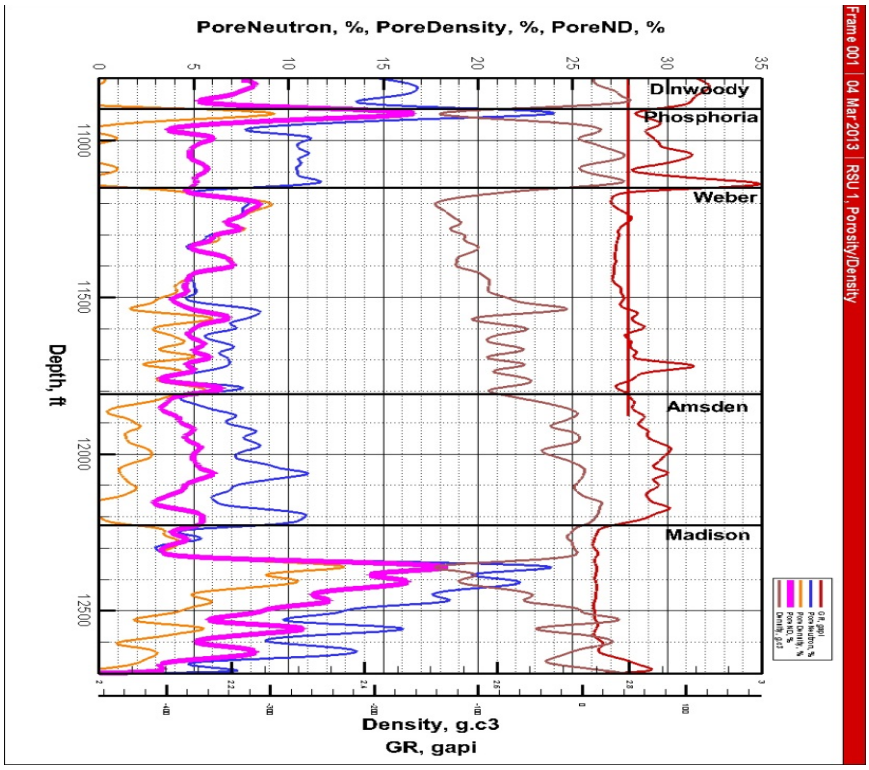


**Figure 5.5:** Plots of gamma ray, bulk density, neutron porosity, and density porosity for the Red Peak Formation, Phosphoria Formation, Weber Sandstone, Amsden Formation and Madison Limestone from the RSU#1 well. The heavy magenta line is neutron-density porosityand is used to establish the function between the porosity and sonic velocity.

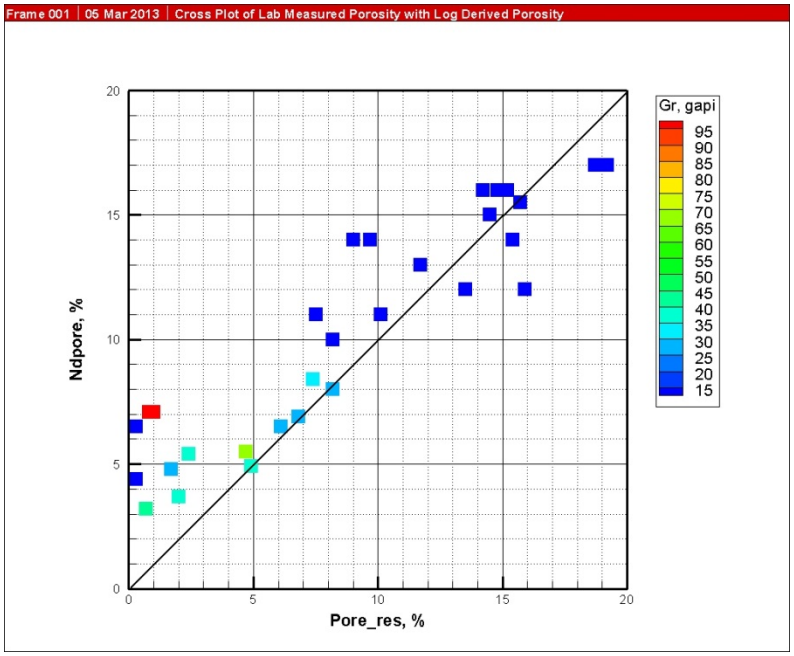


**Figure 5.6:** Cross plot of the laboratory measured porosity at reservoir conditions with the log derived neutron-density porosity.

*Sonic velocity and neutron-density porosity*- In order to characterize the spatial heterogeneity of reservoirs and confining strata, seismic attributes were used in conjunction with the core and petrophysical log properties. The relationships of the neutron-density porosity and sonic velocity logs were established for the Mowry Shale, Chugwater Formation, Red Peak Formation, Dinwoody Formation, and Amsden Formation.

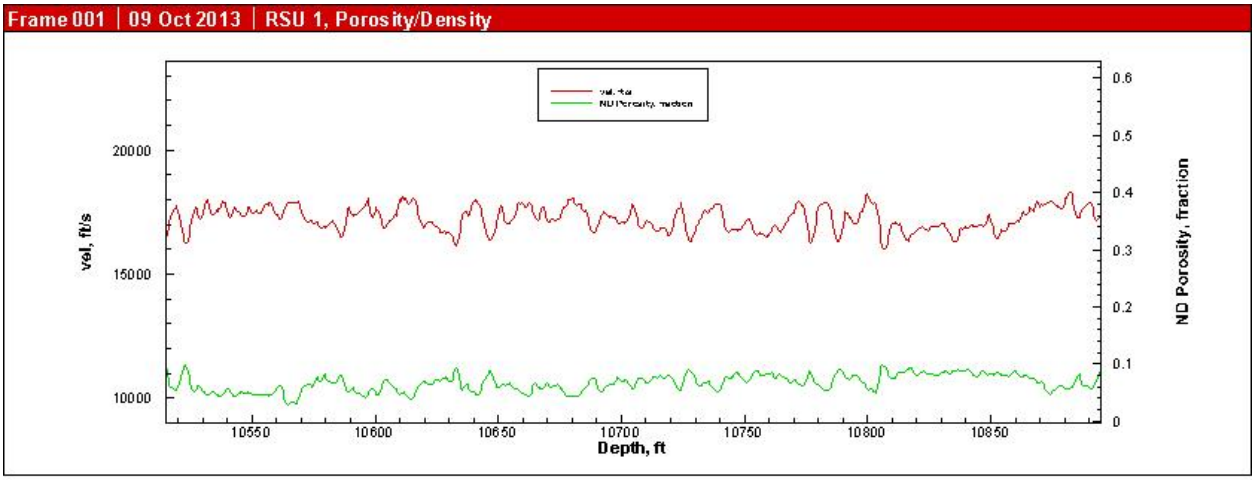


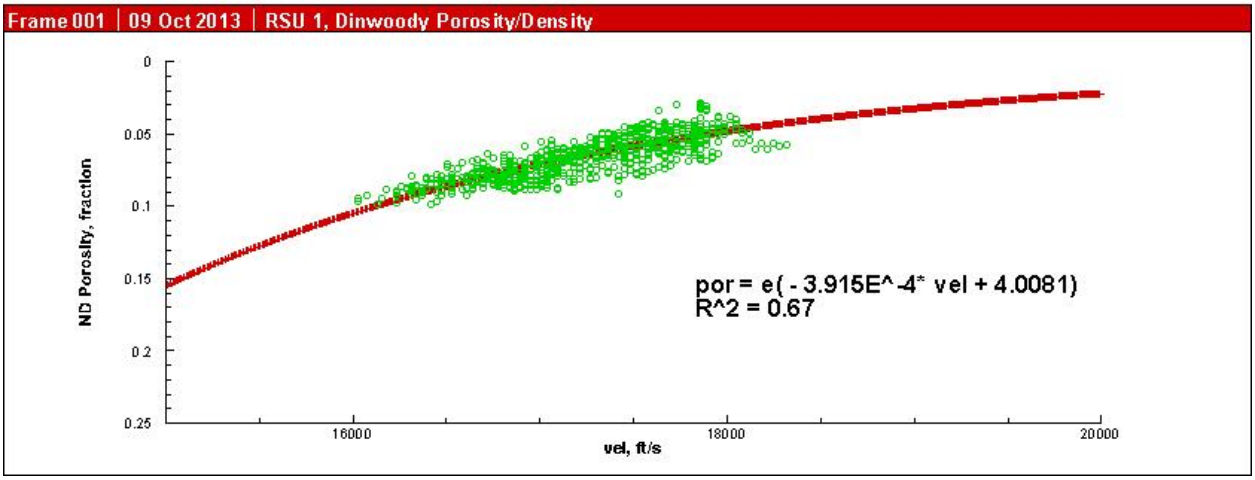


**Figure 5.7a** shows the sonic velocity and neutron-density porosity variations of the lower Triassic Formation in the RSU#1 well. The relationship between the sonic velocity and neutron-density porosity for the Dinwoody Formation is shown in **Figure 5.7b**. The neutron-density porosities of the Dinwoody Formation in the RSU#1 well range from 1 to 10%, with a mean of 6% (**Figure 5.7a**). Applying the function shown in **Figure 5.7b**, porosities derived from the seismic interval velocities range from 1% to 8%, with a mean of 5% (**Figure 5.8**).

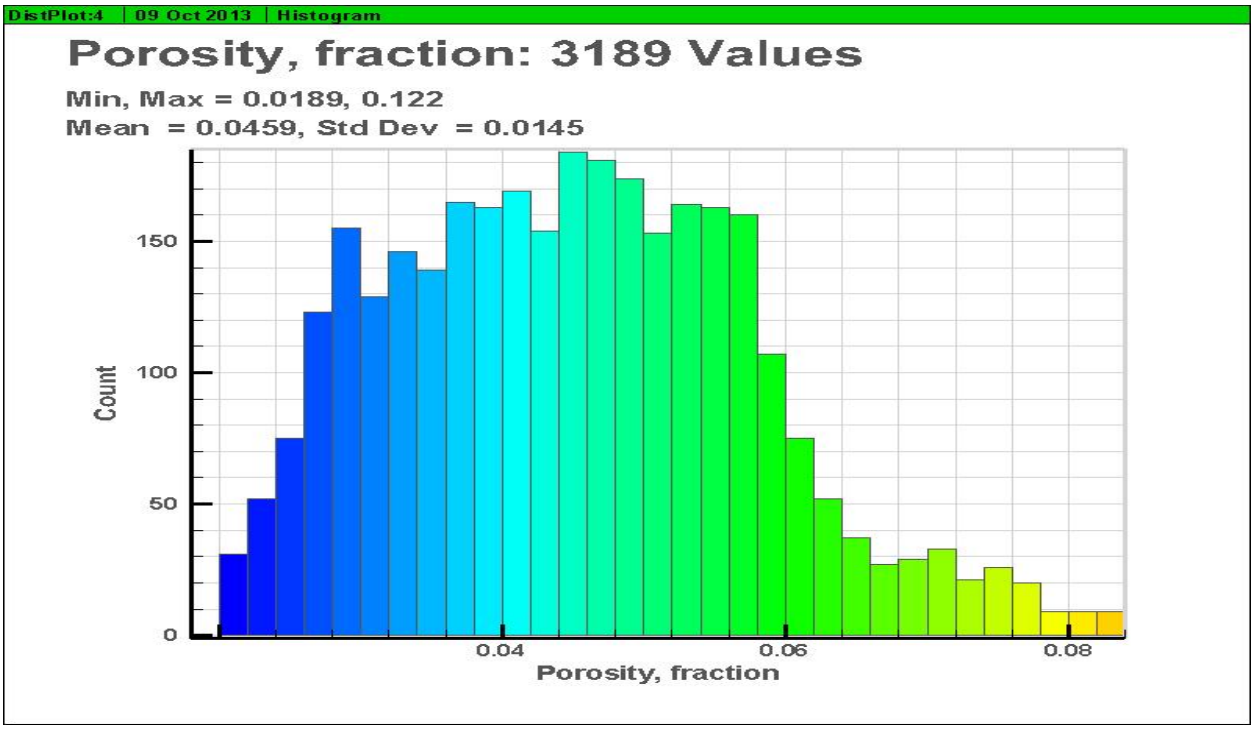


**Figure 5.8:** Histograms generated for porosities of the Dinwoody Formation from seismic data based on the function derived from porosity and sonic logs.

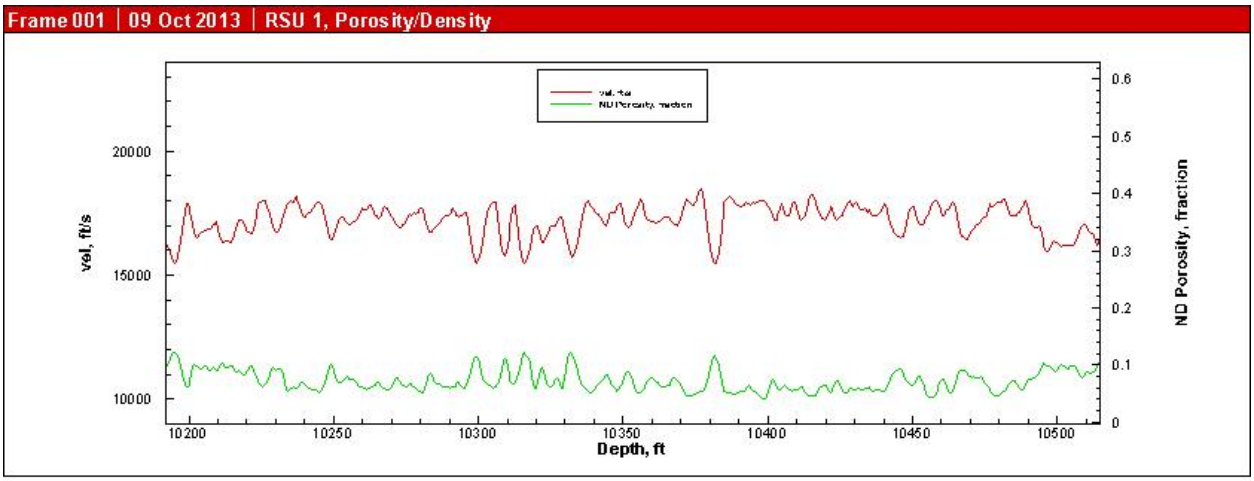


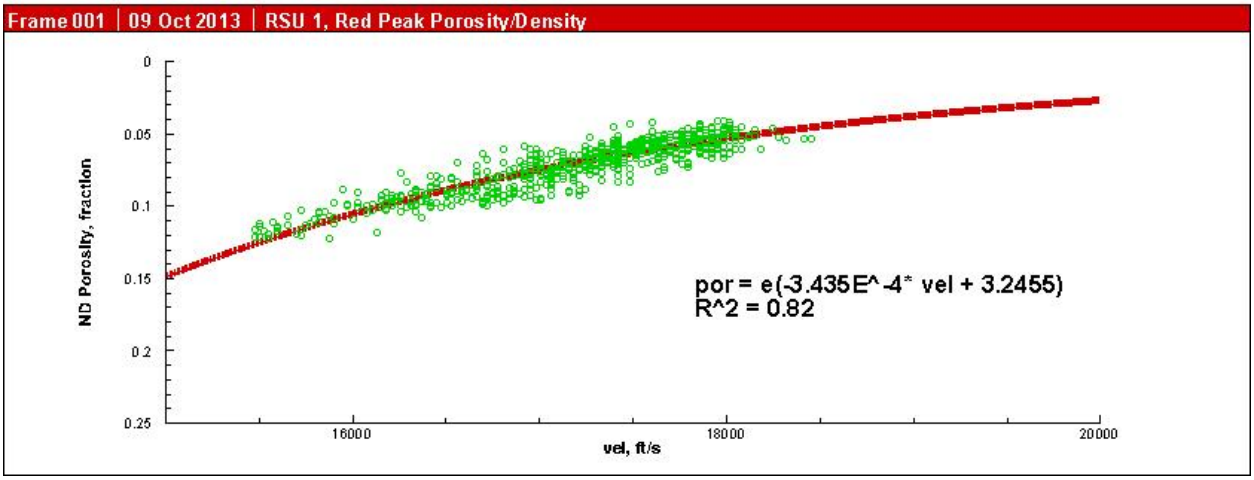


**Figure 5.9a** illustrates the sonic velocity and neutron-density porosity variations of the Red Peak Formation in the RSU#1 well. The relationship between the sonic velocity and neutron-density porosity for the Red Peak Formation is shown on **Figure 5.9b**. The neutron-density porosities for the Red Peak Formation from RSU#1 well logs range from 1 to 10%, with a mean of 7% (**Figure 5.9a**). Applying the function shown on **Figure 5.9b**, porosities derived from the seismic interval velocities of the Jim Bridger 3-D seismic survey range from 1 to 10%, with a mean of 4.5% (**Figure 5.10**).

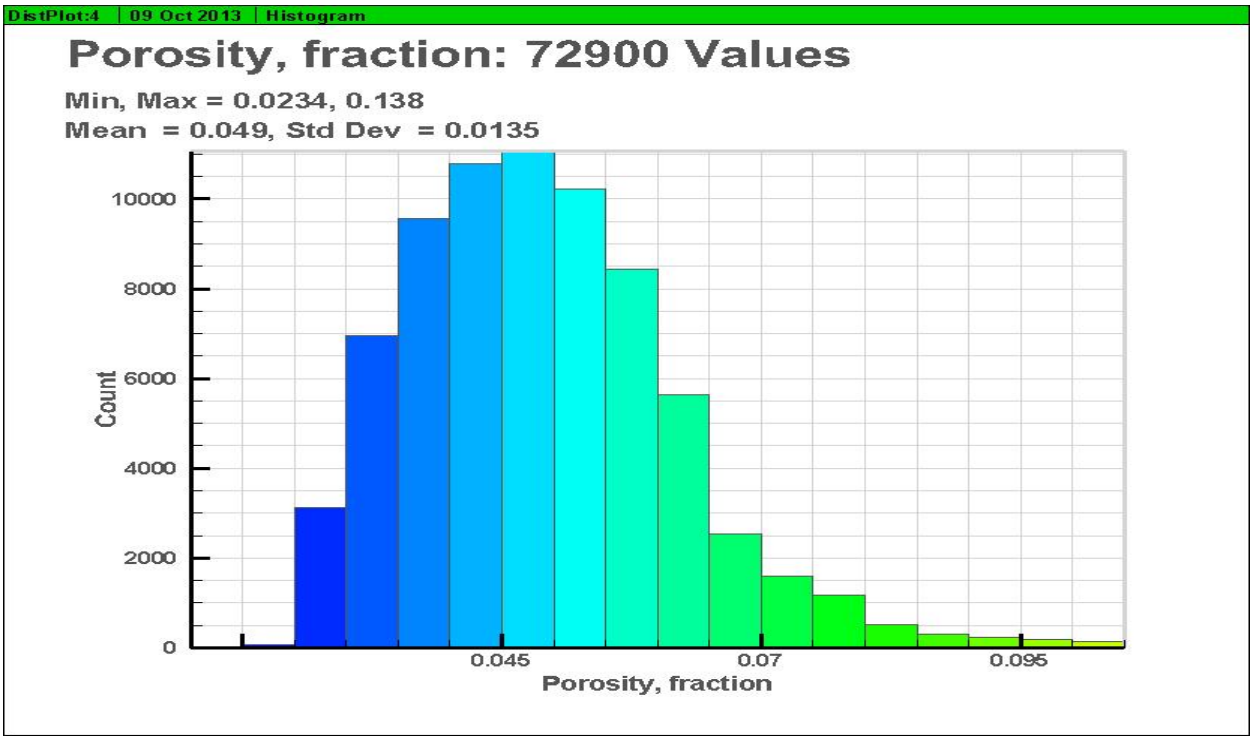


**Figure 5.10:** Histograms generated for porosities of the Red Peak Formation from seismic data based on the function derived from porosity and sonic logs.

*Permeability and porosity spatial distribution*- The spatial distribution of permeability of the study area were estimated using empirical correlations between porosity and permeability. The permeability of the shale and shaley-sandstone is a function of porosity, clay content, effective stress, and diagenesis (Yang and Aplin, 2010). Because of the difficulty in making laboratory measurements on shale samples, high-quality porosity and permeability data for shale and mudstone is relatively rare (Neuzil, 1994). A simple linear regression relationship cannot realistically capture the relationship between porosity and permeability. In light of this complexity, we used the empirical correlation of Yang and Aplin (2010) to compute the permeability of the sealing rocks, assuming a clay content of 25%[1]. The results are illustrated in **Figure 5.11**.

[1] $\ln k = -69.59 - 26.79C + 44.07C0.5 + (-53.61 - 80.03C + 132.78C0.5)\, e + (86.61 + 81.91C - 163.61C0.5)\, e0.5$ (12)

where $e = \theta/(1-\theta)$, e is void ratio and $\theta$ the porosity, k is vertical permeability in unit of $m^2$, and C is clay content in percent.

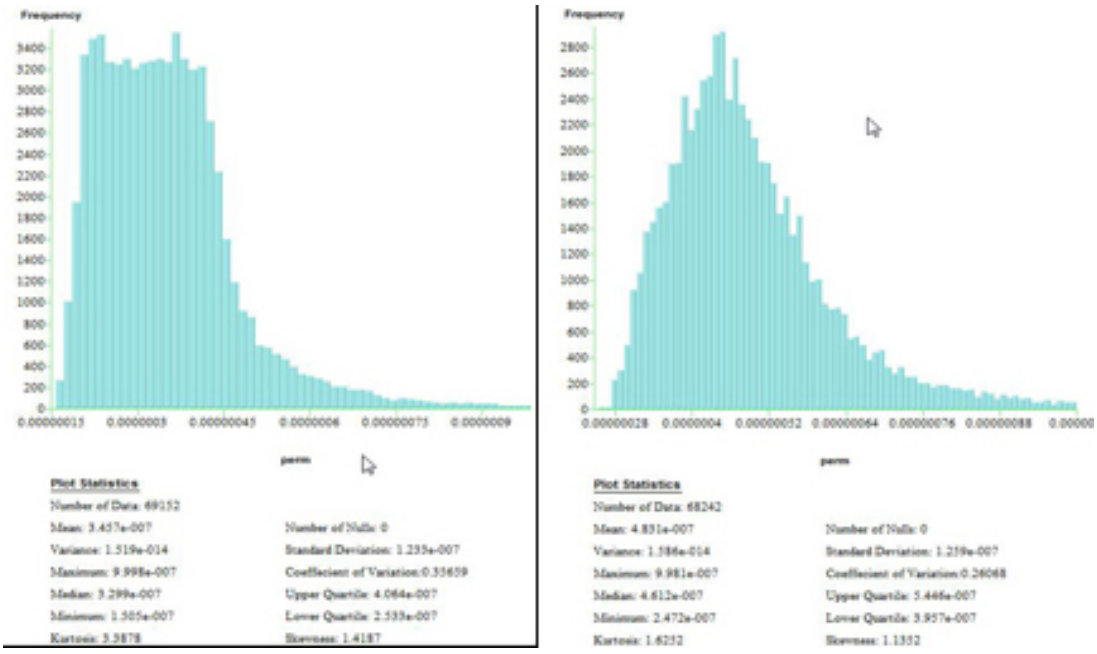


**Figure 5.11:** Histograms showing the permeability distribution of the Dinwoody (A) and Chugwater (B) formations.

*Three-dimensional property modeling*- We constructed 3-D property model for the RSU geological $CO_2$ storage site (8km x 8km) using the calculated spatial distribution of porosity and permeability and other geological data. The model was built in Petrel®. Formation tops below the Cretaceous section were extrapolated from seismic reflections and from well logs. One major fault is included in this geological structural model to the northeast of the injection well. The gridding sizes for the x, y, and z axes are 160 m by 160 m by 30 m, respectively.

By combining geological data with seismic attribute analyses, we believe the spatial heterogeneities in both the vertical and horizontal directions within the modeling domains are justly defined. The porosity distribution of the primary Triassic confining formations are shown in **Figures 5.12** and **5.13**. Both formations are characterized by regionally low porosities ranging from 1 to 10%, with a mean of 5%.

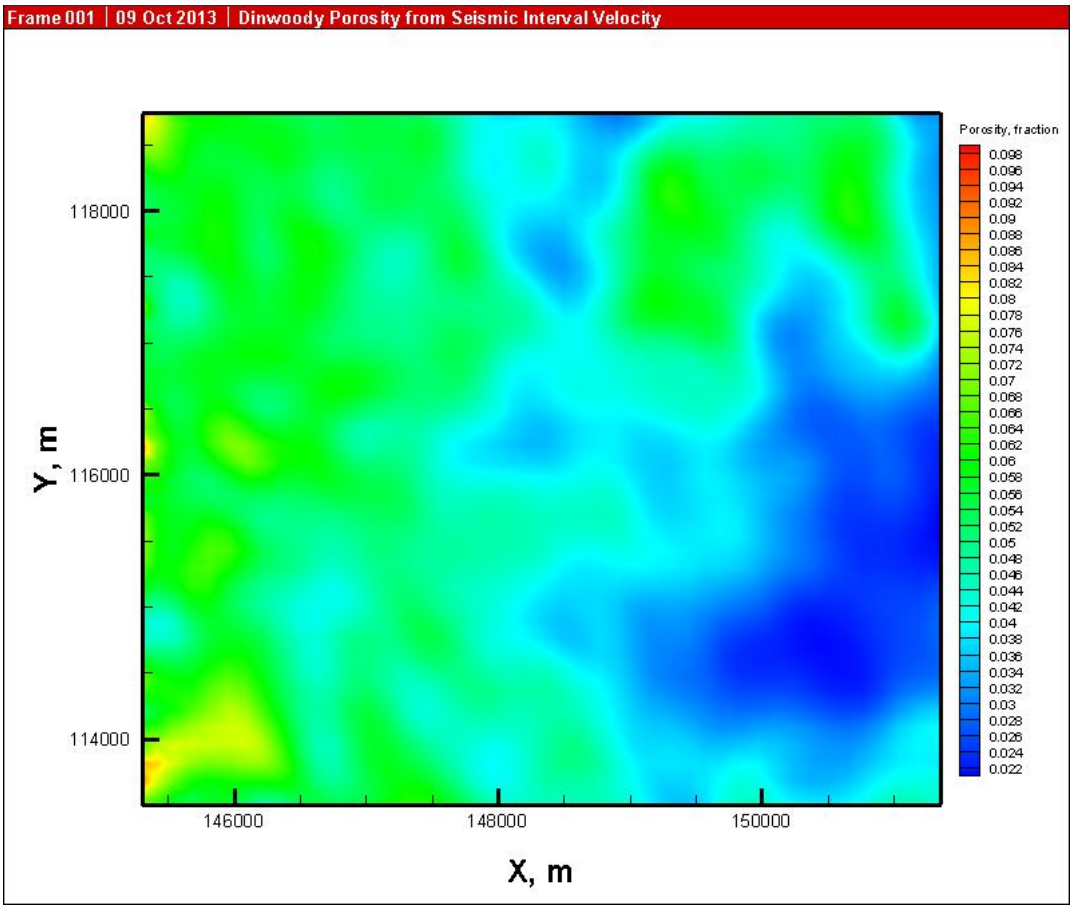


**Figure 5.12:** Contour map of porosity distribution of the Dinwoody Formation at the RSU storage site. Within the domain, the porosity of the Dinwoody Formation ranges from 1 to 10%, with a mean of 4.5%.

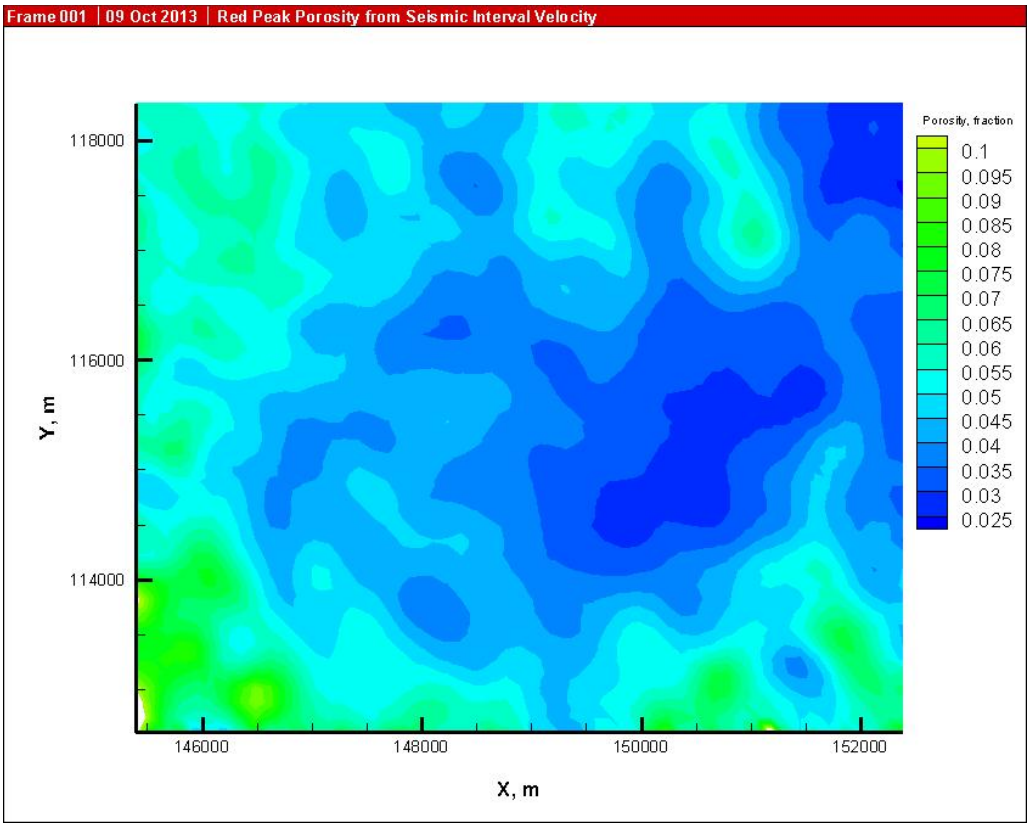


**Figure 5.13:** Contour map of porosity distribution of the Red Peak Formation at the RSU storage site. Within the domain, the porosity of the Red Peak Formation ranges from 1 to 10%, with a mean of 5%.

*Performance assessments of diverse injection scenarios*- Calculating storage site performance and associated leakage risks involves gathering site data that are then used to populate numerical models of plume injection and migration, including time dependent pressure and saturation predictions. The plume estimates are then used to calculate potential leakage through wellbores, faults, and overlying confining layers (Viswanathan et al., 2008). A final step in a risk analysis is to assign consequence values to impacts so that a true risk value can be calculated as *risk = probability x consequence*.

To evaluate the integrity of the confining layers at the study site, various injection scenarios were developed to simulate $CO_2$ injection in the Weber Sandstone. An illustrational injection well was located in Section 16, Township 20 north, and Range 101 West. The thickness of the Weber Sandstone at this location is 700 ft. The reservoir petrophysical properties were held constant. The porosity of the Weber Sandstone was homogeneous at 10%, and the permeability was homogeneous at 1 mD within the models confines. The permeability for confining layers were assigned at 0.01 mD.

A series of injection simulations were performed (injection rates of 0.5 Mt/year, 1 Mt/year, and 1.5 Mt/year). The simulation for 1.0 Mt/year, 10% porosity, and 1 mD of permeability had pressures that remained well below hydro-fracture pressure and leveled off after the 10 years after injection ceased.; It was necessary to remove 66 Mt of formation fluids over the injection

period to maintain the reservoir pressure below the hydro-fracture pressure. Reservoir pressure elevated quickly when the injection was initiated, but remained below the hydro-fracture pressure in response to brine production. After injection ceased, reservoir pressure decreased back to original pressure within 10 years (**Figure 5.14**). At an injection rate of 1.5 Mt/year, the reservoir pressure reached fracture pressure and the simulation was terminated. **Figure 5.15** is an incline view of the injected $CO_2$ plume for the targeted Weber Sandstone after 50 years of injection at 1 Mt/year. After 50 years of injection, the $CO_2$ plume migrated across the formation boundary of the Weber Sandstone into the Phosphoria, Amsden, and the Madison formations. The plume is virtually a circle with a radius of 1,600 m, and covers an area of 8 $km^2$ (**Figure 5.16**). The $CO_2$ plume with lower saturations of 0.05 to 0.9% occupies a space of 1.2 $km^3$. The total volume of the Weber Sandstone above a depth of 5,000 m within the RSU is 412 $km^3$. Therefore, if the full thickness of the Weber Sandstone was used for storage in the RSU, its storage capacity would be 17 Gt of $CO_2$ assuming homogeneity.

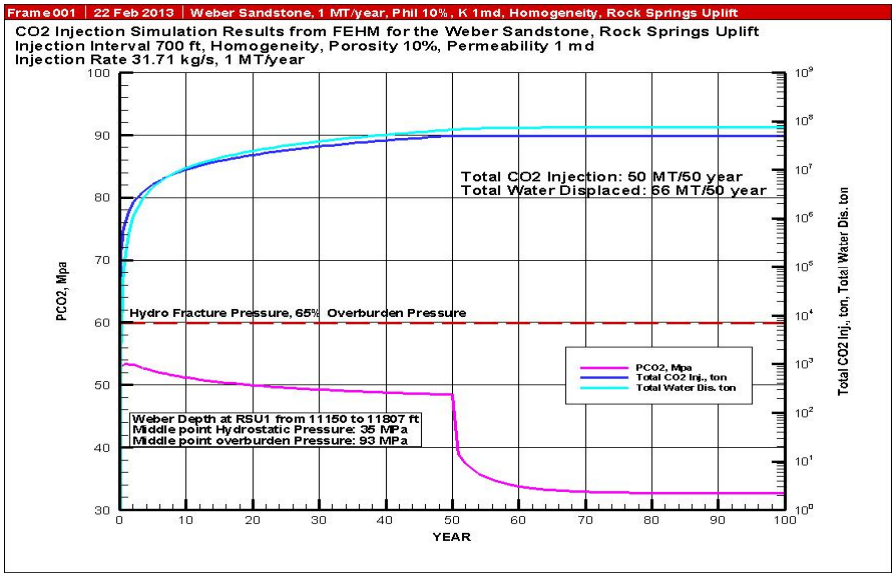


**Figure 5.14:** FEHM $CO_2$ injection simulation results for the Weber Sandstone. The simulations are set up for a homogeneous reservoir with petrophysical conditions of 10% porosity and 1mD of relative permeability. The injection rate of 31.71 kg/s is constant for 50 years, and the simulation is run for another 50 years without $CO_2$ injection. Note that the reservoir pressure is elevated quickly when the injection starts, but kept below the hydro-fracture pressure throughout the injection time. After injection ceased, the reservoir is back to original pressure within 10 years.

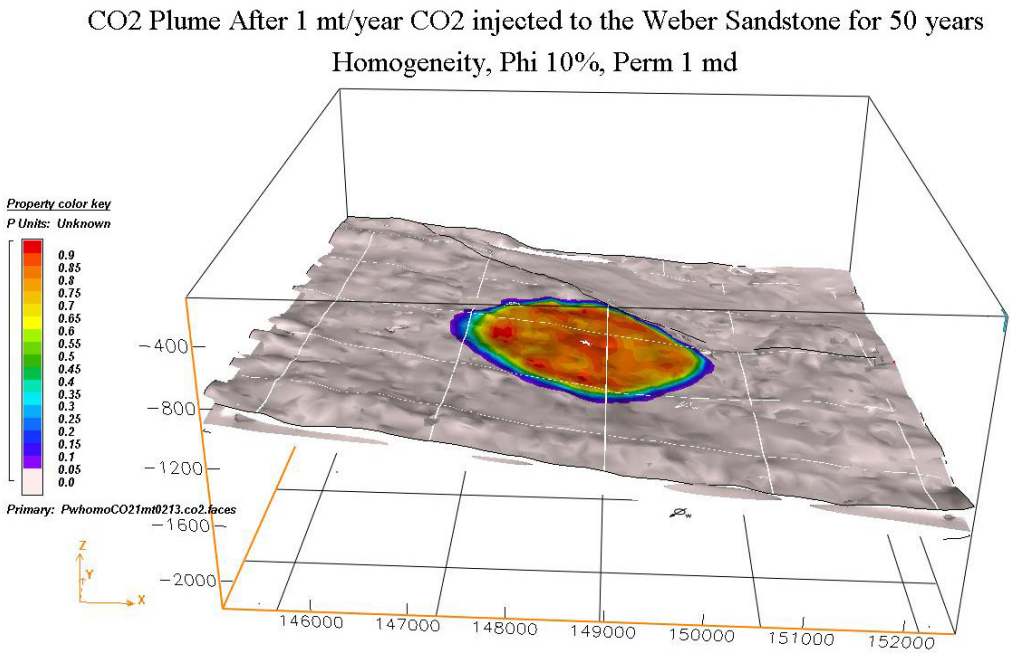


**Figure 5.15:** The $CO_2$ plume distribution in the Weber Sandstone after 50 years of injection from the FEHM simulator within the seismic survey area. The simulation used an injection interval of 700 feet, homogenous porosity (10%) and relative permeability (1 mD), and an injection rate of 1 Mt/year in a single injection well. The up-dip boundary is opened to imitate displaced fluid production. Incline view on an east-west cross section.

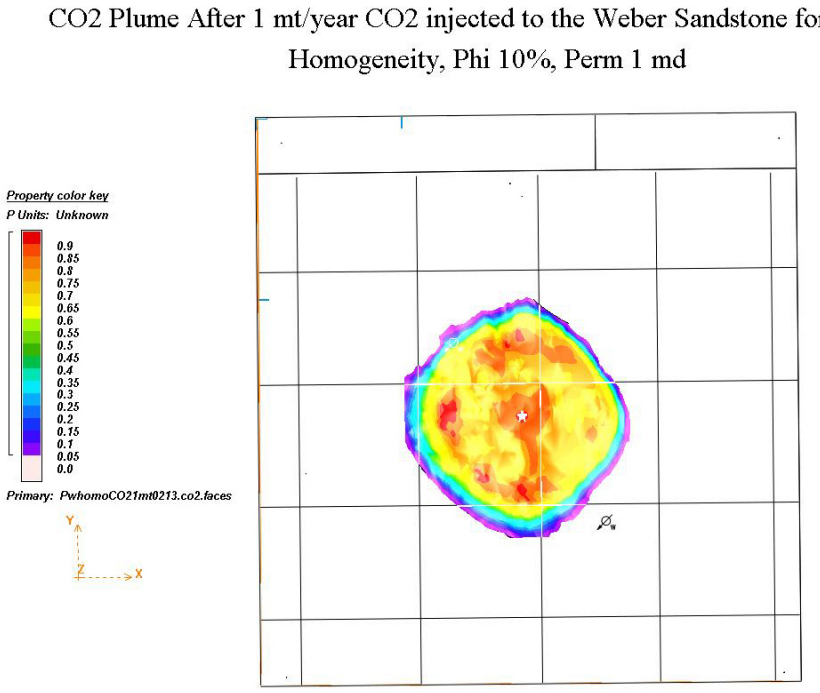


**Figure 5.16:** A map view of the $CO_2$ plume distribution on the top of the Weber Sandstone after 1 MT of $CO_2$ per year for 50 years of injection from the FEHM simulator within seismic survey area. The plume is circle-shaped with a radius of 1,600 m. The white five-pointed star is the location of injection well.

*$CO_2$ Interfacial Tension and Contact Angle*- With an increase in $CO_2$-EOR and carbon storage demonstration projects, the importance of sealing capacity relative to $CO_2$ interfacial tension and wetting angles are slowly being highlighted (Chun and Wilkinson, 1995; Yang et al., 2005; Dickson et al., 2006; Chalbaud et al., 2009; Chiquet et al. 2007; Espinoza and Santamarina 2010; Wollenweber et al., 2010; Daniel et al., 2008; Buursink et al., 2011; Nielsen et al., 2012; Silva et al., 2012; and Edlmann et al., 2013). These studies indicate that sealing capacity increases as pore-throat size decreases, interfacial tension between $CO_2$ and brine increases, and the contact angle of the $CO_2$-rock system decreases.

The existing experimental data has shown that $CO_2$/water interfacial tension values decrease significantly with increased reservoir pressure (Hildenbrand et al., 2004, Chiquet et al., 2007, Espinoza et al., 2010, Wollenweber et al., 2010, and Edlmann et al., 2013). The tension values fall in the range of 20-35 mN/m; and pressures fall in the range of 6-20 MPa at temperatures below 25°C. Espinoza and Santamarina (2010) reported that the interfacial tension between $CO_2$ and water starts at ~72 mN/m at 0.1 MPa and 21.85 °C, and decreases linearly at a rate of ~7 mN/m per MPa increase until the liquid-vapor boundary (~6.43 MPa at 24.85 °C). Thereafter, the interfacial tension remains nearly constant at 20-30 mN/m after $CO_2$ liquefies. The $CO_2$/brine interfacial tension could increase by a few mN/m in higher salinity formation waters (Massoudi and King, 1975). All $CO_2$/brine interfacial tensions reported in the literature have shown that the $CO_2$/brine interfacial tension is much less than the value of the hydrocarbon/brine interfacial tension under similar pressure and temperature conditions. As shown in equation 2[2], the decreases in the $CO_2$/brine interfacial tension will cause the sealing capacity of a given confining layer with respect to $CO_2$ to be much lower than a similar confining layer with respect to hydrocarbons.

Exposure to supercritical $CO_2$ has been shown to decrease the wetting property (increase the contact angle) of various materials (Yang et al. 2005, Siemons et al. 2007, and Chiquet et al., 2007). An increase of the $CO_2$/rock contact angle (loss of the water-wettability) could decrease, even cancel, the confining layer's capillary-sealing efficiency with respect to trapping of injected $CO_2$ (Chiquet et al., 2007). Chiquet et al. (2007) measured the $CO_2$ contact angle on mica and quartz with various NaCl concentrations in the water phase. Their results show that at low pressure, contact angles range from 10 to 30° for both mica and quartz. Increasing the pressure to 11 MPa increases the contact angle to 60° for mica and 35° for quartz. The impact of brine salinity on the wettability is limited in quartz and reduces the water wettability of mica (~25° increase when the brine salinity is increased from 0.1 to 1 m NaCl at fixed pressure (Chiquet et al., 2007).

As the pore throat radius are inversely proportional to the capillary pressure, the interfacial tension between the brine and $CO_2$ and the contact angle between $CO_2$ and rocks will directly affect the sealing capacity of the caprocks.

*Determining sealing capacity of the confining layers*- The petroleum industry has used mercury injection capillary pressure analyses extensively to determine the effectiveness of the sealing

[2] $Pc = \frac{2\gamma\cos\theta}{r}$

capacity in relation to hydrocarbon column height. This technology, with modification, can be applicable in estimating the sealing capacity of a confining layer for geological $CO_2$ storage. The magnitude of the capillary pressure in any hydrocarbon-water-rock system is determined by the largest radius of pore throats, hydrocarbon-water interfacial tension, and the contact angle of hydrocarbon and water against the pore wall (wettability). Therefore, interfacial tension and wettability have a significant effect on the sealing capacity. The sealing capacity assessment of confining layers of a geological $CO_2$ storage reservoir must consider interfacial tension and wettability changes in the $CO_2$-water-rock system. The sealing capacities for multiple sealing stratums for the RSU have been calculated using high-pressure mercury injection data, interfacial tension, and wettability data for a $CO_2$-water-rock system[2].

Confining layers at the study site exceed 2,500 meters of depth. Based on the parameters discussed in the previous section for supercritical $CO_2$, the interfacial tension of 25 mN/m and contact angle of 60° were applied to convert the mercury-air entry pressure to reservoir $CO_2$/brine entry pressure. The interfacial tension and contact angle for oil-brine reservoir conditions are 30 mN/m, and 30° respectively; and the interfacial tension and contact angle for gas-brine at reservoir conditions are 50 mN/m, and 0°, respectively.

A total of 25 samples were sent to Core Laboratory or Intertek Laboratory for high-pressure (up to 60,000 psi) mercury injection tests. Using Schowalter's equation (1979) and the above parameters, the mercury capillary pressure values are converted to subsurface hydrocarbon-water or $CO_2$-water capillary pressure values. The results for $CO_2$/brine, oil/brine, and gas/brine for various confining layer at the RSU geological $CO_2$ storage site are shown in **Table 5.1**.

**Table 5.1:** Laboratory entry pressures and reservoir entry pressures of confining layers, RSU.

| | Interral | | Sample | Grain | Porosity | Entry Pressure (lab) | | | Entry Pressure (res) | | |
|---|---|---|---|---|---|---|---|---|---|---|---|
| Sample | Depth | Formatio | Type | Density | Helium | A-Hg | G-W | O-W | G-W | O-W | scCO2-W |
| ID | ft | ID | | g/cc | % | psi | psia | psia | | | |
| **Containment Layer** | | | | | | | | | | | |
| 214.00 | 12333.90 | Madison 1 | Core Plug | 2.83 | | 3630.11 | 703.49 | 406.16 | 488.53 | 253.85 | 122.13 |
| 206.00 | 12301.00 | Madison | Core Plug | 2.80 | | 3000.00 | 581.38 | 335.66 | 403.73 | 209.79 | 100.93 |
| 16.00 | 10656.40 | Red Peak | Core Plug | 2.60 | 1.00 | 2719.00 | 526.92 | 304.22 | 365.92 | 190.14 | 91.48 |
| 18.00 | 10682.10 | Red Peak | Core Plug | 2.60 | 1.20 | 1521.00 | 294.76 | 170.18 | 204.69 | 106.36 | 51.17 |
| 53.00 | 12197.40 | Amsden | Core Plug | 2.70 | 5.80 | 1381.00 | 267.63 | 154.51 | 185.85 | 96.57 | 46.46 |
| 59.00 | 12250.00 | Madison | Core Plug | 2.80 | 1.30 | 1254.00 | 243.02 | 140.31 | 168.76 | 87.69 | 42.19 |
| 4.00 | 10605.90 | Red Peak | Core Plug | 2.60 | 1.60 | 1140.00 | 220.92 | 127.55 | 153.42 | 79.72 | 38.35 |
| 45.00 | 11766.80 | Weber | Core Plug | 2.70 | 1.30 | 1034.00 | 200.38 | 115.69 | 139.15 | 72.31 | 34.79 |
| M1 | 8220-8250 | Mowry 2 | Cuttings | 2.50 | | 1032.42 | 200.08 | 115.51 | 138.94 | 72.20 | 34.74 |
| 1.00 | 10601.90 | Red Peak | Core Plug | 2.65 | 1.60 | 939.70 | 182.11 | 105.14 | 126.46 | 65.71 | 31.62 |
| GS1 | 9190-9200 | Gypsum S | Cuttings | 2.59 | | 850.34 | 164.79 | 95.14 | 114.44 | 59.46 | 28.61 |
| M1 | 8130-8160 | Mowry 1 | Cuttings | 2.51 | | 701.03 | 135.85 | 78.44 | 94.34 | 49.02 | 23.59 |
| 176.00 | 11725.90 | WebeR 1 | CoLe Plug | 2.70 | | 576.53 | 111.73 | 64.51 | 77.59 | 40.32 | 19.40 |
| B3 | 7590-7620 | Baxter 3 | Cuttings | 2.49 | | 430.62 | 83.45 | 48.18 | 57.95 | 30.11 | 14.49 |
| B1 | 6300-6330 | Baxter 1 | Cuttings | 2.59 | | 390.42 | 75.66 | 43.68 | 52.54 | 27.30 | 13.14 |
| P2 | 11140-111 | Phosphori | Cuttings | 2.65 | | 389.75 | 75.53 | 43.61 | 52.45 | 27.25 | 13.11 |
| P1 | 11040-110 | Phosphori | Cuttings | 2.71 | | 354.48 | 68.70 | 39.66 | 47.71 | 24.79 | 11.93 |
| B2 | 7680-7710 | Baxter 2 | Cuttings | 2.57 | | 217.25 | 42.10 | 24.31 | 29.24 | 15.19 | 7.31 |

The entry pressures in the $CO_2$-brine system range from 7 to 122 psi, which is about half the entry pressure of an oil-brine system, and one-fourth for a gas-brine system. The best, and primary, confining layers in the storage site are the limestone facies of the upper Madison (122 psi), the Triassic Red Peak siltstone (91 psi), the Amsden Formation (51 psi), and marine facies at the base of the Weber Sandstone (35 psi). Redundant seals, such as the Mowry Shale (entry capillary pressure of 35 psi) are also shown to have high entry pressures (**Figure 5.17**).

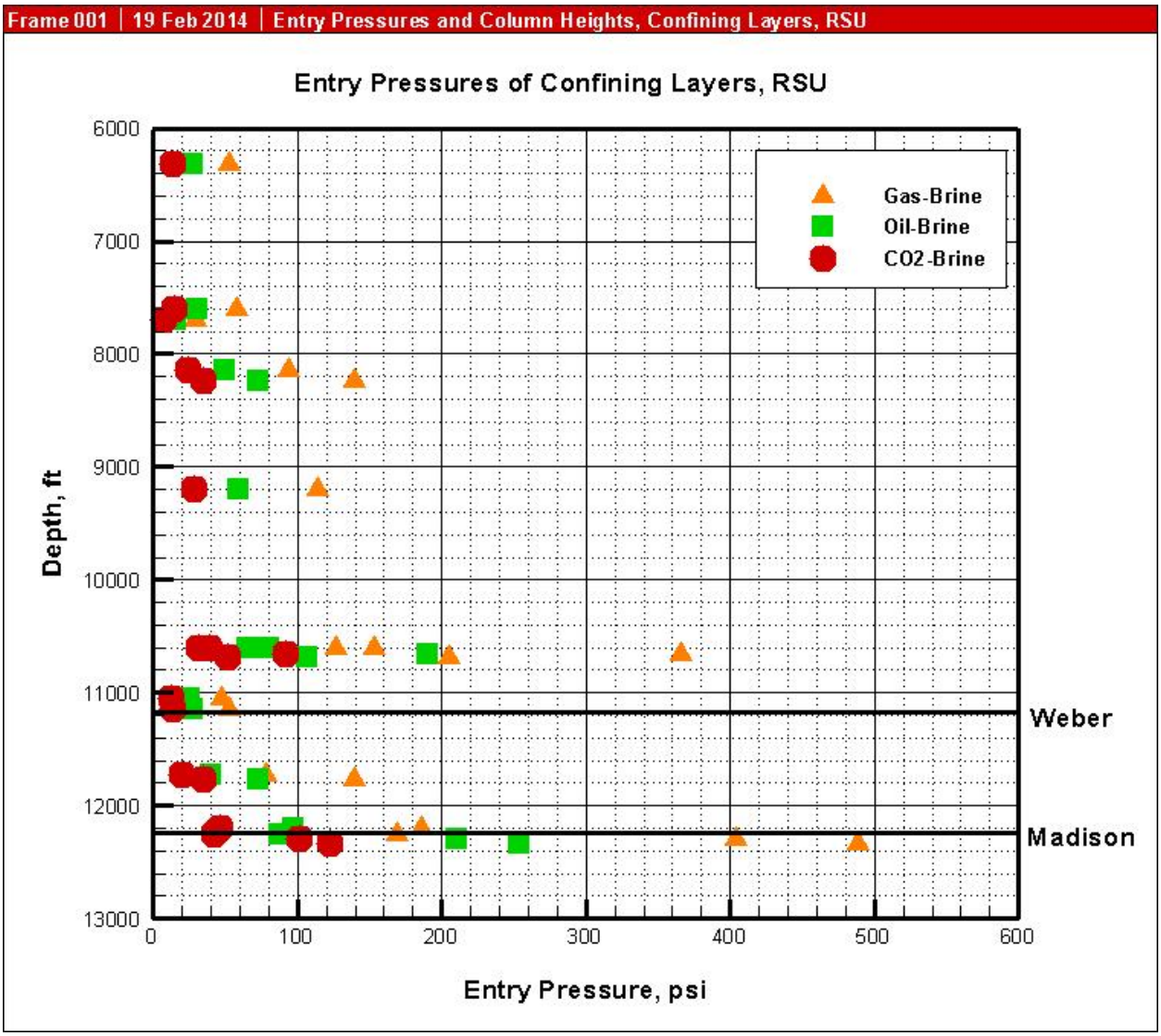


**Figure 5.17:** The $CO_2$-brine and hydrocarbon-brine entry pressures of the confining layers in the $CO_2$-brine-rock and hydrocarbon-brine-rock systems.

*Calculating $CO_2$ column height*- The height of a hydrocarbon or supercritical $CO_2$ column that a confining layer can hold, can be determined by using following equation (Smith, 1966; Schowalter, 1979):

$$H = \frac{\text{Pds} - \text{Pdr}}{(\rho w - \rho co2) * 0.433}$$

where H is the maximum vertical $CO_2$ column in feet above the 100% water level ($CO_2$-water contact) that can be contained by a confining layer; Pds is subsurface $CO_2$-water entry pressure (psi) of the confining layer; Pdr is subsurface $CO_2$-water entry pressure (psi) of the reservoir rock; $\rho$w is the subsurface density (g/cc) of brine; $\rho CO2$ is the subsurface density (g/cc) of the injected supercritical $CO_2$; 0.433 is a unit's conversion factor.

The salinity of the fluid samples from the reservoir intervals is close to 100,000 ppm. The temperature for these targeted reservoirs is over 90 °C. The formation water salinities, pressure and temperatures of the confining layers are assumed to be similar to the reservoir's salinity, pressure, and temperature. Using Schowalter's monographs (1975), the densities are 1.05 g/cm$^3$, 0.75 g/cm$^3$, 0.77 g/cm$^3$ and 0.21 g/cm$^3$ for formation brine, $CO_2$, oil, and gas, respectively. The average $CO_2$/brine entry pressures for the Weber Sandstone and Madison Limestone are 0.73 psi and 0.72 psi, respectively; the average oil/brine entry pressures are 2.39 psi and 2.42 psi, respectively; and the average gas/brine entry pressures are 1.50 psi and 2.91 psi, respectively.

Using Schowalter's equation shown above, the heights of the $CO_2$, oil and natural gas that could be held by various confining layers at the RSU were calculated. The results are shown on Table 5.2 and **Figure 5.18**. The heights of the $CO_2$ that the various confining layers at the RSU could hold range from 53 ft. to 994 ft. The height of the $CO_2$ column held by each confining layer is about half of the value of oil column, and three-quarters of the gas column. The low permeability (>0.001 md) limestone facies at the most upper portion of the Madison Limestone could hold the $CO_2$ column in the Madison Limestone over 900 ft. (average thickness of the Madison Limestone at the RSU study area is 700 ft.). The Amsden Formation just above the Madison Limestone could hold a $CO_2$ column of 375 ft. in the Madison Limestone. The Red Peak Formation, the primary confining layer for the Weber Sandstone reservoir, could hold the $CO_2$ column over 740 ft. (the average thickness of Weber Sandstone at the RSU study area is 400 ft.). The sealing capacity ($CO_2$ column height) of the Cretaceous Mowry Shale and Baxter Shale (over 1000 m thick) ranges from 54 ft. to 279 ft.

The preliminary results from this study suggest that the sealing capacity of a $CO_2$-water-rock system may be significantly lower than previously predicted, based on the numbers used in a hydrocarbon-water-rock system. As previously stated by Li et al., (2006) and Chiquet (2007), it is a risk to assume that a confining layer, if only because it has successfully trapped hydrocarbons over millions of years, will also prevent $CO_2$ leakage. The $CO_2$ injection simulation for the Madison Limestone and Weber Sandstone indicate that the $CO_2$ column heights could rise to 700 ft. in the Madison Limestone and 400 ft. in the Weber Sandstone. This study shows that the multiple confining layers at the RSU geological $CO_2$ site have adequate sealing capacity to safely retain injected $CO_2$.

**Table 5.2:** The heights of $CO_2$ column that confining layers could hold, RSU.

| Sample (ID) | Depth inteval (ft) | Formation | Sample type | Column height within the reservoir | | |
|---|---|---|---|---|---|---|
| | | | | Gas-water (ft) | Oil-water (ft) | $CO_2$-water (ft) |
| 214 | 1233.9 | Madison | Core Plug | 1335.15 | 2072.96 | 994.26 |
| 206 | 12301 | Madison | Core Plug | 1209.58 | 1712.17 | 820.71 |
| 16 | 10656.4 | Red Peak | Core Plug | 1001.93 | 1551.25 | 743.28 |
| 18 | 10682.1 | Red peak | Core Plug | 558.66 | 865.16 | 413.19 |
| 53 | 12197.4 | Amsden | Core Plug | 502.97 | 784.92 | 374.55 |
| 59 | 12250 | Madison | Core Plug | 455.98 | 712.19 | 339.56 |
| 4 | 10605.9 | Red peak | Core Plug | 417.69 | 646.97 | 308.21 |
| 45 | 11766.8 | Weber | Core Plug | 378.47 | 500.98 | 279.01 |
| M1 | 8220-8250 | Mowry | Cuttings | 377.89 | 585.36 | 278.57 |
| 1 | 10601.9 | Red peak | Core Plug | 343.58 | 532.26 | 253.02 |
| GS1 | 9190-9200 | Gypsum Spring | Cuttings | 310.52 | 481.09 | 228.4 |
| MS1 | 8130-8160 | Mowry | Cuttings | 255.27 | 395.58 | 187.26 |
| 176 | 11725.9 | Weber | Core Plug | 209.2 | 324.28 | 152.96 |
| B3 | 7590-7620 | Baxter | Cuttings | 155.22 | 240.72 | 112.76 |
| B1 | 6300-6330 | Baxter | Cuttings | 140.34 | 217.7 | 101.68 |
| P2 | 11140-11170 | Phosphoria | Cuttings | 140.09 | 217.31 | 101.49 |
| P1 | 11040-11070 | Phosphoria | Cuttings | 127.04 | 197.11 | 91.78 |
| B2 | 7680-7710 | Baxter | Cuttings | 76.27 | 118.52 | 53.96 |

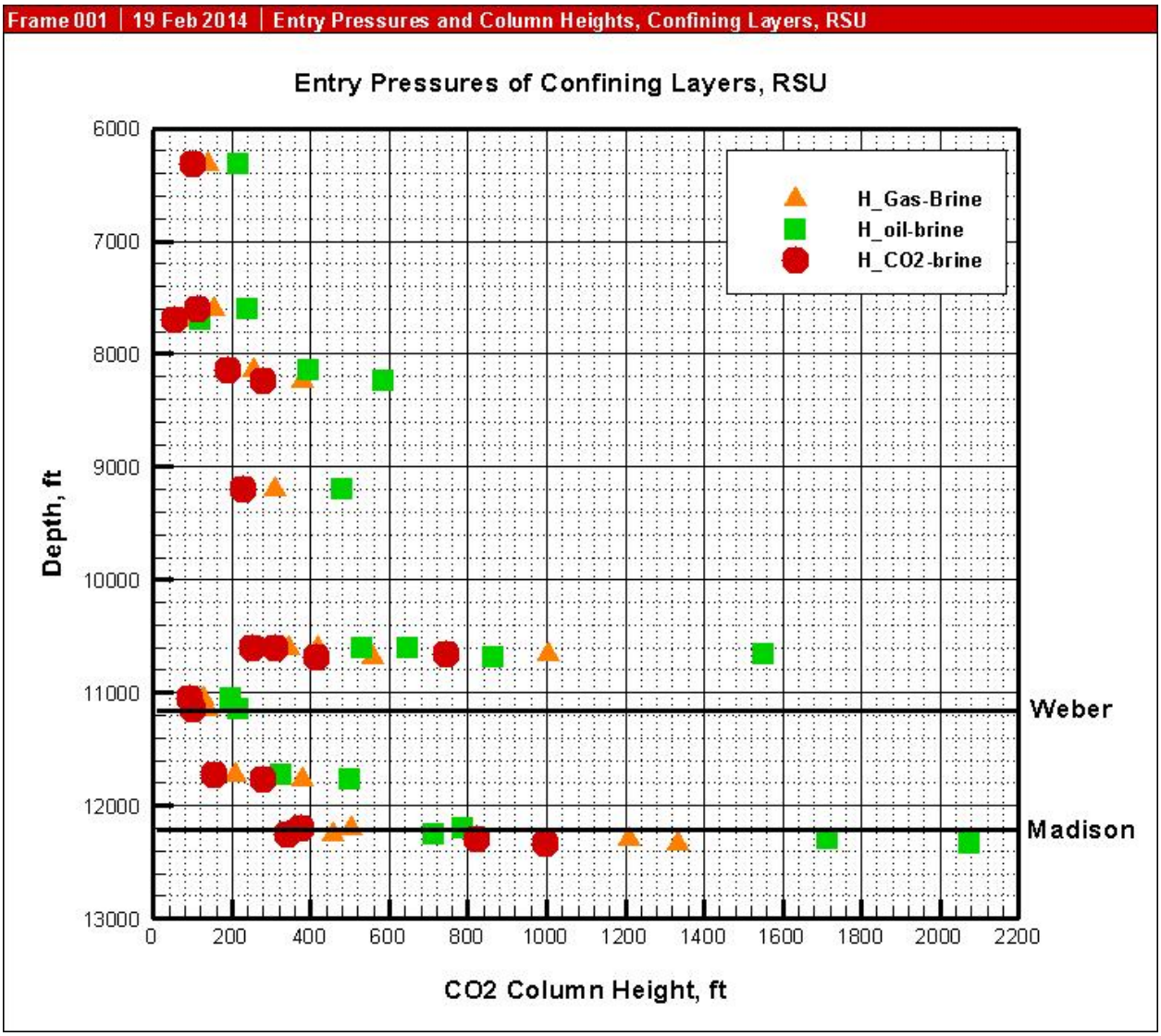


**Figure 5.18:** Plot the calculation results of column heights that confining layers could hold in the $CO_2$-brine-rock and hydrocarbon-brine-rock systems, RSU.

*Sensitivity analyses of critical parameters for determining the sealing capacity*- Predicting the sealing capacity and maximum sustainable column height of an overlying confining layer is an important process to assess the storage capacity of a geologic $CO_2$ storage reservoir. As discussed in the previous section, the sealing capacity and column height are significantly affected by the properties of the confining layer and reservoir rock units. The most important properties include (a) difference in density between formation water and supercritical $CO_2$; (b) contact angle between formation water and $CO_2$; (c) interfacial tension (IFT) between formation water and $CO_2$; and (d) entry pressure/pore throat size of the confining layer. It is necessary to analyze the combined parameter effects on the final sealing capacity and maximum $CO_2$ column height of a specific confining layer.

To complete this task, we performed a sensitivity analysis by varying each parameter independently over a natural range. A Sensitivity Analysis is a "what-if" tool that examines the effect on the sealing capacity and column height when input parameters are increased or decreased. To examine the parameter combination effects, we used Goldsim software to perform a sensitivity analysis. We start by setting the sealing capacity or column height as a function of $CO_2$ and water densities, reservoir entry pressure, confining layer entry pressure, contact angle, and interfacial tension (**Figure 5.19**). Goldsim runs the model multiple times, systematically sampling each variable over the range of each parameter, while holding all of the other variables constant. The results are sensitivity plots showing which parameters sealing capacity and/or column height are most sensitive to.

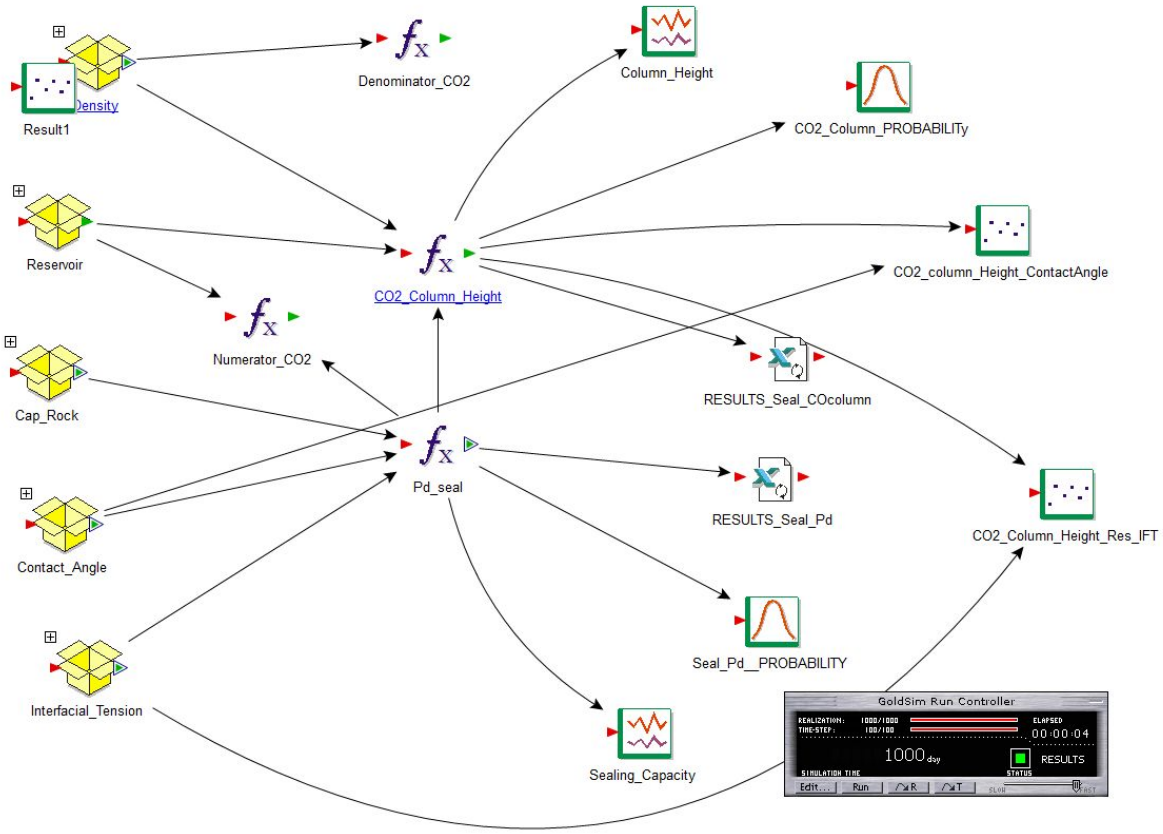


**Figure 5.19:** Goldsim setup for the assessment of the sealing capacity, $CO_2$ column height, and sensitivity analysis of confining layers at the Rock Springs Uplift.

The sealing capacity and maximum column height is directly proportional to $CO_2$ density and capillary pressure (inversely proportional to pore throat size). For the limestone facies of the upper Madison Limestone, we set the natural range of $CO_2$ densities (0.6 to 0.85 g/cm3) and keep all other parameters constant (40° contact angle, 32 mN/m IFT, and 50 nm pore diameter). The simulation suggests that the maximum column height increases by a factor of 1.4. For the natural range of cap-rock pore diameters (5 to 150 nm), maximum column height ranges over an order of magnitude. Therefore, maximum column height increases significantly if either pore throat size decreases or $CO_2$ density increases over natural ranges. The maximum column height is also directly proportional to IFT and cosine of the contact angle. For the natural range of IFT (10 to 60 mN/m) and holding all other parameters constant (0.725 g/cm3 $CO_2$ density, 0.75

cosine contact angle, and 50 nm/m pore diameter), column height increases 5 fold (**Figure 5.20**). In the sensitivity analysis for the natural range of cosine contact angle (0.5 to 0.94), maximum column height increases about 2 fold (**Figure 5.21**).

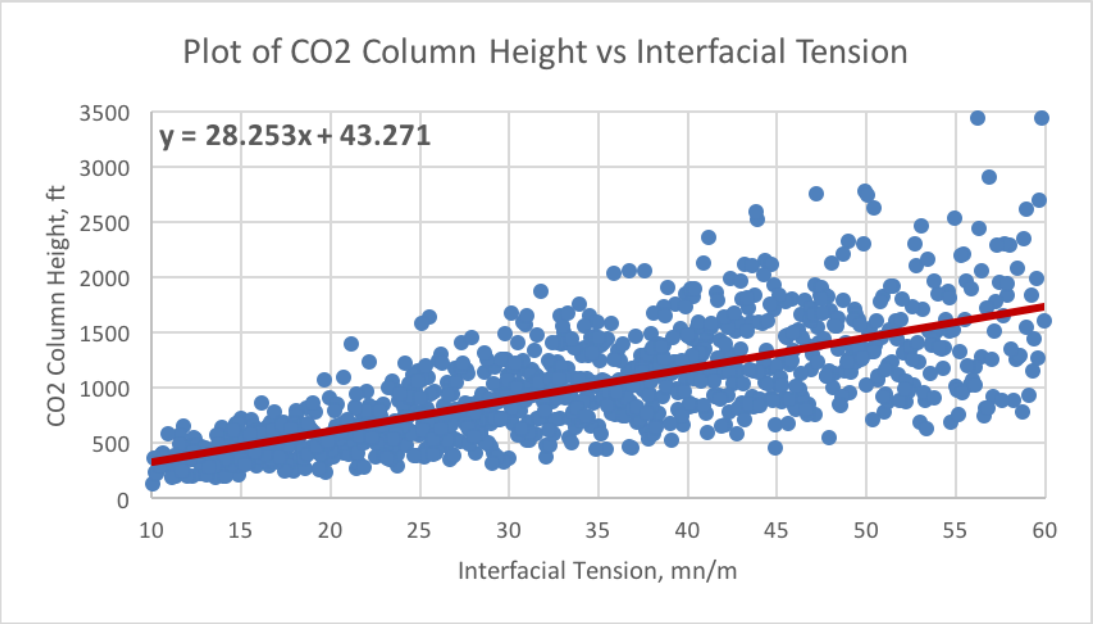


**Figure 5.20:** Plot of $CO_2$ column height vs. $CO_2$/water interfacial tension for the upper Madison Limestone as a regional confining layer (1000 realizations).

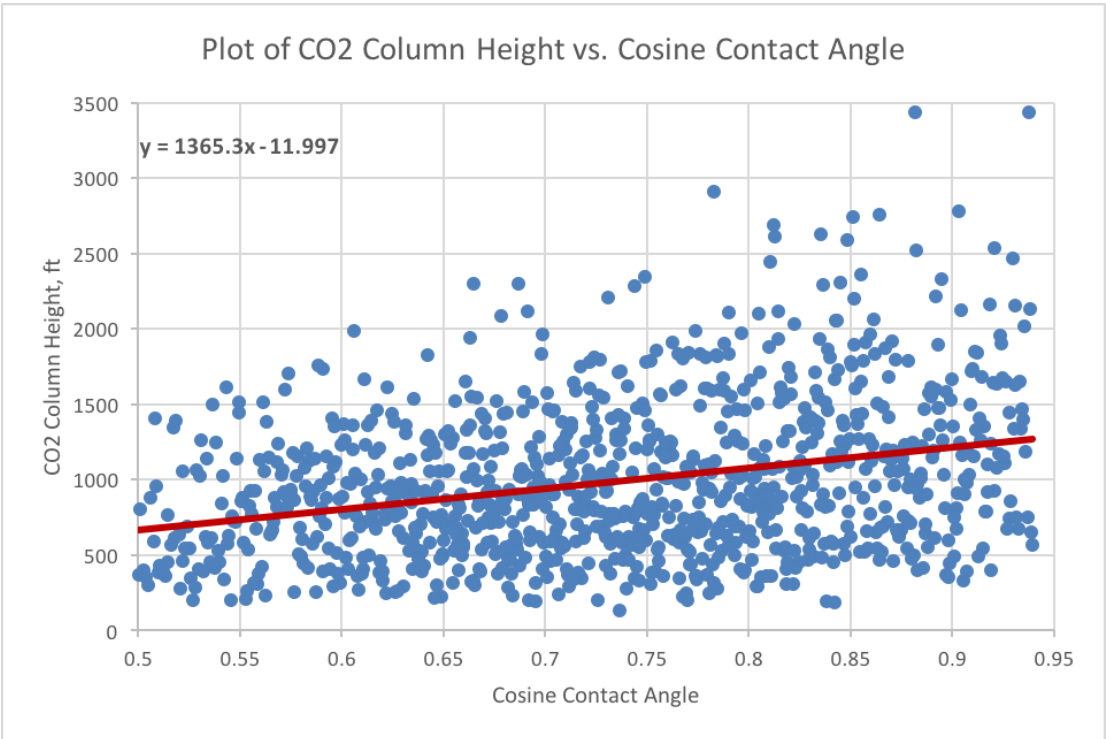


**Figure 5.21:** Plot of $CO_2$ column height vs. $CO_2$/cosine contact angle for the upper Madison Limestone as a regional confining layer (1000 realizations).

**Figure 5.22** is a tornado chart derived from sensitivity analysis for the sealing capacity (displacement pressure) of the upper Madison Limestone. The chart shows that the sealing capacity of the upper Madison Limestone is most sensitive to the changes of the $CO_2$-water interfacial tension at reservoir conditions and the accuracy of the lab measured displaced pressure of the confining layer. For the $CO_2$ column height calculation, we find that it is most sensitive to the $CO_2$-water interfacial tension and $CO_2$ and water density differences (**Figure 5.23**).

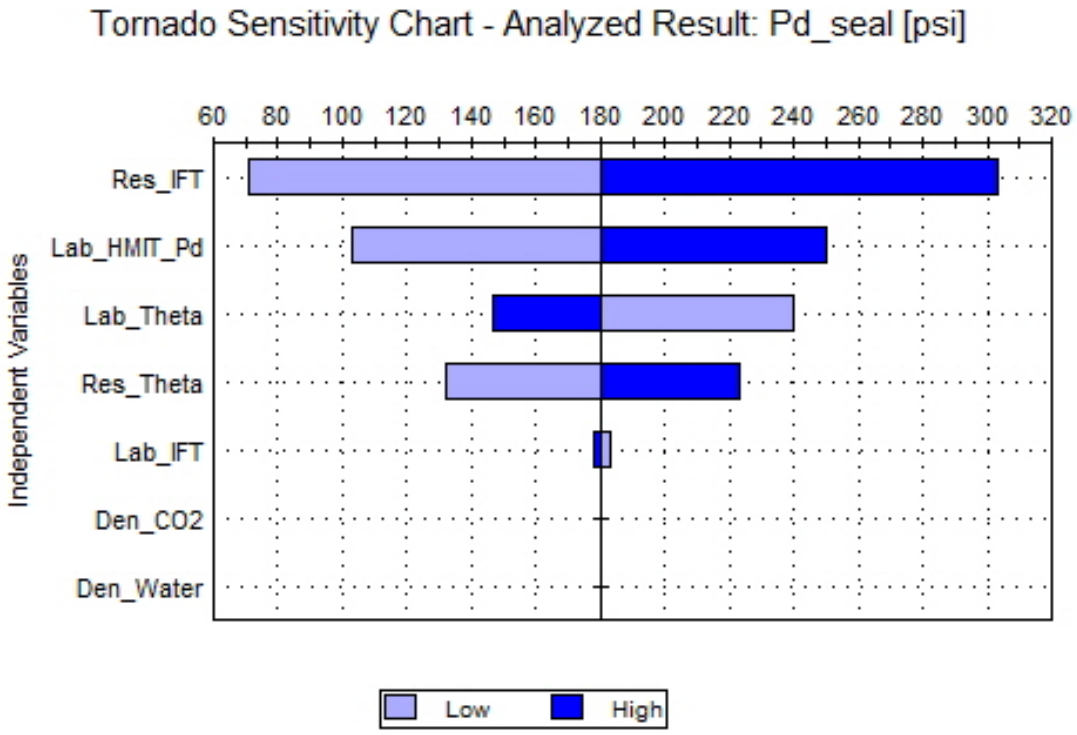


**Figure 5.22:** The tornado chart shows the results from a sensitivity analysis for sealing capacity estimation for the upper Madison Limestone.

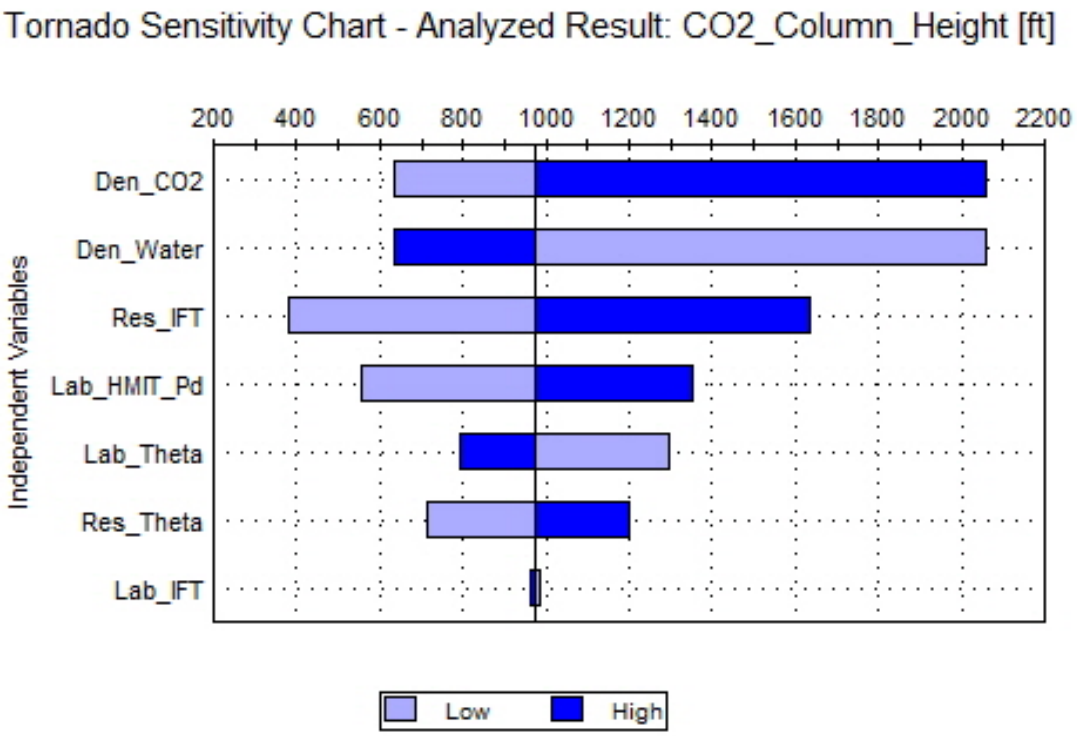


**Figure 5.23:** The tornado chart shows the results from a sensitivity analysis for $CO_2$ column height for the upper Madison Limestone.

## Conclusion

The low solubility of $CO_2$ and slow dissolution rate in water indicates that the time necessary to dissolve the injected $CO_2$ into the brine is expected to be much longer than the injection period (i.e., 50 years, a typical life span for a coal-fired power plant). Subsequently, a majority of the injected $CO_2$, over 90% in first few hundred years, will remain at free-supercritical phase and rise buoyantly to the top of the reservoir, accumulating beneath the low-permeability confining layers. Migration through the water saturated pore network of the confining layer may occur when the $CO_2$ fluid pressure in the reservoir exceeds the capillary entry pressure of the confining layers. Therefore, determining the sealing capacity of the confining layer is key to safely trapping $CO_2$ for the long term (i.e., several hundred years), and becomes one of the critical issues for assessing the storage capacity of the geological $CO_2$ storage site.

An integrated approach was used to characterize the heterogeneities in porosity and permeability for confining layers. The high vertical resolution core measurement data and log data were used to constrain and generate the reservoir and seal heterogeneity property model based on attribute analysis results from the Jim Bridger 3-D seismic survey. The approach is as follows:

- First, the litho-facies are determined for each formation based on detailed core descriptions and petrographic observations.
- Second, the selected core samples from each litho-facies are measured for porosities and permeabilities under in-situ conditions.
- Third, the log porosity is calibrated with the laboratory measured core porosities.

- Fourth, the relationship between the porosity and acoustic velocity is derived from all available logs and measured core data for each formation.
- Fifth, the three dimensional porosity distribution of the RSU $CO_2$ storage site is populated using the velocity volume of the Jim Bridger 3-D seismic survey (modeling domain) and the function between the porosity and acoustic velocity derived from the well logs. Once spatial distributions of porosity in the modeling domain have been populated, permeability spatial distributions are obtained based on empirical correlation between porosity and permeability.
- Then, 3-D numerical simulations of $CO_2$ injection into the Weber Sandstone and Madison Limestone using the heterogeneous reservoir properties are conducted with a finite element multiphase flow simulator, FEHM. The maximum storage pressure is set to 65 percent of the fracture gradient of the containment formations for all $CO_2$ injection scenarios.

The results of the simulations are as follows. The plume of 1 Mt $CO_2$ after 50 years of a single well injection in the Weber Sandstone is nearly a circle with radio of 1600 m, covering an area of 8 $km^2$. The $CO^2$ plume with saturations from 0.05% to 0.9% occupies a space of 1.2 $km^3$. The total volume of the Weber Sandstone above depth of 5,000 m within the RSU is 412 $km^3$. Therefore, if all Weber Sandstone is used for the storage in the RSU, its storage capacity could be 17 Gt of $CO_2$. The column height of supercritical $CO_2$ could rise to 400 feet in the Weber Sandstone and 700 feet in the Madison Limestone without leakage.

Because limited borehole data are used to retrieve geostatistical parameters describing the spatial heterogeneities of porosity and permeability in targeted geological formations at the RSU, a question may reasonably arise about how representative the limited borehole data used are. On the basis of the vertical extension of the borehole data used here, the vertical heterogeneities are more fully captured than the horizontal ones. Combined with regional geological information and detailed 3-D seismic attribute analyses, we believe the spatial heterogeneities in both the vertical and horizontal directions within the modeling domains are accurately captured.

The entry pressures in the $CO_2$-brine system for the confining layers in the RSU geological $CO_2$ storage site range from 7 psi to 122 psi, and is about half of the values in the oil-brine system, one-fourth of the values in the gas-brine system. Generally, the entry pressures increase with burial depth. The best confining layers in the storage site are the limestone facies of the upper Madison Limestone (122 psi), the Red Peak siltstone (91 psi), the Amsden limestone (51 psi), and the fine grain marine facies of the Weber Sandstone at (35 psi). The Mowry shale at a depth of 8220 feet has an entry capillary pressure of 35 psi.

The heights of the $CO_2$ column of the various confining layers at the RSU range from 53 ft. to 994 ft. The $CO_2$ column height in a particular confining layer is about half of the value of the oil column, and three-quarters of the gas column. The low permeability (>0.001 md) limestone facies in the upper Madison Limestone could hold the $CO_2$ column in the Madison over 900 ft. (average thickness of the Madison Limestone at the RSU study area is 700 ft.). The Amsden Formation just above the Madison Limestone could hold the $CO_2$ column of 375 ft. in the Madison. The Red Peak Formation, the primary confining layer for the Weber

Sandstone reservoir, could hold the $CO_2$ column over 740 ft. (the average thickness of Weber Sandstone at the RSU study area is 400 ft.).

The sealing capacity ($CO_2$ column height) of over 3200 ft. of the potential Cretaceous confining layers including the Mowry and Baxter Shales ranges from 54 ft. to 279 ft. On the basis of these results the sealing capacity of a $CO_2$-water-rock system may be significantly lower than previously predicted, based on the numbers used in a hydrocarbon-water-rock system. However, the $CO_2$ injection simulation for the reservoirs of the Madison Limestone and Weber Sandstone indicate that the multiple confining layers at the RSU geological $CO_2$ site have adequate sealing capacity to safely hold high columns of the injected $CO_2$.

The sensitivity analysis results show that the sealing capacity of the upper Madison Limestone is most sensitive to the changes of the $CO_2$-water interfacial tension at reservoir conditions. The $CO_2$ column height is more sensitive to the $CO_2$-water interfacial tension, and $CO_2$ and water density differences.

# Task 6: Simulations of formation brine production to assess wellbore scaling/well integrity and surface treatment

## Overview

This study was conducted to model brine production for pressure management for CCS in the Rock Springs uplift. The objective of the study was to identify possible scale and corrosion problems. The production scheme calls for high pressure brine to be produced from the Madison and Weber formations. The produced brine would be treated at the surface to provide fresh water and allow for production of economic metals (**Figure 6.1**). The surface treatment scheme is assumed to be nanofiltration (NF) and reverse osmosis (RO). In order to optimize the NF/RO equipment, a production pressure of around 1,200 psi is required to be maintained at the wellhead.

Three subtasks were conducted to meet the objective:

- *Subtask 6.1*—Simulate and evaluate wellbore scaling issues
- *Subtask 6.2*—Evaluate the effect of brine chemistry on well construction and casing integrity
- *Subtask 6.3*—Evaluate the effects of brine chemistry on produced water treatment infrastructure

The series of steps required to complete these tasks were:

1. Size production tubing using site-specific fluid data.
2. Use the selected tubing size to calculate fluid profiles (flow velocity, flow volume, pressure, and temperature profiles) along the well.
3. Use the flow profiles in conjunction with site-specific geochemistry data to model potential scale in tubing and surface equipment.
4. Use the flow profiles in conjunction with site-specific geochemistry data to model corrosion potential in tubing and surface equipment.

The scale modelling was conducted using OLI's ScaleChem software. CMI provided brine data from the Madison and Weber formations as inputs for ScaleChem.

This report is divided into sections describing the production well modeling, injection well modeling, the ScaleChem modeling, the corrosion modeling, and conclusions.

## Executive Summary

This Task investigated modeling brine production for pressure management at CCS sites. The objective of the study was to identify possible scale and corrosion issues associated with reservoir pressure management. The production scheme calls for high pressure brine to be produced from the Madison and Weber formations. The produced brine will be treated at the surface to provide fresh water and allow production of lithium present in the brine (**Figure 6.1**). The treatment scheme is likely to be nanofiltration and reverse osmosis. In order to run the NF/RO equipment a production pressure of around 1,200 psi is required at the wellhead. Three tasks were conducted to meet the objective:

- *Subtask 6.1*—Simulate and evaluate wellbore scaling issues
- *Subtask 6.2*—Evaluate the effect of brine chemistry on well construction and casing integrity
- *Subtask 6.3*—Evaluate the effects of brine chemistry on produced water treatment infrastructure

Data collected at CMI's RSU#1 well, data from CMI's reservoir model, and assumptions about the project requirements were provided as inputs to the models. These data were used as inputs to models created using PIPESIM* 2012 or 2013. A production/injection rate of 1,000,000 tonnes per year (31.7 kg/s) was assumed.

The results of Task 1 suggest a well design with a 5-inch tubing string, a 7 5/8-inch production casing, and a 10 ¾ surface casing. The PIPESIM modelling indicates that a minimum of three production wells will be needed to meet the 1,000,000 tonne per year production rate. The brine modelling using OLI ScaleChem indicates that wellbore scale will primarily be calcium carbonate.

The results of Task 2 show exposure to brines likely causes either generalized or pitting corrosion for mild steel, 13-chrome steel, and 304 stainless steel. The results showed that 2205 duplex steel is not likely to corrode. Although 2205 duplex steel performed best, 13-chrome and 304 stainless steel should be considered and evaluated using a cost benefit analysis.

Task 3 required extending the models by adding surface equipment in PIPESIM, ScaleChem, and Corrosion Analyzer. The extended model results were very similar to the model results for the well corrosion models developed for Task 2; the scale and corrosion results for the wellbore apply to the surface equipment before the treatment system.

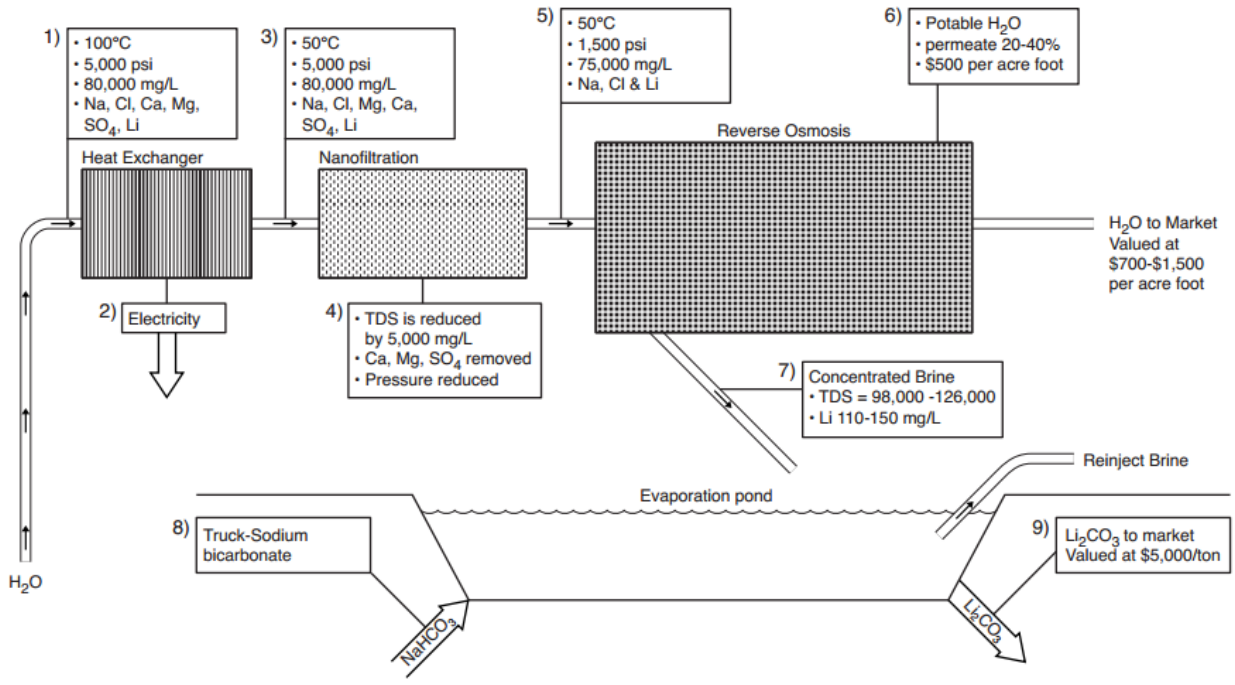


**Figure 6.1:** RSU Brine Production Treatment Scheme (Surdam et al., 2011)

## Methods

*Production Well Sizing and Design-* As a prerequisite to completing all of the subtasks under this task a model production well had to be sized as a basis for estimating pressure, temperature, and flowrate data used in the scale and corrosion modeling. Schlumberger's PIPESIM was used to size the well. PIPESIM is a steady-state, multiphase flow simulator used for the design and diagnostic analysis of oil and gas production and injection systems. The software tools can model multiphase flow from the reservoir to the wellhead. In addition, it can also analyze flowline and surface facility performance to generate comprehensive production system analysis.

Data collected at CMI's RSU#1 well provided inputs to the PIPESIM 2012 and 2013 models that were used to size the tubing (**Table 6.1**). In addition, a production and injection rate of 1,000,000 tonnes per year (31.7 kg/s) was assumed as an injection/production parameter.

**Table 6.1:** Basic data from RSU#1

| | **Weber Sandstone** | **Madison Limestone** |
|---|---|---|
| Depth of target zone (ft)[1] | 11,390 to 11,420 | 12,330 to 12,420 |
| Temperature (°f)[2] | 198 | 204 |
| Pressure (psia)[3] | 7,250 | 9,570 |
| kxy (mD)[2] | 1 | 10 |

1. Baker Hughes, (2013), "Well Intervention End of Report: RSU #1"
2. Baker Hughes, (2011), "Reservoir Characterization Instrument (RCI) Mini-DST/VIT Analysis
3. Personal communication with CMI, (2014)

PIPESIM was used to conduct a nodal analysis to size production well tubing. For each tubing size, the nodal analysis model calculated the possible inflow flowrate and the possible outflow flowrate and identifies where the two flowrates intersect, which is the operating point (called a node) of the well. Examining how the operating point varies with tubing size identifies the selection of tubing sizes that meet the projects requirements.

The nodal analysis was conducted using the data from **Table 6.1**, a wellhead pressure of 1,200 psi, and a well with 7-inch 23lb/ft as a starting point and then varying the tubing size between 2.375- and 9.625-inches (**Table 6.3**). The nodal analysis point was selected above the upper set of perforations to ensure that all flow from both formations was counted in the total mass flowrate. The initial well tubing, casing, packer, and depth and size data are shown in **Table 6.2** and **Figure 6.2**.

**Table 6.2:** Production well data parameters

| | **Casing** | **Tubing** |
|---|---|---|
| OD (in) | 9.625 | 7 |
| Thickness (in) | 0.395 | 0.453 |
| Weight (lb/ft) | 40 | 32 |
| Perforation Depth (ft) | 11,390-11,420 and 12,330-12,420 | - |
| Packer Depth (ft) | 11,200 | 11,200 |
| Setting Depth (ft) | 12,500 | - |

**Table 6.3:** Tubing sizes used for nodal analysis

| OD (inches) | ID (Inches) | Linear mass (lb/ft) |
|---|---|---|
| 2.375 | 1.867 | 5.95 |
| 2.875 | 2.259 | 8.60 |
| 3.5 | 2.992 | 9.20 |
| 4 | 3.548 | 9.50 |
| 4.5 | 4 | 11.60 |
| 5 | 4.408 | 15.00 |
| 5.5 | 4.892 | 17.00 |
| 6.625 | 5.921 | 24.00 |
| 7 | 6.366 | 23.00 |
| 7.625 | 6.969 | 26.40 |
| 8.625 | 8.017 | 28.00 |
| 9.625 | 8.921 | 36.00 |

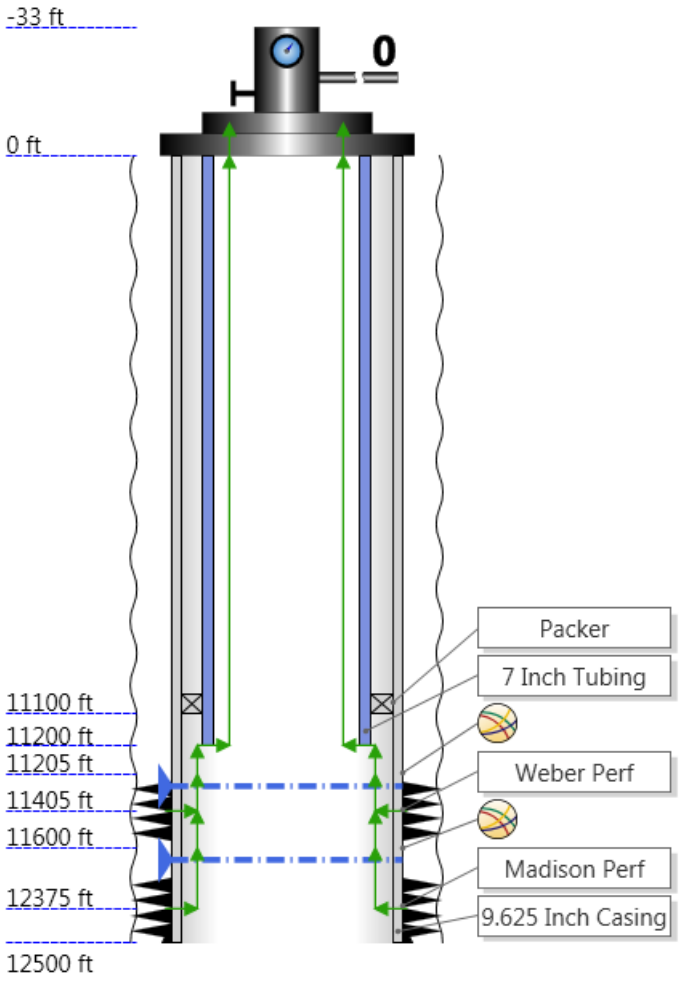


**Figure 6.2:** Schematics for the modeled production well

The tubing size for brine and corrosion modeling was selected from the nodal analysis and used to back out the casing sizes required in the well. The production and surfacing sizes were selected using the chart shown in **Figure 6.3**. PIPESIM was used to calculate the temperature and pressure profiles along the wellbore and the average mass flowrate of the brine as inputs into the scale and corrosion models.

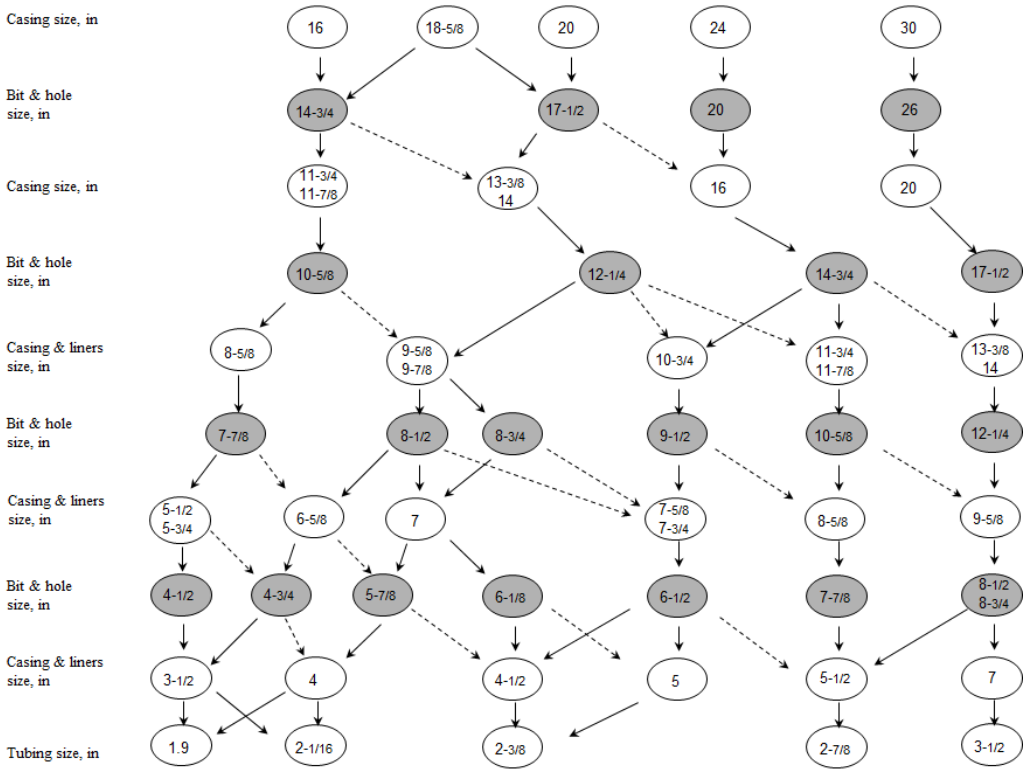


**Figure 6.3:** Casing and bit size selection chart

*Injection Well Sizing*- The injection well model used the same tubing sizes, setting depths, and geologic data as in the production well. However, instead of producing brine a pure $CO_2$ stream was modeled as the reacting fluid. The density of the fluid was initially estimated to have an average gradient of about 2/3 the gradient of water, or 0.29 psi per foot, requiring a wellhead pressure of 6,000 psi to overcome the formation pressure and allow injection. Therefore, wellhead pressures between 6,000 and 7,000 psi were modeled.

*Wellbore Scaling Issues: Subtask 6.1*- Modeling for Subtask 6.1 was completed using the flow data based on modelling of the tubing selected from the production well nodal analysis. Wellbore scale and scaling potential was modeled using OLI's ScaleChem electrolyte modeling software. The software was used to create PVT files governing the families of salts that could precipitate from the ions represented in the brines from RSU #1 (**Table 6.4** and **Table 6.5**). The system was modelled for two different brine chemistries collected in 2011 and 2012. For the 2011 and 2012-data the brine was assumed to be flowing at the average velocity inside the tubing from the PIPESIM production simulations. The brine in the wellbore was assumed to be a mixture of the

Madison and Weber brines. The ionic concentrations of the mixture were calculated based on the ratio of flow out of one production zone when the other zone was turned off in the model.

**Table 6.4:** Brine data from samples collected in 2011

| | **Weber Formation Energy Labs (08/27/2011)** | **Madison Limestone Energy Labs (08/27/2011)** |
|---|---|---|
| **Major Ions** | | |
| Alkalinity, Total as $CaCO_3$ (mg/L) | 509 | 1170 |
| Bicarbonate as $HCO_3$ (mg/L) | 621 | 1420 |
| Calcium (mg/L) | 734 | 1190 |
| Chloride (mg/L) | 60,900 | 50,300 |
| Flouride (mg/L) | 11.5 | 3.5 |
| Magnesium (mg/L) | 37 | 158 |
| Nitrogen, Ammonia as N (mg/L) | 33.4 | 42 |
| Potassium (mg/L) | 0 | 0 |
| Sodium (mg/L) | 40,700 | 29,000 |
| Strontium (mg/L) | 0 | 0 |
| Sulfate (mg/L) | 11600 | 2,800 |
| **Non-Metals** | | |
| Sulfide as hydrogen sulfide (mg/L) | 0.04 | 29 |
| **Metals** | | |
| Aluminum (mg/L) | 0 | 0 |
| Barium (mg/L) | 0 | 1 |
| Copper (mg/L) | 0 | 0 |
| Iron (mg/L) | 0.94 | 0.54 |
| Lead (mg/L) | 0 | 0 |
| Zinc (mg/L) | 0.26 | 0.4 |

**Table 6.5:** Brine data from samples collected in 2012

| | Weber Formation Energy Labs (12/14/12) | Madison Limestone Energy Labs (12/03/12) |
|---|---|---|
| **Major Ions** | | |
| Alkalinity, Total as CaCO3 (mg/L) | 3030 | 2620 |
| Bicarbonate as HCO3 (mg/L) | 3690 | 3190 |
| Calcium (mg/L) | 539 | 1630 |
| Chloride (mg/L) | 57,400 | 51,600 |
| Flouride (mg/L) | 6.1 | 2.8 |
| Magnesium (mg/L) | 45 | 195 |
| Nitrogen, Ammonia as N (mg/L) | 33.1 | 39 |
| Potassium (mg/L) | 1,910 | 3,780 |
| Sodium (mg/L) | 36,500 | 27,900 |
| Strontium (mg/L) | 14 | 51.1 |
| Sulfate (mg/L) | 6030 | 1,820 |
| **Non-Metals** | | |
| Sulfide as hydrogen sulfide (mg/L) | 127 | 87 |
| **Metals** | | |
| Aluminum (mg/L) | 3.5 | 1.9 |
| Barium (mg/L) | 14.3 | 4.48 |
| Copper (mg/L) | 13.6 | 1.35 |
| Iron (mg/L) | 44.1 | 32.2 |
| Lead (mg/L) | 2.91 | 0.305 |
| Zinc (mg/L) | 4.58 | 2.1 |

*The effect of brine chemistry on well construction and casing integrity: Subtask 6.2-* The corrosion modelling required in Subtask 6.2 built upon the three previous Subtasks. Potential corrosion of the wellbore tubing was modeled to understand how different alloys behave under flowing and shut-in conditions with either the 2011 or 2012 brine regimes. The modeling was conducted using OLI's Corrosion Analyzer. The flowing corrosion analysis assumed the brine was flowing at the average velocity inside the tubing based in the earlier PIPESIM simulations. The temperatures of the points modeled for the flowing corrosion simulation were calculated using the pressure-temperature profile simulation in PIPESIM. The shut-in pressure was assumed to be the reservoir pressure at the bottom of the well decreasing hydrostatically to the wellhead. The temperature used in the shut-in simulation was calculated using the temperature gradient provided for the area assuming that the temperature stabilized after flow stopped. **Table 6.6** provides the depths and respective temperatures used in the corrosion models.

**Table 6.6:** True vertical depth (TVD) and respective temperature data for flowing and shut-in corrosion simulations

| True Vertical Depth (ft) | Flowing Temperature (Degrees f) | Shut-in Temperature (Degrees f) |
|---|---|---|
| 12,375 | 211 | 204 |
| 11,405 | 198 | 198 |
| 11,200 | 198 | 196 |
| 11,000 | 198 | 193 |
| 10,000 | 197 | 180 |
| 9,000 | 195 | 167 |
| 8,000 | 192 | 154 |
| 7,000 | 188 | 141 |
| 6,000 | 184 | 128 |
| 5,000 | 179 | 115 |
| 4,000 | 173 | 102 |
| 3,000 | 167 | 89 |
| 2,000 | 160 | 76 |
| 1,000 | 153 | 63 |
| 0 | 145 | 50 |

Corrosion was modeled for flowing and shut-in conditions in mild steel, 13-chrome steel, 304 stainless steel, and 2205 duplex steel materials. Mild steel and 13-chrome steels are very common oilfield materials. 304 stainless steel and 2205 duplex steels are not very common but are used for special applications.

*The effect of brine chemistry on produced water treatment infrastructure: Subtask 6.3*- To model the effect of brine and corrosion the PIPESIM model used for the production well modeling was modified by adding the surface equipment required to model nano-filtration and reverse osmosis processes (NF/RO). The model used one third of the overall design mass flow rate for the brine, 333,333 tonnes/year, as the design mass flow rate. The additional components of the model consisted of a flowline to transport the brine to the NF/RO system and the NF/RO system. **Figure 6.4** shows a schematic of the system that was modeled. Although a heat exchanger was initially planned for the model, the temperature of the brine at the wellhead and along the flow line was within the range of commercial NF/RO systems suggests that no cooling of the brine was needed.

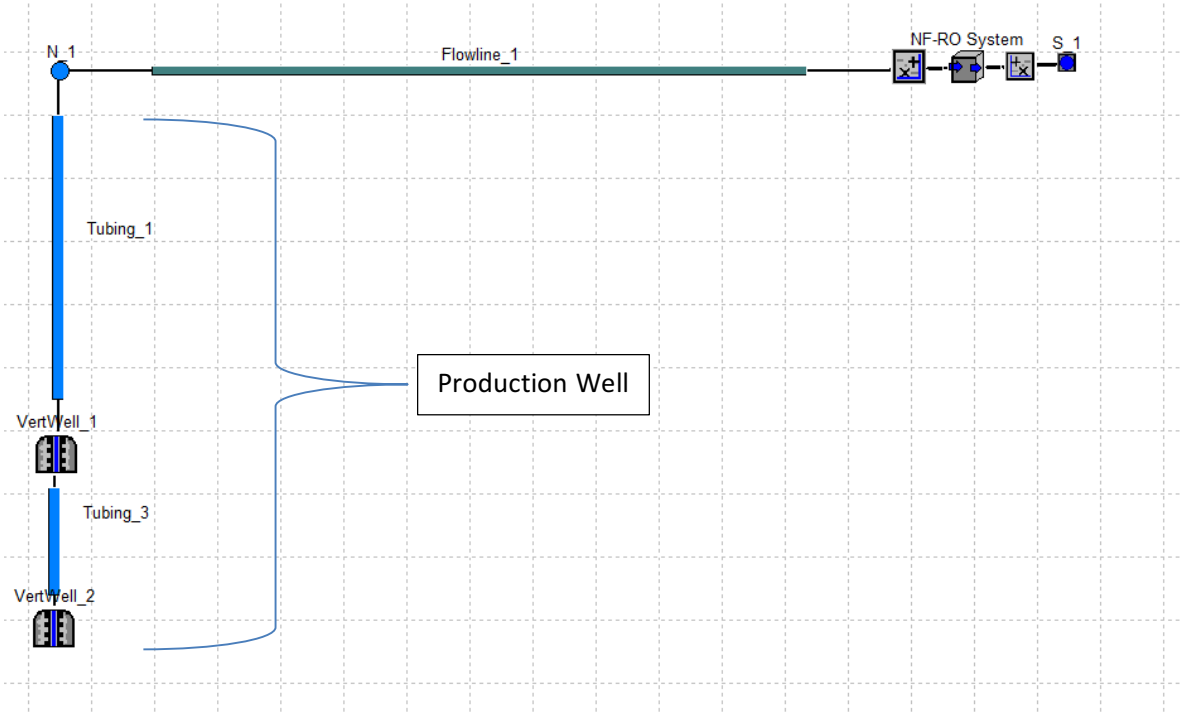


**Figure 6.4:** PIPESIM schematic showing surface equipment

## Results

*Production Well Sizing and Design*- Pressure and permeability data were incorporated into the model to calculate the ambient flow of brine between the target zones and the surface. The results show that flow can reach the surface while keeping a wellhead pressure of 1,200 psi. The operating point in the well (with 7-inch tubing) had a mass flowrate of 13.25 kg/s. The nodal analysis used the same bottom hole and wellhead pressures as the initial simulation but it included tubing sizes with outside diameters (OD) between 2.375- and 9.625-inches. The nodal analysis point was selected above the upper set of perforations to ensure that all flow from both formations was counted in the total mass flowrate. The operating points calculated in the nodal analysis ranged between 6.82 kg/s and 13.26 kg/s. **Table 6.7** and **Figure 6.5** show the results of the nodal analysis. The maximum mass flow rate was 13.26 kg/s which means that it will take at least three production wells to produce the required 31.7 kg/s required. The maximum flow rate in the analysis is achieved in the 7-inch tubing and increasing the tubing size above 7-inches does not add additional production as shown where the curve of mass flowrate versus inside diameter flattens out in **Figure 6.6.**

**Table 6.7:** Production well nodal analysis with 1200 psi wellhead pressure

| OD (inches) | ID (Inches) | Pressure at nodal point (psi) | Mass flowrate at nodal point (lbm/s) | Mass flowrate at nodal point (kg/s) |
|---|---|---|---|---|
| 2.375 | 1.867 | 7592.81 | 15.04 | 6.82 |
| 2.875 | 2.259 | 7128.86 | 20.03 | 9.09 |
| 3.5 | 2.992 | 6586.71 | 25.82 | 11.71 |
| 4 | 3.548 | 6408.63 | 27.71 | 12.57 |
| 4.5 | 4 | 6340.07 | 28.44 | 12.90 |
| 5 | 4.408 | 6307.32 | 28.79 | 13.06 |
| 5.5 | 4.892 | 6285.32 | 29.02 | 13.16 |
| 6.625 | 5.921 | 6268.13 | 29.20 | 13.25 |
| 7 | 6.366 | 6265.66 | 29.23 | 13.26 |
| 7.625 | 6.969 | 6265.66 | 29.23 | 13.26 |
| 8.625 | 8.017 | 6265.66 | 29.23 | 13.26 |
| 9.625 | 8.921 | 6268.14 | 29.20 | 13.25 |

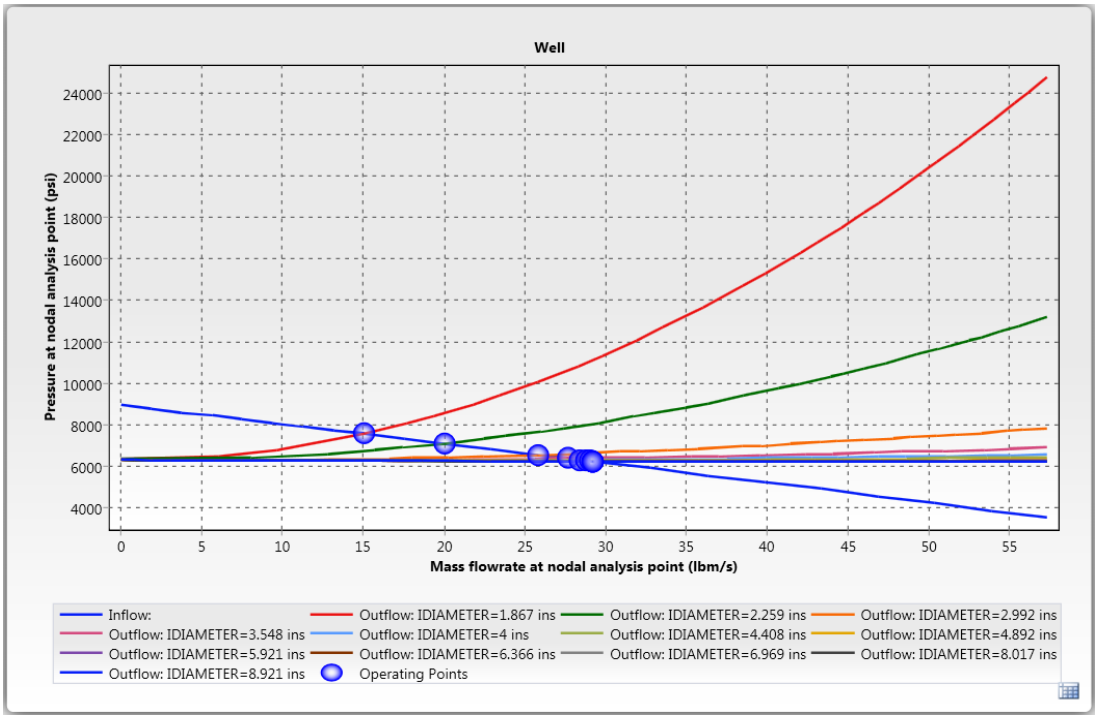


**Figure 6.5:** Production well nodal analysis results with 1200 psi wellhead pressure.

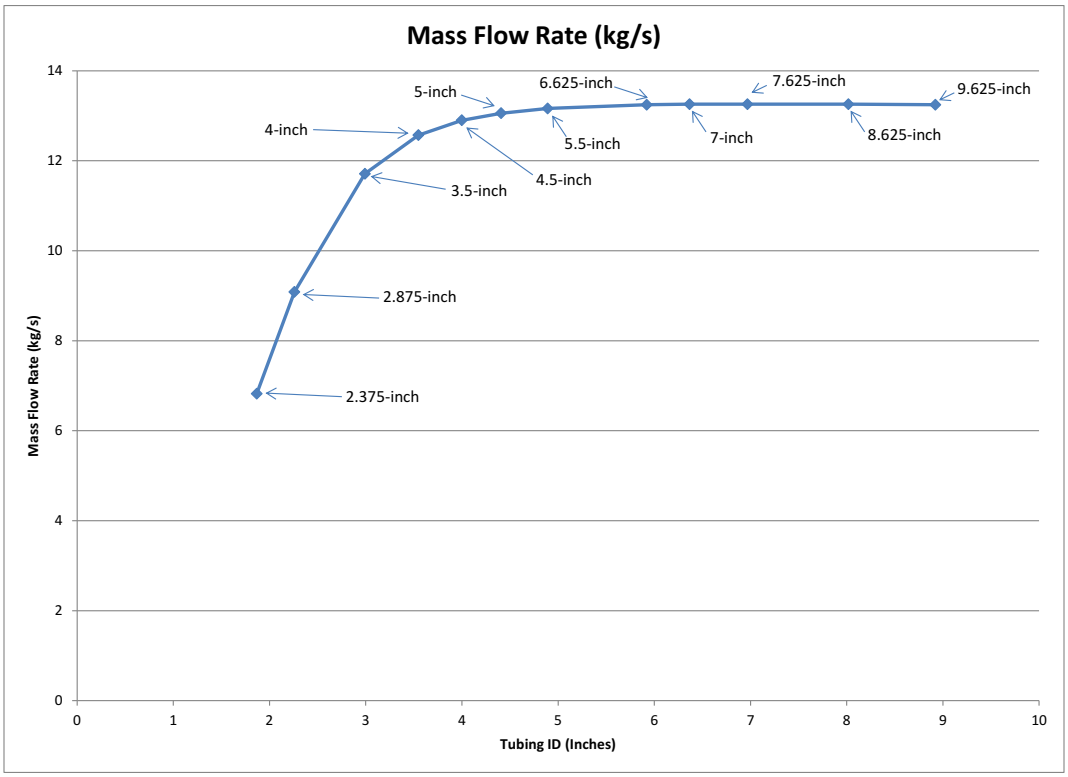


**Figure 6.6:** Mass flowrate versus tubing inside diameter for the production well nodal analysis.

Based on the nodal analysis a 5-inch tubing was selected. The production and surfacing sizes were selected using the chart shown in **Figure 6.3**. The casing details are provided in **Figure 6.7** and **Table 6.8**. It is important to note that the casing sizes have been selected but the casing strings have not been designed to withstand any specific.

**Table 6.8:** Tubing and casing details

| String | Size | Top (ft) | Bottom (ft) |
|---|---|---|---|
| Surface | 10.75 in | 0 | 2,000 |
| Production Casing | 7.625 in | 0 | 12,500 |
| Production Tubing | 5 in 15lb/ft | 0 | 11,200 |

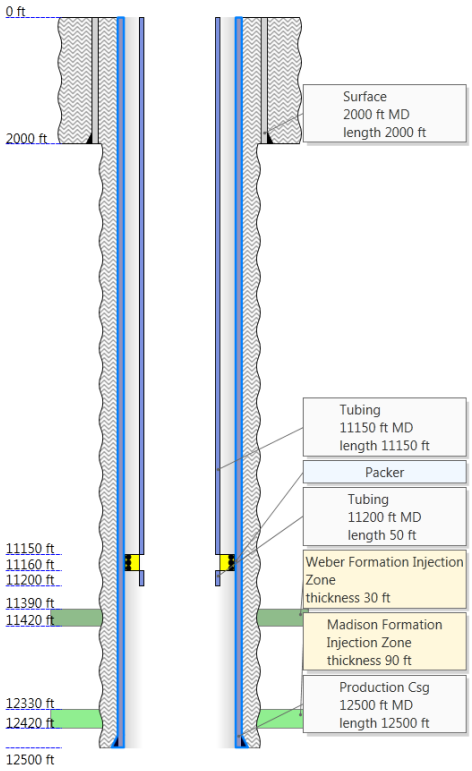


**Figure 6.7:** Well schematic for a production well with 5-inch 15lb/f tubing

*Injection Well Sizing*- The nodal analysis of the injection well with tubing ranging from 2.375 to 9.625 inches in diameter did not have any operating points meeting the 31.7 kg/s mass flow rate requirement (**Table 6.9** and **Figure 6.8**). The injection wellhead pressure was raised in 100 psi increments until one of the tubing sizes met the required operating point. At 6,500 psi, an injection rate of 31.7 kg/s was met. (**Figure 6.9** and **Table 6.10**). Additional simulations were run with the wellhead pressure set to 6,700 and 7,000 psi to show the range of pressure needed to have an injector with smaller tubing; by 7,000 psi tubing as small as 5-inch (OD) exceeds the 31.7 kg/s (**Table 6.11** and **Table 6.12** and **Figure 6.10-12**).

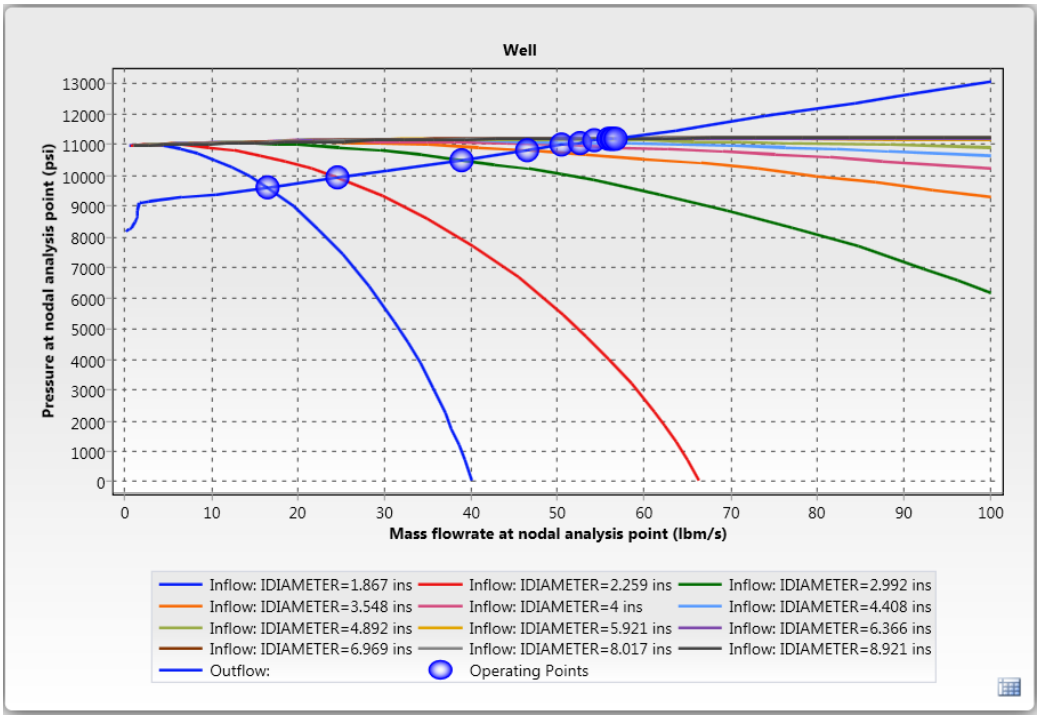


**Figure 6.8:** Injection well nodal analysis results with wellhead pressure equal to 6,000 psi

**Table 6.9:** Injection well nodal analysis results with wellhead pressure equal to 6,000 psi

| Operating point | OD (inches) | ID (Inches) | Pressure at nodal analysis point (psi) | Mass flowrate at nodal analysis point (kg/s) |
|---|---|---|---|---|
| IDIAMETER=1.867 ins Flowrate=16.40714 lb/sec | 2.375 | 1.867 | 9614.98 | 7.44 |
| IDIAMETER=2.259 ins Flowrate=24.57801 lb/sec | 2.875 | 2.259 | 9929.44 | 11.15 |
| IDIAMETER=2.992 ins Flowrate=38.93016 lb/sec | 3.5 | 2.992 | 10512.64 | 17.66 |
| IDIAMETER=3.548 ins Flowrate=46.48599 lb/sec | 4 | 3.548 | 10829.07 | 21.09 |
| IDIAMETER=4 ins Flowrate=50.37091 lb/sec | 4.5 | 4 | 10991.71 | 22.85 |
| IDIAMETER=4.408 ins Flowrate=52.599 lb/sec | 5 | 4.408 | 11083.82 | 23.86 |
| IDIAMETER=4.892 ins Flowrate=54.24411 lb/sec | 5.5 | 4.892 | 11149.03 | 24.60 |
| IDIAMETER=5.921 ins Flowrate=55.85394 lb/sec | 6.625 | 5.921 | 11206.64 | 25.33 |
| IDIAMETER=6.366 ins Flowrate=56.17231 lb/sec | 7 | 6.366 | 11215.26 | 25.48 |
| IDIAMETER=6.969 ins Flowrate=56.43537 lb/sec | 7.625 | 6.969 | 11219.85 | 25.60 |
| IDIAMETER=8.017 ins Flowrate=56.64594 lb/sec | 8.625 | 8.017 | 11218.03 | 25.69 |
| IDIAMETER=8.921 ins Flowrate=56.67382 lb/sec | 9.625 | 8.921 | 11212.06 | 25.71 |

**Table 6.10:** Injection well nodal analysis with wellhead pressure at 6,500 psi

| Operating point | OD (inches) | ID (Inches) | Pressure at nodal analysis point (psi) | Mass flowrate at nodal analysis point (lbm/s) | Mass flowrate at nodal analysis point (kg/s) |
|---|---|---|---|---|---|
| IDIAMETER=1.867 ins Flowrate=18.80678 lb/sec | 2.375 | 1.867 | 9705.73 | 18.81 | 8.53 |
| IDIAMETER=2.259 ins Flowrate=28.35902 lb/sec | 2.875 | 2.259 | 10080.47 | 28.36 | 12.86 |
| IDIAMETER=2.992 ins Flowrate=45.73669 lb/sec | 3.5 | 2.992 | 10803.81 | 45.74 | 20.75 |
| IDIAMETER=3.548 ins Flowrate=55.28644 lb/sec | 4 | 3.548 | 11219.27 | 55.29 | 25.08 |
| IDIAMETER=4 ins Flowrate=60.37389 lb/sec | 4.5 | 4 | 11441.19 | 60.37 | 27.39 |
| IDIAMETER=4.408 ins Flowrate=63.38556 lb/sec | 5 | 4.408 | 11570.61 | 63.39 | 28.75 |
| IDIAMETER=4.892 ins Flowrate=65.67434 lb/sec | 5.5 | 4.892 | 11665.09 | 65.67 | 29.79 |
| IDIAMETER=5.921 ins Flowrate=68.08337 lb/sec | 6.625 | 5.921 | 11754.16 | 68.08 | 30.88 |
| IDIAMETER=6.366 ins Flowrate=68.62168 lb/sec | 7 | 6.366 | 11769.73 | 68.62 | 31.13 |
| IDIAMETER=6.969 ins Flowrate=69.114 lb/sec | 7.625 | 6.969 | 11780.70 | 69.11 | 31.35 |
| IDIAMETER=8.017 ins Flowrate=69.54535 lb/sec | 8.625 | 8.017 | 11785.54 | 69.55 | 31.55 |
| IDIAMETER=8.921 ins Flowrate=69.75155 lb/sec | 9.625 | 8.921 | 11783.14 | 69.75 | 31.64 |

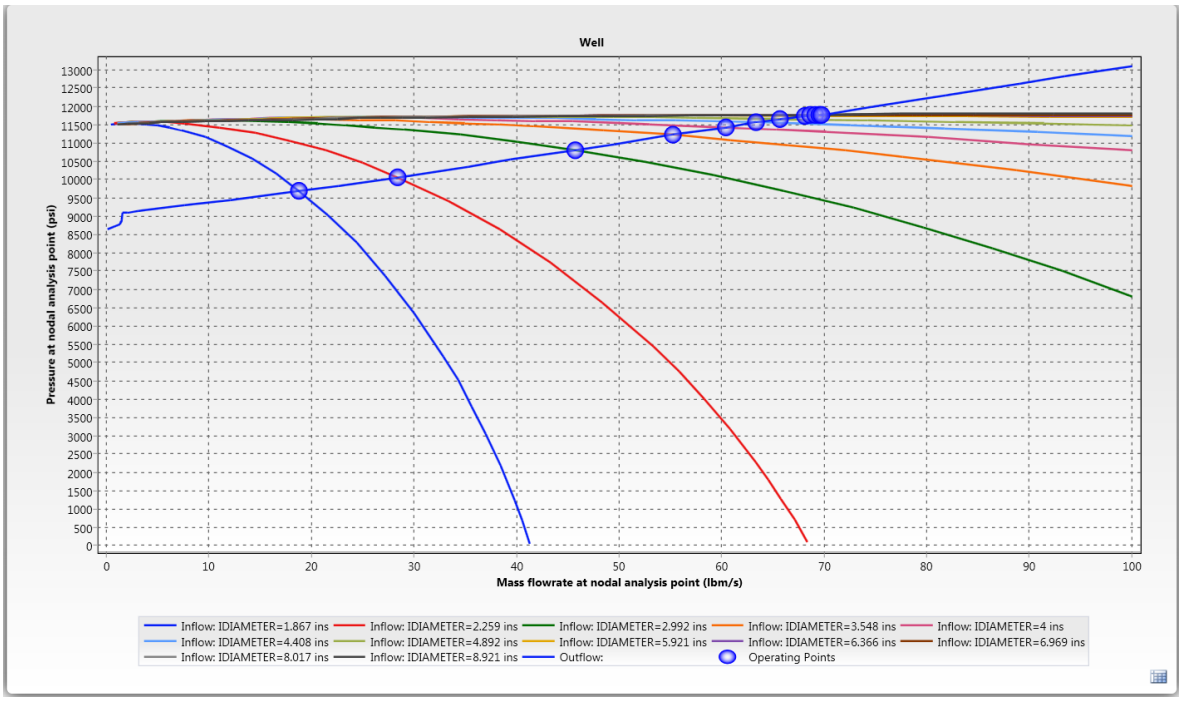


**Figure 6.9:** Injection well nodal analysis results with wellhead pressure at 6,500 psi

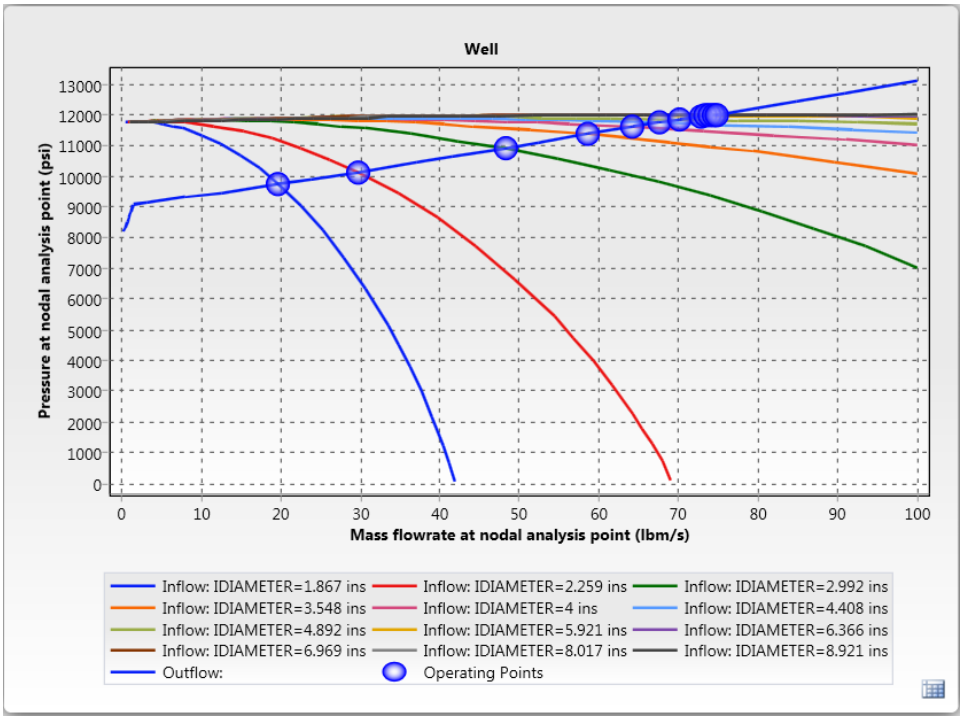


**Figure 6.10:** Injection well nodal analysis results with the wellhead pressure set to 6,700 psi

**Table 6.11:** Injection well nodal analysis results with the wellhead pressure at 6,700 psi.

| Operating point | OD (inches) | ID (Inches) | Pressure at nodal analysis point (psi) | Mass flowrate at nodal analysis point (kg/s) |
|---|---|---|---|---|
| IDIAMETER=1.867 ins Flowrate=19.69557 lb/sec | 2.375 | 1.867 | 9739.68 | 8.93 |
| IDIAMETER=2.259 ins Flowrate=29.76634 lb/sec | 2.875 | 2.259 | 10137.26 | 13.50 |
| IDIAMETER=2.992 ins Flowrate=48.27907 lb/sec | 3.5 | 2.992 | 10915.69 | 21.90 |
| IDIAMETER=3.548 ins Flowrate=58.61475 lb/sec | 4 | 3.548 | 11370.36 | 26.59 |
| IDIAMETER=4 ins Flowrate=64.18514 lb/sec | 4.5 | 4 | 11616.44 | 29.11 |
| IDIAMETER=4.408 ins Flowrate=67.50696 lb/sec | 5 | 4.408 | 11761.34 | 30.62 |
| IDIAMETER=4.892 ins Flowrate=70.04293 lb/sec | 5.5 | 4.892 | 11868.02 | 31.77 |
| IDIAMETER=5.921 ins Flowrate=72.74122 lb/sec | 6.625 | 5.921 | 11970.21 | 32.99 |
| IDIAMETER=6.366 ins Flowrate=73.35311 lb/sec | 7 | 6.366 | 11988.64 | 33.27 |
| IDIAMETER=6.969 ins Flowrate=73.92425 lb/sec | 7.625 | 6.969 | 12002.12 | 33.53 |
| IDIAMETER=8.017 ins Flowrate=74.51423 lb/sec | 8.625 | 8.017 | 12009.55 | 33.80 |
| IDIAMETER=8.921 ins Flowrate=74.77154 lb/sec | 9.625 | 8.921 | 12008.50 | 33.92 |

**Table 6.12:** Injection well nodal analysis results with the wellhead pressure set to 7,000 psi

| Operating point | OD (inches) | ID (Inches) | Pressure at nodal analysis point (psi) | Mass flowrate at nodal analysis point (lbm/s) | Mass flowrate at nodal analysis point (kg/s) |
|---|---|---|---|---|---|
| IDIAMETER=1.867 ins Flowrate=20.966 lb/sec | 2.375 | 1.867 | 9788.55 | 20.97 | 9.51 |
| IDIAMETER=2.259 ins Flowrate=31.78063 lb/sec | 2.875 | 2.259 | 10219.53 | 31.78 | 14.42 |
| IDIAMETER=2.992 ins Flowrate=51.94475 lb/sec | 3.5 | 2.992 | 11078.71 | 51.94 | 23.56 |
| IDIAMETER=3.548 ins Flowrate=63.45682 lb/sec | 4 | 3.548 | 11591.64 | 63.46 | 28.78 |
| IDIAMETER=4 ins Flowrate=69.77205 lb/sec | 4.5 | 4 | 11874.26 | 69.77 | 31.65 |
| IDIAMETER=4.408 ins Flowrate=73.57737 lb/sec | 5 | 4.408 | 12042.93 | 73.58 | 33.37 |
| IDIAMETER=4.892 ins Flowrate=76.47851 lb/sec | 5.5 | 4.892 | 12168.73 | 76.48 | 34.69 |
| IDIAMETER=5.921 ins Flowrate=79.56802 lb/sec | 6.625 | 5.921 | 12291.32 | 79.57 | 36.09 |
| IDIAMETER=6.366 ins Flowrate=80.27548 lb/sec | 7 | 6.366 | 12314.14 | 80.28 | 36.41 |
| IDIAMETER=6.969 ins Flowrate=80.94867 lb/sec | 7.625 | 6.969 | 12331.56 | 80.95 | 36.72 |
| IDIAMETER=8.017 ins Flowrate=81.69601 lb/sec | 8.625 | 8.017 | 12342.83 | 81.70 | 37.06 |
| IDIAMETER=8.921 ins Flowrate=82.12347 lb/sec | 9.625 | 8.921 | 12343.68 | 82.12 | 37.25 |

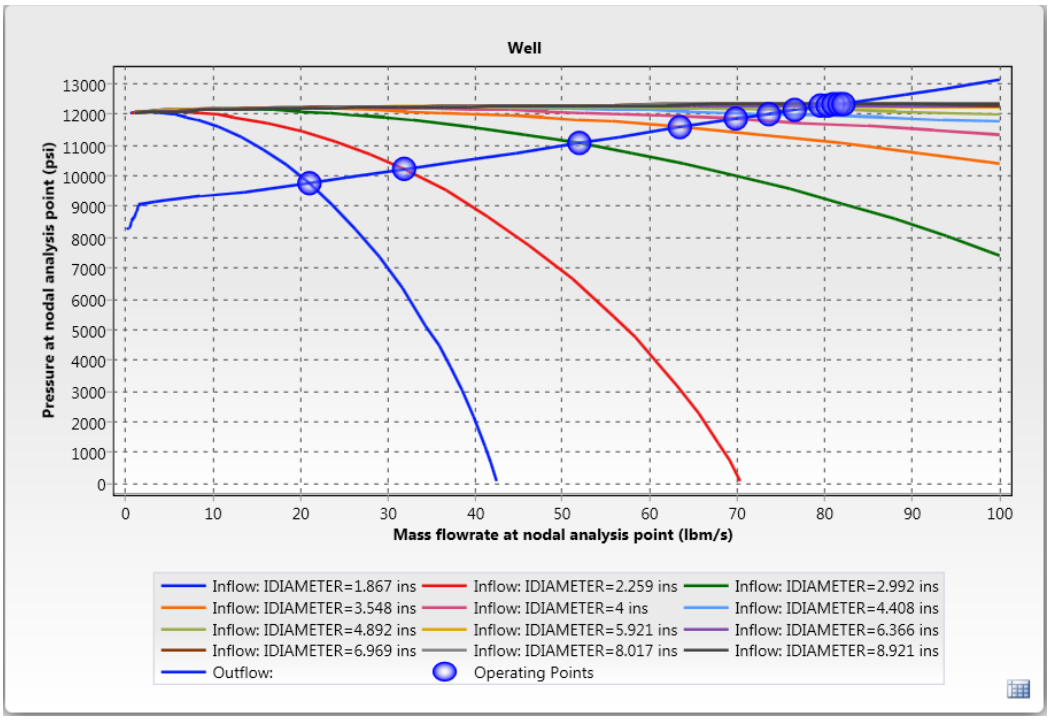


**Figure 6.11:** Injector well nodal analysis results with the wellhead pressure set to 7,000 psi

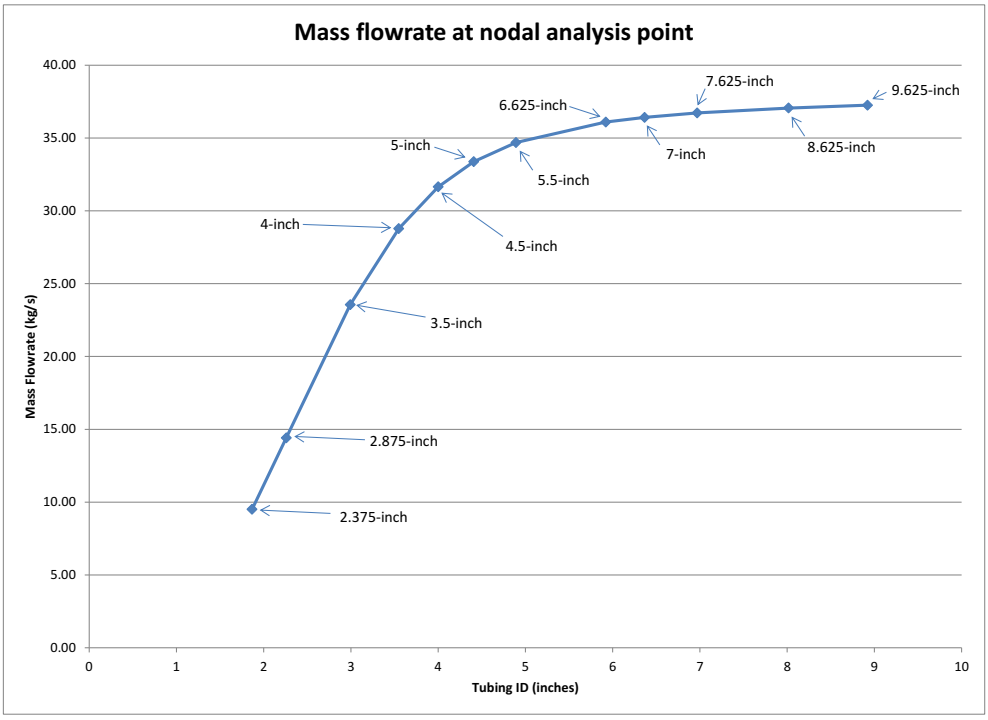


**Figure 6.12:** Mass flowrate versus tubing inside diameter for the injection well with wellhead pressure set to 7,000 psi.

Additional nodal analyses were conducted with a 7,000 psi wellhead pressure with either the Weber or Madison formation perforations partitioned off. With Madison Limestone perforations partitioned off, the mass flowrate injected ranged between 1.96 and 2.00 kg/s (**Table 6.13** and **Figure 6.13**). With Weber Sandstone partitioned off, the flowrate ranged between 9.38 and 35.3 kg/s (**Table 6.14** and **Figure 6.14**). The results indicate that the Madison is constrained by low permeability.

**Table 6.13:** Injection well nodal analysis with wellhead pressure set to 7,000 psi and the Madison Limestone perforations turned off

| Operating point | OD (inches) | ID (Inches) | Mass flowrate at nodal analysis point (kg/s) |
|---|---|---|---|
| IDIAMETER=1.867 ins Flowrate=4.325249 lb/sec | 2.375 | 1.867 | 0.85 |
| IDIAMETER=2.259 ins Flowrate=4.38122 lb/sec | 2.875 | 2.259 | 1.02 |
| IDIAMETER=2.992 ins Flowrate=4.406555 lb/sec | 3.5 | 2.992 | 1.36 |
| IDIAMETER=3.548 ins Flowrate=4.407956 lb/sec | 4 | 3.548 | 1.61 |
| IDIAMETER=4 ins Flowrate=4.407956 lb/sec | 4.5 | 4 | 1.81 |
| IDIAMETER=4.408 ins Flowrate=4.407956 lb/sec | 5 | 4.408 | 2.00 |
| IDIAMETER=4.892 ins Flowrate=4.406017 lb/sec | 5.5 | 4.892 | 2.22 |
| IDIAMETER=5.921 ins Flowrate=4.403528 lb/sec | 6.625 | 5.921 | 2.69 |
| IDIAMETER=6.366 ins Flowrate=4.403528 lb/sec | 7 | 6.366 | 2.89 |
| IDIAMETER=6.969 ins Flowrate=4.401405 lb/sec | 7.625 | 6.969 | 3.16 |
| IDIAMETER=8.017 ins Flowrate=4.400333 lb/sec | 8.625 | 8.017 | 3.64 |
| IDIAMETER=8.921 ins Flowrate=4.39867 lb/sec | 9.625 | 8.921 | 4.05 |

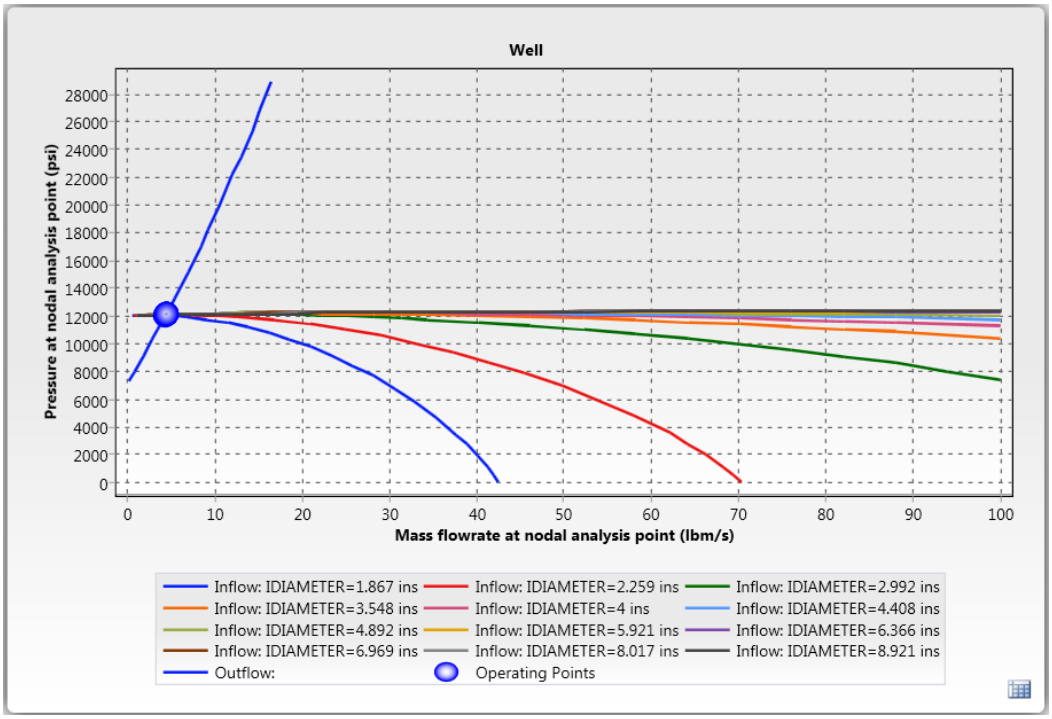


**Figure 6.13:** Injection well nodal analysis with the Madison Limestone perforations partitioned off and the wellhead pressure set to 7,000 psi.

**Table 6.14:** Injection well nodal analysis with the Weber Limestone perforations partitioned off and the wellhead pressure set to 7,000 psi.

| Operating point | Pressure at nodal analysis point (psi) | Mass flowrate at nodal analysis point (lbm/s) | Mass flowrate at nodal analysis point (kg/s) |
|---|---|---|---|
| IDIAMETER=1.867 ins Flowrate=20.6829 lb/sec | 9867.44 | 20.68 | 9.38 |
| IDIAMETER=2.259 ins Flowrate=31.20042 lb/sec | 10304.30 | 31.20 | 14.15 |
| IDIAMETER=2.992 ins Flowrate=50.42248 lb/sec | 11157.67 | 50.42 | 22.87 |
| IDIAMETER=3.548 ins Flowrate=61.11912 lb/sec | 11651.54 | 61.12 | 27.72 |
| IDIAMETER=4 ins Flowrate=66.87716 lb/sec | 11917.78 | 66.88 | 30.34 |
| IDIAMETER=4.408 ins Flowrate=70.28414 lb/sec | 12074.54 | 70.28 | 31.88 |
| IDIAMETER=4.892 ins Flowrate=72.86602 lb/sec | 12189.99 | 72.87 | 33.05 |
| IDIAMETER=5.921 ins Flowrate=75.5896 lb/sec | 12301.03 | 75.59 | 34.29 |
| IDIAMETER=6.366 ins Flowrate=76.20014 lb/sec | 12321.41 | 76.20 | 34.56 |
| IDIAMETER=6.969 ins Flowrate=76.79469 lb/sec | 12336.76 | 76.79 | 34.83 |
| IDIAMETER=8.017 ins Flowrate=77.44727 lb/sec | 12346.29 | 77.45 | 35.13 |
| IDIAMETER=8.921 ins Flowrate=77.8279 lb/sec | 12346.55 | 77.83 | 35.30 |

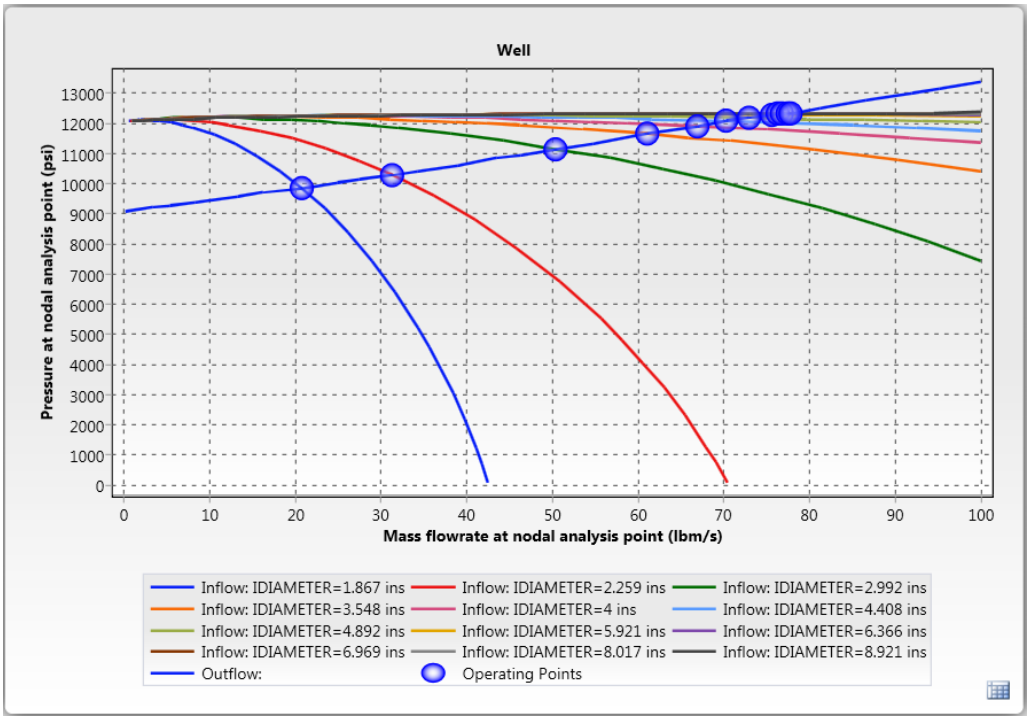


**Figure 6.14:** Injection well nodal analysis with the Weber Sandstone partitioned off and the wellhead pressure set to 7,000 psi.

*Wellbore Scaling Issues: Subtask 6.1*- The ScaleChem model assumed that the wellbore fluid was a mix of the Weber and Madison formation waters. The ratio was calculated to be 0.009 (Weber/Madison). This ratio indicates that the Madison formation brines dominate the wellbore fluid chemistry. The scale lines show where possible scales may precipitate or dissolve in the pressure and temperature range of modeled production well (**Figure 6.15** and **Figure 6.18**). This does not indicate which salts are likely to form based on the actual brines collected from RSU #1. To understand the salts that may form, it is more instructive to look at the scale tendency (**Figure 6.16**) and scale mass fraction data (**Figure 6.17** and **Figure 6.19**). These model results indicate that the bulk of the scale that is likely to form is calcium carbonate ($CaCO_3$). It is important to note that $CaCO_3$ does not appear in **Figure 6.15** because the appear-disappear window is larger than the pressure-temperature range modeled ($CaCO_3$ exists throughout the plot). The brine analyses show that oxygen was introduced to the subsurface from well operations between 2011 and 2012, which led to more possible scale species. **Figure 6.18** shows the appear and disappear plot for the 2012 data. In comparison to the 2011 data (**Figure 6.15**), it shows more potential species. Although the 2012 data has more possible scale minerals, the actual scale is still dominated by CaCO3. However, iron sulfide (FeS or FEIIS on the plots below) is higher in the 2012 data than in the 2011 data (**Figure 6.18** and **Figure 6.19**).

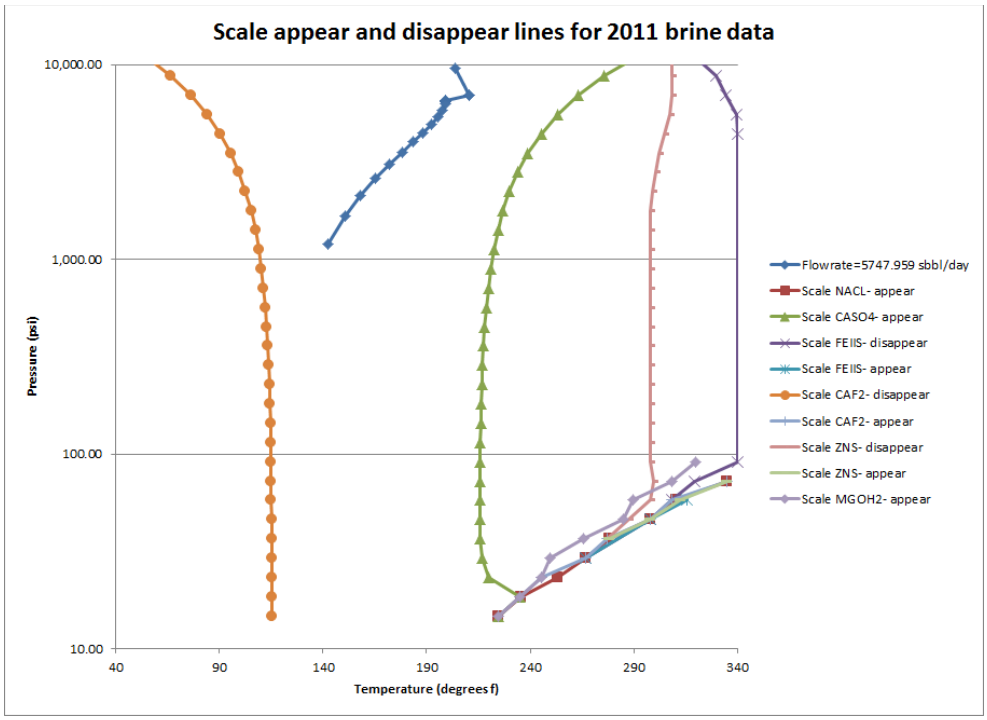


**Figure 6.15:** Scale appear and disappear data for the 2011 geochemical data

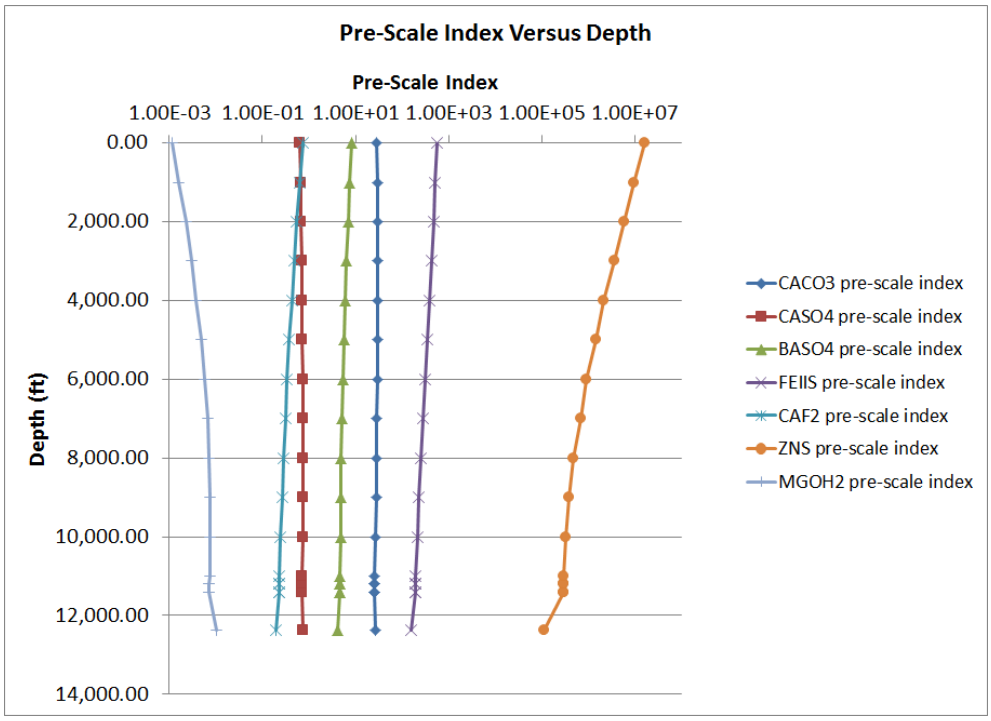


**Figure 6.16:** Pre-scale indices for potential salt based on 2011 data

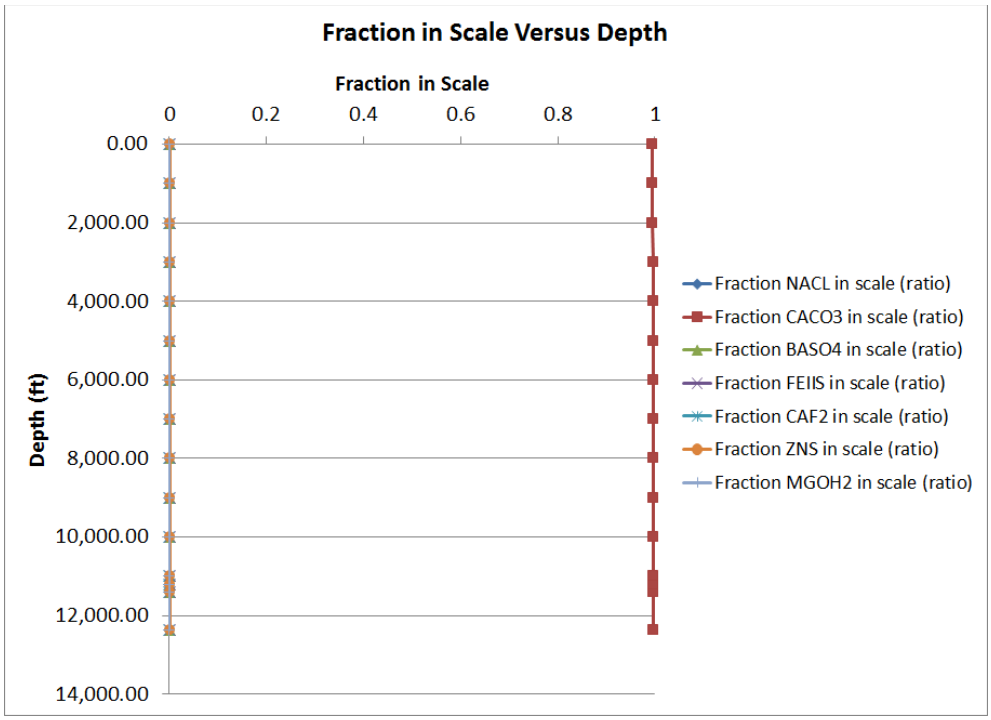


**Figure 6.17:** Scale mass-fraction data for 2011 data set.

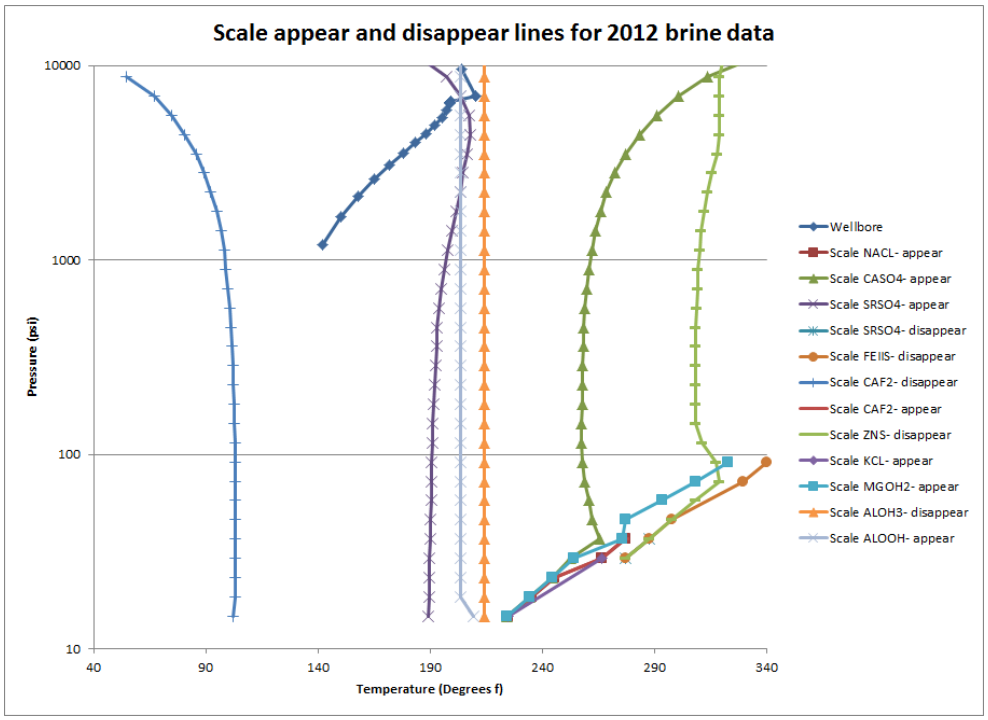


**Figure 6.18:** Scale appear and disappear data for the 2012 data set.

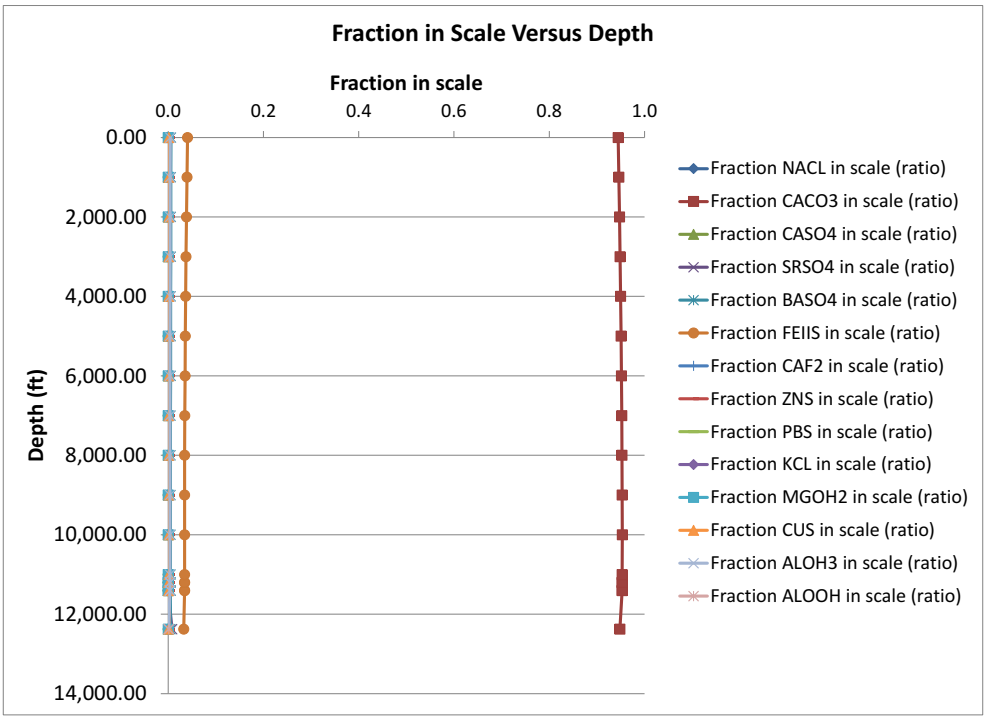


**Figure 6.19:** Scale mass fractions based on 2012 chemical data

*The Effect of brine chemistry on well construction and casing integrity: Subtask 6.2*- Corrosion from exposure to brine was modeled for flowing and shut-in conditions using the 2011 and 2012 brine sample geochemistries.

Flowing Conditions: For flowing simulations, 2205 and 304 series steel performed best with respect to general corrosion with corrosion rates in the thousandths or hundredths of millimeters per year, respectively. The mild steel had the worst general corrosion performance under flowing conditions with the 2011 chemistry, with corrosion rates of tenths of millimeters per year. The 13 chrome steel had the worst general performance under flowing conditions with brine 2012 chemistry with corrosion rates over 1 mm per year (**Figure 6.20**). Localized corrosion (pitting) potentially occurs when corrosion potential is larger than passivation potential. Under both brine chemistries, 2205 and 13-chrome steels are not expected to have localized corrosion. Mild steel is expected to have localized corrosion along the entire length of tubing for both the 2011 and 2012 data. 304 series steel does not show localized corrosion under 2011 data, but does show localized corrosion in the lower portion of the well with 2012 data. **Figures 6.21-24** show the plots for localized corrosion for each metallurgy using 2011 and 2012 data.

Shut-in Conditions: Under shut-in conditions, 2205 and 304 series steel also perform the best with general corrosion rates in the ten thousandths and thousandths of a millimeter per year. 13-chrome steel had the poorest general corrosion performance with 2011 brine conditions and in the upper half of the well with 2012 brine data. Both 2205 and 13-chrome steels show no localized corrosion. Mild steel shows the potential for pitting along the whole length of the tubing. 304 series steel has good pitting corrosion performance with the 2011 brine, but could

have pitting in the lower half of the well with the 2012 brine. **Figures 6.25-29** show the shut in corrosion model results.

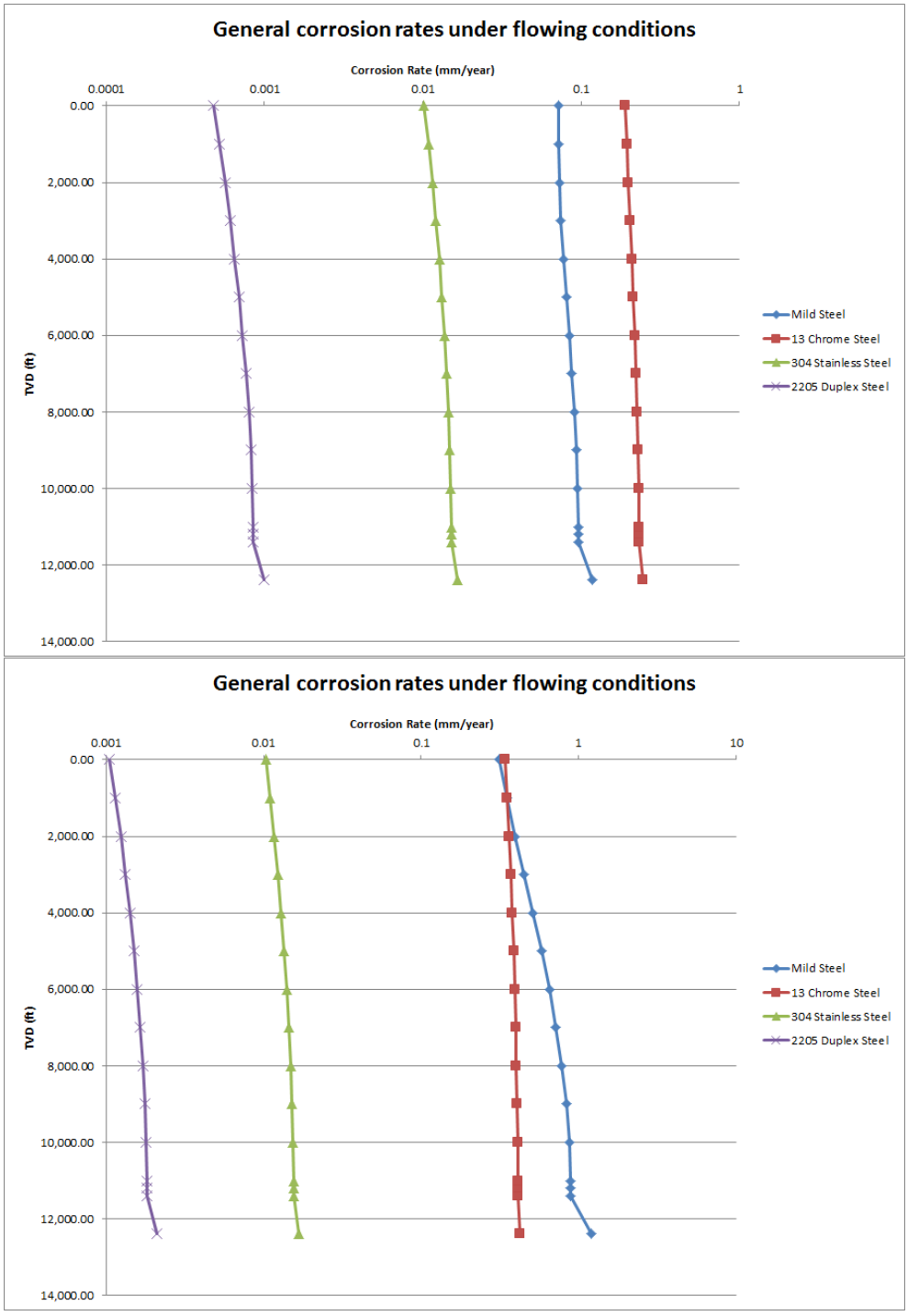


**Figure 6.20:** Simulated corrosion versus depth using the 2011 (top) and 2012 (bottom) geochemical data under flowing conditions

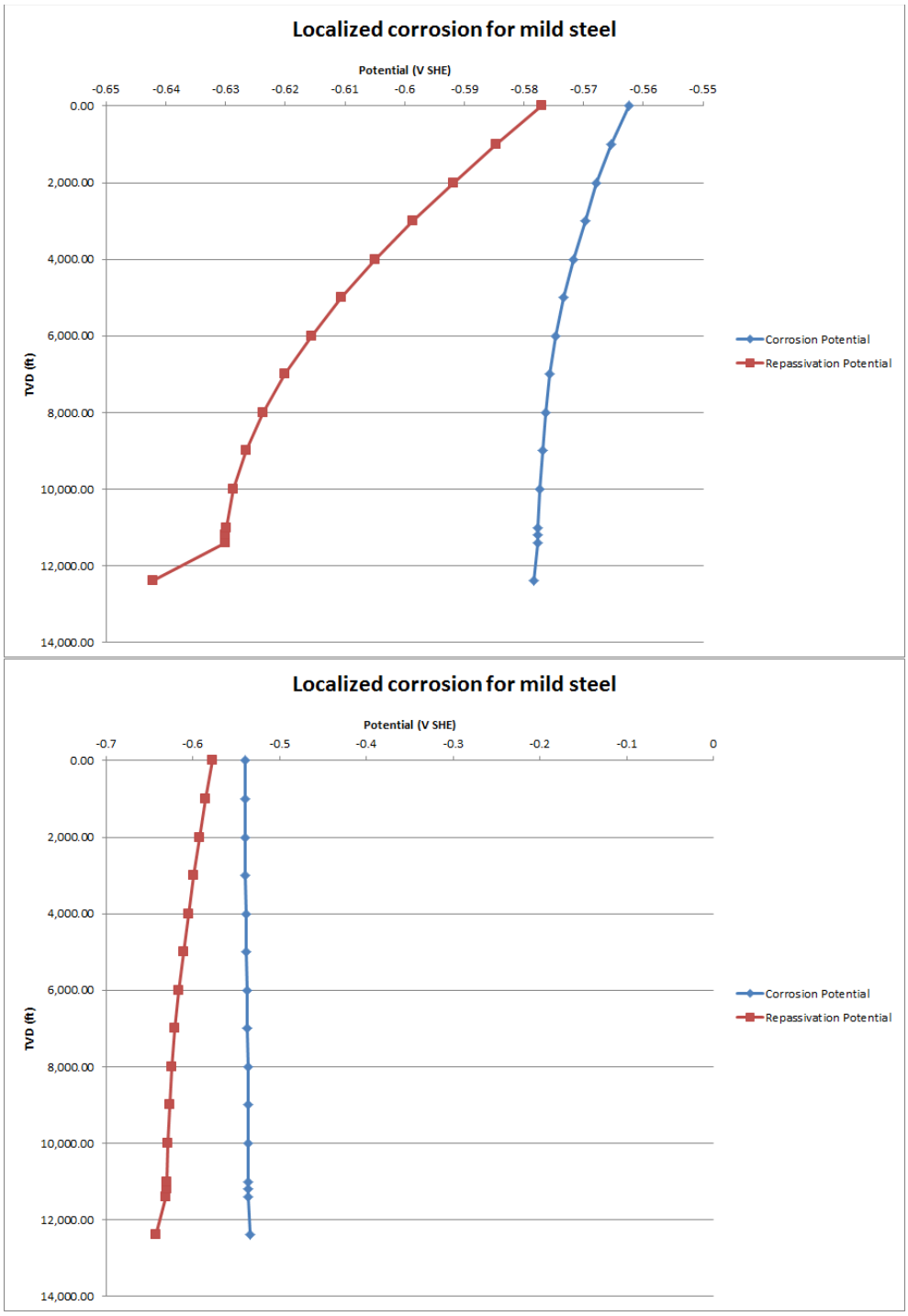


**Figure 6.21:** Localized corrosion potential for mild steel under flowing conditions using 2011 (top) and 2012 (bottom) brine data

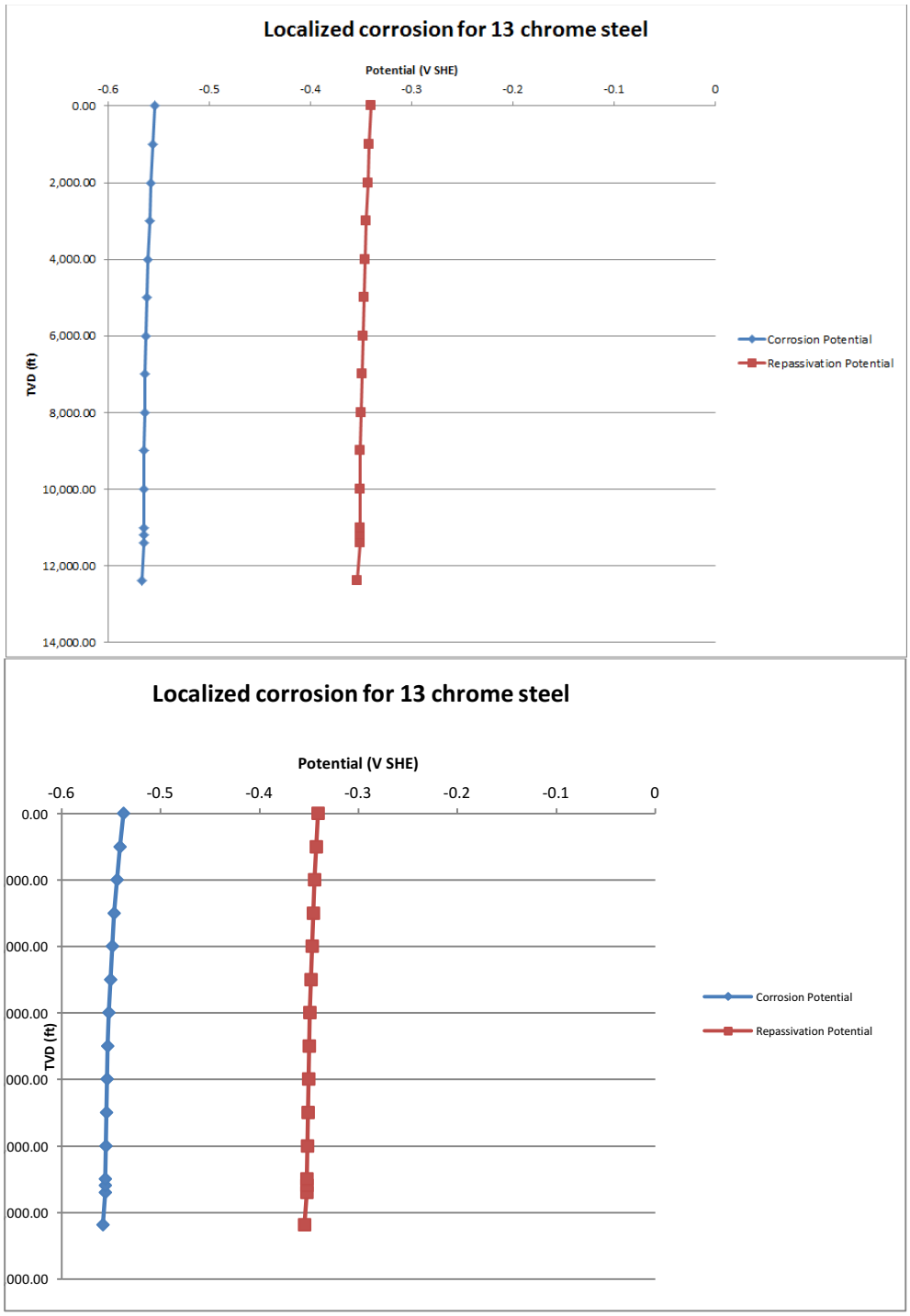


**Figure 6.22:** Localized corrosion potential for 13-chrome steel under flowing conditions using 2011 (top) and 2012 (bottom) brine data

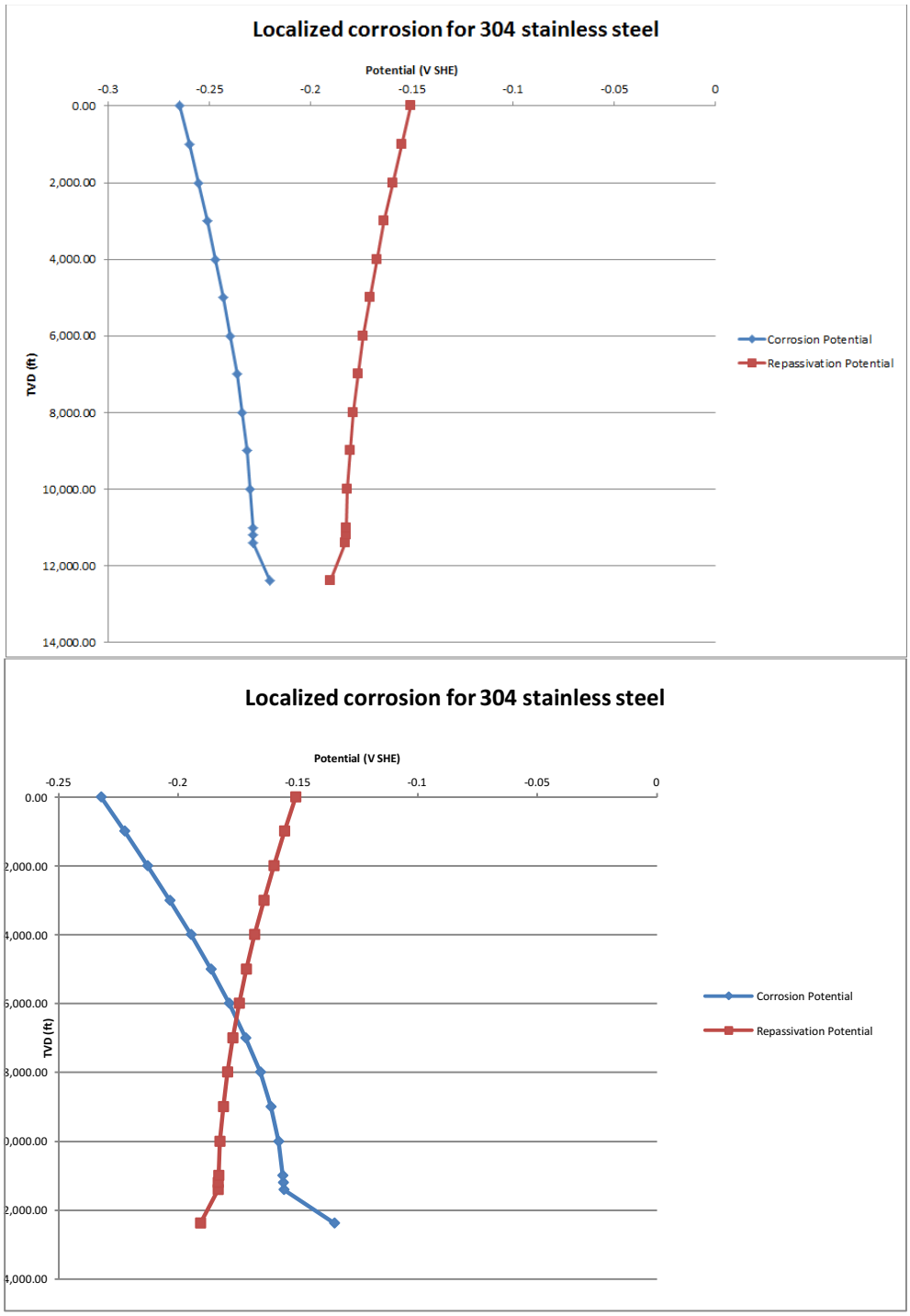


**Figure 6.23:** Localized corrosion potential for 304 stainless steel under flowing conditions using 2011 (top) and 2012 (bottom) brine data

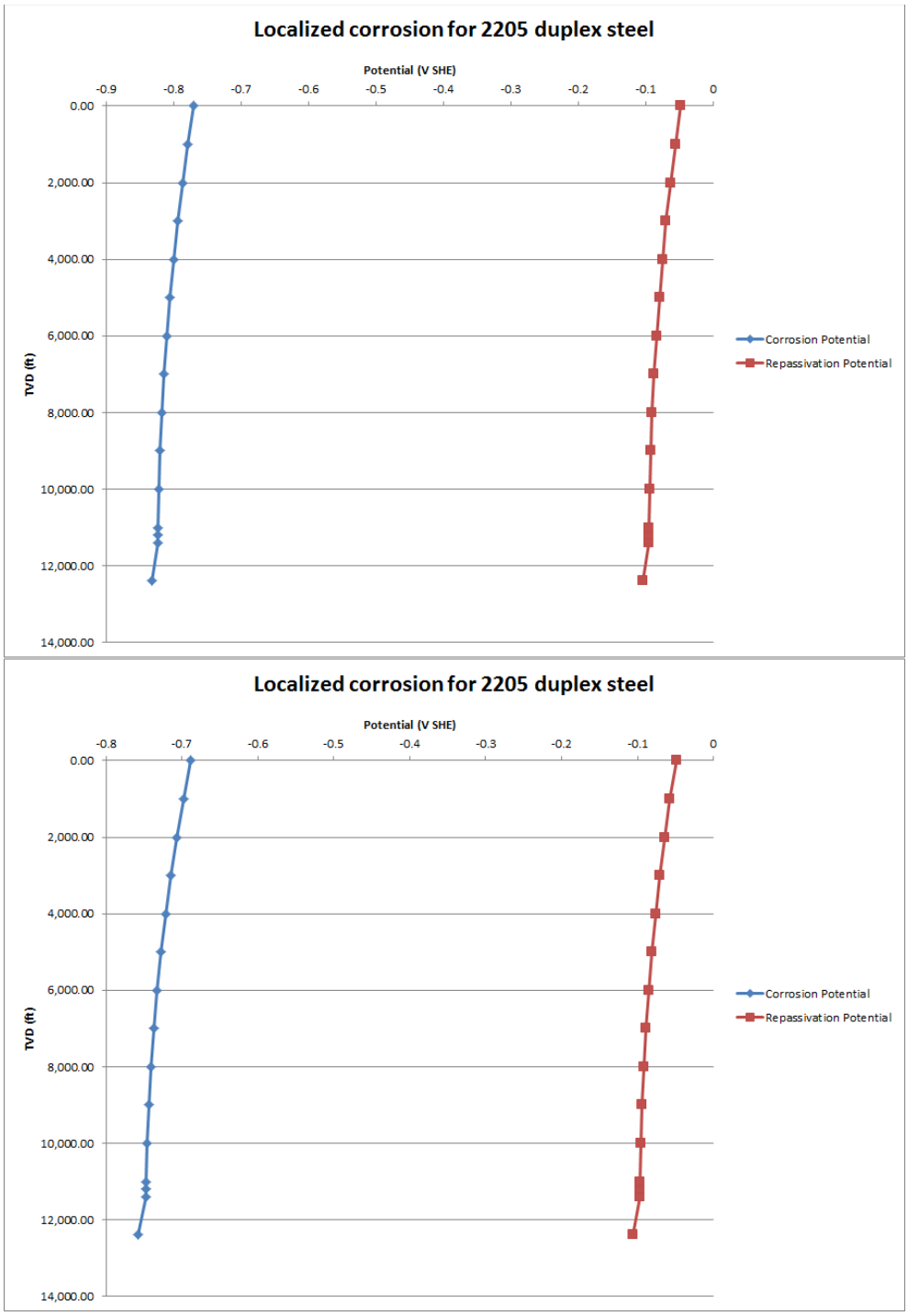


**Figure 6.24:** Localized corrosion potential for 2205 duplex steel under flowing conditions using 2011 (top) and 2012 (bottom) brine data

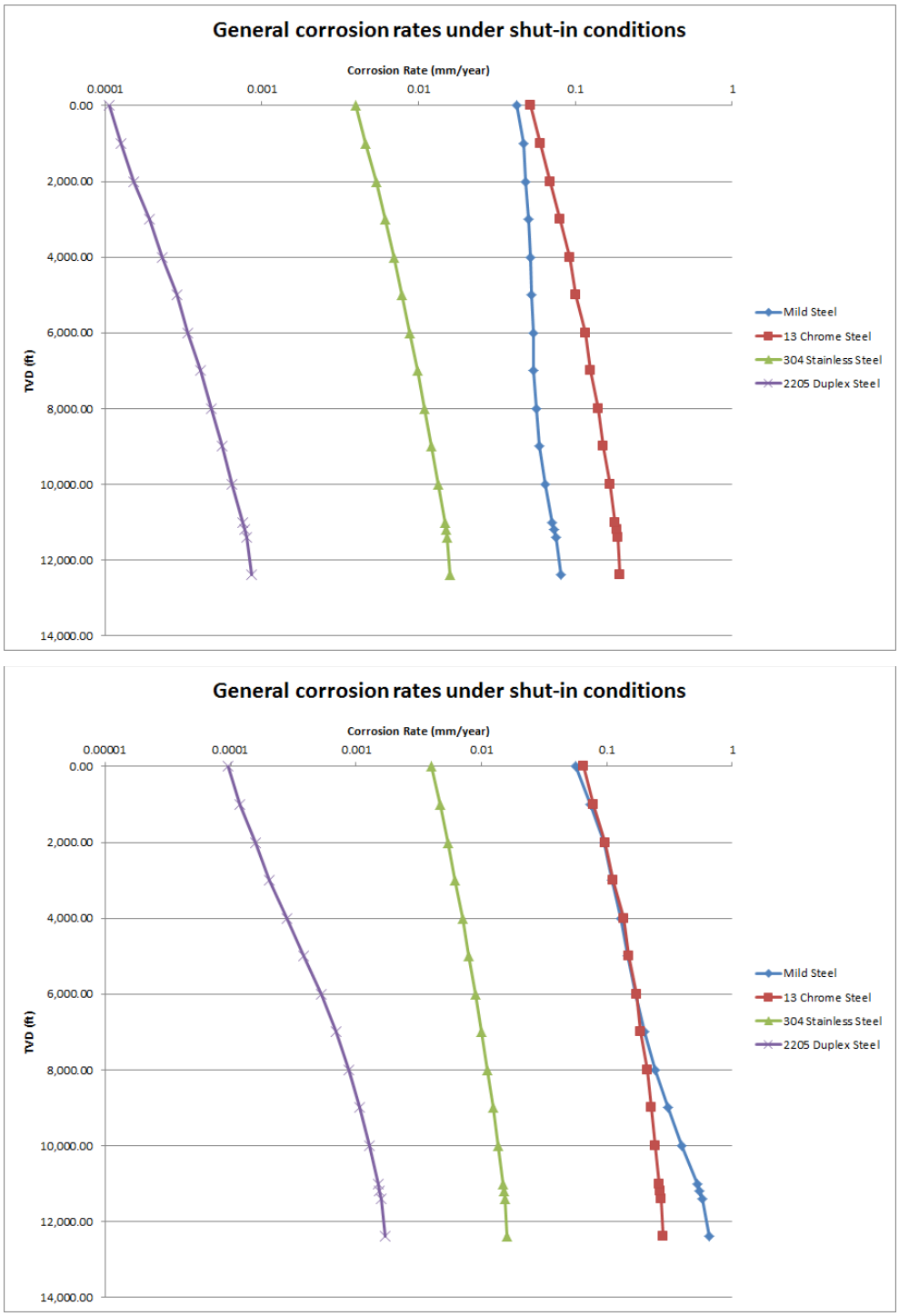


**Figure 6.25:** Simulated corrosion versus depth using the 2011(top) and 2012 (bottom) geochemical data under shut-in conditions

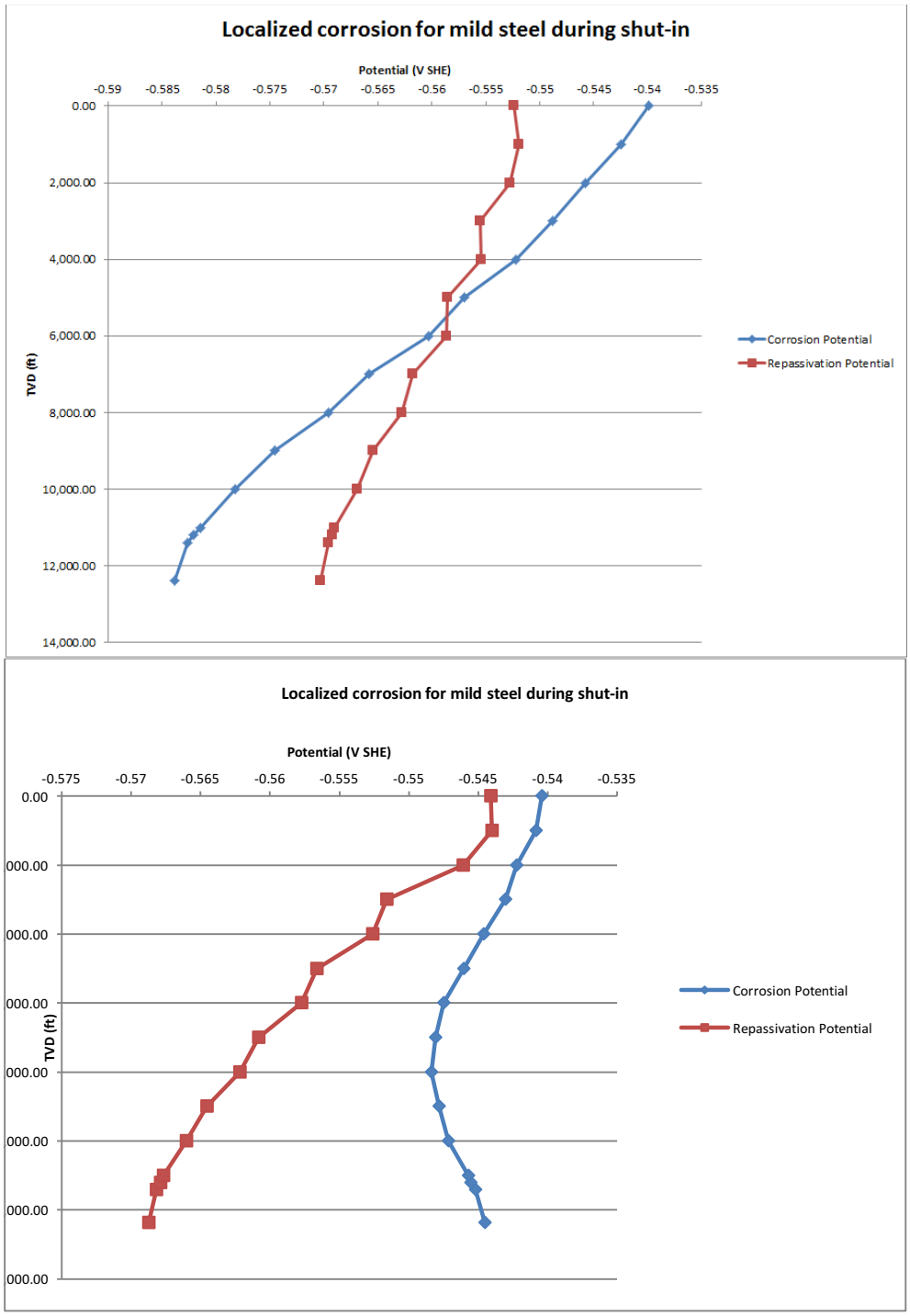


**Figure 6.26:** Localized corrosion potential for mild steel under shut-in conditions for 2011 (top) and 2012 (bottom) brine data

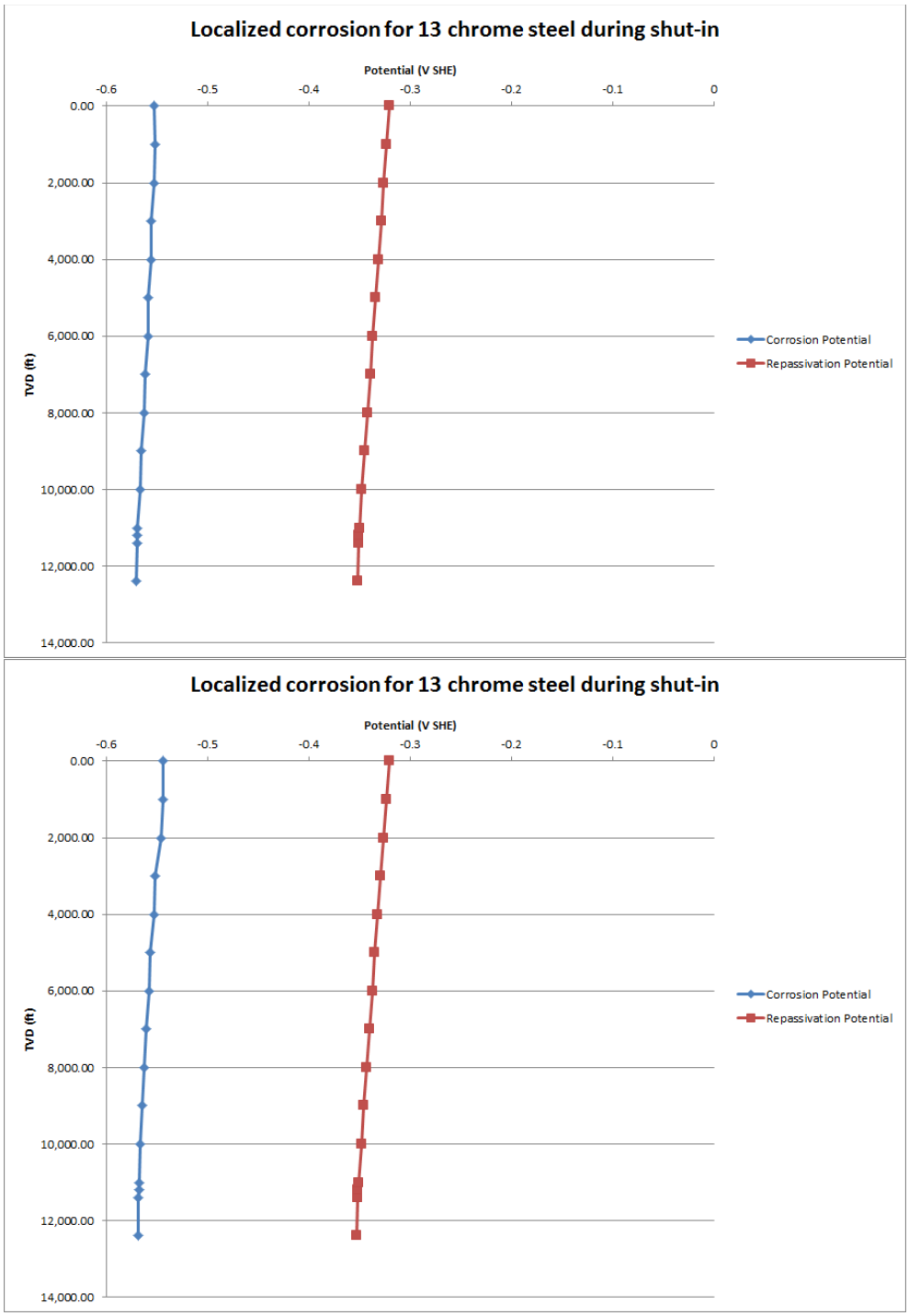


**Figure 6.27:** Localized corrosion potential for 13-chrome steel under shut-in conditions for 2011 (top) and 2012 (bottom) brine data

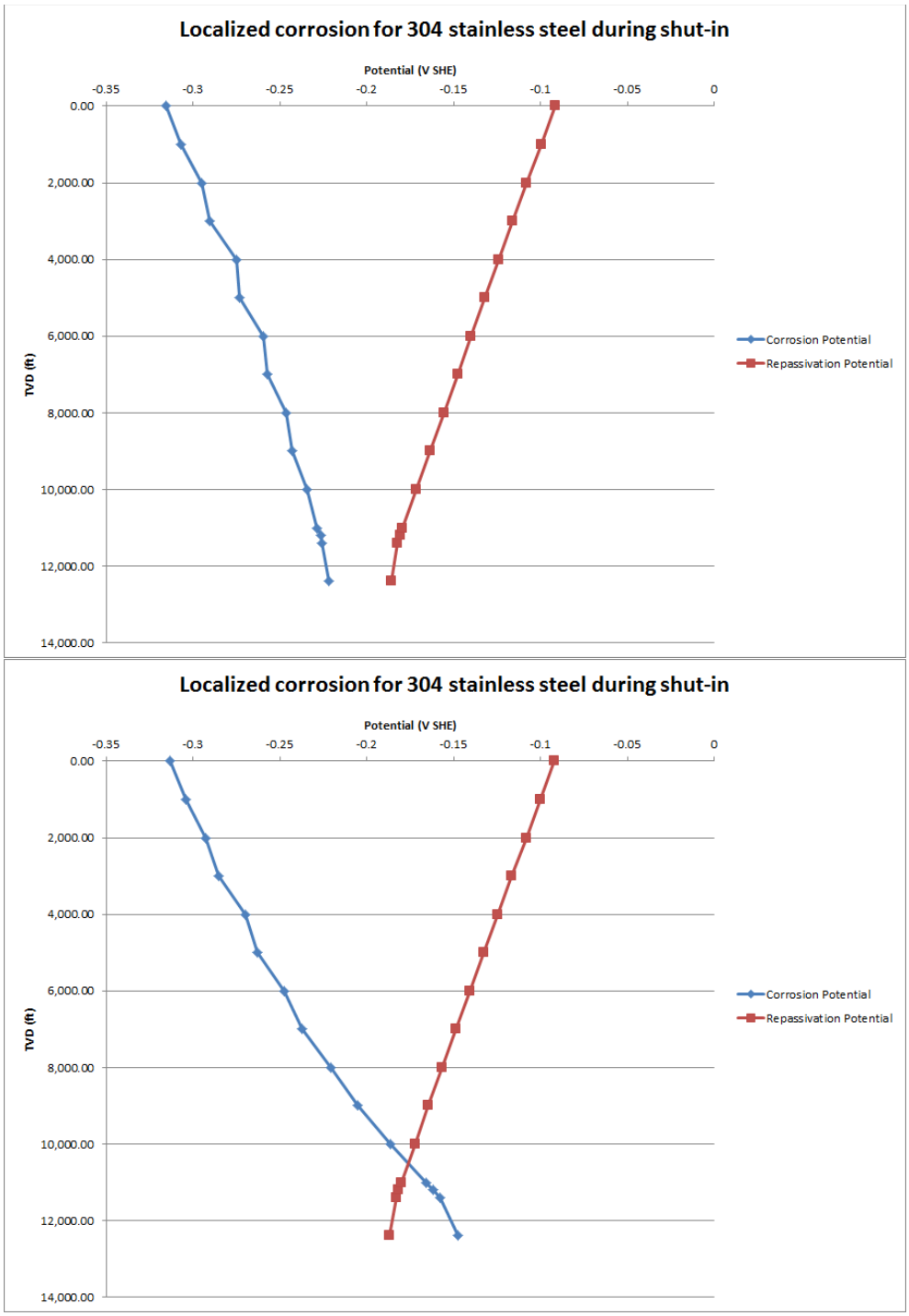


**Figure 6.28:** Localized corrosion potential for 304 stainless steel under shut-in conditions for 2011 (top) and 2012 (bottom) brine data

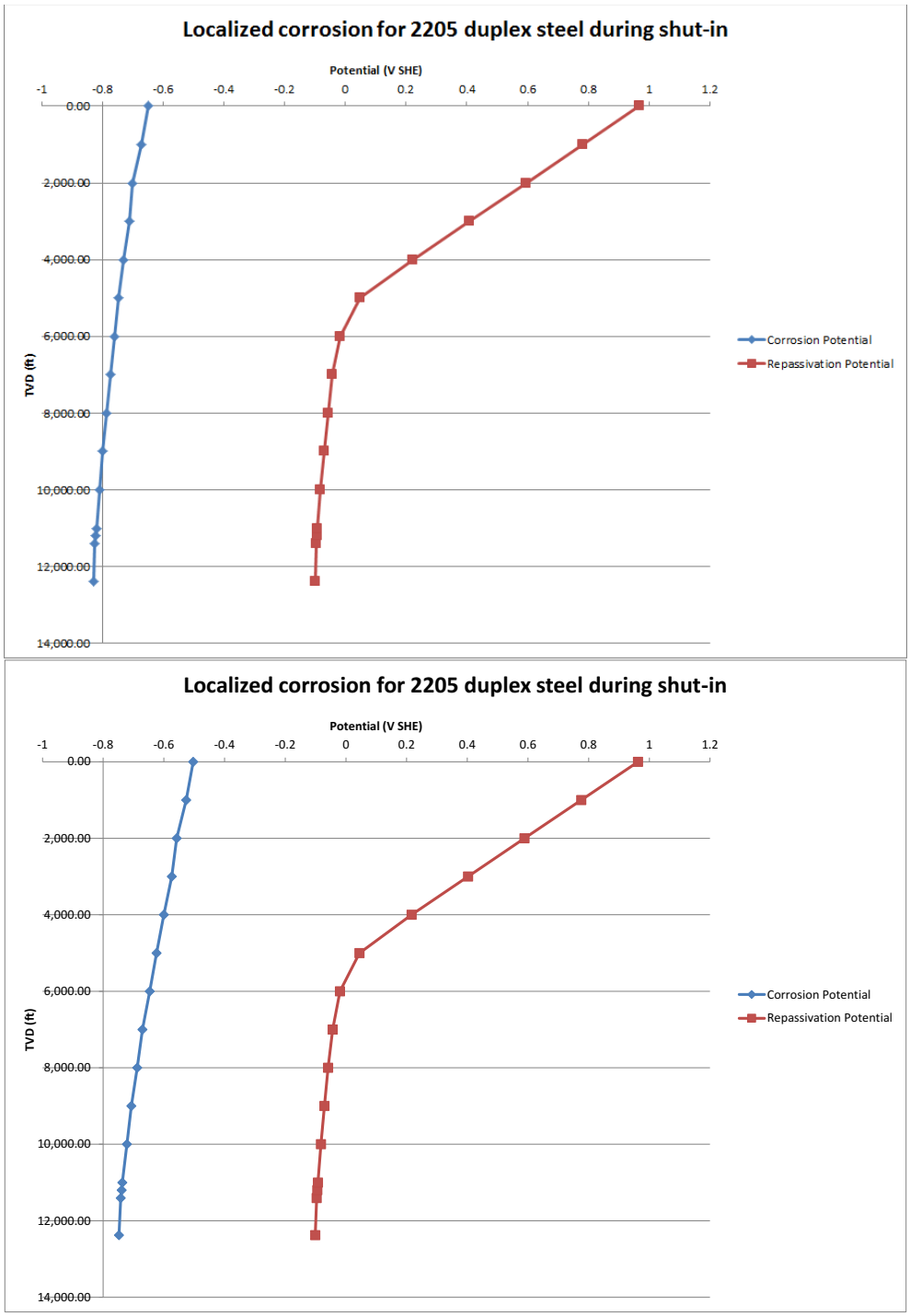


**Figure 6.29:** Localized corrosion potential for 2205 duplex steel under shut-in conditions for 2011 (top) and 2012 (bottom) brine data

*The effect of brine chemistry on produced water treatment infrastructure*- The results of the PIPESIM simulation, including surface equipment, were very similar to previous results with very little pressure drop from the surface equipment. A 50 psi pressure drop was assumed for the NF/RO based on the (The Dow Chemical Company) "DOW Water and Process Solutions; FILMTEC Reverse Osmosis Membranes Technical Manual". **Figure 6.30** and **Figure 6.31** show the results temperature versus total distance. The last three points on the right on the plot in **Figure 6.31** represent the surface equipment.

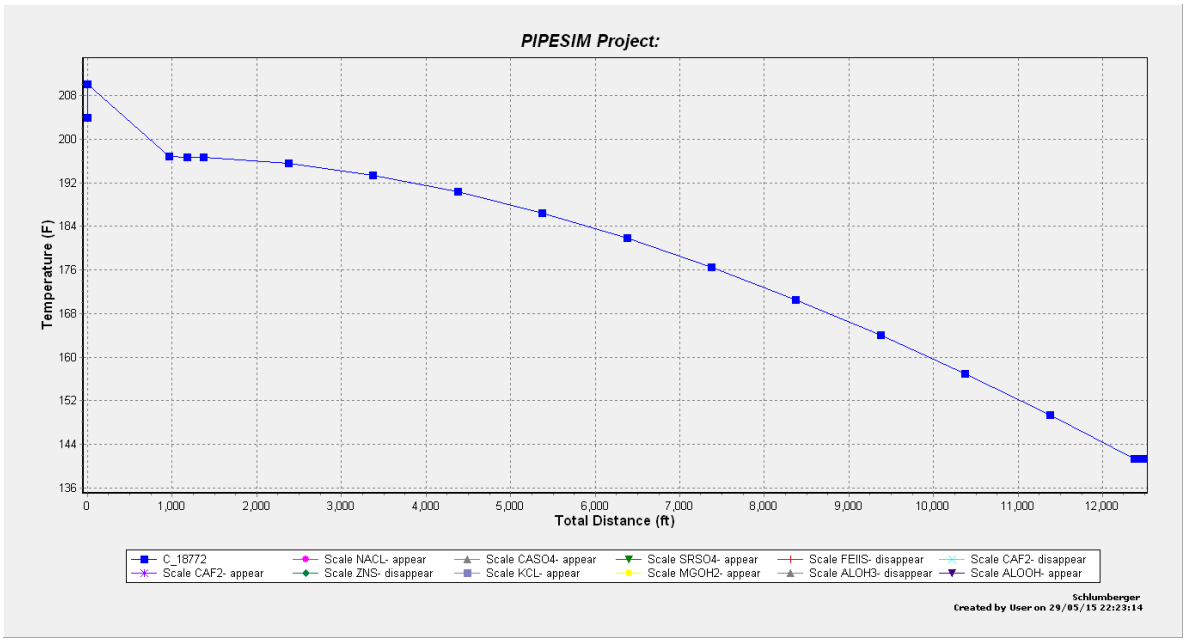


**Figure 6.30:** Temperature vs total distance for entire system, one of 3 wells operating at 333,333 tonnes per year. Note the wellbore conditions are represented by C_18772 on the plot. No salts are shown.

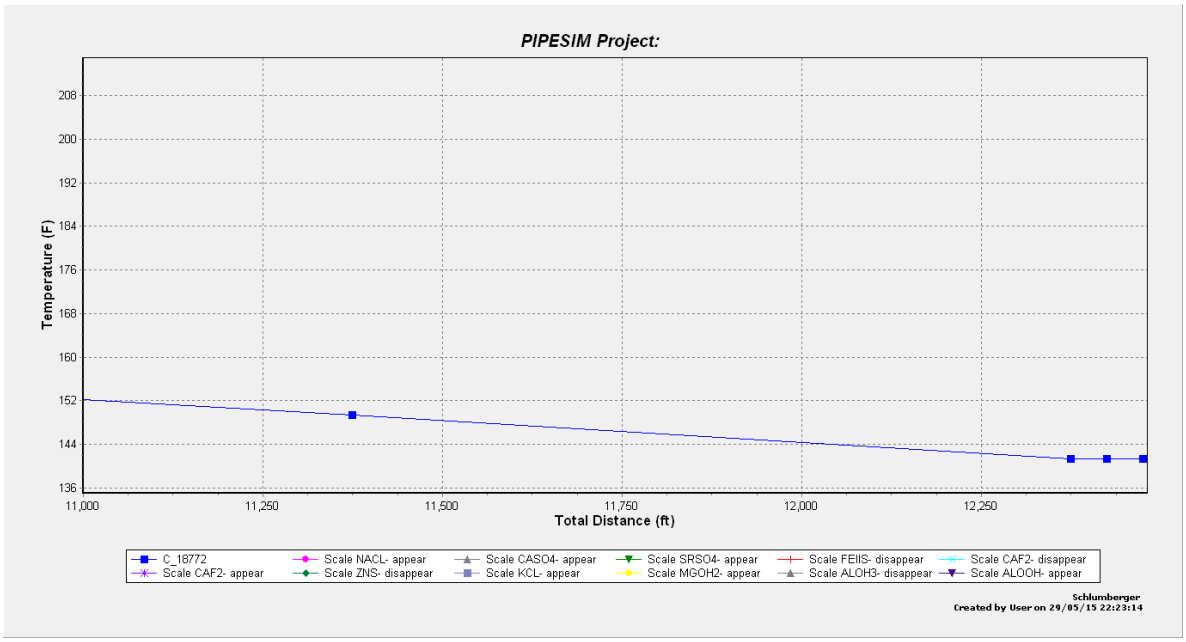


**Figure 6.31:** Temperature vs total distance for entire system, one of 3 wells operating at 333,333 tonnes per year. Note the wellbore conditions are represented by C_18772 on the plot. No salts are shown.

**Figures 6.32-35** shows pressure versus temperature plots for the system with surface equipment and the phase appearance and disappearance lines for potential scale phases. The scale phases, pressures, and temperatures for the system with surface equipment are not significantly different from the wellbore only simulations, as the results cover the same general range of values and fall into the same pressure and temperature range.

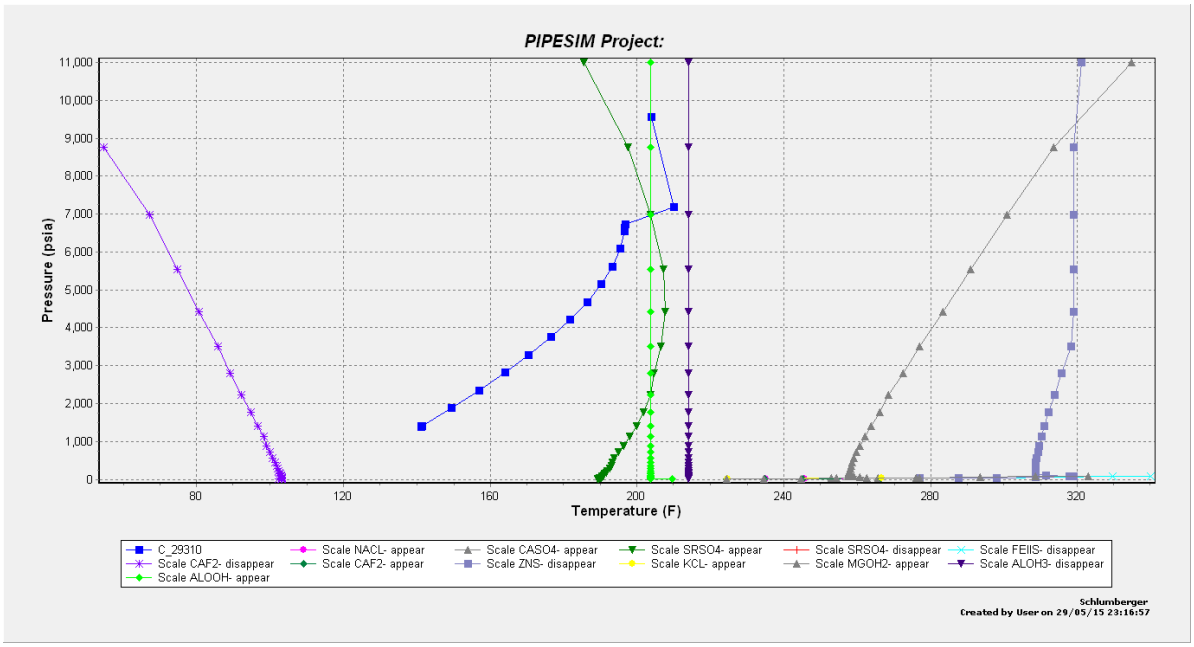


**Figure 6.32:** Pressure vs temperature plot for the system including surface equipment using the 2012 geochemical data. Note the wellbore conditions are represented by C_29310 on the plot.

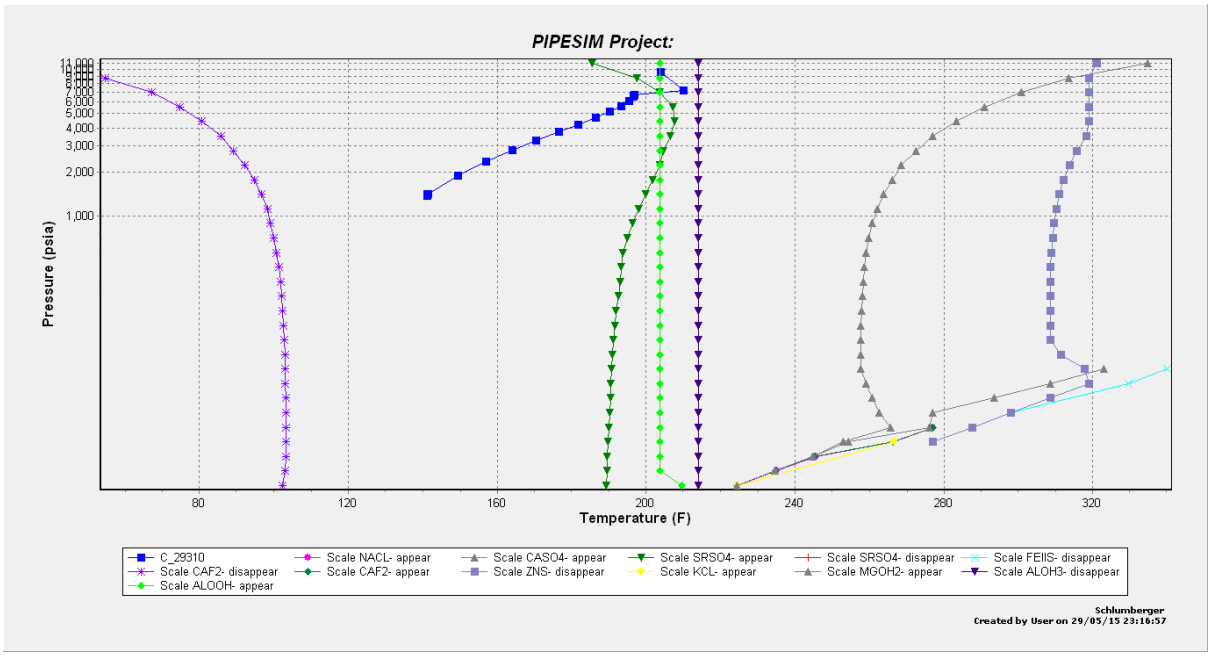


**Figure 6.33:** Pressure vs temperature plot for the system including surface equipment using the 2012 geochemical data (logarithmic pressure axis). Note the wellbore conditions are represented by C_29310 on the plot.

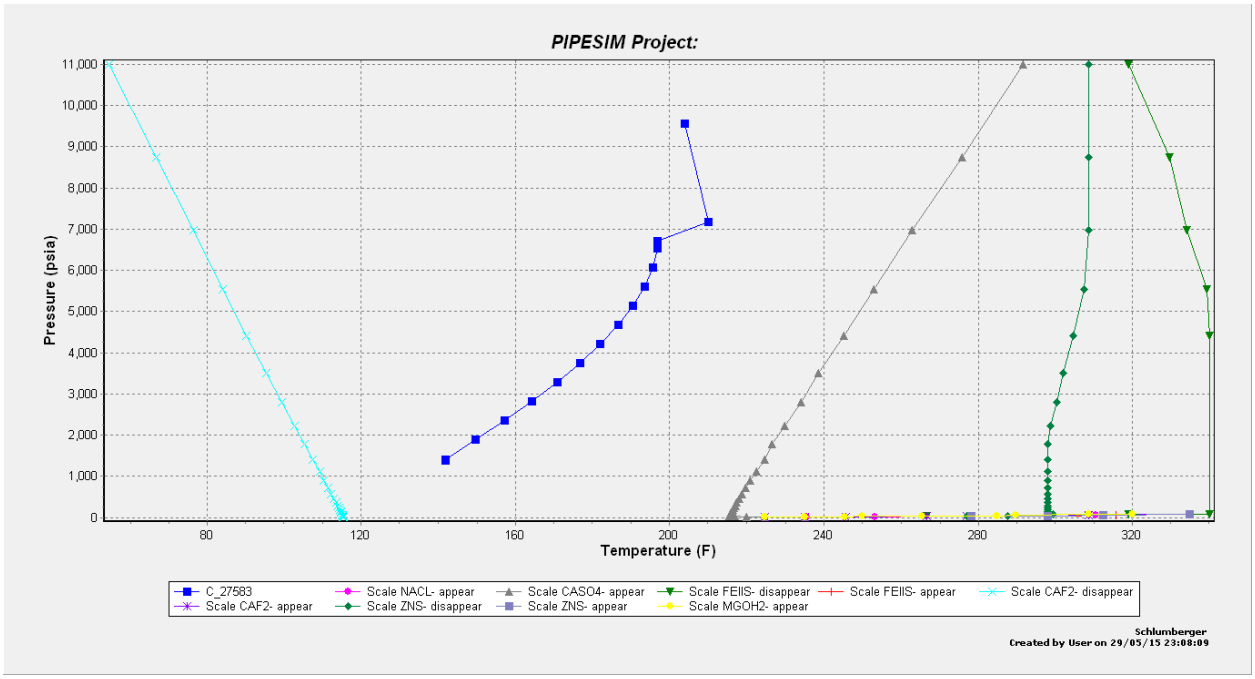


**Figure 6.34:** Pressure vs temperature plot for the system including surface equipment using the 2011 geochemical data. Note the wellbore conditions are represented by C_27583 on the plot.

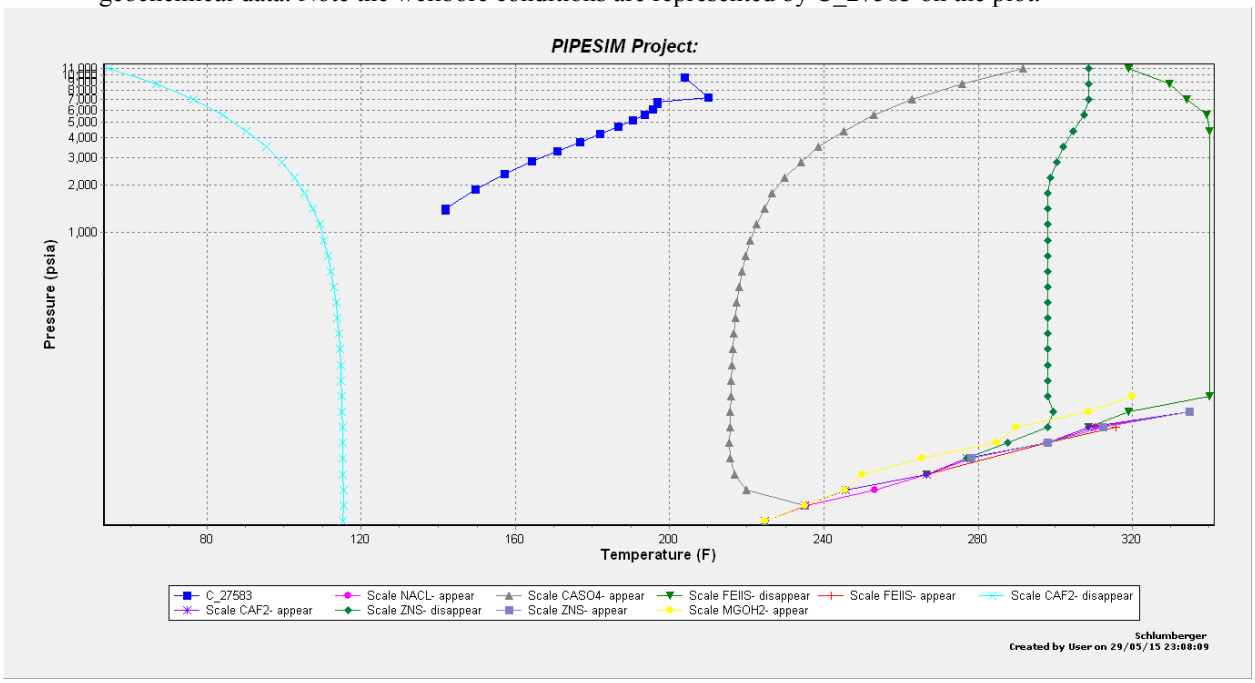


**Figure 6.35:** Pressure vs temperature plot for the system including surface equipment using the 2011 geochemical data (logarithmic pressure axis). Note the wellbore conditions are represented by C_27583 on the plot.

Because the temperature and pressure ranges for the system with and without surface equipment are similar, the corrosion modeling for the system without surface equipment (over the same temperature and pressure range) is applicable the model including the surface system. This implies that 2205 duplex steel would perform best on the pre-treatment side of the system.

However, the selection of materials should be based on the expense of the equipment and the expected lifetime of the equipment.

## Discussion

Sizing of the production well led to a design with 5-inch 15lb/ft tubing, 7 5/8-inch surface casing, and 10 ¾-inch surface casing, a scale is dominantly $CaCO_3$, and with FeS in the 2012 brine. The possibility of scaling means that scale removal will need to be considered in brine production scenarios. Scale removal may include acid treatment to remove CaCO3 and chelation or dissolution to remove FeS. The corrosion modeling indicates that the best choice for tubing material was 2205 duplex steel.

The corrosion modeling for the well indicates that 2205 series duplex steel performs best; it has the smallest generalized corrosion and does not show potential for localized pitting. However, 2205 is an unusual metallurgy for oilfield applications, although duplex steels have been used for three Shell Quest injection wells. To select a final metallurgy for a project in the Rock Springs Uplift, an economic analysis would need to be performed that takes into account the cost of the tubing for each metallurgy and the lifespan of the tubing as compared to the length of the project. It is important to note that the addition of oxygen to the reservoir between 2011 and 2012 led to more severe corrosion conditions for the brine production well and surface equipment. It may be advisable to consider limiting operations that introduce oxygen for long-term projects.

Modelling of the production well also showed that the Madison reservoir was more than 100 times more productive than the Weber reservoir, which may imply that CCS and brine production in the Weber may not be effective and that both injection and production wells should be completed only in the Madison formation.

It is important to point out that a wellhead pressure above 5,000 psi may require a wellhead with special seals or valves. It may be useful to perform a study to see if it is more cost effective to operate the reservoir and a lower pressure and use pumps to produce brine instead of relying on injection to pressurize the reservoir for production.

## Conclusion

Scaling and corrosion from brine production was modelled using data collected from the RSU#1 well, the CMI reservoir model, and assumptions about the needs of a hypothetical project. The project was broken into three tasks:

- *Subtask 1*—Simulate and evaluate wellbore scaling issues
- *Subtask 2*—Evaluate the effect of brine chemistry on well construction and casing integrity
- *Subtask 3*—Evaluate the effects of brine chemistry on produced water treatment infrastructure

Completing the three tasks in the modelling project required four steps. Based on the first step:

1. Use the selected tubing size to calculate fluid profiles (flow velocity, flow volume, pressure, and temperature profiles) along the well. The tubing for the production well was selected as 5-inch 15 lb/ft based on a nodal analysis in PIPESIM. Three wells using 5-inch 15lb/ft are required to withdraw the required 1,000,000 tonnes per year of brine. The tubing size was used to select a 7 5/8-inch long-string casing and a 10 ¾-inch surface casing. Modelling of the production well also showed that the Madison reservoir was more than 100 times more productive than the Weber reservoir, implying that CCS and brine production in the Weber is not as effective.
2. Use the flow profiles in conjunction with site-specific geochemistry data to model potential scale in tubing and surface equipment;
3. Use the flow profiles, in conjunction with site-specific geochemistry, data to model potential scale in tubing and surface equipment.
4. Use the flow profiles, in conjunction with site-specific geochemistry data, to model corrosion potential in tubing and surface equipment.

The wellbore scale modelling showed that the scale, under either the 2011 or 2012 brine regimes, was dominated by $CaCO_3$. The corrosion modelling, showed that 2205 duplex steel performed best with very low general corrosion rates and no localized corrosion potential. However, the 13-chrome and 304 stainless alloys both performed better than mild steel and a cost benefit analysis should be conducted to select the appropriate alloy. The extended surface model results were very similar to the model results of the wells, suggesting that the brine and corrosion well models developed are directly applicable to surface processing equipment. The results of the corrosion modeling indicate that the introduction of oxidizing agents within the reservoir fluids causes more severe corrosion conditions. For future operations it may be advisable to limit oxygen introduction or materials should be selected based on the more severe brine regime.

## Task 7: Rock Springs Uplift integrated geological and geophysical $CO_2$ storage assessment

The framework data, analysis, techniques and conclusions that were deemed critical to reducing uncertainty relative to long-term $CO_2$ storage were combined in a Best Practices Manuel (See Appendix) for this task. The manual is organized by subsurface data requirements and analysis, geologic evaluation and framework analysis, engineering constraints, and modeling requirements and constraints. The document is expected to be transferrable to other sites for seal analysis, and has helped to refine safe total injection volumes.

## PROJECT SUMMARY

This study of confining layer properties at the potential CCS study site at the Rock Springs Uplift in southwest Wyoming has identified four primary confining layers, in addition to multiple redundant confining layers, that could competently retain commercial volumes of injected $CO_2$ within targeted seals. This project employed the evaluation and integration of physical subsurface data to identify risks associated with $CO_2$ migration through a confining layer in order to reduce uncertainties at the site. This allowed us to refine dynamic injection models and define new conservative, low-risk volume estimates (25MT over 50 years), identify those parameters that introduced the highest degree of uncertainty on the confining systems, and develop injection/production field scenarios that optimize storage and minimize confinement risk. We suggest that safe, long-term, $CO_2$ injection is valid at the Rock Springs Uplift study site, particularly through the development of a reservoir pressure management strategy.

# GRAPHICAL MATERIALS LIST(S)

## Figures

**Figure 2.1:** 3-D seismic amplitude volume after reprocessing at Echo Geophysical Co. Note an overall northeast dip of seismic reflections. Projection of the RSU 31 well (white circle) is shown on the horizontal time slice.

**Figure 2.2:** Color-coded structure maps of the interpreted horizons: (a) lower Triassic and (b) Madison Limestone. Contour interval is 100 feet for all maps. The depth reference point is the Kelly bushing (KB) at RSU #1 well.

**Figure 2.3:** Horizon slice through the top of the Madison reservoir from a most-negative curvature volume generated from post-stack migrated seismic data (a). Azimuths of interpreted lineaments (red segments) are displayed in the rose diagram (b), according to relative frequencies (number of occurrences).

**Figure 2.4:** Horizon slice through the top of the Lower Triassic level from a most-negative curvature volume generated from post-stack migrated seismic data (a). Azimuths of interpreted lineaments (red segments) are displayed in the rose diagram (b), according to relative frequencies (number of occurrences).

**Figure 2.5:** (a) Sandstone outcrop four miles southwest of the RSU #1 well (aerial photograph from GeoMAC Viewer). Joints in the Cretaceous Rock Springs Formation are marked as red segments, (b) orientations of the marked joints in (a) combined in the form of Rose diagram.

**Figure 2.6:** Interpreted southwest-northeast section through the seismic amplitude volume (north from the RSU #1 well). Red segments indicate interpreted discontinuities in a reflectivity pattern.

**Figure 2.7:** Interpreted southwest-northeast section through the seismic coherence volume (energy-normalized amplitude gradients). Red segments indicate interpreted discontinuities in a reflectivity pattern.

**Figure 2.8:** Interpreted southwest-northeast section through the seismic amplitude volume. Red segments indicate interpreted discontinuities in a reflectivity pattern.

**Figure 2.9:** Seismic coherency map on top of the Middle Madison unit. Coherence changes from high (light color) in areas with continuous reflections to low in areas of intense fracturing, faulting (dark elongated features), and dissolution pipes development (dark, isolated oval features). Green lines indicate locations of vertical sections shown in Figures 6-8. Note an overall high coherency of seismic reflections in the updip direction (south and west from the RSU #1 well).

**Figure 2.10:** Seismic coherency map on top of the Amsden stratigraphic unit. Coherence changes from high (light color) in areas with continuous reflections to low in areas of intense fracturing, faulting (dark elongated features), and dissolution pipes development (dark, isolated oval features). Green lines indicate locations of vertical sections shown in Figures 6-8. Red arrowhead indicates interpreted dissolution pipe outlined in Figure 8.

**Figure 2.11:** Seismic coherency map on top of the Dinwoody stratigraphic unit. Coherence changes from high (light color) in areas with continuous reflections to low in areas of intense fracturing, faulting (dark elongated features), and dissolution pipes development (dark, isolated oval features). Green lines indicate locations of vertical sections shown in Figures 6-8. Note an increased amount of isolated oval features that we interpret as dissolution pipes.

**Figure 2.12:** 3-D perspective display made of two orthogonal vertical sections (in-line 70 and cross-line 94) and two stratal slices at Madison and Triassic stratigraphic levels. Data selection is done over the volume of Rock Integrity attribute: a view from the northeast. Note a karst collapse feature (marked with red arrowheads) that originates at the top of the Madison reservoir and cuts through the rock sequence well above the Triassic horizon.

**Figure 2.13:** 3-D perspective display made of two orthogonal vertical sections (in-line 168 and cross-line 91) and two stratal slices at Madison and Triassic stratigraphic levels. Data selection is done over the volume of Rock Integrity attribute: a view from the southeast. Note a karst collapse feature (marked with red arrowheads) that

originates at the top of the Madison reservoir and cuts through the rock sequence well above the Triassic horizon. The basement-rooted reverse faults are marked with black arrowheads.

**Figure 2.14:** Density log from the bottom part of the RSU #1 well (black bar graph in the middle panel) and its spectrogram (right-most panel). Spectral amplitude intensifies from yellow to blue color. Note peak amplitudes with wavelengths ranging from 10 to about 50 feet in the Middle Madison unit that correlate with the area of dolomitization and solution cavities development. Morphological observations are from Sando (1988) for north-central Wyoming throughout the outcrop area of the Madison paleokarst.

**Figure 3.1** Idealized seal chart by lithology. Lithology types from this study are highlighted by red box. Figure modified from IEAGHG, March 2009

**Figure 3.2:** Stress diagram for sample 2V, from the Chugwater Group. The "warble" at the beginning of measured axial and radial strain indicates ductility and elasticity.

**Figure 3.3:** Stress diagram for sample 31V from the Weber Sandstone showing near instantaneous depletion of axial and radial strain at failure, indicating a relatively brittle formation.

**Figure 3.4:** Histogram of pore throat sizes from cuttings form the Dinwoody Formation (from 10,820 to 10,840 ft.). Pore throat sizes are dominantly micro to nano size.

**Figure 3.5:** Previous studies have identified a correlation between specific lithology and sealing potential. This study shows comparable (and the highest) sealing potential between marine sediments, but continental sediments (i.e. the Red Peak Formation) at our study site has enhanced sealing potential relative to other investigated siltstones.

**Figure 3.6:** Gamma log showing formation tops, thicknesses, depths, and cored intervals for the RSU#1 well. This data suggests that there are multiple units with lithological characteristics similar to analyzed seals.

**Figure 3.7:** 10603.2 XRD clay fraction diagram. This sample had noticeably steeper peaks than other Triassic samples. Petrographic analysis suggests a high percentage of mudstone relative to other samples.

**Figure 3.8:** 10,636.3. XRD clay fraction diagram. This sample has illite as a primary clay with minimal mixed-layer clays. This supports the thin section analysis and burial history interpretations.

**Figure 3.9:** 10,680.05. XRD clay fraction diagram. Note the consistency with Figure 3.8.

**Figure 3.10:** 10,780-10,800. XRD clay fraction diagram from cuttings. The illite and chlorite spikes are more pronounced than the Red Peak samples, indicating higher proportions of clay in the Dinwoody Formation.

**Figure 3.11:** 10,820-10,840. XRD clay fraction diagram from cuttings. Note the consistency with Figure 3.10 indicative of the homogeneous lithology of Triassic units.

**Figure 3.12:** 10,840-10,860. XRD clay fraction diagram from cuttings. Again, this shows a high degree of similarity to other Triassic samples.

**Figure 3.13:** Spectral log analysis of clay species. Note the increasing chemical maturity of the deeper shales such as the Chugwater Group relative to the Mowry Shale.

**Figure 3.14:** Advanced spectral log analysis of the oxidation states various sealing lithologies. Note that relatively organic-rich shales, such as the Phosphoria/Parky City and Mowry formations, are generally reduced and that the redbeds of the Chugwater Group are the most oxidized seals.

**Figure 3.15:** Stable isotopic analysis of potential seals from the RSU#1 well site. Primary, unaltered carbonates of the Madison and the Amsden record similar isotopic compositions, samples from the Red Peak (Chugwater Group) have enriched carbon values, similar to the dolostone in the Madison. None of the samples are similar to high temperature calcite vugs/veins, though additional Amsden samples are being tested. *

**Figure 4.16:** Mineral precipitation and dissolution in the fractures in the event of failure.

**Figure 5.1:** The injected $CO_2$ is trapped below the most upper portion of the Madison Limestone and the Amsden Formation and the $CO_2$ column can be 450 ft. of height.

**Figure 5.2:** Plot of porosity and density versus depth for the Dinwoody Formation and Amsden Formation (containment strata). Both porosities measured under 800 psi NCS and reservoir NCS are shown.

**Figure 5.3:** Plot showing the air and Klinkenberg permeability variations in both targeted reservoirs and containment formations under 800 psi NCS and reservoir NCS.

**Figure 5.4:** Cross plot of the laboratory measured porosity at reservoir conditions with the log derived bulk density porosity (A) and neutron porosity (B).

**Figure 5.5:** Plots of gamma ray, bulk density, neutron porosity, and density porosity for the Dinwoody Formation, Phosphoria Formation, Weber Sandstone, Amsden Formation and Madison Limestone from the RSU#1 well. The heavy magenta line is neutron-density porosity: it is calculated from neutron and density porosity, and is used to establish the function between the porosity and sonic velocity.

**Figure 5.6:** Cross plot of the laboratory measured porosity at reservoir conditions with the log derived neutron-density porosity.

**Figure 5.7:** The smoothed sonic velocity and neutron-density porosity highly of change through the Dinwoody Formation in the RSU 1well (A). The relationship between the sonic velocity and neutron-density porosity for the Dinwoody Formation is derived from the cross plot (B).

**Figure 5.8:** Histograms generated for porosities of the Dinwoody Formation from Jim Bridger 3-D seismic data based on the function derived from porosity and sonic logs from the RSU #1 well.

**Figure 5.9:** The smoothed sonic velocity and neutron-density porosity highly of change through the Red Peak Formation in the RSU#1 well (A). The relationship between the sonic velocity and neutron-density porosity for the Red Peak Formation is derived from the cross plot (B).

**Figure 5.10:** Histograms generated for porosities of the Red Peak Formation from Jim Bridger 3-D seismic data based on the function derived from porosity and sonic logs from the RSU#1 well.

**Figure 5.11:** Histograms showing the permeability distribution of the containment formations Dinwoody (A) and Chugwater (B) in the RSU geological $CO_2$ storage simulation domain.

**Figure 5.12:** Contour map of the porosity distribution of the Dinwoody Formation in the potential RSU geological $CO_2$ storage site. Within the domain, the porosity of the Dinwoody Formation ranges from 1% to 10%, with a mean of 4.5%.

**Figure 5.13:** Contour map of the porosity distribution of the Red Peak Formation in the potential RSU geological $CO_2$ storage site. Within the domain, the porosity of the Red Peak Formation ranges from 1% to 10%, with a mean of 5%.

**Figure 5.14:** FEHM $CO_2$ injection simulation results for the Weber Sandston, RSU. The simulation is setup for a homogeneity reservoir petropgysical conditions with 10% of porosity and 1md of relative permeability. The injection rate of 31.71 kg/s is constant for 50 years, then the injection ceased, and the simulation still run for other 50 years without $CO_2$ injection. Note that the reservoir pressure is elevated quickly when the injection starting, but kept below the hydro-fracture pressure through all injection time. After the injection ceased, the reservoir pressure is back to original pressure within 10 years.

**Figure 6.32:** P vs T plot for the system including surface equipment using the 2012 geochemical data. Note the wellbore conditions are represented by C_29310 on the plot.

**Figure 6.33:** P vs T plot for the system including surface equipment using the 2012 geochemical data (logarithmic pressure axis). Note the wellbore conditions are represented by C_29310 on the plot.

**Figure 6.34:** P vs T plot for the system including surface equipment using the 2011 geochemical data. Note the wellbore conditions are represented by C_27583 on the plot.

Figure 6.35: **P vs T plot for the system including surface equipment using the 2011 geochemical data (logarithmic pressure axis). Note the wellbore conditions are represented by C_27583 on the plot.**

**Figure A.1:** Amsden Formation, 12,209': Bimodal siltstone. This facies represents a local period of regression, as shown by the influx of detrital clasts. Interestingly, the clasts are composed of quartz, with minor heavy accessory minerals. The lack of detrital feldspars, and the kaolinite/siliceous matrix, indicate thorough diagenetic alteration of this facies. Petrographic analyses show little to no porosity.
**Figure A.2:** Amsden Formation, 12,182': Clastic carbonate. Detrital clasts in a dolomitic matrix; large vug in the center of the slide is filled with late-stage ferroan and non-ferroan dolomites. This facies represents the transitional facies between siltstone and carbonate. Petrographic analyses show little to no porosity.
**Figure A.3:** Amsden Formation, 12,199': Dolomite. Fine-grained, sub- to –euhedral, sucrosic dolomite with no relict textures. Petrographic analyses show little to no porosity.

**Figure A.4:** Amsden Formation, 12,169.8'. Limestone. Fossiliferous micrite with minor secondary (post-deposition) crystallization within molds. Petrographic analyses show little to no porosity.

**Figure A.5:** Amsden Formation, 12,219.5': Neomorphic calcite with relict detrital clasts, chert, dolomite and stylolites. This facies has been thoroughly altered by burial diagenesis. Petrographic analyses show little to no porosity.

**Figure A.6:** Amsden Formation, 12,225': Shaly siltstone at the base of the formation. Laminated siltstone, carbonate, and hematitic shale at the contact between the Amsden and the Madison. Identified as a paleosol elsewhere in the state. Petrographic analyses show little to no porosity.

**Figure A.7:** Triassic red bed, 10,680.05: Red siltstone. Siltstone, some cross beds, with a matrix of hematite and calcite. Also includes some intraclasts, anhydrite and clays. Petrographic analyses show little to no porosity.

**Figure A.8:** Triassic red bed, 10,633.8: Green siltstone. Similar to Figure A-7, except matrix is dominantly anhydrite and calcite (no hematite). This zone either reduced post-burial, or was never oxidized at the surface. Note the large mud intraclast, and smaller rounded carbonate intraclast. Petrographic analyses show little to no porosity.

**Figure A.9:** Upper limestone facies of the Madison Limestone, 12,247.0: Micritic limestone, with some pelites and relict fossils. Very little secondary recrystallization. Petrographic analyses show little to no porosity.

**Figure A.10:** Shale/siltstone at the base of the Weber, 11,725.1': Clastic shale with chert nodules. This facies has sealing capacity.

**Figure A.11:** Analysis of clastic quartz composition of section at 10,656'4.32". Total quartz grains approximately 12.5% of total area.

**Figure A.12a:** Clastic grain distribution, 10,603'2.4"

**Figure A.12b:** Minor bimodal distribution, the majority of clasts are small.

**Figure A.13a:** Clastic grain distribution, 10,680'

**Figure A.13b:** A more pronounced bimodal distribution relative to A-12b due to a spike in larger grain sizes.

**Figure A.14a:** Clastic grain distribution, 10,682'1.2"

**Figure A.14b:** A continuing trend of bimodal distribution.

**Figure A.15:** 10,604 anhydrite surrounding mudstone rip-up clasts

**Figure A.16:** 10,671.8 Evidence of chaotic bedding

**Figure A.17:** A bedding unconformity at 10,633'9.6" indicating a period of scouring. Grain sizes and mineralogy in the top left corner differs; the unconformity has an increased concentration of Fe-stained clays.

**Figure A.18:** 10,638'1.44" increased calcite cement, glauconite and micritic dolostones rip-up clasts.

**Figure A.19:** 10,633'9.6" chickenwire anhydrite and mud rip-up clast

**Figure A.20:** 10,662 evidence of a reduction in Chugwater Group strata including lack pyrite and dispersed calcite.

**Figures A.21-32:** Clay proportion XRC diagrams from cuttings of different potential sealing units. Note the decrease in mixed-layer clays with depth, and the increase in illite (example Figure A.32)

- **Figure A.21:** 4,140-4,170
- **Figure A.22:** 5,160-5,190
- **Figure A.23:** 8,040-8,070
- **Figure A.24:** 8,100-8,130
- **Figure A.25:** 9,100-9,110
- **Figure A.26:** 9,200-9,210
- **Figure A.27:** 9,870-9,880
- **Figure A.28:** 11,120-11,130
- **Figure A.29:** 10,940-10,960
- **Figure A.30:** 12178.45’
- **Figure A.31:** 12,216’
- **Figure A.32:** 12,220’

**Figure A.33:** Th/K spectral log graph for sediment maturity.

**Figure A.34:** Chugwater Group and Dinwoody Formation combined thickness.

**Figure A.35:** Amsden Formation thickness and A-A’ cross-section location.

**Figure A.36:** Upper Madison limestone facies thickness.

**Figure A.37:** Type 5 Double End Hydrocarbon Sample Cylinder

## Tables

# REFERENCES


Al-Bazali, Talal M, et al (2005) "Measurement of the sealing capacity of shale caprocks" SPE Annual Technical Conference and Exhibition. Society of Petroleum Engineers

API RP40 (1988) American Petroleum Institute Codes: www.techstreet.com/**API**+**RP**+**40**

Asquith G, Gibson C (1982) Basic well log analysis for geologists: Methods in Exploration Series, AAPG, Tulsa, p 216

Bethke C M (1996) Geochemical reaction modeling: concepts and applications. Oxford University Press

Brown E M, Skuuogstad W, Fishman M J (1970), Methods for collection and analysis of water samples for dissolved minerals and gases, laboratory analysis, US Geological Survey Technical Water Resource Investigation 5(C1)

Busch A, Alles S, Gensterblum Y, Prinz D, Dewhurst D N, Raven M D, Stanjek H, and Krooss B M (2008) Carbon dioxide storage potential of shales. International Journal of Greenhouse Gas Control 2, no 3: 297-308.

Buursink M A, Covault, Jahediesfanjani H (2011) Geologic carbon dioxide sequestration column height sensitivity analysis, AAPG Pacific Section Meeting, Abstract

Carpenter A B (1978) Origin and chemical evolution of brines in sedimentary basins. Oklahoma Geological Survey 79:60–77

Chalbaud C, Robin M, Lombard J, Martin F, Egermann P, and Bertin H (2009) Interfacial tension measurements and wettability evaluation for geological $CO_2$ storage. Advanced Water Research 32, 98–109

Chiquet P J, Daridon D, Broseta, Thibeau S (2007) $CO_2$/water interfacial tension under pressure and temperature conditions of $CO_2$ geological storage: Energy Conservation and Management, v. 48, p. 736-744

Chopra, Satinder, Marfurt (2007) Seismic attributes for prospect identification and reservoir characterization, Geophysical Developments No. 11, Society of Exploration Geophysicists; 1st edition, 464 pages

Chun BS, Wilkinson G T (1995) Interfacial tension in high-pressure carbon dioxide mixtures. Industrial & Engineering Chemical Research; 34:4371–7

Cooper S P, Hart B, Goodwin L B, Lorenz J C, Milliken M (2003) Outcrop and seismic analysis of natural fractures, faults and structure at Teapot Dome, Wyoming, in Horn MS ed., Wyoming basins/reversing the decline: Wyoming Geological Society Field Guidebook 2002/2003, p 63-74

Cooper S P, Hart B, Goodwin L B, Lorenz J C (2006) Fracture and fault patterns with basement-cored anticlines: The example of Teapot Dome, Wyoming. American Association of Petroleum Geologists Bulletin v. 90, no. 12, p 1903-1920

Daniel R, Kaldi J (2008) Evaluating seal capacity of caprocks and intraformational barriers for the geosequenstration of $CO_2$: PESA Eastern Australian Basins Symposium III, p 475-484

Dickson J L, Gupta G, Horozov T S, Binks B P, Johnston K P (2006) Wetting phenomena at the $CO_2$/water/glass interface: *Langmuir*, v. 22, no. 5, p. 2161–2170

Duan, Z, Hu J, Li D, and Mao S (2008) Densities of the $CO_2$–$H_2O$ and $CO_2$–$H_2O$–NaCl Systems Up to 647 K and 100 MPa, *Energy Fuels,* v. 22, p. 1666-1674.

Espinoza D N, Santamarina J C (2010) Water–$CO_2$–mineral systems: interfacial tension, contact angle, and diffusion – Implications to $CO_2$ geological storage: Water Resources. Res. 46, W07537. doi:10.1029/2009WR008634

Edlmann K S, Haszeldine, McDermott C (2013) Experimental investigation into the sealing capability of naturally fractured shale caprocks to supercritical carbon dioxide flow: Environmental Earth Science, v. 70 p.3393-3409

Hassanzadeh H M, Poladi-Darvish, Keith D (2009) Accelerating $CO_2$ dissolution in saline aquifers for geological storage – mechanistic and sensitivity studies: Energy and Fuel (2009) V. 23, p 3328-3336

Hennings P H, Olson J E, Thompson L B (2000) Combining outcrop data and three-dimensional structural models to characterize fractured reservoirs: An example from Wyoming: American Association of Petroleum Geologists Bulletin v. 84, no. 6, p 830–849

Hildenbrand A, Schlomer S, Krooss BM, Littke R. Gas breakthrough experiments on pelitic rocks: comparative study with N2, $CO_2$ and CH4. Geofluids 2004; 4:61–80. Neuzil, C E, 1994. How permeable are clays and shales? Water Resources Research 30, 145–150.

Jiao Z, Surdam R (2013) Advances in estimating the geologic $CO_2$ storage capacity of the Madison Limestone and Weber Sandstone on the Rock Springs Uplift by utilizing detailed 3-D reservoir characterization and geologic uncertainty reduction: in Geological $CO_2$ storage characterization, Surdam editor, Springer, p 191-232

Li S, Dong M, Li Z, and Huang S, (2006) $CO_2$ sequestration in depleted oil and gas reservoirs – caprock characterization and storage capacity: Energy Conversion and Management, v. 47, p. 1372-1382.

Ligthelm R B, de Boer R B, Brint J F (1991) Reservoir souring: an analytical model for $H_2S$ generation and transport in an oil reservoir owing to bacterial activity. Society of Petroleum Engineers SPE 23141 p 369–378

Massoudi R, King A, (1975) Effect of pressure on the surface tension of aqueous solutions. Adsorption of hydrocarbon gases, carbon dioxide, and nitrous oxide on aqueous solutions of sodium chloride and tetra n butylammonium bromide at 25: Journal of Physical chemistry, v. 79, p. 1670-1675.

McCaffrey M A, Lazar B, Holland H D (1987) The evaporation path of seawater and the coprecipitation of $Br^-$and $K^+$ with halite. Journal Sediment Res 57:928–937

McLing, Travis, Smith W, and Smith R (2014) Utilizing Rare Earth Elements as Tracers in High TDS Reservoir Brines in CCS Applications. Energy Procedia 63 (2014): 3963-3974.

Neuzil C E (1994) How permeable are clays and shales? Water Resource Res 30:145–150

Nielsen L, Bourg I, Sposito G (2012) Predicting $CO_2$-water interfacial tension under pressure and temperature conditions of geological $CO_2$ storage: Geochimica et Cosmochimica Acta, v. 81, p 28-38
Oil and Gas Fields Symposium Committee (eds) (1979) Wyoming oil and gas fields symposium, Greater Green River Basin, Wyoming. Wyoming Geologic Association Publications on DVD (1946-2003) 2nd edition A (2010)

Purcell W (1949) Capillary pressures – their measurements using mercury and the calculation of permeability therefrom: AIME Petroleum Trans., v. 186, p 39-48

Rittenhouse G (1967) Bromine in oil-field waters and its use in determining possibilities of origin of these waters. American Association of Petroleum Geologists Bulletin 51:2430–2440

Rohmer J, and Seyedi D M (2010) Coupled Large Scale Hydrochemical Modelling for Caprock Failure Assessment of CO2 Storage in Deep Saline Aquifers, Oil and Gas Science and Technology, Vol. 65 No. 3, p 503-517

Sando W J (1988) Madison Limestone (Mississippian) paleokarst – A geologic synthesis, in James N P, Choquette P W eds., Paleokarst: New York, Springer-Verlag, p 256-277

Schowalter TT (1979) Mechanics of secondary hydrocarbon migration and entrapment: AAPG Bulletin, v. 63, p 723–760

Siemons N, Busch A, (2007) Measurement and interpretation of supercritical $CO_2$ adsorption on worldwide coals: int. J. coal Geology, v. 69, p 229-242

Silva P, Ranjith P (2012) A study of methodologies for $CO_2$ storage capacity estimation of saline aquifers: Fuel, v. 93, p 13-27

Smith, D A, (1966) Theoretical considerations of sealing and non-sealing faults: AAPG Bulletin, v. 50, p. 363-374.

Surdam R C, Jiao J (2007) The Rock Springs Uplift – an outstanding geologic CO2 sequestration site in southwest Wyoming. Wyoming State Geologic Survey Challenges in Geologic Resource Development No. 2

USGS, Produced waters database, http://energy.cr.usgs.gov/prov/prodwat/, accessed March, 2015

USGS Southwestern Wyoming Province Assessment Team (2005) Petroleum Systems and Geologic Assessment of Oil and Gas in the Southwestern Wyoming Province, Wyoming, Colorado, and Utah, USGS Digital Data Series DDS-69-D, Version 1.0

Vavra, C L, Kaldi J G, Sneider R M (1992) Geological applications of capillary pressure: a review (1), AAPG Bulletin 76.6: 840-850.

Viswanathan, H S, Pawar, R J, Stauffer, P H, Kaszuba, J P, Carey, J W, Olsen, S C, Keating, G N, Kavetski, D, Guthrie, G D (2008) Development of a hybrid process and system model for the assessment of wellbore leakage at a geologic $CO_2$ sequestration site: Environmental Science & Technology 42, 7280–7286

Walter L M, Stueber A M, Huston T J (1990) Br–Cl–Na systematics in Illinois Basin fluids: constraints on fluid origin and evolution. Geology 18:315–318

Wollenweber, J, Alles S, Busch A, Krooss B M, Stanjek H, and Littke R (2010) "Experimental investigation of the $CO_2$ sealing efficiency of caprocks." International Journal of Greenhouse Gas Control 4, no. 2 231-241.

Wyoming Oil and Gas Commission, http://wogcc.state.wy.us/, accessed March, 2013

Wyoming Oil and Gas Conservation Commission http://wogcc.state.wy.us/. Accessed 2014-15

Yang D, Tontiwachwuthikul P, Gu Y. Interfacial interactions between reservoir brine and $CO_2$ at high pressures and elevated temperatures. Energy Fuels 2005; 19:216–23

Yang Y, Aplin A C, (2010) A permeability-porosity relationship for mudstone: Marine and Petroleum Geology 27. p 1692–1697

Zyvoloski G A, Robinson B A, Dash Z V, Trease L L, (1997) Summary of the models and methods for the FEHM application – a finite element heat-and mass-transfer code: Rep. LA-13307-MS, Los Alamos National Laboratory, Los Alamos, New Mexico

# LIST OF ACRONYMS AND ABBREVIATIONS

***API-****American Petroleum Institute well identification number*

***aq-*** *aqueous*

***BPM****-Best Practices Manual*

***BTEX****-Benzene, toluene, Ethylbenzene and xylenes*

***CMI****-Carbon Management Institute*

***CMP****-common midpoint*

***CV****-calcite vug*

***FEHM****-Finite Element Heat and Mass Transfer Code*

***Fm****-Formation*

***GR****-gamma ray*

***HREE****-heavy rare earth elements*

***ICP-MS****- inductively coupled plasma mass spectrometry*

***ID****-inside diameter*

***IFT****-interfacial tension*

***LREE****-light rare earth elements*

***mD****-milli-Darcy*

***NCS****-net confining stress*

***ND****-neutron density*

***NF****-nanofiltration*

***OD****-outside diameter*

***psi-*** *pounds per square inch*

***PSTM****-Pre-stack Time Migration*

***RCI****-Reservoir Characterization Instrument*

***REE****-rare earth elements*

***RO****-reverse osmosis*

***RSU****- Rock Springs Uplift*

***Ss****-Sandstone*

***TDS****-total dissolved solids*

***USGS-*** *United States Geological Survey*

***VOC****-volatile organic compounds*

***VSP****-vertical seismic profile*

***WGA****-Wyoming Geological Association*

***WOGCC****-Wyoming Oil and Gas Commission*

***WSGS****-Wyoming State Geological Association*

***WY-CUSP****-Wyoming Carbon Underground Storage Project*

# APPENDIX A

**Figures A.1-36:** Petrographic thin sections and regional petrophysical data

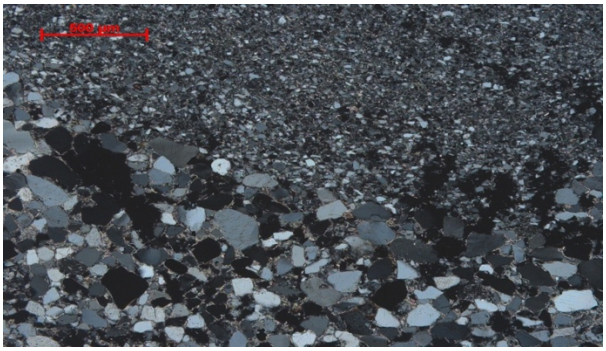

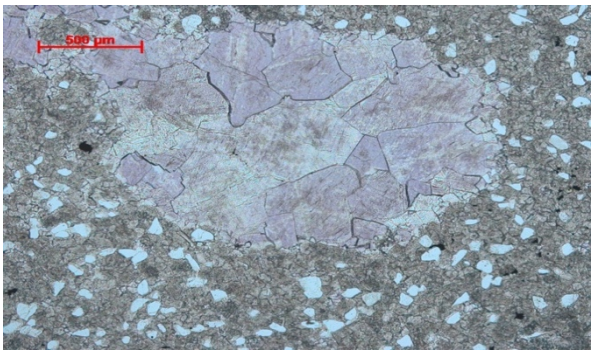


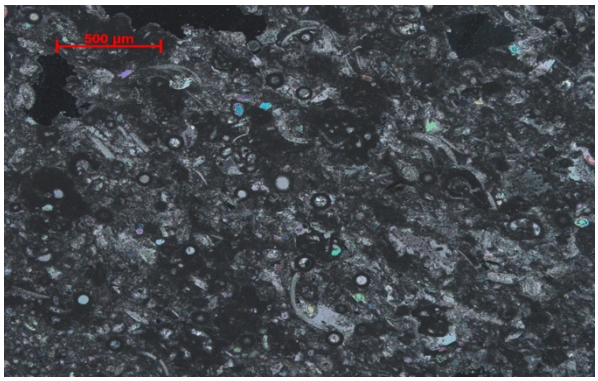


**Figure A.1:** Amsden Formation, 12,209': Bimodal siltstone. This facies represents a local period of regression, as shown by the influx of detrital clasts. Interestingly, the clasts are composed of quartz, with minor heavy accessory minerals. The lack of detrital feldspars, and the kaolinite/siliceous matrix, indicate thorough diagenetic alteration of this facies. Petrographic analyses show little to no porosity.

**Figure A.2:** Amsden Formation, 12,182': Clastic carbonate. Detrital clasts in a dolomitic matrix; large vug in the center of the slide is filled with late-stage ferroan and non-ferroan dolomites. This facies represents the transitional facies between siltstone and carbonate. Petrographic analyses show little to no porosity.

**Figure A.3:** Amsden Formation, 12,199': Dolomite. Fine-grained, sub- to –euhedral, sucrosic dolomite with no relict textures. Petrographic analyses show little to no porosity.

**Figure A.4:** Amsden Formation, 12,169.8'. Limestone. Fossiliferous micrite with minor secondary (post-deposition) crystallization within molds. Petrographic analyses show little to no porosity.

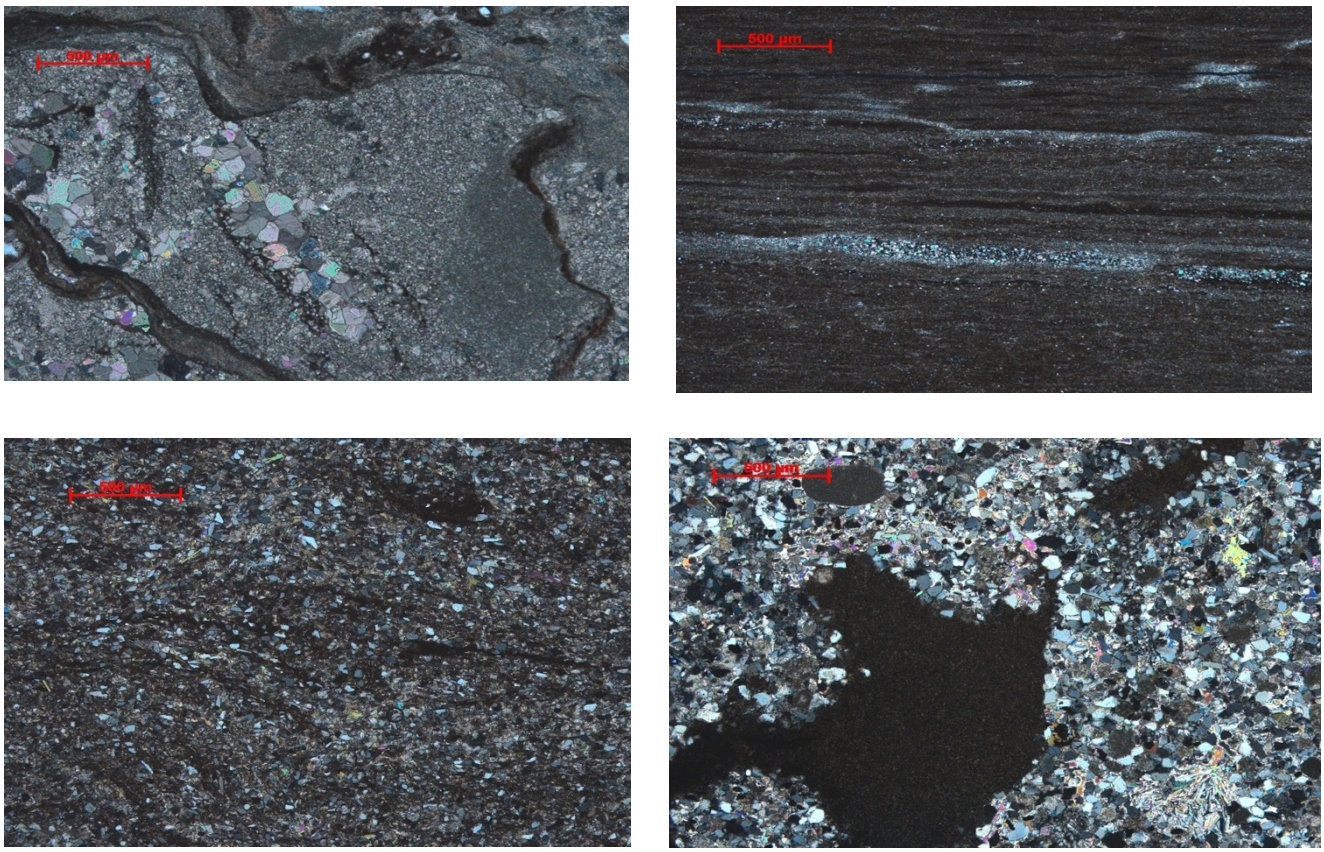


**Figure A.5:** Amsden Formation, 12,219.5': Neomorphic calcite with relict detrital clasts, chert, dolomite and stylolites. This facies has been thoroughly altered by burial diagenesis. Petrographic analyses show little to no porosity.

**Figure A.6:** Amsden Formation, 12,225': Shaly siltstone at the base of the formation. Laminated siltstone, carbonate, and hematitic shale at the contact between the Amsden and the Madison. Identified as a paleosol elsewhere in the state. Petrographic analyses show little to no porosity.

**Figure A.7:** Triassic red bed, 10,680.05: Red siltstone. Siltstone, some cross beds, with a matrix of hematite and calcite. Also includes some intraclasts, anhydrite and clays. Petrographic analyses show little to no porosity.

**Figure A.8:** Triassic red bed, 10,633.8: Green siltstone. Similar to Figure A-7, except matrix is dominantly anhydrite and calcite (no hematite). This zone either reduced post-burial, or was never oxidized at the surface. Note the large mud intraclast, and smaller rounded carbonate intraclast. Petrographic analyses show little to no porosity.

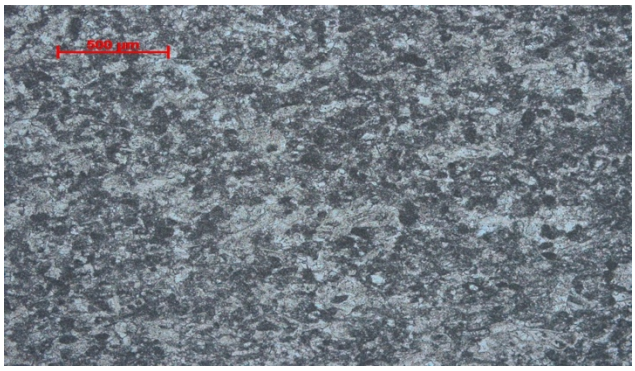

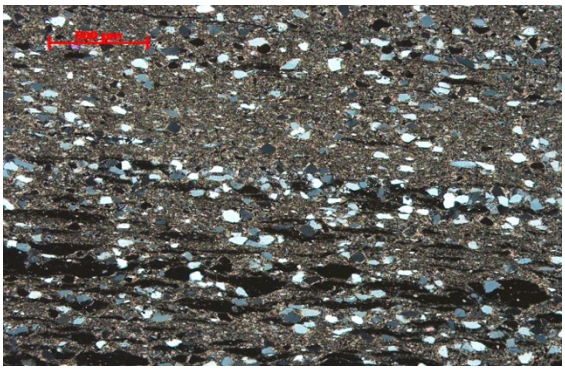

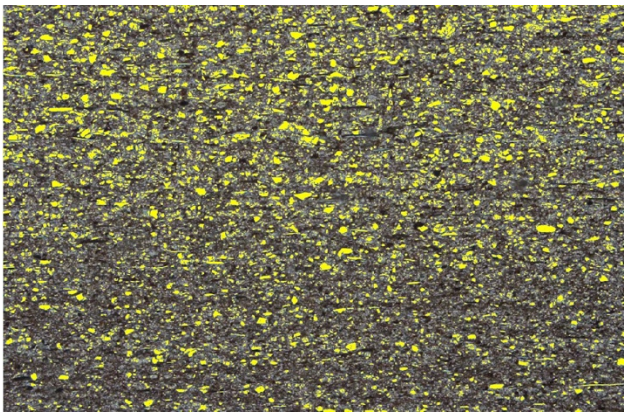

**Figure A.9:** Upper limestone facies of the Madison Limestone, 12,247.0: Micritic limestone, with some pelites and relict fossils. Very little secondary recrystallization. Petrographic analyses show little to no porosity.

**Figure A.10:** Shale/siltstone at the base of the Weber, 11,725.1': Clastic shale with chert nodules. This facies has sealing capacity.

**Figure A.11:** Analysis of clastic quartz composition of section at 10,656'4.32". Total quartz grains approximately 12.5% of total area.

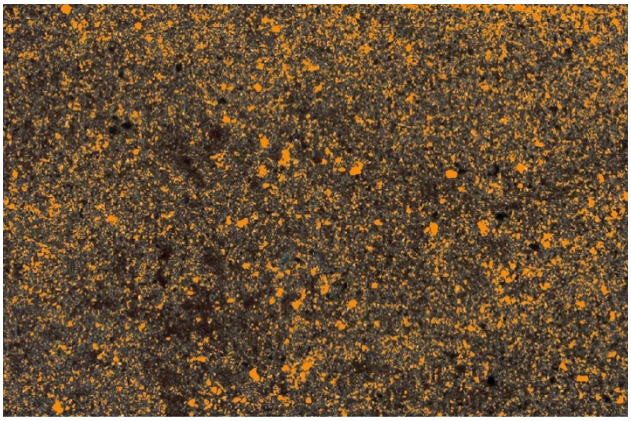

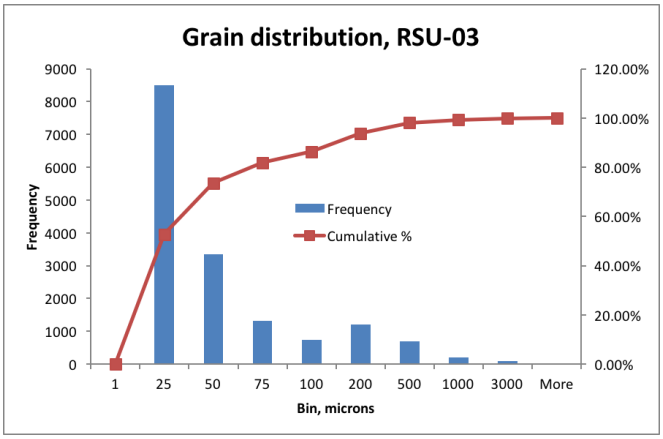


**Figure A.12a:** Clastic grain distribution, 10,603'2.4"
**Figure A.12b:** Minor bimodal distribution, the majority of clasts are small

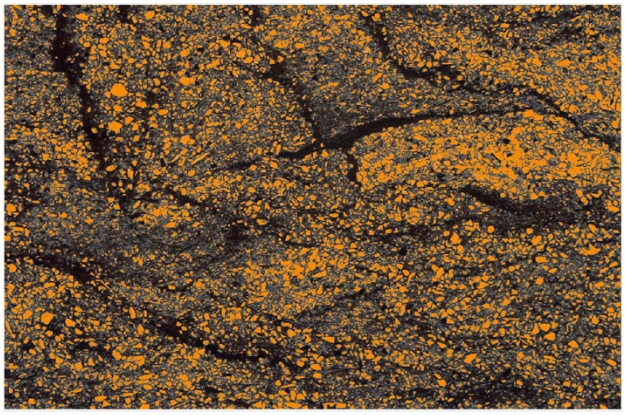

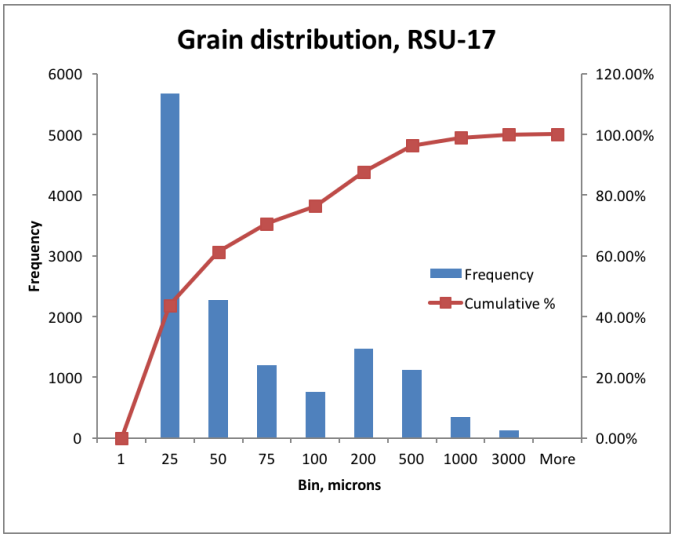


**Figure A.13a:** Clastic grain distribution, 10,680'
**Figure A.13b:** A more pronounced bimodal distribution relative to A.12b due to a spike in larger grain size

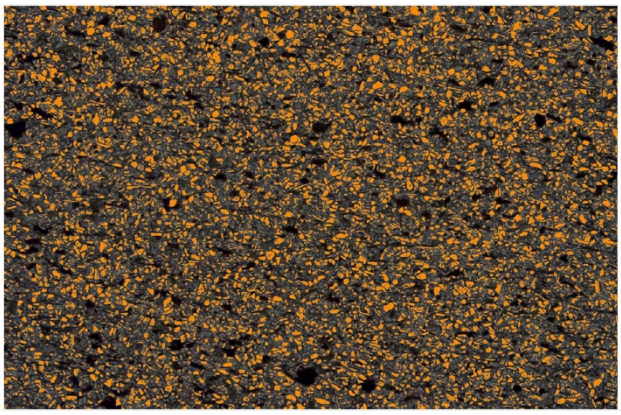

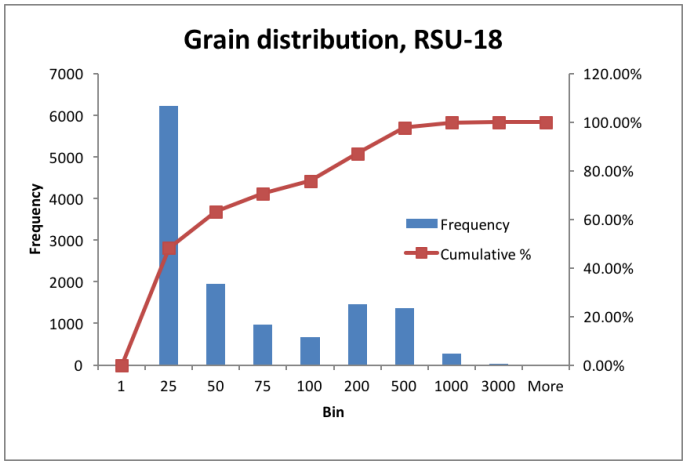


**Figure A.14a:** Clastic grain distribution, 10,682'1.2"
**Figure A.14b:** A continuing trend of bimodal distribuion

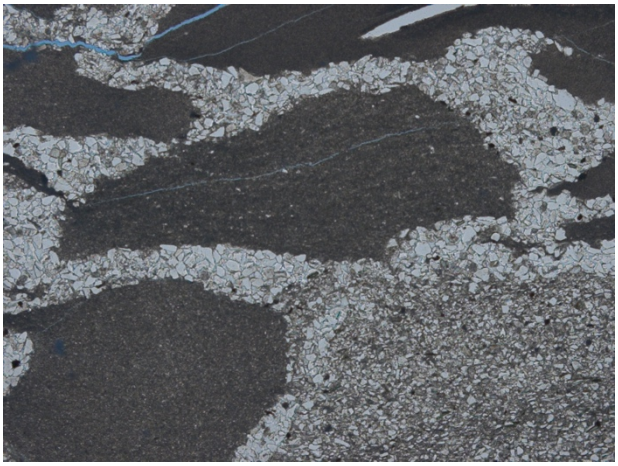
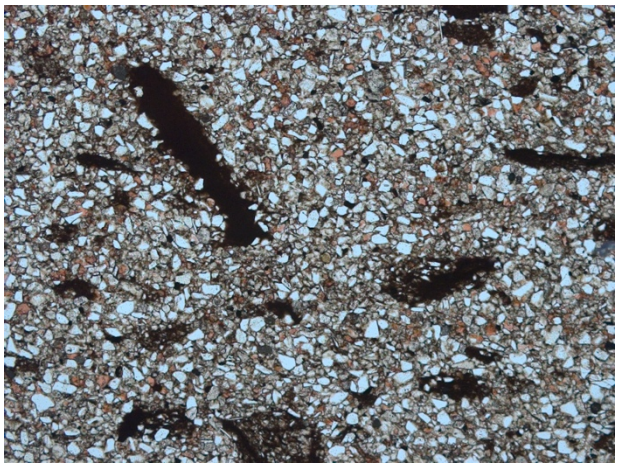
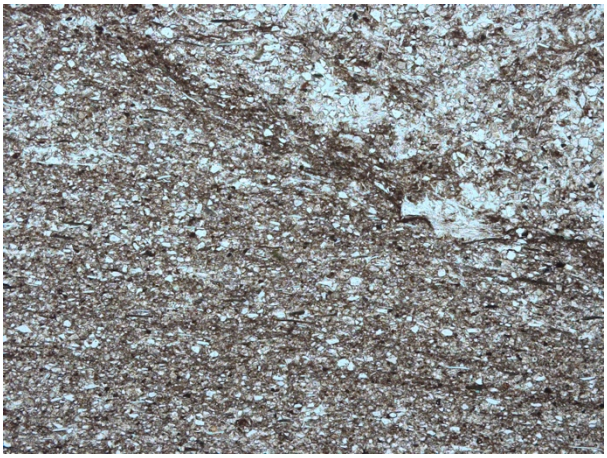
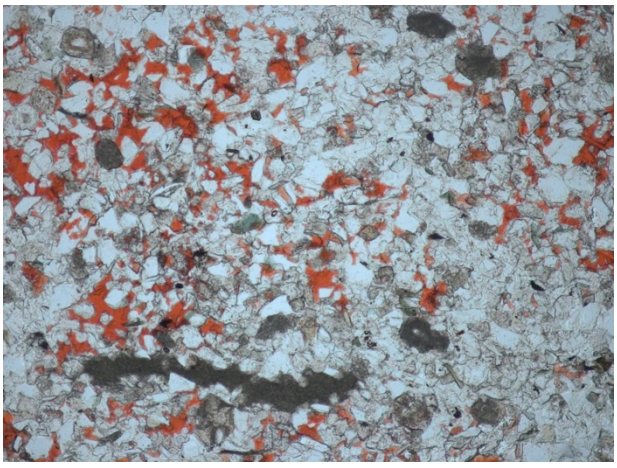
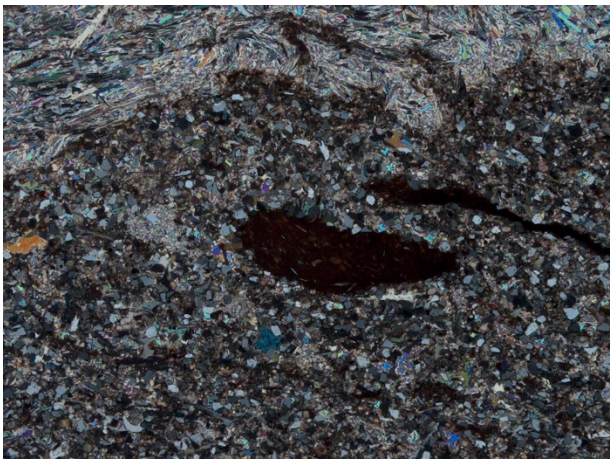


**Figure A.15:** 10,604 anhydrite surrounding mudstone rip-up clasts

**Figure A.16:** 10,671.8 Evidence of chaotic bedding

**Figure A.17:** unconformity 10,633'9.6"

**Figure A.18:** 10,638'1.44" increased calcite cement, glauconite and miciritic dolostones rip-up clasts.

**Figure A.19:** 10,633'9.6" chickenwire anhydrite and mud rip-up clast

**Figure A.20:** 10,662 evidence of a reduction in Chugwater Group strata including lack pyrite and dispersed calcite.

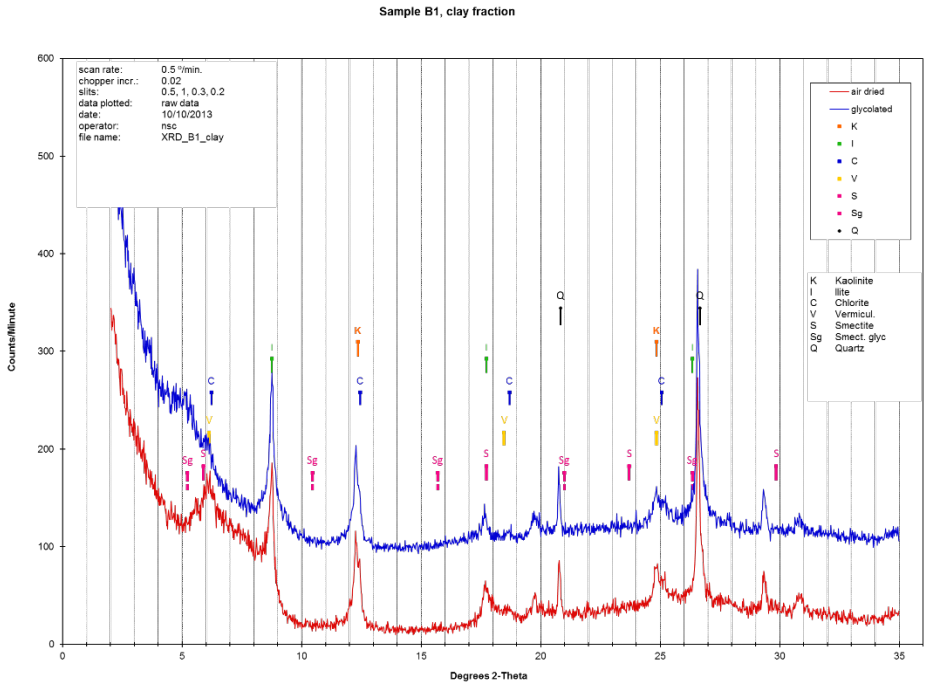


**Figure A.21**: 4,140-4,170

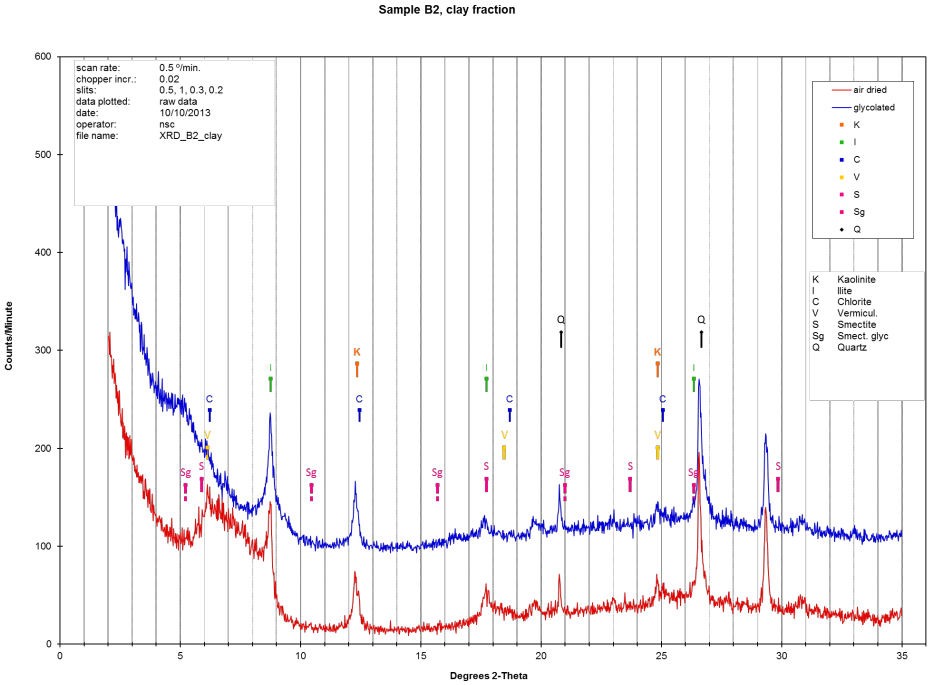


**Figure A.22:** 5,160-5,190

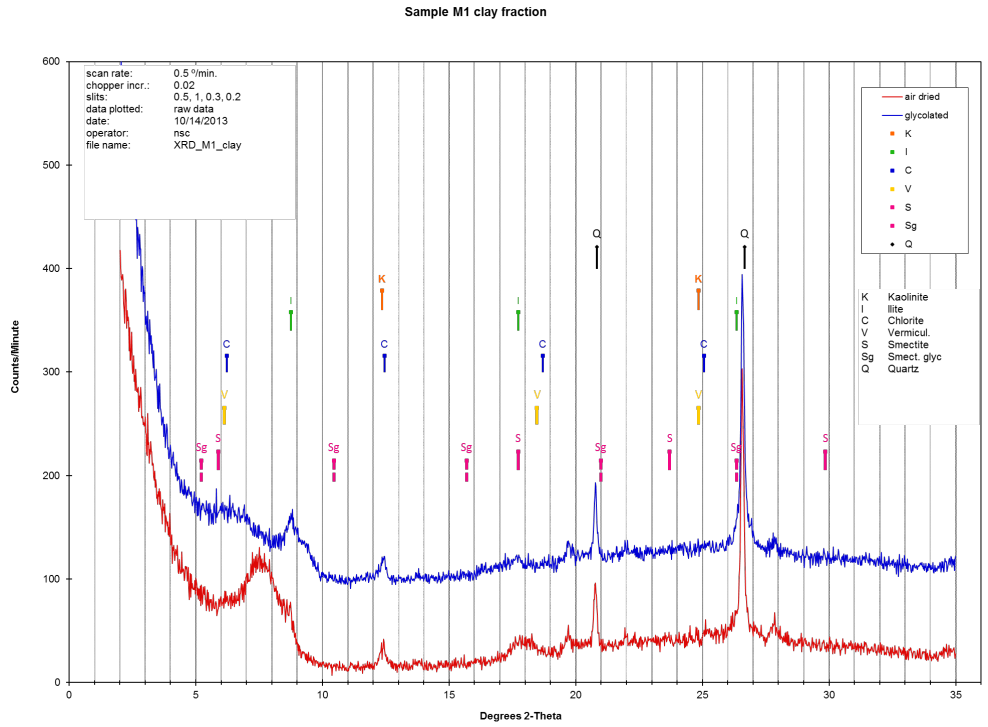


**Figure A.23:** 8,040-8,070

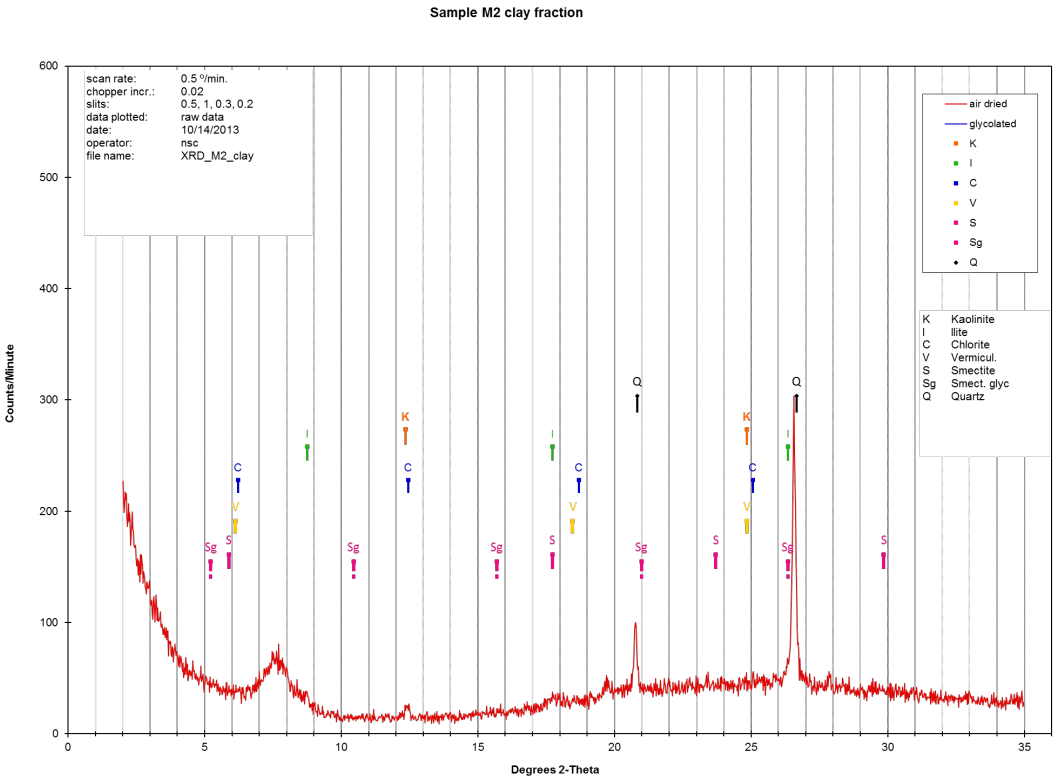


**Figure A.24:** 8,100-8,130

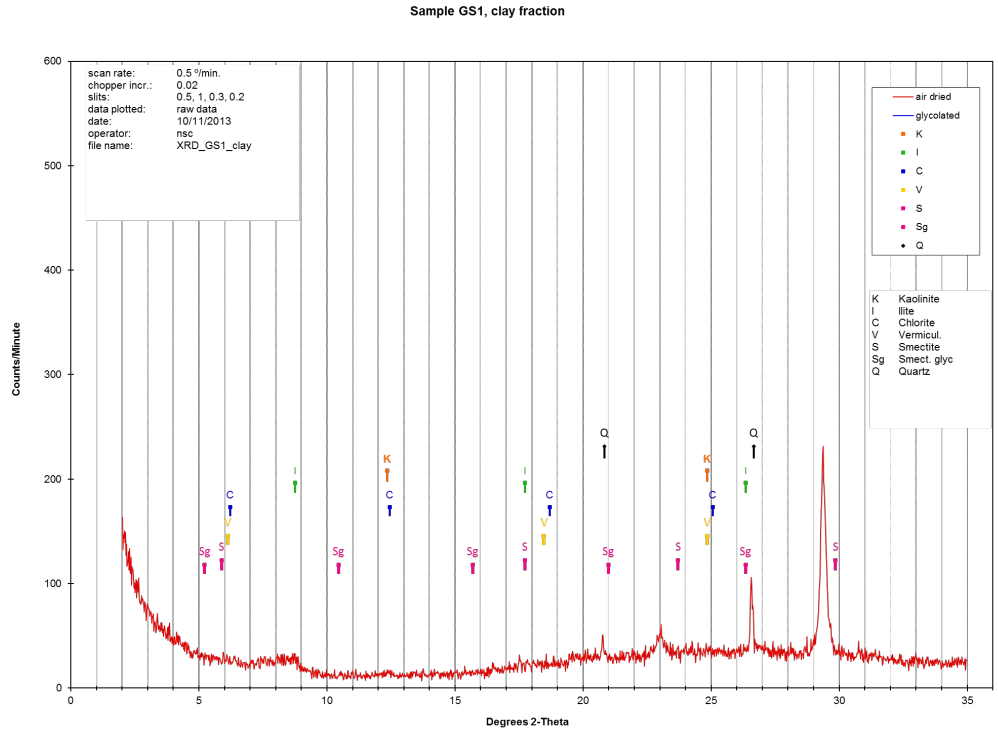


**Figure A.25:** 9,100-9,110

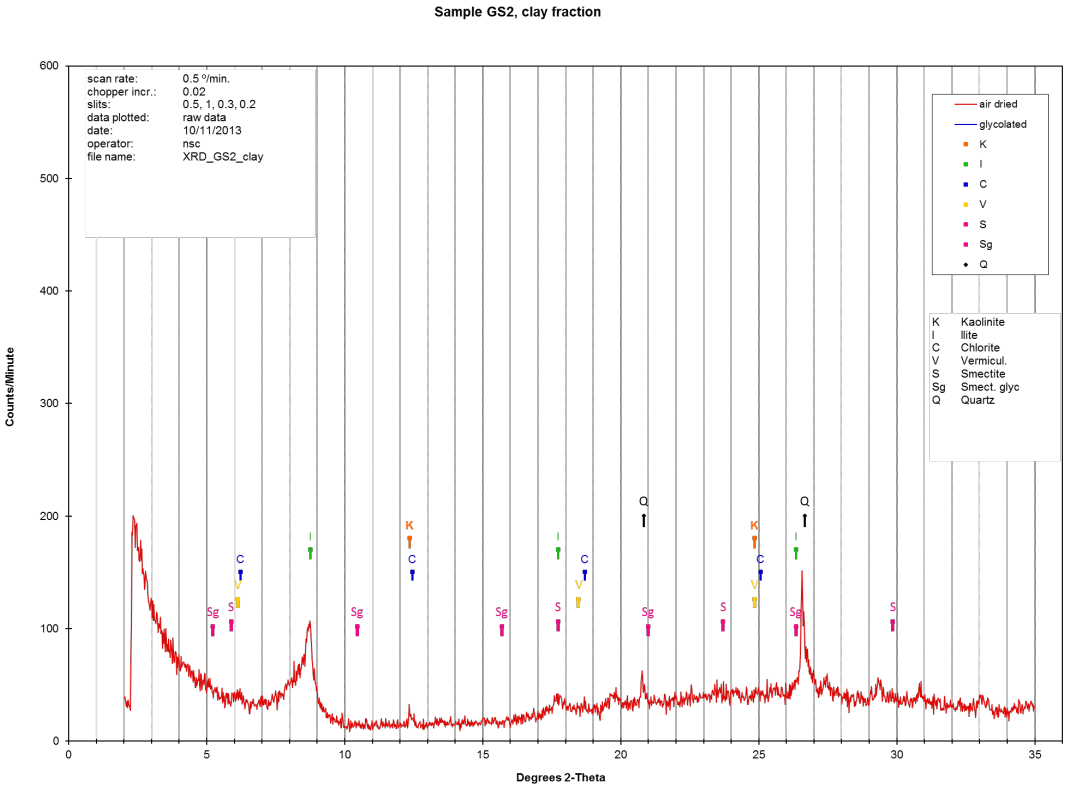


**Figure A.26:** 9,200-9,210

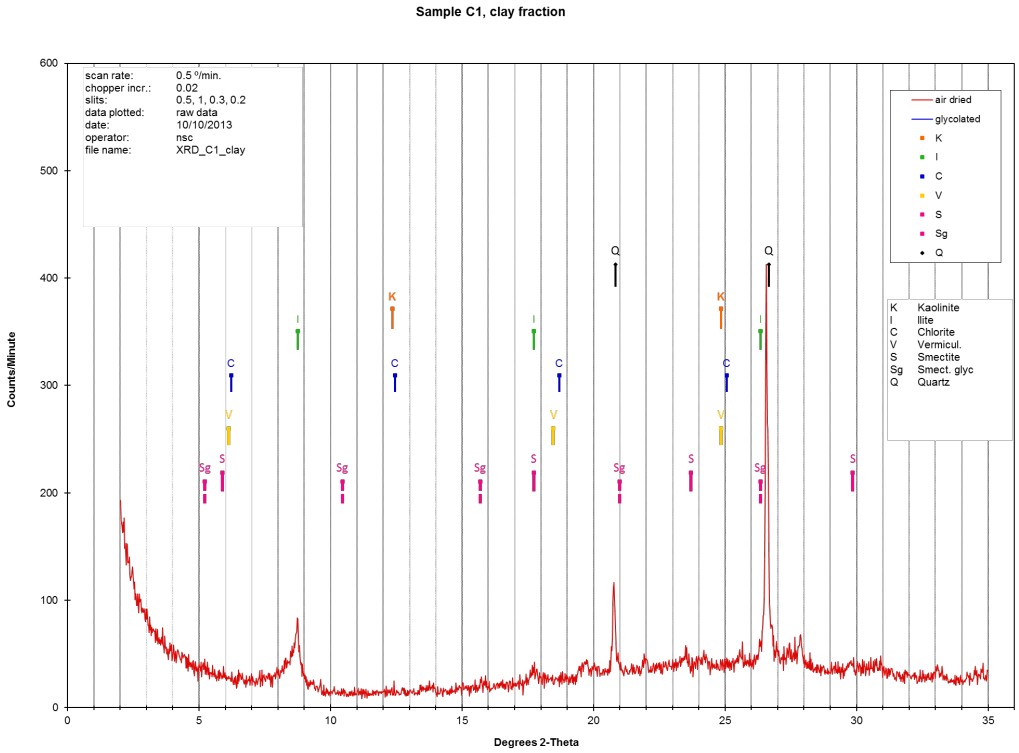


**Figure A.27:** 9,870-9,880

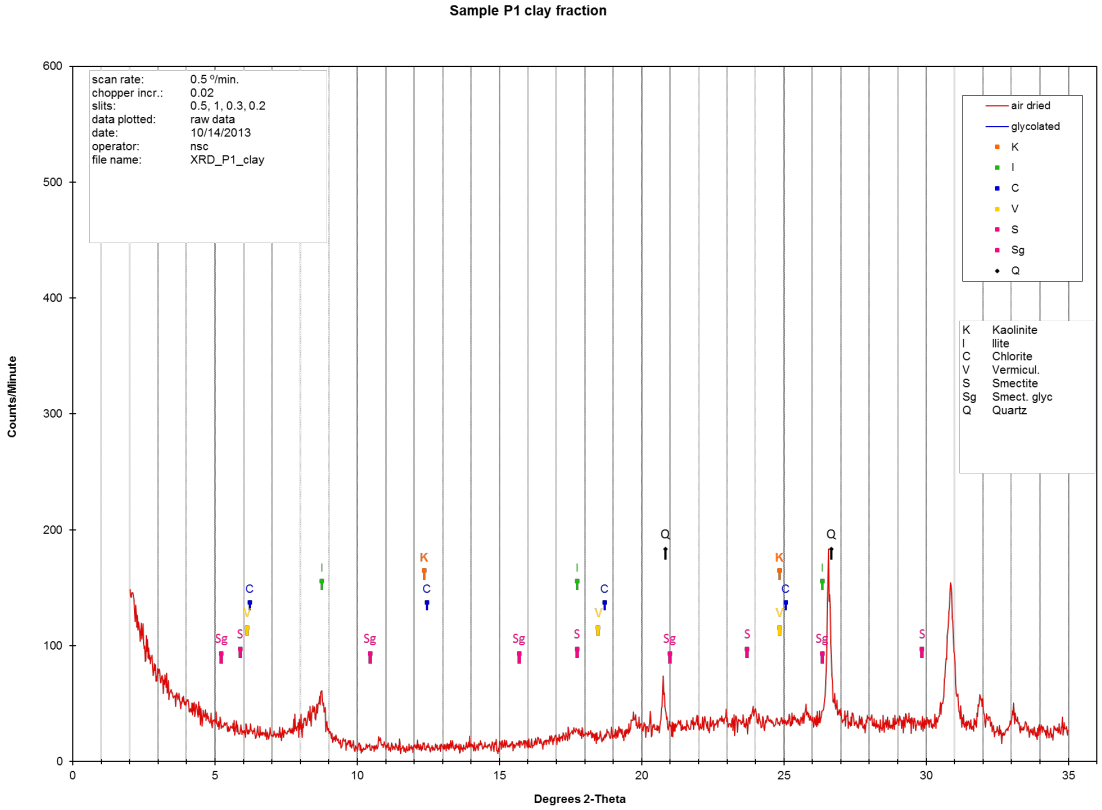


**Figure A.28:** 11,120-11,130

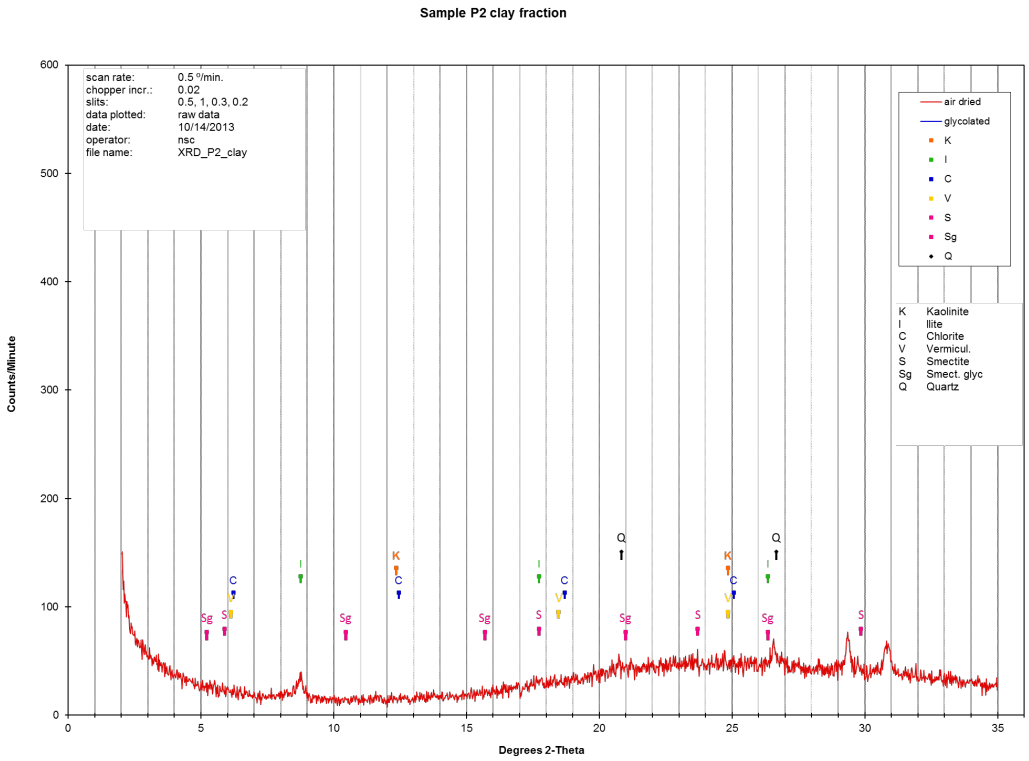


**Figure A.29:** 10,940-10,960

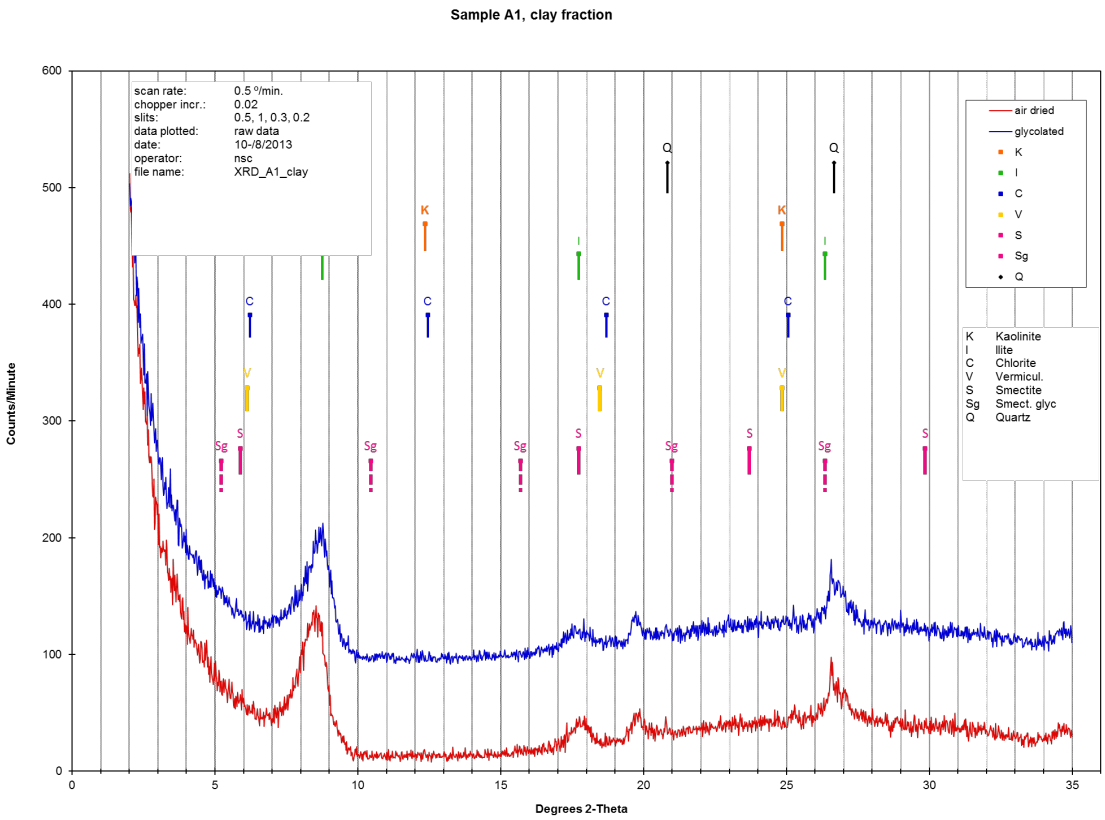


**Figure A.30:** 12178.45'

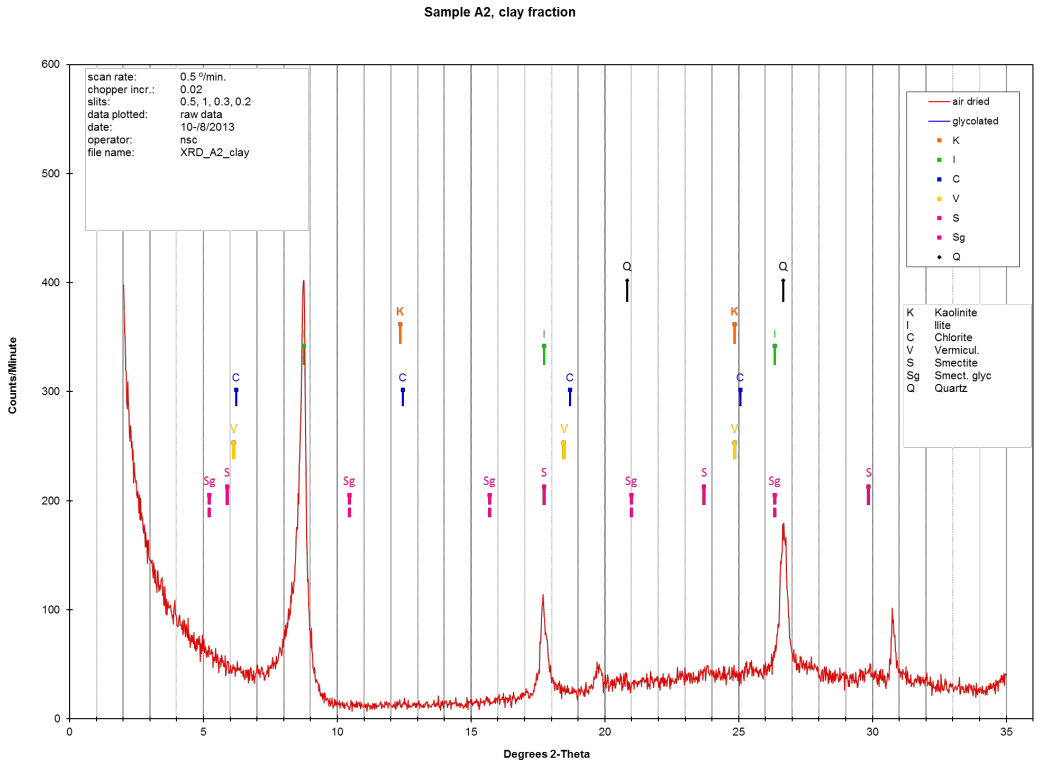


**Figure A.31:** 12,216'

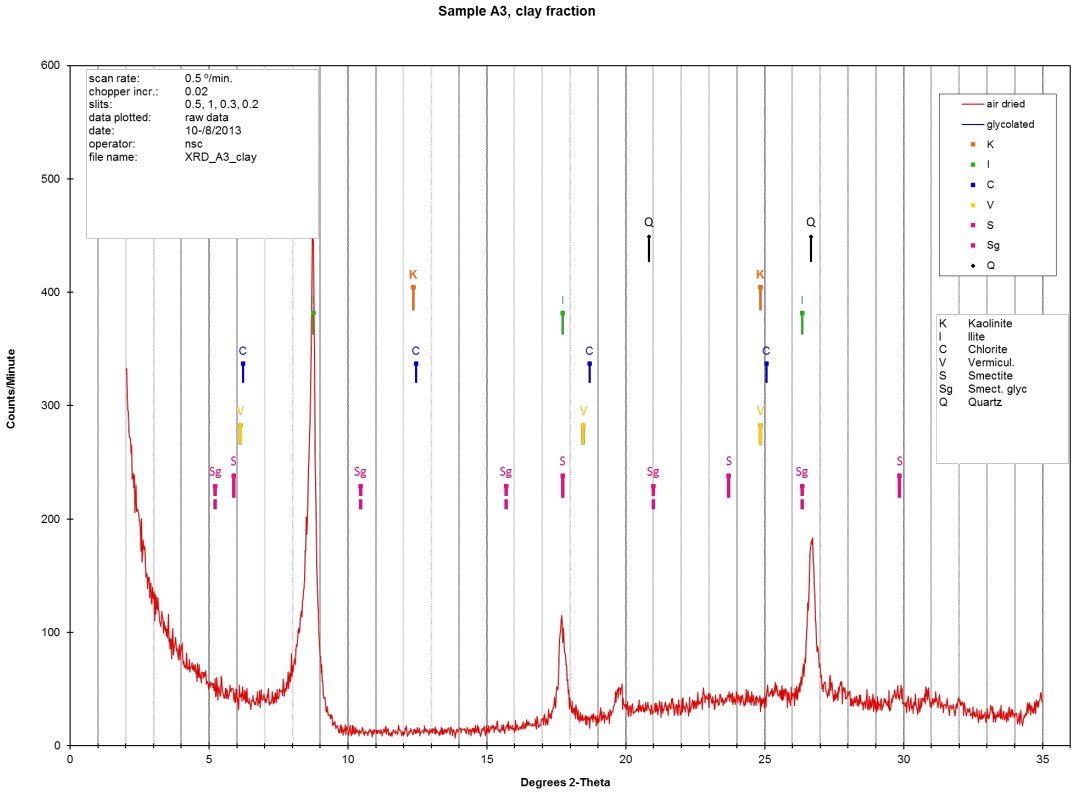


**Figure A.32:** 12,220'

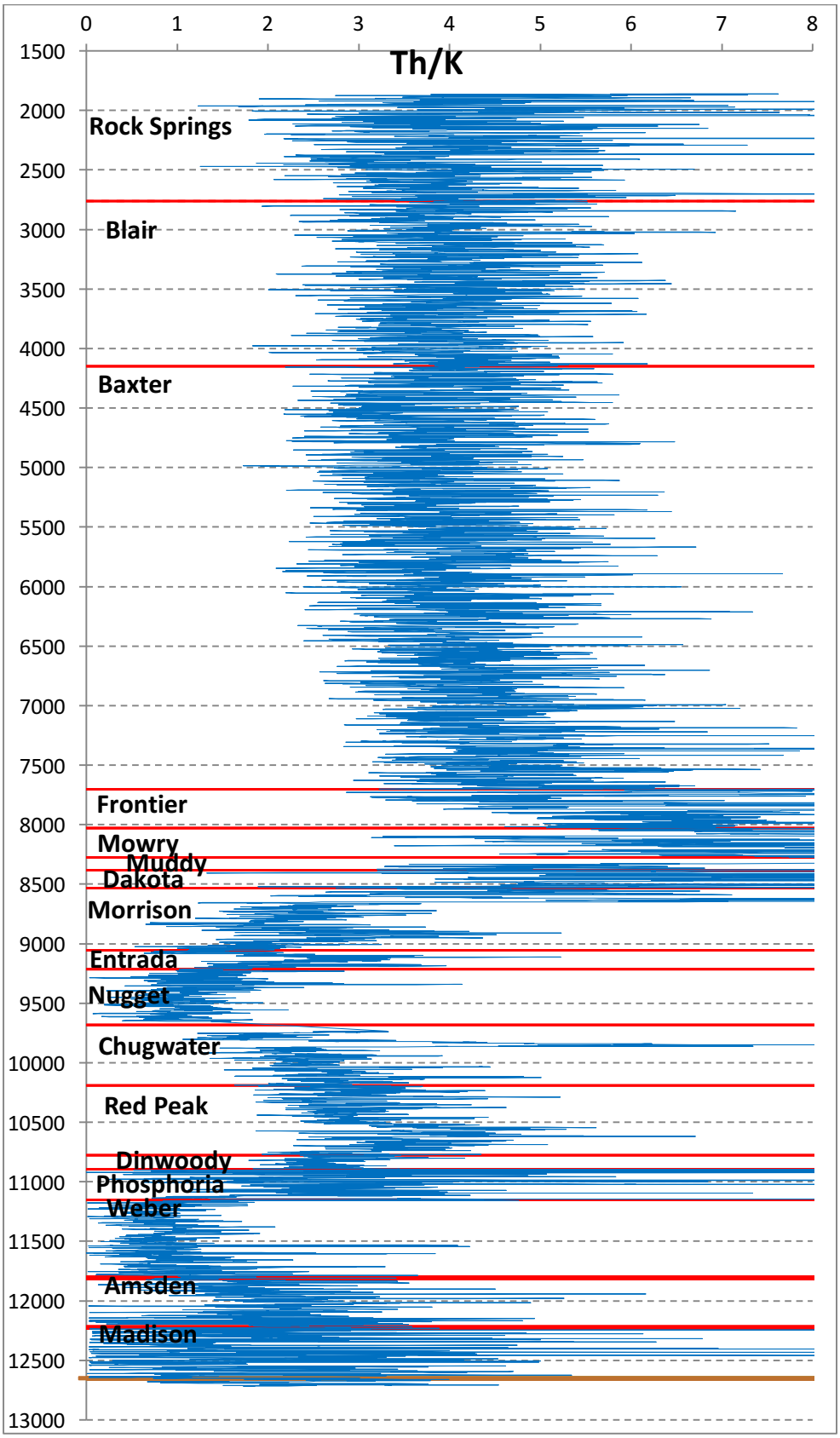


**Figure A.33:** Th/K spectral log graph for sediment maturity.

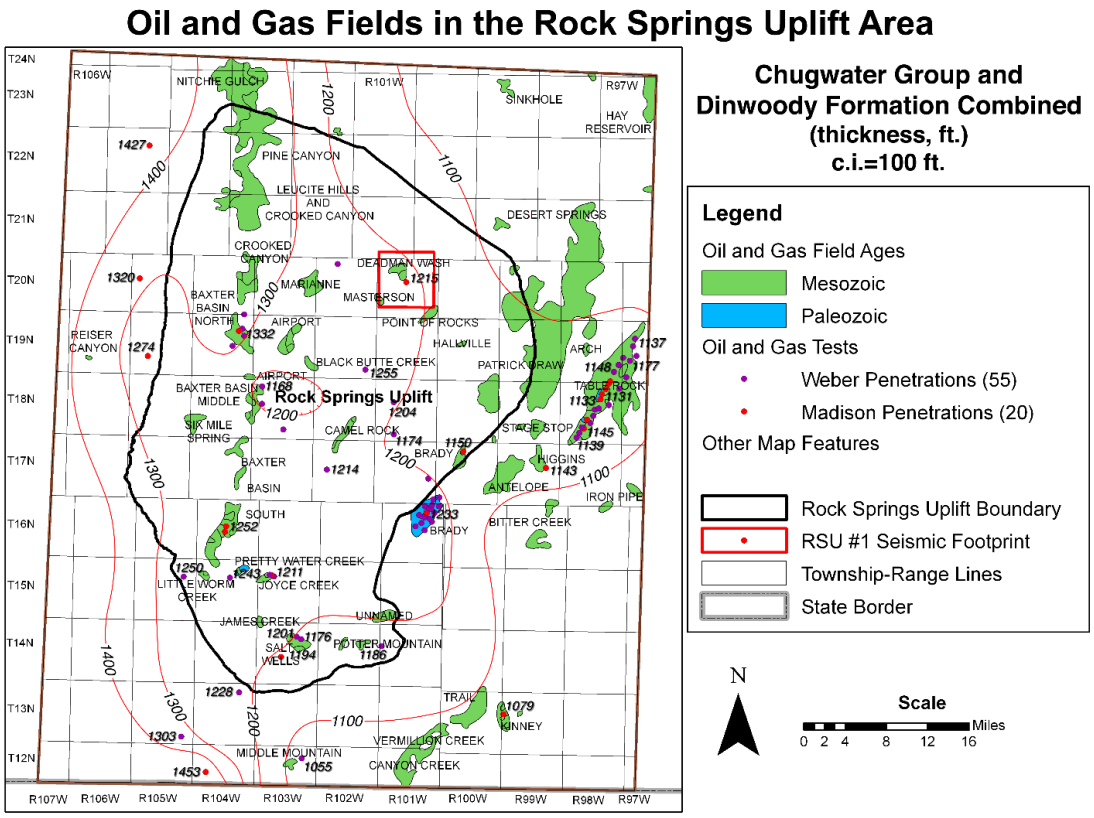


**Figure A.34:** Chugwater Group and Dinwoody Formation combined thickness.

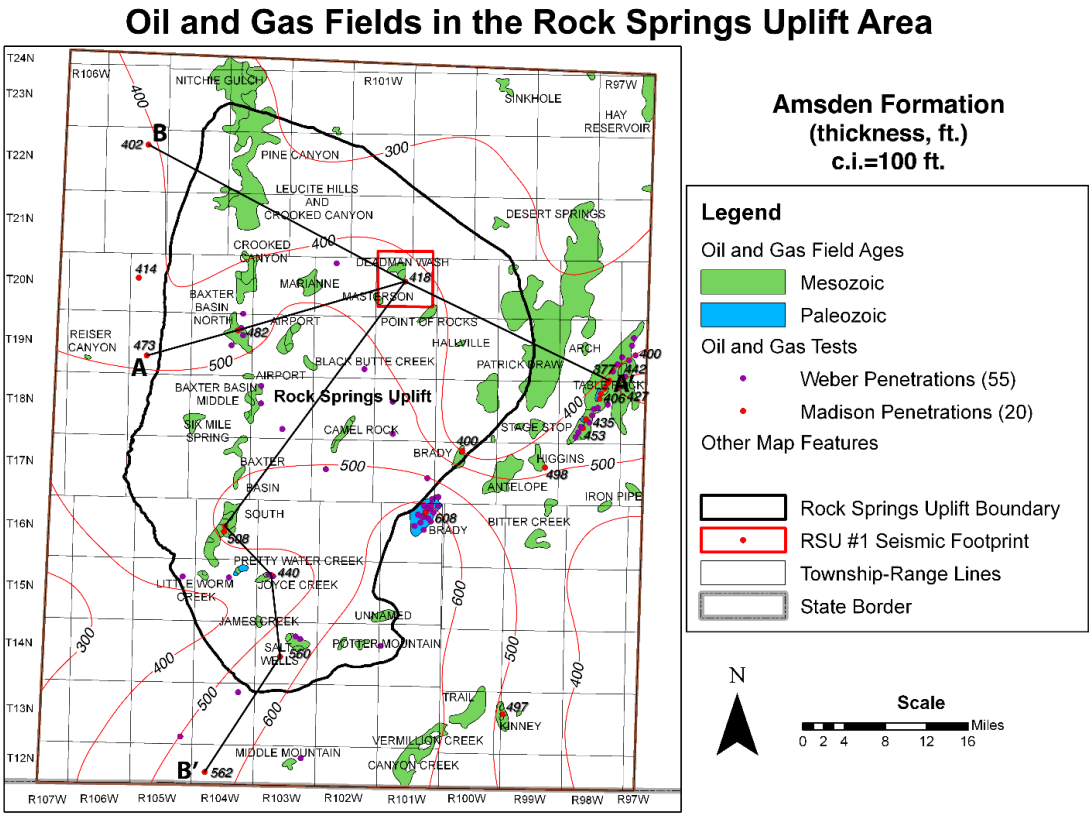


**Figure A.35:** Amsden Formation thickness and A-A' cross-section location.

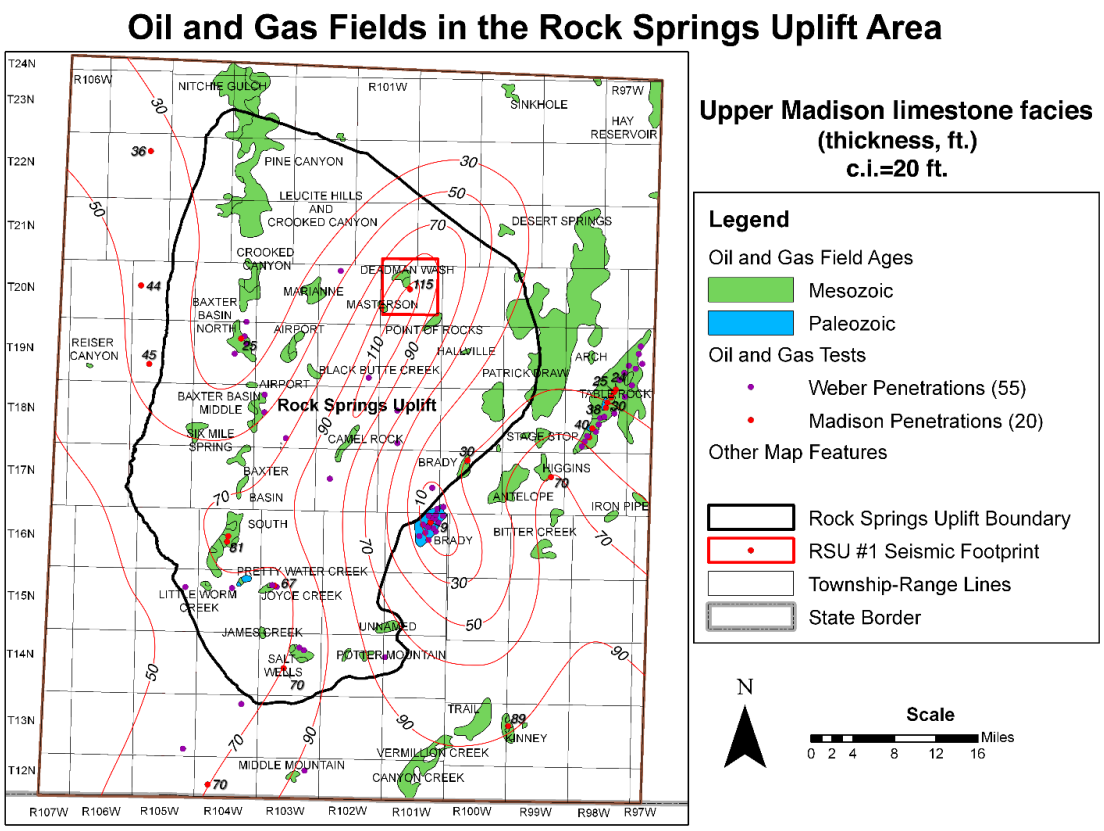


**Figure A.36:** Upper Madison limestone facies thickness.

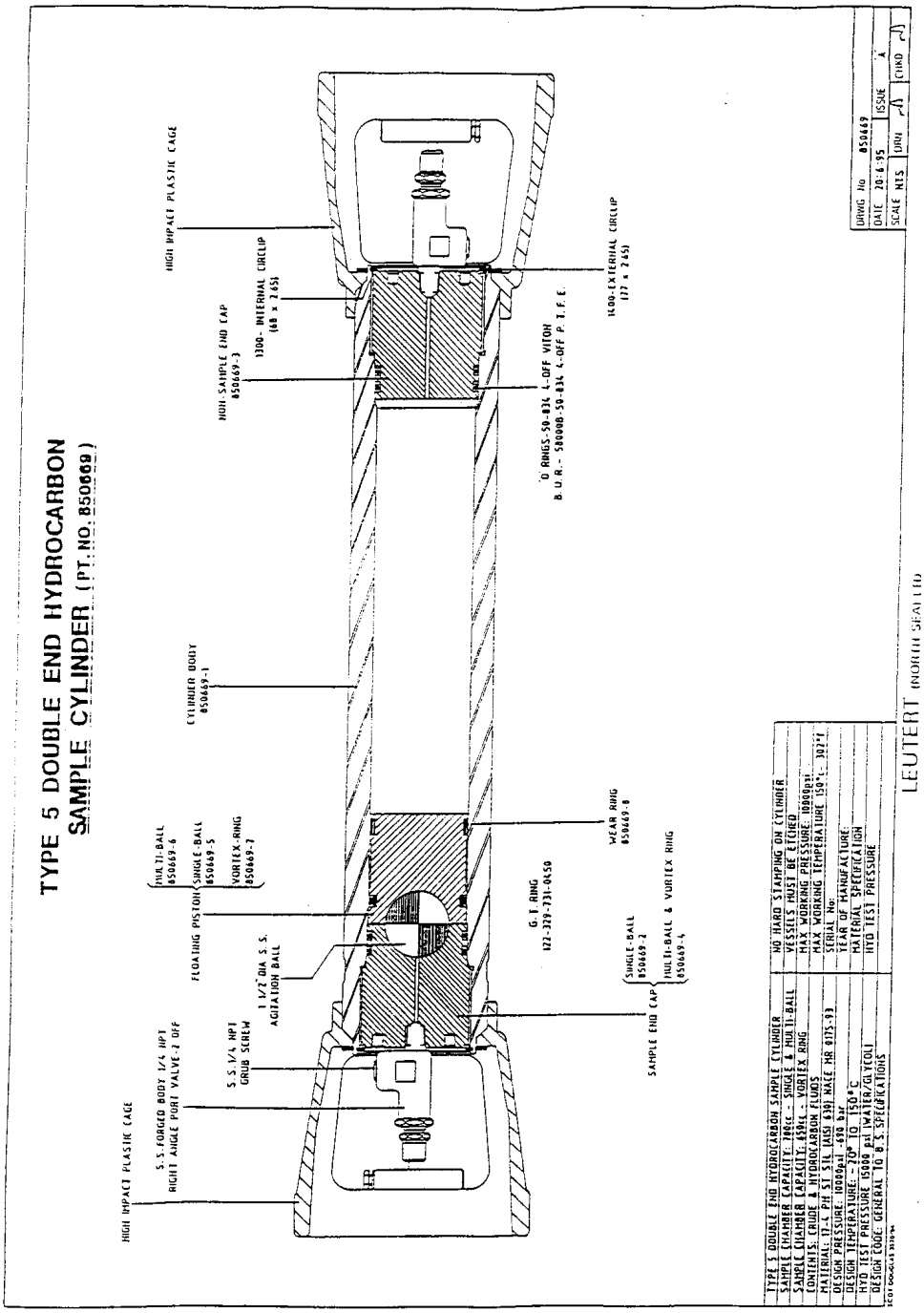


**Figure A.37:** Type 5 Double End Hydrocarbon Sample Cylinder

**Table A.1:** Regional core available for analysis and sampling and deemed relevant to helping to expand the geologic knowledge of the targeted strata. Data corresponds to existing analysis of these samples.

Rock Springs Uplift Cores

| Well name | Core Number | API Number | Latitude | Longitude | Min Depth | Max Depth | Age | Formation | Data | | |
|---|---|---|---|---|---|---|---|---|---|---|---|
| 2-27 AMOCO CHAMPLIN | B116 | 4903721023 | 41.9351 | -109.0563 | 7895 | 7915 | CRET | FRONTIER | 1 Analysis | | |
| 1-23 AMOCO-CHAMPLIN | B196 | 4903720933 | 41.86929 | -109.04671 | 6976 | 7017 | CRET | FRONTIER | Photo Sequence | | |
| | | | | | 7020 | 7036 | CRET | FRONTIER | | | |
| 1-25 AMOCO-CHAMPLIN | A885 | 4903720923 | 41.84814 | -109.14291 | 6825 | 6885 | CRET | FRONTIER | Thin Sections | | |
| 3-15 AMOCO CHAMPLIN | S336 | 4903720945 | 41.79044 | -109.06575 | 5270 | 5330 | CRET | FRONTIER | | | |
| 1 DINES UNIT | D698 | 4903720965 | 41.72497 | -109.29744 | 12821 | 13505 | CRET | FRONTIER | Thin Sections | | |
| 2 DINES UNIT | D699 | 4903721172 | 41.70922 | -109.29499 | 13106 | 13113 | CRET | FRONTIER | Thin Sections | | |
| 2-210 AMOCO CHAMPLIN | B062 | 4903721103 | 41.69326 | -109.14211 | 4140 | 4189 | CRET | FRONTIER | Thin Sections | | |
| 1 FEATHERSTONE | E313 | 4903705789 | 41.70271 | -109.09411 | 3549 | 3556 | CRET | DAKOTA | Thin Sections and Anlysis | | |
| | | | | | 3593 | 3603 | | DAKOTA | | | |
| | | | | | 3682 | 3695 | | DAKOTA | | | |
| 3-35 AMOCO-CHAMPLIN | A803 | 4903720944 | 41.83386 | -108.93043 | 7904 | 7939 | CRET | FRONTIER | Photo Sequence | | |
| 195-B CHAMPLIN | A890 | 4903720826 | 41.74722 | -108.80583 | 7966 | 8030 | CRET | FRONTIER | | | |
| 2 GOVERNMENT ROWLAND | C621 | 4903705701 | 41.65845 | -108.64503 | 2525 | 2569 | CRET | ERICSON | | | |
| BC-1 BITTER CREEK | R074 | N/A | 41.65139 | -108.68366 | 19 | 329 | CRET | LANCE | 1 Analysis | | |
| | | | | | 359 | 366 | CRET | LANCE | | | |
| | | | | | 398 | 410 | CRET | FOX HILLS | | | |
| 3-3 AMOCO CHAMPLIN | A995 | 4903720971 | 41.65021 | -108.78683 | 6547 | 6634 | CRET | FRONTIER | Photo Sequence, 2 Analysis, Thin Sections | | |
| 13-14 FEDERAL BAXTER | C830 | 4903721503 | 41.62091 | -108.99711 | 3693 | 3738 | CRET | DAKOTA | Thin Section | | |
| 1 C STONE | R339 | 4903705593 | 41.61944 | -109.07669 | 3474 | 4541 | JURA | SUNDANCE | | | |
| 1 C C CLARKE | T185 | 4903705630 | 41.63491 | -109.09239 | 2560 | 3980 | CRET | DAKOTA | | | |
| 4 UPRR-11-19-104 | D037 | 4903705655 | 41.64011 | -109.105 | 6404 | 6580 | PENN | WEBER | Photo Sequence | | |
| | | | | | 6580 | 7490 | PENN | AMSDEN | | | |
| | | | | | 7490 | 7850 | MISS | MADISON | | | |
| | | | | | 7850 | 7991 | DEVO | DARBY | | | |
| | | | | | 7991 | 8400 | CAMB | CAMBRIAN | | | |
| | | | | | 8400 | 8905 | CAMB | GROS VENTRE | | | |
| | | | | | 8905 | 9139 | CAMB | FLATHEAD | | | |
| | | | | | 9260 | 9264 | CAMB | FLATHEAD | | | |
| | | | | | 9264 | 9290 | PREC | GRANITE WASH | | | |
| 14-1 FEDERAL | B868 | 4903721012 | 41.62674 | -109.10567 | 3007 | 3159 | CRET | DAKOTA | Thin Sections, 2 Analyses | | |
| 1 BETTY HOYT | R859 | 4903705485 | 41.57515 | -109.05905 | 2432 | 3015 | CRET | FRONTIER | | | |
| 1 T OSBORNE | R878 | 4903705404 | 41.54643 | -109.08042 | 2018 | 2480 | CRET | FRONTIER | Thin Sections | | |
| | | | | | 2480 | 2493 | CRET | DAKOTA | | | |
| 1 MOSEY | R654 | 4903705395 | 41.5445 | -109.07801 | 1950 | 2610 | CRET | DAKOTA | | | |
| 1 LAUZER | R594 | 4903705359 | 41.5156 | -109.07805 | 1819 | 1860 | CRET | FRONTIER | | | |
| 2-7 UNION PACIFIC | R591 | 4903705421 | 41.55801 | -109.06509 | 2625 | 2667 | CRET | FUSON | | | |
| | | | | | 2667 | 2703 | CRET | LAKOTA | | | |
| 2 CR HETZLER | R586 | 4903705440 | 41.56071 | -109.06147 | 1935 | 2050 | | FRONTIER | Photo Sequence | 115 | |
| | | | | | 2050 | 2487 | | ASPEN | | 437 | Mowry=Aspen |
| | | | | | 2487 | 2940 | | DAKOTA | | 453 | |
| | | | | | 2940 | 3125 | | MORRISON | | 185 | |
| | | | | | 3125 | 3277 | | CURTIS | | 152 | |
| | | | | | 3277 | 3378 | | ENTRADA | | 101 | |
| | | | | | 3378 | 3542 | | TWIN CREEK | | 164 | |
| | | | | | 3542 | 4060 | | NUGGET | | 518 | |
| | | | | | 4060 | 4500 | | JELM | | 440 | |
| | | | | | 4500 | 5120 | | CHUGWATER | | 620 | |
| | | | | | 5120 | 5228 | | DINWOODY | | 108 | |
| | | | | | 5228 | 5510 | | PHOSPHORIA | | 282 | |
| | | | | | 5510 | 6940 | | TENSLEEP | | 1430 | |
| 1 CR HETZLER | R567 | 4903705429 | 41.55672 | -109.05785 | 1776 | 2157 | CRETACEOUS | FRONTIER | Core Analysis | | |
| | | | | | 2420 | 2485 | CRETACEOUS | MOWRY | | | |

| | | | | | | | | | | |
|---|---|---|---|---|---|---|---|---|---|---|
| | | | | | 2485 | 2550 | CRETACEOUS | DAKOTA | | |
| | | | | | 2550 | 2618 | CRETACEOUS | CLOVERLY | | |
| | | | | | 2618 | 2736 | JURASSIC | MORRISON | | |
| 3 CR HETZLER | R571 | 4903705407 | 41.54807 | -109.05786 | 1788 | 2135 | CRET | FRONTIER | Photo Sequence | |
| | | | | | 2135 | 2335 | CRET | MOWRY | | |
| | | | | | 2335 | 2423 | CRET | DAKOTA | | |
| | | | | | 2423 | 2512 | CRET | FUSON | | |
| | | | | | 2512 | 2516 | CRET | LAKOTA | | |
| | | | | | 2516 | 2519 | JURA | MORRISON | | |
| 1 AGNES FAY | R616 | 4903705377 | 41.53631 | -109.06151 | 2506 | 2552 | JURA | MORRISON | Dinwoody 5110-5210 | |
| | | | | | 3325 | 3350 | JURA | NUGGET | | |
| | | | | | 4135 | 4247 | TRIA | JELM | | |
| | | | | | 5498 | 5499 | PENN | TENSLEEP | | |
| 1 CHIMNEY ROCK | T203 | 4903705405 | 41.54674 | -108.8595 | 674 | 1046 | CRET | MESAVERDE | 2 Analysis | |
| 5 PATRICK DRAW UNIT | C810 | 4903705399 | 41.54598 | -108.53444 | 4978 | 5015 | CRET | ALMOND | | |
| 14 UNIT | B238 | 4903720259 | 41.51701 | -108.54407 | 4790 | 4800 | CRET | LEWIS | Photo Sequence | |
| 3 HIGGINS | A821 | N/A | 41.45548 | -108.5296 | 15775 | 15777 | JURA | NUGGET | Thin Sections | |
| | | | | | 15854 | 15855 | JURA | NUGGET | | |
| 2-1 AMOCO-CHAMPLIN | A994 | 4903720970 | 41.47571 | -108.85385 | 6390 | 6448 | CRET | FRONTIER | Analysis, Photo Sequence | |
| | R370 | 4903705301 | 41.41718 | -109.10094 | 3434 | 4166 | CRET | DAKOTA | Analysis | |
| 1 CHAMPLIN 269 AMOCO | S221 | 4903720783 | 41.38587 | -108.38553 | 13206 | 13266 | CRET | MESAVERDE | Photo Squence | |
| 1 BITTER CREEK UNIT | T985 | 4903705883 | 41.39408 | -108.59522 | 9074 | 9106 | CRET | ALMOND | | |
| | | | | | 9115 | 9164 | CRET | ERICSON | | |
| | | | | | 9164 | 9289 | CRET | ERICSON | | |
| 21-11 BRADY UNIT 1 | E032 | 4903720341 | 41.38693 | -108.75011 | 11743 | 11780 | JURA | NUGGET | Thin Sections | |
| | | | | | 11819 | 11835 | JURA | NUGGET | | |
| 1-1 POLUMBUS FEDERAL | **A829** | 4903720973 | 41.30377 | -109.07923 | | | | PHOSPHORIA | WOGCC Dinwoody log at 6556, however CMI pcik at 6828 or so | |
| | | | | | | | | Check out cuttings! | | |
| 1 CAPITAL | D641 | 4903705236 | 41.29585 | -109.10653 | | | | FRONTIER | | |
| | | | | | | | | ASPEN | | |
| | | | | | | | | MOWRY | | |
| | | | | | | | | DAKOTA | | |
| | | | | | | | | CLOVERLY | | |
| | | | | | | | | MORRISON | | |
| 2-31 ENSOURCE FEDERAL | C842 | 4903722332 | 41.23103 | -109.0576 | | | | FRONTIER | | |
| | | | | | | | | MOWRY | | |
| | | | | | | | | DAKOTA | | |
| | A544 | 4903706394 | | 15 UNIT TABLE | 15684 | 15712 | | CHUGWATER | | dinwoody at 16660? |
| | | | | | 16918 | 17020 | | PHOSPHORIA | | |
| | | | | | | | | WEBER | | |
| | B087 | 4903721098 | | | | | | Nugget | | dinwoody at 7436-7482 (our pick at 7440) |
| | | | | | 7497 | 7505 | | Phosphoria | | |
| | | | | | 7809 | 7854 | | Tensleep | | |
| | C890 | 4903720007 | | | | | | TENSLEEP | | |

## **Table A.2:** Seal Thicknesses for Rock Springs Uplift Deep Wells

**Seal Thicknesses for Deep Wells on Rock Springs Uplift**

**Explanation** Blanks = well not deep enough or one average thickness used for entire field area, for example South Brady Field Upper Madison @ 9 feet
All tops are subsea depths picked from well logs. Trc = Chugwate, Pp = Phosphoria, Pa = Amsden, Mm = Madison
Column B Field name, WC = Wildcat well
Column H Thickness of Chugwater and Dinwoody combined = Trc-Pp, top of Chugwater (Trc) to top of Phosphoria (Pp)
Column J Thickness of Amsden= Pa-Mm, top of Amsden (Pa) to top of Madison (Mm)
Column L Thickness of Upper Madison Limestone, derived from well in-house log picks

| API Number | Field Name | Section-Township-Range | X | Y | Trc top | Pp top | Trc-Pp | Pa Tops | Pa-Mm | Mm Tops | Upper Mm |
|---|---|---|---|---|---|---|---|---|---|---|---|
| 3705377 | M Baxter Basin | 18-18-103 | 41.53631 | -109.06151 | 3900 | 5200 | 1300 | | | | |
| 3705440 | M Baxter Basin | 6-18-103 | 41.56071 | -109.061466 | 4060 | 5228 | 1168 | | | | |
| 3705514 | WC 35-19-102 | 35-19-102 | 41.58669 | -108.869178 | 7200 | 8455 | 1255 | | | | |
| 3705655 | N Baxter Basin | 11-19-104 | 41.64011 | -109.105 | 4608 | 5940 | 1332 | 7008 | 482 | 7490 | 25 |
| 3707154 | RSU #1 | 16-20-101 | 41.71261 | -108.79482 | 9680 | 10895 | 1215 | 11807 | 418 | 12225 | 115 |
| 3720007 | Middle Mountain | 11-12-103 | 41.03931 | -108.97601 | 15135 | 16190 | 1055 | | | 17221 | |
| 3720341 | S. Brady | 11-16-101 | 41.38693 | -108.75011 | 12147 | 13380 | 1233 | 14403 | 608 | 15011 | 9 |
| 3720347 | Joyce Creek | 8-15-103 | 41.29584 | -109.037289 | 5365 | 6576 | 1211 | 7648 | 440 | 8088 | 67 |
| 3720384 | S. Brady | 15-16-101 | 41.37244 | -108.759662 | 12143 | 13602 | 1459 | | | 15110 | |
| 3720385 | S. Brady | 2-16-101 | 41.39795 | -108.740538 | 12402 | 13578 | 1176 | | | 15092 | |
| 3720392 | Joyce Creek | 8-15-103 | 41.29639 | -109.04131 | 5290 | 6444 | 1154 | | | | |
| 3720396 | S. Baxter Basin | 16-16-104 | 41.36321 | -109.12389 | 4198 | 5450 | 1252 | 6472 | 508 | 6980 | 81 |
| 3720405 | Salt Wells | 10-14-103 | 41.21001 | -108.989307 | 7782 | 8983 | 1201 | | | 10129 | |
| 3720417 | S. Brady | 12-16-101 | 41.3869 | -108.73561 | 12739 | 13972 | 1233 | | | 15479 | |
| 3720456 | Kinney | 18-13-99 | 41.1053 | -108.602163 | 15265 | 16344 | 1079 | 17120 | 497 | 17617 | 89 |
| 3720499 | S. Brady | 31-17-100 | 41.40875 | -108.726717 | 12810 | 14086 | 1276 | | | 15497 | |
| 3720519 | WC 35-13-105 | 35-13-105 | 41.06668 | -109.200568 | 13330 | 14633 | 1303 | | | 15769 | |
| 3720545 | S. Brady | 2-16-101 | 41.39654 | -108.75375 | 12294 | 13527 | 1233 | | | 15038 | |
| 3720551 | N. Brady | 4-17-100 | 41.47372 | -108.683518 | 12280 | 13430 | 1150 | 14538 | 400 | 14938 | 30 |
| 3720565 | Table Rock | 35-19-98 | 41.57486 | -108.410112 | 15572 | 16720 | 1148 | 17635 | 377 | 18012 | |
| 3720584 | WC 11-22-105 | 11-22-105 | 41.89632 | -109.281767 | 15077 | 16504 | 1427 | 17560 | 402 | 17962 | 36 |
| 3720588 | S. Brady | 10-16-101 | 41.3836 | -108.764154 | 12401 | 13600 | 1199 | | | 15106 | |
| 3720589 | WC 17-17-102 | 17-17-102 | 41.44548 | -108.93795 | 6360 | 7574 | 1214 | | | 8986 | |
| 3720618 | S. Brady | 11-16-101 | 41.37448 | -108.740482 | 12791 | 14060 | 1269 | | | 15560 | |
| 3720633 | S. Brady | 36-17-101 | 41.40605 | -108.737943 | 12778 | 13980 | 1202 | | | 15494 | |
| 3720654 | WC 32-18-101 | 32-18-101 | 41.49641 | -108.813841 | 8628 | 9802 | 1174 | | | 11312 | |
| 3720655 | S. Brady | 1-16-101 | 41.39641 | -108.727559 | 12766 | 13952 | 1186 | | | 15472 | |
| 3720661 | S. Brady | 14-16-101 | 41.36246 | -108.753625 | 12709 | 14000 | 1291 | | | 15501 | |
| 3720675 | Table Rock | 10-18-98 | 41.54938 | -108.42821 | 15719 | 16852 | 1133 | 17846 | 406 | 18252 | 38 |
| 3720705 | Joyce Creek | 8-15-103 | 41.29401 | -109.03301 | 5533 | 6731 | 1198 | | | | |
| 3720712 | Table Rock | 21-18-98 | 41.52056 | -108.45287 | 16220 | 17413 | 1193 | 18408 | 450 | 18858 | 40 |
| 3720724 | WC 18-14-101 | 18-14-101 | 41.1987 | -108.830878 | 11334 | 12520 | 1186 | | | 13644 | |
| 3720754 | WC 17-12-104 | 17-12-104 | 41.01759 | -109.15339 | 12490 | 13943 | 1453 | 15252 | 562 | 15814 | 70 |
| 3720832 | Higgins | 14-17-99 | 41.45217 | -108.528324 | 16905 | 18048 | 1143 | 19142 | 498 | 19640 | 70 |
| 3720875 | Table Rock | 2-18-98 | 41.56399 | -108.41846 | 15608 | 16722 | 1114 | 17712 | 424 | 18136 | 40 |
| 3720893 | Table Rock | 32-18-98 | 41.49522 | -108.472072 | 16284 | 17423 | 1139 | | | 18931 | |
| 3720948 | Table Rock | 2-18-98 | 41.5716 | -108.412907 | 15568 | 16699 | 1131 | 17658 | 442 | 18100 | 24 |
| 3721074 | Table Rock | 11-18-98 | 41.55677 | -108.42542 | 15689 | 16815 | 1126 | 17791 | 412 | 18203 | 25 |
| 3721157 | WC 11-15-105 | 11-15-105 | 41.2915 | -109.20154 | 9938 | 11188 | 1250 | | | 12647 | |
| 3721172 | WC 18-20-105 | 18-20-105 | 41.70922 | -109.294985 | 15582 | 16902 | 1320 | 18013 | 414 | 18427 | 44 |
| 3721188 | WC 10-15-104 | 10-15-104 | 41.29122 | -109.115386 | 5791 | 7034 | 1243 | | | 8477 | |
| 3721201 | WC 29-19-105 | 29-19-105 | 41.60053 | -109.276995 | 15302 | 16576 | 1274 | 17644 | 476 | 18120 | 45 |
| 3721250 | WC near Salt Wells | 21-14-103 | 41.18116 | -109.01736 | 9046 | 10240 | 1194 | 11318 | 560 | 11878 | 70 |
| 3721285 | Table Rock | 28-18-98 | 41.508 | -108.458309 | 15981 | 17225 | 1244 | 18202 | 496 | 18698 | 86 |
| 3721700 | South Brady | 11-16-101 | 41.3804 | -108.754797 | 12187 | 13372 | 1185 | | | 14873 | |
| 3721920 | WC 3-12-107 | 3-12-107 | 41.04321 | -109.45222 | 18300 | 19400 | 1100 | | | 20694 | |
| 3721981 | WC 2-13-104 | 2-13-104 | 41.13023 | -109.094412 | 11436 | 12664 | 1228 | | | 13770 | |
| 3722105 | South Brady | 2-16-101 | 41.39381 | -108.7495 | 12228 | 13404 | 1176 | | | 14902 | |
| 3722403 | South Brady | 2-16-101 | 41.39235 | -108.742193 | 12386 | 13570 | 1184 | | | 15080 | |
| 3722579 | WC 17-18-101 | 17-18-101 | 41.54181 | -108.814831 | 7964 | 9168 | 1204 | | | 10685 | |
| 3723561 | Salt Wells | 11-14-103 | 41.20661 | -108.980542 | 8002 | 9178 | 1176 | | | 10310 | |
| 3723638 | Table Rock | 8-19-97 | 41.63504 | -108.364483 | 16153 | 17290 | 1137 | | | 18695 | |
| 3725125 | South Brady | 11-16-101 | 41.37869 | -108.744914 | 12549 | 13744 | 1195 | 14640 | 600 | 15240 | |
| 3725366 | Table Rock | 22-18-98 | 41.52613 | -108.440977 | 16175 | 17306 | 1131 | | | 18691 | |
| 3725459 | Table Rock | 15-18-98 | 41.53666 | -108.431036 | 16040 | 17175 | 1135 | 18177 | 405 | 18582 | |
| 3725634 | Table Rock | 21-18-98 | 41.51582 | -108.446471 | 16244 | 17382 | 1138 | | | 18776 | |
| 3725716 | Table Rock | 29-18-98 | 41.50205 | -108.466822 | 16117 | 17262 | 1145 | | | 19263 | |
| 3726027 | Table Rock | 25-19-98 | 41.59806 | -108.394661 | 15838 | 16968 | 1130 | | | 18397 | |
| 3726144 | Table Rock | 31-19-97 | 41.58099 | -108.38023 | 16401 | 17532 | 1131 | | | 18943 | |
| 3726340 | Table Rock | 20-19-97 | 41.61099 | -108.36131 | 16452 | 17605 | 1153 | | | 19013 | |
| 3726614 | Table Rock | 19-19-97 | 41.60399 | -108.37358 | 16271 | 17448 | 1177 | | | 18863 | |
| 3726652 | Table Rock | 1-18-98 | 41.56474 | -108.393031 | 16556 | 17697 | 1141 | | | 19134 | |
| 3726754 | Table Rock | 11-18-98 | 41.54158 | -108.41206 | 16184 | 17325 | 1141 | | | 18726 | |
| 3726884 | Table Rock | 17-19-97 | 41.62453 | -108.367964 | 16176 | 17323 | 1147 | | | 18706 | |

**Table A.3:** Geochemical analysis of formation brines

| Analyses | Weber Formation Energy Labs (08/27/2011) | Weber Formation Core Labs (08/27/2011) | Weber Formation Energy Labs (12/14/12) | Madison Limestone Energy Labs (08/27/2011) | Madison Limestone Core Labs (08/27/2011) | Madison Limestone Energy Labs (12/03/12) |
|---|---|---|---|---|---|---|
| **Microbiological** | | | | | | |
| Heterotrophic (MPN/mL) | < 2 | – | 40 | 2 | – | 10 |
| **Major Ions** | | | | | | |
| Alkalinity, Total as $CaCO_3$ (mg/L) | 509 | – | 3030 | 1170 | – | 2620 |
| Carbonate as $CO_3$ (mg/L) | ND | 0 | ND | ND | 0 | ND |
| Bicarbonate as $HCO_3$ (mg/L) | 621 | 720 | 3690 | 1420 | 1,610 | 3190 |
| Calcium (mg/L) | 734 | 705 | 539 | 1190 | 1,280 | 1630 |
| Chloride (mg/L) | 60,900 | 61,830 | 57,400 | 50,300 | 52,290 | 51,600 |
| Fluoride (mg/L) | 11.5 | 8.4 | 6.1 | 3.5 | 13 | 2.8 |
| Magnesium (mg/L) | 37 | 40 | 45 | 158 | 170 | 195 |
| Nitrogen, Ammonia as N (mg/L) | 33.4 | – | 33.1 | 42 | – | 39 |
| Nitrogen, Nitrate+Nitrite as N (mg/L) | 0.1 | ND | ND | ND | ND | 0.1 |
| Nitrogen, Nitrite as N (mg/L) | ND | ND | ND | ND | ND | ND |
| Phosphate | – | ND | – | – | ND | – |
| Potassium (mg/L) | – | 1,940 | 1,910 | – | 4,210 | 3,780 |
| Silicon (mg/L) | – | 26 | 45.2 | – | 36 | 59.5 |
| Sodium (mg/L) | 40,700 | 43,250 | 36,500 | 29,000 | 32820 | 27,900 |
| Strontium (mg/L) | – | 26 | 14 | – | 67 | 51.1 |
| Sulfate (mg/L) | 11,600 | 10,320 | 6030 | 2,800 | 2,280 | 1,820 |
| **Non-Metals** | | | | | | |
| Dissolved inorganic carbon (mg/L) | 144 | – | 786 | 355 | – | 724 |
| Dissolved organic carbon (mg/L) | 2.9 | – | 4.5 | 1 | – | 4.4 |
| Total organic carbon (mg/L) | 2.7 | – | 4.7 | 1 | – | 4.5 |
| UV Absorbance at 254 nm (cm-1) | 0.92 | – | 1.99 | 0.558 | – | 1.28 |
| Total recoverable phenolics (mg/L) | 0.61 | – | 0.16 | 0.05 | – | 0.7 |
| Total cyanide (mg/L) | ND | – | 0.098 | ND | – | 0.339 |
| Sulfide (mg/L) | 0.04 | | 120 | 28 | 0 | 82 |
| Sulfide as hydrogen sulfide (mg/L) | 0.04 | – | 127 | 29 | – | 87 |
| **Physical properties** | | | | | | |
| Chemical oxygen demand (mg/L) | 2420 | – | 9120 | 1940 | – | 3050 |
| pH | 7.54 | 7.11 | 6.46 | 7.36 | 6.01 | 6.43 |
| Total dissolved solids @ 180 C (mg/L) | 89,800 | 119,155 | 109,000 | 75,000 | 95,126 | 89,800 |
| BOD (mg/L) | 56.7 | – | 517 | 50.2 | – | 234 |

| | | | | | | |
|---|---|---|---|---|---|---|
| Sodium adsorption ratio | 397 | – | 380 | 209 | – | 174 |
| **Metals** | | | | | | |
| Aluminum (mg/L) | ND | ND | 3.5 | ND | ND | 1.9 |
| Arsenic (mg/L) | 0.095 | – | 0.444 | 1.76 | – | 0.376 |
| Barium (mg/L) | ND | ND | 14.3 | 1 | ND | 4.48 |
| Beryllium (mg/L) | ND | – | 0.007 | ND | – | 0.037 |
| Bismuth (mg/L) | – | – | 0.02 | – | – | 0.02 |
| Boron (mg/L) | 61.1 | – | 71.8 | 95.2 | – | 101 |
| Borate (mg/L) | – | 81 | | – | 120 | |
| Bromide (mg/L) | – | 94 | 99 | – | 115 | 140 |
| Cadmium (mg/L) | ND | ND | 0.006 | ND | ND | ND |
| Chromium (mg/L) | ND | ND | 0.61 | 0.06 | ND | 0.576 |
| Cobalt (mg/L) | 0.02 | ND | 0.019 | ND | ND | 0.009 |
| Copper (mg/L) | ND | ND | 13.6 | ND | ND | 1.35 |
| Iodide (mg/L) | – | ND | 2 | – | ND | ND |
| Iron (mg/L) | 0.94 | 2.2 | 44.1 | 0.54 | 8.1 | 32.2 |
| Lead (mg/L) | ND | ND | 2.91 | ND | ND | 0.305 |
| Lithium (mg/L) | 92.8 | 100 | 90..5 | 91.9 | 105 | 91.6 |
| Manganese (mg/L) | 0.07 | 0.07 | 0.777 | 0.12 | 0.35 | 7.76 |
| Mercury (mg/L) | ND | – | 0.0006 | ND | – | ND |
| Molybdenum (mg/L) | – | ND | – | – | ND | – |
| Nickel (mg/L) | ND | ND | 0.093 | ND | ND | 0.03 |
| Phosphorus | – | ND | – | – | ND | – |
| Selenium (mg/L) | 0.0004 | – | 0.054 | 0.013 | – | 0.041 |
| Silver (mg/L) | ND | – | ND | ND | – | 0.001 |
| Uranium (mg/L) | – | – | 0.0187 | – | – | 0.0004 |
| Vanadium (mg/L) | ND | – | 0.26 | ND | – | 0.01 |
| Zinc (mg/L) | 0.26 | – | 4.58 | 0.4 | – | 2.1 |
| | | | | | | |
| **Radionuclides** | | | | | | |
| Gross Alpha (pCi/L) | – | – | -400 | – | – | 157 |
| Gross Beta (pCi/L) | – | – | 1630 | – | – | 2990 |
| Radium 226 (pCi/L) | – | – | 24 | – | – | 39 |
| Radium 228 (pCi/L) | – | – | 14 | – | – | 1.2 |
| Cesium 134 (pCi/L) | – | – | – | – | – | 0 |
| Cesium 137 (pCi/L) | – | – | – | – | – | 0 |
| | | | | | | |
| **Data Quality** | | | | | | |
| Anion/Cation Balance (± 5) | -3.15% | 0.37% | -5.42% | -3.71% | 2.61% | -4.57% |
| | | | | | | |
| **Organic Acids** | | | | | | |
| Acetate (mg/L) | – | 5.5 | – | – | 0 | – |
| Butyrate (mg/L) | – | 0 | – | – | 0 | – |

| | | | | | | |
|---|---|---|---|---|---|---|
| Formate (mg/L) | – | 5.4 | – | – | 1.7 | – |
| Glycolate (mg/L) | – | 0 | – | – | 0 | – |
| Propionate (mg/L) | – | 0 | – | – | 0 | – |
| Valerate (mg/L) | – | 0 | – | – | 0 | – |
| | | | | | | |
| **Volatile organic compounds** | | | | | | |
| 1,1,1,2-Tetrachloroethane (µg/L) | ND | – | ND | ND | – | ND |
| 1,1,1-Trichloroethane (µg/L) | ND | – | ND | ND | – | ND |
| 1,1,2,2-Tetrachloroethane (µg/L) | ND | – | ND | ND | – | ND |
| 1,1,2-Trichloroethane (µg/L) | ND | – | ND | ND | – | ND |
| 1,1-Dichloroethane (µg/L) | ND | – | ND | ND | – | ND |
| 1,1-Dichloroethene (µg/L) | ND | – | ND | ND | – | ND |
| 1,1-Dichloropropene (µg/L) | ND | – | ND | ND | – | ND |
| 1,2,3-Trichlorobenzene (µg/L) | ND | – | ND | ND | – | ND |
| 1,2,3-Trichloropropane (µg/L) | ND | – | ND | ND | – | ND |
| 1,2,4-Trichlorobenzene (µg/L) | ND | – | ND | ND | – | ND |
| 1,2,4-Trimethylbenzene (µg/L) | 210 | – | 190 | 190 | – | 73 |
| 1,2-Dibromo-3-chloropropane (µg/L) | ND | – | ND | ND | – | ND |
| 1,2-Dibromoethane (µg/L) | ND | – | ND | ND | – | ND |
| 1,2-Dichlorobenzene (µg/L) | ND | – | ND | ND | – | ND |
| 1,2-Dichloroethane (µg/L) | ND | – | ND | ND | – | ND |
| 1,2-Dichloropropane (µg/L) | ND | – | ND | ND | – | ND |
| 1,3,5-Trimethylbenzene (µg/L) | 30 | – | 62 | 30 | – | 54 |
| 1,3-Dichlorobenzene (µg/L) | ND | – | ND | ND | – | ND |
| 1,3-Dichloropropane (µg/L) | ND | – | ND | ND | – | ND |
| 1,4-Dichlorobenzene (µg/L) | ND | – | ND | ND | – | ND |
| 2,2-Dichloropropane (µg/L) | ND | – | ND | ND | – | ND |
| 2-Chloroethyl vinyl ether (µg/L) | ND | – | ND | ND | – | ND |
| 2-Chlorotoluene (µg/L) | ND | – | ND | ND | – | ND |
| 4-Chlorotoluene (µg/L) | ND | – | ND | ND | – | ND |
| Benzene (µg/L) | ND | – | 230 | ND | – | 13 |
| Bromobenzene (µg/L) | ND | – | ND | ND | – | ND |
| Bromochloromethane (µg/L) | ND | – | ND | ND | – | ND |
| Bromodichloromethane (µg/L) | ND | – | ND | ND | – | ND |
| Bromoform (µg/L) | ND | – | ND | ND | – | ND |
| Bromomethane (µg/L) | ND | – | ND | ND | – | ND |
| Carbon tetrachloride (µg/L) | ND | – | ND | ND | – | ND |
| Chlorobenzene (µg/L) | ND | – | ND | ND | – | ND |
| Chlorodibromomethane (µg/L) | ND | – | ND | ND | – | ND |
| Chloroethane (µg/L) | ND | – | ND | ND | – | ND |
| Chloroform (µg/L) | ND | – | ND | ND | – | ND |
| Chloromethane (µg/L) | ND | – | ND | ND | – | ND |
| cis-1,2-Dichloroethene (µg/L) | ND | – | ND | ND | – | ND |

| | | | | | | |
|---|---|---|---|---|---|---|
| cis-1,3-Dichloropropene (µg/L) | ND | – | ND | ND | – | ND |
| Dibromomethane (µg/L) | ND | – | ND | ND | – | ND |
| Dichlorodifluoromethane (µg/L) | ND | – | ND | ND | – | ND |
| Ethylbenzene (µg/L) | 20 | – | 54 | 20 | – | 26 |
| Hexachlorobutadiene (µg/L) | ND | – | ND | ND | – | ND |
| Isopropylbenzene (µg/L) | 30 | – | 9 | 20 | – | 8.4 |
| m+p-Xylenes (µg/L) | 55 | – | 280 | 50 | – | 98 |
| Methyl ethyl ketone (µg/L) | ND | – | 280 | ND | – | 88 |
| Methyl tert-butyl ether (MTBE) (µg/L) | ND | – | ND | ND | – | ND |
| Methylene chloride (µg/L) | ND | – | ND | ND | – | ND |
| n-Butylbenzene (µg/L) | 57 | – | 44 | 40 | – | 53 |
| n-Propylbenzene (µg/L) | ND | – | 27 | ND | – | 28 |
| Naphthalene (µg/L) | 190 | – | 74 | 190 | – | 77 |
| o-Xylene (µg/L) | ND | – | 110 | ND | – | 66 |
| p-Isopropyltoluene (µg/L) | ND | – | 16 | ND | – | 15 |
| sec-Butylbenzene (µg/L) | ND | – | 15 | ND | – | 16 |
| Styrene (µg/L) | ND | – | ND | ND | – | ND |
| tert-Butylbenzene (µg/L) | ND | – | ND | ND | – | ND |
| Tetrachloroethene (µg/L) | ND | – | ND | ND | – | ND |
| Toluene (µg/L) | ND | – | 490 | ND | – | 86 |
| trans-1,2-Dichloroethene (µg/L) | ND | – | ND | ND | – | ND |
| trans-1,3-Dichloropropene (µg/L) | ND | – | ND | ND | – | ND |
| Trichloroethene (µg/L) | ND | – | ND | ND | – | ND |
| Trichlorofluoromethane (µg/L) | ND | – | ND | ND | – | ND |
| Vinyl chloride (µg/L) | ND | – | ND | ND | – | ND |
| Xylenes (µg/L) | | – | 380 | | – | 160 |
| | | | | | | |
| **Organic Characteristics** | | | | | | |
| Oil and Grease (HEM) mg/L | 270 | – | 1100 | 490 | – | 510 |
| | | | | | | |
| **Compositional Analysis of Flash Gas** | | | | | | |
| Nitrogen (Mole %) | – | 78.888 | – | – | 16.75 | – |
| Carbon Dioxide (Mole %) | – | 14.738 | – | – | 82.892 | – |
| Hydrogen Sulfide (Mole %) | – | 0 | – | – | 0 | – |
| Methane (Mole %) | – | 2.537 | – | – | 0.189 | – |
| Ethane (Mole %) | – | 0.297 | – | – | 0 | – |
| Propane (Mole %) | – | 0.213 | – | – | 0.021 | – |
| Iso-Butane (Mole %) | – | 0.043 | – | – | 0.004 | – |
| N-Butane (Mole %) | – | 0.071 | – | – | 0.011 | – |
| Iso-Pentane (Mole %) | – | 0.397 | – | – | 0.04 | – |
| N-Pentane (Mole %) | – | 0.02 | – | – | 0.004 | – |
| Hexanes (Mole %) | – | 2.119 | – | – | 0.006 | – |

| | | | | | | |
|---|---|---|---|---|---|---|
| Heptanes (Mole %) | – | 0.244 | – | – | 0.015 | – |
| Octanes (Mole %) | – | 0.116 | – | – | 0.026 | – |
| Nonanes (Mole %) | – | 0.08 | – | – | 0.012 | – |
| Decanes Plus (Mole %) | – | 0.237 | – | – | 0.03 | – |

# APPENDIX B

Carbon Management Institute

School of Energy Resources

University of Wyoming
School of Energy Resources
Carbon Management Institute
Department 4902
1000 E. University Ave.
1020 Lewis Street
Laramie, WY 82071
(307) 766-6216
cmi@uwyo.edu
www.uwyo.edu/cmi

***BEST PRACTICES for:***

# Seal Evaluation and Responses at the RSU Study Site in Southwest Wyoming:

## Optimizing accuracy of determinations of $CO_2$ storage capacity and permanence, and designing more efficient $CO_2$ storage operations: An example from the Rock Springs Uplift, Wyoming

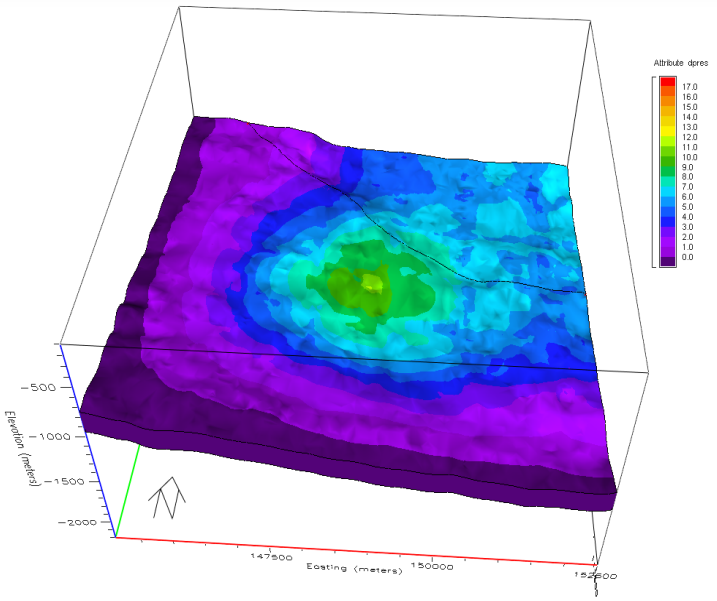


***2015 Edition***

UNIVERSITY OF WYOMING

# DISCLAIMER*

# Optimizing accuracy of determinations of $CO_2$ storage capacity and permanence, and designing more efficient storage operations: An example from the Rock Springs Uplift, Wyoming

## (2015 Edition)

DOE Award Number: DE-FE0009202

Carbon Management Institute
University of Wyoming
1020 E. Lewis Street, Energy Innovation Center
Dept. 4902, 1000 E. University Ave.
Laramie, WY 82071-2000

# Table of Contents

## Executive Summary

This manual aims to define *best practices* as it relates to the procedures, processes, and analytical data necessary to reduce the uncertainty of numerical simulations of dynamic $CO_2$ storage in targeted stratigraphic intervals in Wyoming. Our study focuses on the geologic confining units of Rock Springs Uplift (RSU) carbon storage site located in southwest Wyoming. Here we provide the project scope, brief descriptions, and recommendations of the methodologies employed, which are transferrable to other saline reservoirs. We direct the reader to the final report for a full description of the methodologies, data, and findings of the study.

*Crossbedded sands in core collected from the Triassic section*

## Project Definition and Management

### Project Analysis:

The project goal is to assess risk associated with sealing capacity and $CO_2$ injection at the study site by investigating the following major themes:

- Geophysical assessment of sealing strata
- Geological and mechanical characterization of confining lithologies
- Characterization of formation fluids
- Integration of petrophysical, geophysical and core analysis
- Injection simulations to evaluate seal integrity, injection rate, and pressure responses
- Simulations of formation brine production to assess wellbore scaling/well integrity and surface treatment for optimized field engineering/development
- Field-scale integration of the $CO_2$ storage assessment relative to conservative sealing capacity at the RSU

These themes were devised by numerous subsurface studies of reservoir/seal relations in oil and gas reservoirs, enhanced oil recovery sites, groundwater resource sites, and other CCUS sites. This project shows that these methodologies significantly reduce scientific uncertainties and are therefore applicable and recommended practices for many subsurface evaluations.

### Role of participants:

Our team is comprised of industrial and academic professionals, providing a balanced approach to delivering applicable results and novel methodologies. The use of a multidisciplinary team allows for the integration of industry-standard tools and software, and top-of-the-line analytical equipment available at the University of Wyoming. We recommend this dual-team approach for any project investigating the deep subsurface, as both partners gain benefits through combining expertise and goals. This also eases management constraints related to software licensing, equipment purchasing/rental, training, and budget/human resource protocols.

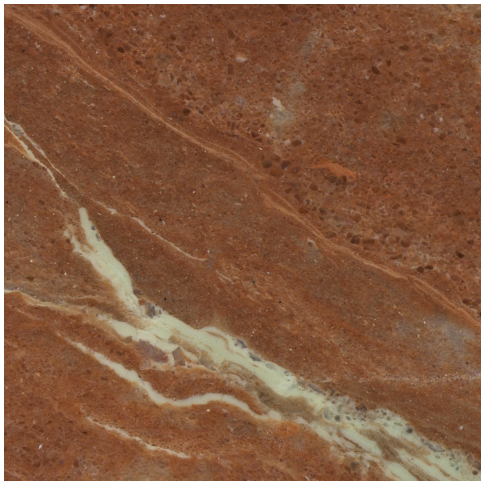

*Dissolution features in carbonaceous shale*

The reporting structure for this project was successful as is described as follows: Primary contacts from each institution reported directly to the Principal Investigator and Project Manager. The Project Manager maintained reporting requirements, maintained budgets, and coordinated work plans for all Task leaders. The Principal Investigator guided the scientific investigations and was responsible for the scientific rigor of the project. Task leaders were responsible for meeting milestones as well as objectives of specific subtasks. The Project Manager maintained regular contact with the Project Coordinator at DOE.

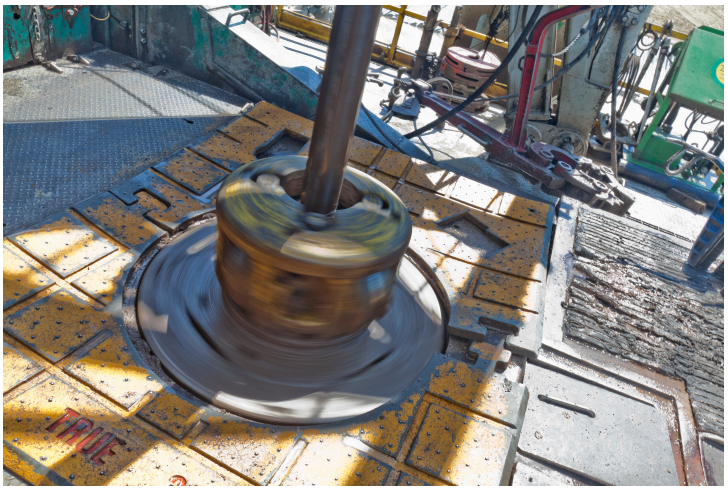

*Drilling the RSU #1 well*

### Resources:

The material resources that were available and crucial to the completion of this project included a 3-D seismic survey, core collected from the reservoir and sealing lithologies, petrophysical log data, in-situ well tests, and formation fluids. These data were collected during a reservoir site characterization project (DE-FE-0002142), which allowed this project to build off previous resources invested by the Department of Fossil Energy.

Human scientific resources deemed critical include a multidisciplinary team of petroleum engineers, reservoir engineers, well site engineers, drilling specialists, seismic/vibraphone engineers, petrophysicists, hydrogeologists, geophysicists, geologic modelers, petroleum geologists, geochemists, and petrologists. The team had access to multiple analytical specialists and equipment at industrial, commercial, and university labs, as well as proprietary/in-house software.

It is also worth noting that this project benefited from experienced program managers, land managers, compulsory litigation/legal experts, and the support of vested landholders/stakeholders such as the Rock Springs Grazing Association (leasing surface owner), Anadarko Petroleum (leasing mineral owner), Jim Bridger power station and coalmine (owns and maintains roadways) and the Black Butte coalmine.

### Schedule:

The project took place over a three-year period. Data collection and field-testing took place during the first two years, allowing time for evaluation and integration as well as adaption to data requirements.

## Successful Analytical Assessments for Seal Lithology Validation at the Rock Springs Uplift

Below is a summary description of identified methodologies deemed the most beneficial for assessing sealing capacity at the study site.

### Geophysical assessment of the sealing lithology:

A 3-D seismic survey was a keystone data component of this project. A variety of seismic attributes were evaluated including curvature, amplitude and velocity. From these evaluations, researchers were able to build and populate a dynamic spatial model, identify structural risks, define the distribution of heterogeneity, propagate lithologic character, and bound storage volumes. The following four outcomes were deemed the most relevant regarding applicable seismic evaluation;

1. ***Extrapolating lithologic and petrophysical character of the stratigraphic test well across the seismic volume-*** Seismic attribute analysis, when calibrated with petrophysical data, were used to approximate geologic properties throughout the seismic domain. This analysis was used to inform spatial distributions of porosity, permeability, lithologic character, and lateral continuity, leading to reduction of lithologic uncertainty. Using these methodologies, we combined the high-resolution geophysical log suite obtained from the RSU #1 stratigraphic test well to extrapolate geologic heterogeneity in three dimensions. The data compiled from this assessment formed the basis of spatial (lateral/vertical) reservoir assessments.

2. ***Populating/volumetric 3-D dynamic models-*** Seismic data, and the interpretation thereof was used to populate the matrix/cells of a dynamic model. Seismic data provided more accurate model parameters than subsurface mapping alone. Below we highlight a couple of innovative analyses that utilized the dynamic model to investigate seal integrity within the project domain.

3. ***Identifying (seismically derived) primary seal bypass systems-*** The sealing lithology within the project domain was investigated for geologic features that may affect the integrity of the seal. These features are referred to as seal bypass systems. Seal bypass systems are considered to be of great risk to long-term confinement, and defining their presence, character, and location within the project domain is essential to address long-term storage potential. We utilized the dynamic model derived from the seismic attribute analysis to locate and describe potential seal bypass features. The results of these investigations identified karsted topography, dissolution pipes, and the family of faults/fractures and major lineaments for risk assessment.

4. ***Improving storage uncertainty with a low-density data set-*** Prior to the CCUS site characterization conducted for the RSU study site (DE-FE0002142), very little preexisting subsurface data had been collected in the area. For example, many CCUS sites are located near oil and gas development, and can benefit from large preexisting datasets. However, existing development does increase the risk of leakage through existing wellbores. The lack of prior subsurface data did limit the amount of reservoir/seal lithologic data available for this case study (i.e. data from several wells). For this instance, the value of the 3-D seismic survey cannot be understated, as it dramatically improved the volume of subsurface data available to researchers within the project domain, resulting in reduced uncertainty.

*Drilling the RSU #1 stratigraphic test well*

**Geological and mechanical characterization of confining lithologies using laboratory measurements and petrophysical data:** Analysis of the properties of seal and reservoir rocks were determined from core, cuttings, thin section and petrophysical log data. These data served to define the lithologic and diagenetic properties of sealing formations on a micro-scale. Conclusions from these analyses were used to inform numerical simulations for conservative capacity analysis.

***Rock mechanics-*** Mechanical analysis of physical and mechanical properties of the seal and reservoir rocks were identified as critical to determining the potential for induced seismicity and holding capacity with respect to $CO_2$ injection. For this case study, mechanical rock properties were determined through triaxial shear analysis, in-situ step-rate injection tests, drill and velocity stem tests, image log analysis, seismic analysis, geologic mapping, and Brinell hardness testing to calculate the following rock properties:

- Shear strength
- Mechanical failure response
- Fracture tolerance
- Fracture gradient
- Fracture/joint pattern and spacing

Major conclusions from these analyses show that primary sealing lithologies have higher fracture tolerance than the targeted injection zone. Thus, the increased pressure within the reservoir would cause the reservoir to fail before the sealing lithology. These data also indicate that injection-related pressure responses might include induced fracture aperture widening in a northwest-southeast direction. This could influence the flow of the plume perpendicular to dip, mitigating upward migration and increasing the expected storage capacity.

***Core and cuttings analysis of sealing lithology-*** In addition to mechanical properties, we analyzed core and cuttings from potential confining units to evaluate responses to injected fluids and associated pressure fronts. These calculations identified the following parameters as the most instructive to evaluating sealing capacity:

- Permeability
- Porosity (volume and architecture)
- Relative permeability
- Capillary entry pressures of seals and reservoirs
- Pore throat character and distribution
- The depositional and diagenetic history of sealing lithology

*Drill pipe*

We concluded that rock property analyses are necessary for determining seal character during site characterization. These data show that the RSU carbon storage site has numerous, distinct seals capable of maintaining a column of injected $CO_2$ at commercial scales.

***Regional well log interpretation of sealing lithologies-*** This project benefited from regional well log analysis to determine lateral continuity of the sealing formations in a regional context (10s to100s

of miles). Petrophysical well logs were evaluated from regional oil and gas wells outside of the immediate study area (that penetrated the targeted seals) for lithologic type and stratigraphic correlations. This analysis highlighted the lateral continuity and mapped the facies structure of the targeted seals, and allowed for the extrapolation of depositional and diagenetic history outside of the stratigraphic test well and 3-D seismic domain. All of these investigations resulted in reducing the overall uncertainties.

*The Jim Bridger Power Station adjacent to the study site*

***Diagenetic alteration of sealing lithology/facies relative to increased/reduced bypass risk-*** Diagenesis and burial processes can affect the sealing/storage capacity of the seals and reservoirs. We assessed post-burial alteration/diagenesis using petrophysical, petrographic, and geochemical data to determine dominant diagenetic trends within the sealing lithology relative to impact on sealing capacity. We note several processes that had a direct impact on sealing potential. Thin section analysis observes that dolomitization occurred in the carbonates of the Amsden, Madison, and marine units of the Weber. We observe this process to have differing effects on the various units. Because of dolomitization, the Amsden and the Weber record a net porosity reduction likely due to coeval compaction. Thus, dolomitization in the Amsden confining unit increases the overall sealing capacity. Dolomitization in the Madison records an overall porosity gain. Therefore, the same diagenetic processes that occurred in the sealing lithology to increase the sealing potential are shown to decrease sealing potential in similar lithologies. Thermochemical reduction of sulfate was identified in the Madison, Amsden, and marine facies of the Weber, and resulted in a net decrease in porosity. Calcic and silicic cementation events observed in the Chugwater Group sediments had the greatest impact on sealing potential overall, as all primary porosity was destroyed. Silicic cementation in portions of the Weber was shown to decrease porosity and increase sealing potential, though the process was selective and laterally uncertain.

***Recommended assessments for characterization of confining lithologies using laboratory measurements and petrophysical data-*** On the basis of reducing geologic uncertainties relative to seal failure, holding capacity, rock properties, and regional geologic evaluations, we have identified the following rock evaluation criteria/parameters as crucial to defining long-term, low-risk storage at potential CCUS sites. These assessments involve various disciplines and analyses.

- Geophysics and Seismic Attributes
- Petrography
- Displacement Pressure
- Porosity/Permeability
- Rock Mechanics
- Coupled Geochemistry
- Basin and Sediment Evolution
- Porosity Architecture and Pore Throat Systems
- Petrophysical Analysis
- Diagenetic History

Additionally, we suggest investigating relative permeability of reservoirs, interfacial tension angles, fluid inclusion volatiles analysis of seals

for fluid history assessments, wettability responses to introduced fluids, formation damage assessments, and reactive transport modeling of seal mineralogy.

## Formation fluid characterization:

***Formation fluid analysis and baseline conditions-*** Evaluation of baseline formation fluid character is necessary to determine geochemical reactions, but also can be used to assess hydraulic connectivity, formation fluid histories, and estimate water-rock reactions. We analyzed formation fluids, collected in-situ at pressure/temperature and from the wellbore for major/minor and trace elements, dissolved gas compositions, radionuclides, isotopic compositions, rare earth element trends, and organics. In addition to baseline character and fluid history, these evaluations were crucial to determine the impact of drilling, completion and in-situ testing on fluid character. Sequential samples showed evidence of wellbore souring. If soured samples were determined to be baseline conditions, the geochemical models and engineering schemes would not have been representative of the majority of fluid conditions.

***Characterize formation fluids to determine hydraulic isolation of target formation-*** Reservoir formation fluids, collected at pressure/depth and within the flowing wellbore were critical for the determination of fluid history, mixing potential, and recharge evaluations, but were most importantly used to determine hydraulic connectivity of different reservoirs. This project helped to define the benefits of investigating fluids at sites with stacked reservoir systems. We used brine chemistry analysis, specifically analyte geochemistry and isotopic geochemistry, to test for reservoir hydraulic connection between the Madison and Weber reservoirs. These analyses provided immediate results pertinent to seal capacity between the reservoirs, and showed that the lower reservoir fluids in the Madison were not mixing with Weber fluids. Indicating that seals between the reservoirs were competent, and that potential seal bypass systems are closed. In-situ pressure analysis and other downhole testing further validated these results.

***Designing geochemical models-*** Geochemical models are instructive to predict water/rock/$CO_2$ reactions. For this project, we calibrated geochemical models with the formation brine compositions, mineralogy from the petrographic analysis, and experimental data from laboratory measurements. Allowing for more realistic approach to the geochemical models. Applying this approach to the geochemical models helps to design reservoir management plans that are better suited for the geologic conditions. The geochemical models were used to estimate:

- Risk of alteration to reservoir and or seals from $CO_2$ reactions
- Impact of geochemical responses on total storage volumes
- Reactive species assessment
- Correlation of geochemical responses to scaling models
- Surface treatment needs relative to geochemical responses

*Drill crew tripping pipe*

*Equipment on the well site*

## Simulations to evaluate seal integrity, injection rate, and pressure management:

A major goal of this project was to build a dynamic geologic/numerical model to assess seal integrity under varying injection scenarios. Models were built in Petrel and utilized Eclipse software. Diverse injection scenarios were generated using 3-D numerical computation models to create performance assessments and to evaluate seal integrity, reservoir injection feasibility and storage capacity, and to evaluate displaced fluid and pressure responses for management. Simulations of $CO_2$ injection volumes were run on the LANL multiphase porous flow simulator FEHM. 3-D fluid flow simulations include detailed calculations of subsurface fluid movement, including flow through injection wellbores, faults, and fractures under variable scenarios. We developed a probability-based PA model to evaluate the confining layer sealing capacity and integrity, and to evaluate the importance of parameters for numerical simulation of confining layers. Monte Carlo simulations were used to optimize $CO_2$ injection feasibility, storage capacity, reservoir pressure, and displaced fluid management scenarios. The importance and effects of the simulation input parameters were prioritized. These methods were evaluated to choose crucial input parameters for $CO_2$ injection numerical simulations using 3-D property model constructions relative to sealing capacities.

Important physical properties include (a) difference in density between formation water and supercritical $CO_2$; (b) contact angle between formation water and $CO_2$; (c) interfacial tension (IFT) between formation water and $CO_2$; and (d) entry pressure/pore throat size of the confining layer. Manipulative parameters, such as injection rate, were interpreted to have lower risk influences, as they were controllable. It is necessary to analyze the combined parameter effects on the final sealing capacity and maximum $CO_2$ column height of a specific confining layer.

***Determinations from dynamic simulation modeling-*** The most pertinent results from injection simulations include:

- Determinations of conservative sealing capacity of the confining layers at the study site
- $CO_2$ column height relative to individual confining layer properties
- Highest uncertainty parameters from sensitivity analysis
- Ideal low/risk well spacing
- Conservative injection rates
- Modeling constraints/additional data requirements
- Conservative injection volumes
- Failure thresholds of primary seals
- Active reservoir management for risk reduction with,
    - Integrated brine production/treatment facility
    - Pressure management scenarios
- Simulations of formation brine production to assess wellbore scaling/well integrity and surface treatment

***Well spacing and field design-*** Pressure management is identified as necessary to maintain low-risk pressure regimes within the reservoir during injection. As such, this project investigated the engineering risks associated with formation fluid production and treatment. Wellbore engineering evaluations identified the

materials best suited for reducing the risk of corrosional failure, and suggested best strategies for well spacing and radius. It was also determined the number of injection and production wells needed to obtain injection rates, and produced fluid for pressure maintenance in the uplift.

Utilizing Schlumberger software, production and injection well scenarios were developed to test risk relative to expected life-cycle and injection parameters. These provided the following results;

- Scaling response relative to formation brines/pressures
- Challenges associated with a single injector well in multiple, heterogeneous reservoirs
- Optimized well design using low-risk materials
- The need for a cost/risk assessment of prospective design packages

Well design assessments lowered the overall risks associated with failure due to corrosion, and helped define site specific results that would impact performance.

*Core retrieved from the reservoir and seal intervals of the RSU #1 stratigraphic test well*

## Suggested Research Gaps

We have identified several research gaps during the completion of this project. Some data were recognized to have a literature/published studies base that was too small to provide useful as analogs to this study site, or could have potentially relied on anomalous samples. Additionally, some of these methods are currently too expensive to create bulk databases for analogous projects; we suggest effort must be made to increase the amount of available data and lower the costs of these sorts of testing.

*Cutting samples from the varying stratigraphic intervals retrieved from the stratigraphic test will*

***IFT (interfacial tension angles) Analysis-*** Sensitivity analysis identified IFT as a crucial component to determine the holding potential of $CO_2$ of differing analyses. Furthermore, the available literature shows that the holding capacity of a sealing lithologies in the presence of injected $CO_2$ will be less than in hydrocarbon systems. This is certainly a concern for any CCS project, indicating that even if a reservoir has shown to hold oil and/or gas, it may not be enough to retain $CO_2$. IFT angles can vary within the same formation, increasing the uncertainty of using only one measurement per formation. Given the importance of defining IFT of seal and reservoir rocks in subsurface systems, we suggest implementing a program whose objective is to amass IFT data relative to analogous geology for use in subsurface studies. A program of this type would aid future CCUS projects, as well as hydrocarbon and groundwater studies.

***FIV (fluid inclusion volatiles) of reservoirs and seal cuttings-*** FIV can be used to help define prominent hydrocarbon systems relative to sealing responses across a vertical length of core and well cuttings. As these analyses are both expensive and destructive, they are not commonly performed. Furthermore, these studies benefit from correlative assessment from

analysis from several wells; though not as common, FIV results can vary well to well relative to geologic heterogeneity. The data and interpretations provided by IFT are broad and far-reaching. Combining multiple FIV analysis across a basin can be used to define total petroleum systems, the impact of seal bypass systems, fluid migration histories, and potential of leakage at given sites. We suggest that regularly incorporating FIV analysis into subsurface studies could reduce risks to $CO_2$ injection, hydrocarbon resource management, and reduce multiple subsurface risks on a basinal scale. We suggest implementing a program, similar to IFT, that builds an FIV database for use in advanced subsurface studies.

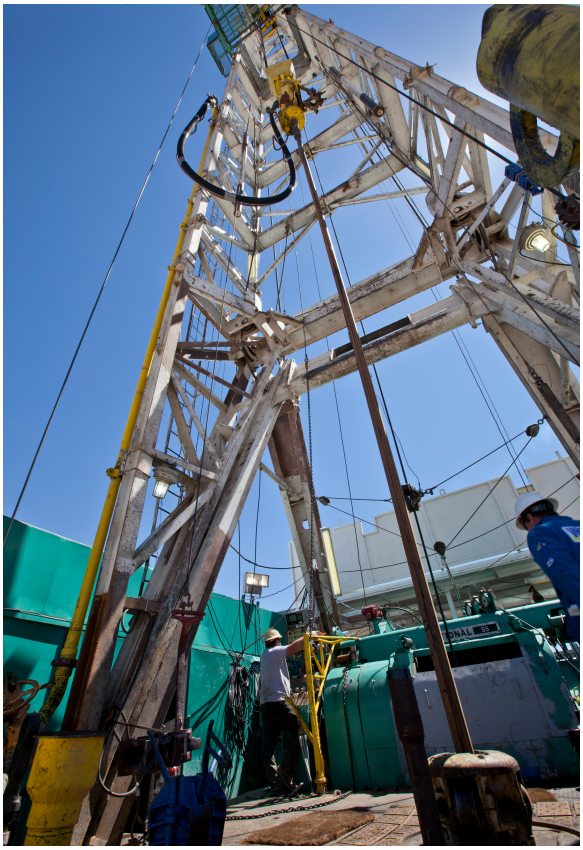

*Upward view of rig*

***Analysis of surface fluid systems-*** Multiple studies have evaluated the fluid systems at the surface of study sites to analyze both baseline conditions and the potential for preexisting deep fluid migration. Though local water wells were identified, complex studies of near-surface fluid and gases were not evaluated and would provide valuable data if injection were to occur. Suggested studies include near-surface water geochemical analysis, soil gas analysis, and isotopic ratios of gases.

***Additional core flooding-*** Data from additional core flooding might help to further refine numerical models. However, these tests are both expensive and time consuming and providing realistic type-sections from limited core data commonly leads to assumptions. Therefore, providing a core flooding dataset from analogous, transferrable lithology (i.e. various sandstones, carbonates, pore architectures, perme abilities) would be a great benefit to CCUS research.

## Challenges

This study identified several research gaps and analytical challenges that are pertinent to other CCS study sites.

***Lack of a Comprehensive Subsurface Brine Analysis Laboratory-*** One of the biggest constraints identified with a comprehensive analysis of formation brine was the lack of a single laboratory that was able to analyze multiple analytes and isotopic suites at pressure with low volumes of material. Commercial isotope and geochemistry labs require sample volumes that are not practical for retrieval at pressure. Academic labs are commonly constructed to handle a distinct set of isotopic suites (i.e. not a comprehensive set) and few have rarely worked with saline brines typical of CCUS sites. Not only were analytical capabilities determined to be restrictive, few institutions have developed methodologies capable of maintaining conditions for low-volume, pressurized samples. Sandia National Labs was recognized as a potential institution with the technical and analytical expertise/capabilities to handle this task, though their lack of experience with saline brines ended up being a limiting factor. Overall, this was frustrating with regard to the time, expense and effort our team put in to the sample collection and potential outcomes for this project. As the importance of the Nation's groundwater

resources become more apparent, we suggest that the development of methods and analytical techniques to evaluate low volumes of high saline brine at pressure is a crucial research gap with high potential benefits.

*Drill rig and slurry pit for RSU #1 (foreground), Jim Bridger coal-fired power plant (background)*

***Seismic data type relative to the near-surface features-*** A common discussion during initial design of the study parameters at the RSU was what the seismic survey should accomplish. As the targeted injection reservoirs are deep, the seismic survey collected at the study site was designed to intercept deeper formations. This resulted in a good survey for reservoir and seal assessment, but introduced a high degree of noise in the upper portions of the stratigraphic column. Though not a true hindrance to the project's goals, it did result in uncertainty in assessing faults near the surface. We felt this is worth noting to inform future/similar projects.

***Activity and character of large faults-*** This study identified one large fault, northeast and downdip of the possible injection site. As no wells penetrate this fault, it is difficult to assess its character. Given the current data, it is not possible to tell if this fault/fault system is permeable, and what pressure constraints could induce slippage. Therefore, we suggest utilizing a conservative injection strategy that would not result in testing the faults parameters.

*Mud log samples*

***Establishing baseline conditions and data parameters-*** All potential CCUS sites need to establish robust, reliable baseline fluid, reservoir and seal conditions. This project has shown that obtaining a representative sample of the formation fluid can be problematic. In fact, it can be compromised by well completion and testing strategies. This led to altered geochemical and engineering results, and might have changed suggested reservoir management strategies. We feel it is very important to highlight the challenge of establishing certain baseline datasets, and suggest creating unified technical review protocols for review of these data.

## Conclusions

This manual provides an overview of the recommended *Best Practices* to evaluate seal integrity at a CCUS site in southwest Wyoming. We employed a multidiscipline approach consisting of petroleum engineers, reservoir engineers, well site engineers, drilling specialists, seismic/vibraphone engineers, petrophysicists. Multiple, competent seals were identified using these methodologies. These methods are recommended and fully transferrable to other CCUS sites. A full description of this project and the employed methodologies are provided in the final report issued to the Department of Fossil Energy.